

Preferential Flow

Stokes Approach to
Infiltration and Drainage

Peter Germann

Preferential Flow -
Stokes Approach to
Infiltration and Drainage

GEOGRAPHICA BERNENSIA

Published by Lectureres of the Institute of Geography
University of Bern, Switzerland

Series A	African Studies
Series B	Field Guides (German only)
Series G	Basic Research (mainly in German)
Series P	Applied Geography (German only)
Series U	Teaching Materials (German only)

G 88

Arbeitsgemeinschaft GEOGRAPHICA BERNENSIA
in cooperation with
Geographical Society of Bern
Hallerstrasse 12 CH-3012 Bern (Switzerland)

Preferential Flow -

Stokes Approach to

Infiltration and Drainage

Peter F. Germann
Professor Emeritus of Soil Science
University of Bern

Institute of Geography
University of Bern

The book draws from projects financially supported by the following agencies:

Swiss National Science Foundation
Swiss Federal Office for the Environment
US-National Science Foundation
US-Environmental Protection Agency
US-Agricultural Research Service
US-Forest Service
New Jersey Agricultural Experiment Station

Prof. em. Peter F. Germann
Haldenackerweg 21
CH-3065 Bolligen (Switzerland)
pf.germann@bluewin.ch

Cover

Stains in a paddy soil under rice, Pakistan.
Courtesy by Anna Fehlmann and Bettina Wolfgramm
Design by Alexander Hermann

Published by

Geographica Bernensia, University of Bern

Graphics by

Alfred Bretscher, Peter Germann, Alexander Hermann
Institute of Geography, University of Bern

Printed by

Publikation Digital AG
Bolacker 3, 4564 Obergerlafingen, Switzerland

Geographica Bernensia 2014
Print version: ISBN 978-3-905835-34-2

Geographica Bernensia 2018
Corrected online version: doi: 10.4480/GB2018.G88

© GEOGRAPHICA BERNENSIA 2018
Institute of Geography, University of Bern, Switzerland



Creative Commons Licences

*To Dorothee,
who had different views
on our first five years of
retirement*

Preface

About the book

There are two ways of irrigating a potted plant. Water is either added to the plate at the pot's bottom from where the soil sucks it up gradually or it is sprinkled on the surface from where it infiltrates and drains rapidly. Preferential flow deals with the second way of irrigation.

Preferential flow in permeable media concerns various disciplines like the sciences of soils and ecosystems at large, the hydrology of soils, catchments, and aquifers as well as various areas of geology and geophysics. Preferential flow also relates to numerous applications such as irrigation and drainage, and it raises issues of water quality and sanitation. Equally diverse are the backgrounds of experts dealing with preferential flow. This has produced a wide number of approaches to preferential flow of both, the experimental and the modeling kinds.

This book offers a unifying concept based on first principles of hydrodynamics, leading to viscous flow in permeable media. This starting point notwithstanding, the issues are easy to understand, requiring but skills in mathematics and physics offered to BSc-students attending university science or engineering courses. Einstein's recommendation of *Everything should be made as simple as possible, but not simpler* is highly regarded.

Part I develops a track of concepts from Newton (1729) to Stokes (1845, 1851) and then Lamb (1932). It presents the principles of viscous flow in permeable media, supplemented with the mathematical tool of the kinematic wave theory of Lighthill and Witham (1955). Accordingly, flow in partially saturated permeable media is only dependent on time-variable boundary conditions and time-invariant properties of the medium. Thus, flow is treated with ordinary differential equations similar to Darcy's law describing flow in water-saturated permeable media.

Part II applies these principles to data recorded in systems of various complexity. It also explores the theory's limitations in space and time. In addition, it provides information detailed enough that the readers can calculate the examples for themselves as personal exercises.

Preferential Flow – Stokes Approach to Infiltration and Drainage may serve students, teachers, researchers, and practitioners alike as a handbook that presents an old phenomenon in a fresh and comprehensive manner.

About the context

It is a privilege to look back at the trials, errors and occasional successes over the last four decades presented in numerous articles, chapters, proceedings, proposals, theses and dissertations. The enviable position of a professor emeritus includes release from obligations whereas the forced cessation of experimentation offers an opportunity to reshape accumulated knowledge in a manner similar to sculpting: chisel all unnecessary material away from the chunk in the expectation that the remainder will catch attention.

All began when Felix Richard, the first Soil-Physics Professor at the ETH in Zürich, sparked my interest in his subject during my education as a forestry engineer. He lectured about drainage of forest soils aimed at improving root aeration in soils of lesser quality at sites foreseen for reforestation. At that time the expansion of the forested area in the Swiss Pre-Alps was still a national mandate based on, among other reasons, the Forest Hydrological Paradigm that forests are the canopies that reduce flood-flows most efficiently. My PhD-project with Felix Richard at the Swiss Federal Forest Research station (EAFV, today's WSL) concentrated on the weekly soil-water balances of forest and grass-land patches, based on the Darcy-Richards relationships. The data base was two years of periodic in-situ suction measurements with hundreds of tensiometers and the determination of soil-water functions on dozens of soil samples. However, closing the water balance occasionally produced apparently negative evapo-transpiration values. The environmental physicist Paul Schmid-Haas at the EAFV had already in the early 1970s begun to question the general applicability of the underlying relationships.

Difficulties with the Richards-approach continued during my Post-Doc with Herbert Lang's team at the Laboratories of Hydraulics, Hydrology and Glaciology (VAW) at the ETH-Zürich, where our group investigated hydro-meteorological relationships in the first-order watershed Rietholzbach. It was suspected that occasional fast flows along root channels were severely disturbing the closure of the water balance.

A major breakthrough came in 1979 when the Swiss National Science Foundation granted me a one-year study leave at the Institute of Hydrology (IH) in Wallingford (UK). Keith Beven and I collected reported deviations from Darcy-Richards type flow. Not surprisingly, the notion surfaced of kinematic-wave theory as a feasible alternative, merely because Dave Woolhiser, then introducing the theory to hydrology, had visited the IH the preceding year. The continuing exchange with Keith was particularly intense from 1980 to 1982 when he lured me to the faculty of the Environmental-Sciences Department at the University of Virginia, where he had been offered a position as Assistant Professor in late 1979. We recorded flow in blocks of undisturbed soils with the university hospital's X-ray facility. We soon concluded that the

integration periods of measuring soil water contents with gamma-ray- and neutron-probes were far too long to test any of our hypotheses during presumed macropore flows, and that we should turn to direct flow measurements instead. The still cited paper of 1982 in *Water Resources Research* about *Macropores and Water Flow in Soils* expresses the climax of our co-operation. We are now wondering about the fate of its 2013-revisit in the same journal.

Projects with Bill Edwards and Bob Pierce during the summer breaks at the USDA-watershed at Coshocton (OH) (1981) and at Hubbard Brook (NH) watersheds, operated by the US-Forest Service (1982) added experimental evidence of fast flows in soils. At Coshocton we investigated in columns of undisturbed soils the spatial distribution of bromide in the vicinity of stained macropores after infiltrating a solution of dye and salt. We demonstrated the kinematic wave's applicability at Hubbard Brook by measuring with a bucket, stop watch and spring balance drainage flows from an inclined glacial till upon sprinkling on the isolated soil block above it. Technical advances in fast in-situ water-pressure logging switched our attention to the rise of a shallow water table as a reaction to ponded infiltration. The methodology was implemented at Adelphia Research Farm, operated by Cook College of Agriculture at Rutgers University, where I served as an Associate Research Professor of Soil Physics from 1986 to 1989 in the Soils-and-Crops department.

However, the attraction of becoming the first chaired Professor of Soil Science at the Institute of Geography, University of Bern was stronger. Theses and dissertations applied the TDR-technique to the fast in-situ recordings of water-content waves due to controlled sprinkler infiltration. With the uncorrupted mind of the practitioner André Chervet of the soil protection agency of the Canton of Bern (Switzerland) recognized immediately fast drainage as independent flow between saturation and field capacity when he first glanced at a graph of such a wave. Discussions with Liliana Di Pietro from INRA in Avignon (France) and Vijay P. Singh, then professor at the Louisiana State University and a former PhD-student of Dave Woolhiser's, led to the application of kinematic waves to in-situ measured water content waves. With the help of Peter Vontobel, Eberhard Lehmann and René Hassanein at the Paul-Scherrer-Institute in Villigen (Switzerland) we applied neutron radiography to sand-box infiltrations which revealed the theory's applicability to finger flow. Discussions with Christine Riedtmann, Jürg Schmid, Hanspeter Bieri, and Jürg Gasser from the Institutes of Mathematics, Applied Mathematics and Physics at Bern University cleared theoretical hurdles. Dani Or, third Soil Physics Professor at the ETH in Zürich and always a reliable sparing partner, provided valuable links to porous-media flow. Yvo Flammer, a Post-Doc from applied physics, and his group recorded with acoustic tomography the dynamic patterns of water content distributions in soil columns. However, the spatial resolution did not suffice to investigate flow but it was

sensitive enough to record soil rigidity. Peter Lüscher with his co-workers from soil-protection at WSL applied the infiltration method and found that mainly the soil under the forest, rather than the forest canopy, controls flood mitigation, while root densities only in poorly drainable substrates are of significance to the Forest Hydrological Paradigm.

From here the thread is spooled further back. Arnold Engler was professor of silviculture at the ETH in Zürich and was also instrumental in 1903 in initiating the comparative precipitation-runoff investigations in heavily forested Sperbelgraben and the poorly forested Rappengraben, both small catchments in the Swiss Pre-Alps. Under Engler's guidance the dissertation of Hans Burger focused on infiltration. In his later function as director of EAFV/WSL Burger hired Felix Richard in 1951, who had then just returned from a two-year study-leave at Berkeley and Cornell where he picked up the latest on soil physics.

The stroll upstream to the confluences and sources of the concepts and ideas developed in this book expresses my gratitude to those who were involved, while the responsibility for the book rests entirely with me.

Acknowledgments

Wilfried Brutsaert (Cornell University), Rudi Hilfer (University of Stuttgart), Jean-Yve Parlange (Cornell University), and Andreas Verdun (University of Bern) paved the way to Newton, Stokes, and Lamb. Said alHagrey and his colleagues (Christian-Albrechts-Universität zu Kiel) provided the sand-tank data. Alfred Bretscher (Bern) and Alexander Hermann (Bern) took care of the graphs, while Richard Randell (Bern) helped with the English. Stephan Brönnimann and Monika Wälti (Bern) from the publisher kept the process going. The book draws from projects supported by grants from the Swiss National Science Foundation since 1969, US-NSF, US-EPA, USDA, and BAFU (Switzerland). The Institute of Geography, University of Bern, provided technical support.

Peter Germann
Bolligen (Switzerland)
March 2014

Foreword

Soil physics and catchment hydrology

Keith Beven

I first met Peter Germann in 1979 when he arrived with his family to spend a year at the Institute of Hydrology at Wallingford as a post-doctoral research fellow funded by the Swiss National Science Foundation. This was soon after he had completed his PhD thesis work with its remarkable set of observed soil water potential data in a forest soil of loess near Basel, Switzerland. Thirty-seven profiles on a 8-m triangular grid, each with 12 tensiometers at 9 depths, with 3 measurements per week over 20 months. Later, when we were both at the University of Virginia we calculated about 2000 variograms based on that data set (for every level and every day of adequate data). The exercise conditioned my attitude to geostatistical analysis for ever, since we found that the data showed every possible form of variogram, including triangular shapes, shapes with consistently declining variance with distance, as well as the more acceptable text book shapes. The analysis was never published because of the difficulty of making sense of it all. There was structure in the data, the pattern of wetting progressing into the profiles could be distinguished for some events, but it was clear that the soil physics that lay behind the observations was much more complex than the textbooks at that time described.

While at Wallingford Peter and I worked together on field, laboratory and modelling to try and understand this complexity a little better, particularly the role of macropore flows and bypassing of storage in the soil matrix. This resulted in a number of papers, including the highly cited review of *Macropores and Water Flow in Soils* published in Water Resources Research in 1982. In that paper, building on the earlier work of Johan Bouma in the Netherlands, and Thomas, Phillips and Quisenberry in the United States, we effectively set down a challenge to the soil physics community to take more account of preferential flows in the representation of water flows at the profile to catchment scales. We recently reviewed progress in doing so in the intervening 30 years in *Macropores and Water flow in Soils Revisited* (Water Resources Research, 2013).

It had to be concluded from that review that not much progress has been made in soil physics in its use at larger scales. I am a hydrologist, I am interested in the representation of water flows at profile, hillslope and catchment scales, with all the heterogeneities of soil properties and structure and flow pathways that entails. In that 30 years there have been numerous and exten-

sive tracing experiments that demonstrate the complexities of water flows in the soil, but without any concomitant development of a coherent soil physics theory to address the problem. Certainly some modifications have been made in soil water models based on the Darcy-Richards equation to try and take some account of preferential flows (dual porosity, dual permeability, dual continuum and modified conductivity characteristic approaches) but none of these are particularly satisfactory.

But as Peter demonstrates so nicely in the text that follows, the problem is more fundamental than that. Traditional soil physics and the Darcy-Richards equation are based on the wrong experiment. The experiments of Lorenzo A. Richards, reported in 1931, were a nice piece of physics with well-controlled boundary conditions maintaining steady flows under unsaturated equilibrium conditions. It is just that water flows in real soils are not like that. The air phase is not generally at less than atmospheric pressure (Robert Horton had already recognised the importance of macropores in equilibrating air pressures during infiltration in the 1930s). And capillary potential gradients do not equilibrate over any significant distance. In fact, even if the Darcy-Richards equation did hold at the small scale, then the theory suggests that for an unsaturated heterogeneous soil a different equation should be used at larger scales because the gradient and nonlinear conductivity terms do not average linearly. This is not at all a new insight but has not had a great impact on practice.

So why has the hydrologist persisted with the Darcy-Richards approach for so long? I think there are a number of reasons. Firstly, other more conceptual models at the hillslope and catchment scales have been available and, with some calibration, can often be shown to give acceptable predictions of observations of discharges without any need to consider flow pathways. Secondly, the development of software based on the Darcy-Richards equation has made the theory easy to use (though having developed an early finite element methods for hillslope hydrology in my own PhD thesis, I wonder what numerical tricks are being used in modern solutions to constrain stability, convergence and mass balance). Thirdly, there has been no new development capable of dealing with the complexity of flows revealed by tracing experiments. Perhaps the more surprising question is why have soil physicists persisted with the Darcy-Richards approach for so long, when they really should know better by now?

This book represents a major effort to change this situation. Peter, to his great credit, has persisted with his research on finding a more realistic representation of water flow in soils throughout that 30 years. He has persisted with trying to develop new methods of observing flow phenomena, both in the field and laboratory, and with testing different theoretical representations of the phenomena observed. For my part, I had a couple of attempts at better ways of representing preferential flows at large scales (including the recent

Multiple Interacting Pathways model, which is compatible with the concepts presented in this book) but I have been mostly distracted by other things, particularly the similarly difficult problem of dealing with epistemic uncertainties in hydrological models (one of which is the lack of understanding of preferential flow on hillslopes and its impact on hydrographs and transport processes).

In following these different careers we have both had to deal with criticism and uncomprehending referees. But we both had a belief that, in these different domains, better approaches were possible. This book represents the culmination of Peter's work, presented in a consistent and coherent framework based on Stokes flow for that part of the water flow regime concerned with rapid wetting and drying in the laminar flow range. One of the nice features of this approach, from a hydrologist's point of view, is the relative scale independence of the theory. Use of the Stokes flow representation, and the way in which the flow organises to deal with different flux rates, can be justified at larger hillslope and catchment scales (though there will still be an issue of dealing with non-laminar flows in discrete preferential flow pathways at these scales).

So there is an opportunity here to change the way the hydrologist approaches process-based soil water models. Another feature of the theory is that it provides hypotheses about rates of wetting and drying front displacement that can be tested in the field, both for vertical infiltration and initial drying and downslope flows. The past dominance of Darcy-Richards theory needs to be questioned. More rigorous testing of Darcy-Richards, and alternatives to it, as hypotheses would be valuable in doing so.

However, there are difficulties in doing so, not least because of the limitations of current measurement methodologies. There have been many studies in the past, for example, where profile measurements based on tensiometers and piezometers have revealed that deeper tensiometers have wetted more quickly than shallower tensiometers during infiltration to the extent that the apparent hydraulic gradient is negative with respect to the vertical. The flux is known to be downwards so a calculation of hydraulic conductivity would also yield (nonsensical) negative values. Clearly, based on the measurements alone this is a falsification of the Darcy-Richards equation. Yet I cannot think of any papers where this has been stated explicitly. I do know of some cases where negative conductivities were not reported and where the issue has been reported it is generally seen as a problem of experimental technique rather than of the underlying Darcy-Richards concept.

This could be read as a failure of the scientific method in soil physics, but there are (of course) mitigating circumstances in that a few tensiometers in a profile cannot give a full picture of the 3D complexity of water flows which

might then (possibly) be consistent with Darcy-Richards at smaller scales. Similar problems arise in going to larger scales. Point measurements of soil water content or water table elevations do not give a full picture of the 3D complexity of flows on a hillslope, and it is impossible to measure bulk values of storage or discharge at the hillslope scale (particularly where there may be deeper preferential flows in the underlying regolith and bedrock). Stream discharges can be measured at the catchment scale but are then an integral of all the complex flow processes and pathways at the smaller scale. Tracer experiments again suggest that preferential flows are important but while this has been recognised in a number of perceptual models of how hillslopes and small catchments function, it has rarely been treated explicitly in quantitative models.

Thus, doing better science and better hypothesis testing is dependent on having better measurement techniques. It would seem that for the foreseeable future this will be easier at the laboratory scale (see some of the results presented in this book) than at the hillslope and catchment scales. We can speculate about alternative approaches at the larger scale (see Beven and Germann, 2013, and Chapter 13 in this book) but testing alternative hypotheses will remain difficult. That is not to suggest, of course, that such a challenge should not be taken up with creative enthusiasm. That is, after all, how science progresses.

Keith Beven
Lancaster Environment Centre
Lancaster University, UK
April 2013

Preface	i
Foreword	v
Table of Content	ix

Preferential Flow - Stokes-Approach to Infiltration and Drainage

1. Introduction	1
1.1 Synopsis	1
1.2 Soils representing permeable media	4
1.3 Preferential flow	5
1.4 Assumptions and restrictions	9
1.5 Guide to the book	9

Part I Stokes-Flow Applied to Preferential Infiltration

2. Fundamentals	12
2.1 Introduction	12
2.2 Gravity	13
2.3 Viscosity	15
2.4 Elements of Stokes flow	17
2.5 Surface tension, capillarity, and water retention	19
3. The water-content wave, WCW	25
3.1 Introduction	25
3.2 Adaptation of Stokes-flow to infiltration	26
3.3 Draining front and trailing wave	27
3.4 Profiles of mobile water content, $w(z, \tau)$	29
3.5 Time series of mobile water contents $w(\zeta, t)$	31
3.6 Initial and boundary conditions (IC and BC)	33
4. Routing input pulses as kinematic waves	37
4.1 Introduction	37
4.2 Kinematic wave theory	38
4.3 Propagation of a single pulse	40
4.4 The interception function	43
4.5 Propagation of a decreasing jump	44
4.6 Propagation of an increasing jump	47
4.7 Superposition of kinematic waves	49
4.8 Kinematic waves that include a sink term	50
4.9 Summary	51

5. Geometries of flow	53
5.1 Introduction	53
5.2 Flow between two parallel walls - plane-Poiseuille flow (<i>pP</i>)	54
5.3 Flow along a vertical cylinder - Hagen-Poiseuille flow (<i>HP</i>)	55
5.4 Corner-flow (<i>Co</i>)	57
5.5 Impact of the presumed flow geometries on viscous flow	59
5.6 Dominance of viscosity	61
6. Darcy's law and the Richards equation in view of viscous flow	63
6.1 Introduction	63
6.2 Saturated permeable media - Darcy's (1856) law	63
6.3 Darcy's law and viscous flow	66
6.4 Partially saturated permeable media – the Richards (1931) equation	68
6.5 Richards equation and viscous flow	71
6.6 Capillary number, Ca , and Bond number, Bo	72
6.7 Domains of flow in permeable media	73
7. Part I Conclusion	75
7.1 Achievements	75
7.3 Preview of Part II	77

Part II

Viscous Flow Applied to Infiltration and Drainage

8. Experimental protocol, data acquisition and interpretation	80
8.1 Introduction	80
8.2 Experimental protocol	82
8.3 Estimation of F and L from drainage flow, $q(Z, t)$	83
8.4 Estimation of F and L from a water-content time series, $\theta(Z, t)$	87
8.5 Summary	90
9. Procedures at the local level	91
9.1 Introduction	91
9.2 Wetting front arrival	91
9.3 Rivulet approach	92
9.4 Water abstraction from a WCW	94
9.5 Restricted drainage flow	97
9.6 Minimal interval for analyzing $q(z, t)$ and $\theta(z, t)$	99
9.7 Relationship $v_F(q)$	101
9.8 Viscous flow in fissured rocks	103
9.9 Summary	105

10. Procedures at the profile level	107
10.1 Introduction	107
10.2 Evolution of a WCW	107
10.3 Viscous flow initiation in dry soil	109
10.4 Viscous flow restrictions at interfaces	115
10.5 Viscous flow and finger flow	119
10.6 Viscous flow and dye staining	130
10.7 Summary	130
11. Procedures at the system level	133
11.1 Introduction	133
11.2 The Kiel sand tank	133
11.3 Viscous flow matching to the data	135
11.4 Spatial structures of viscous flow	137
11.5 Capillary heads h_{cap}	142
11.6 Summary	145
12. Procedures at the flow-path level	147
12.1 Introduction	147
12.2 Superposition of kinematic waves – Lorin’s candle	147
12.3 Plausibility of v_F and L in unconsolidated sands	149
12.4 Viscous flow between SWI and AWI	153
12.5 Viscous flow and capillary heads	157
12.6. Viscous flow and structural voids	164
13. On scales and extents of viscous flow	167
13.1 Introduction	167
13.2 Temporal scaling of viscous flow	168
13.3 Spatial scaling of viscous flow	170
13.4 Macropore flow	171
13.5 Wetting front velocities	172
13.6 Temporal and spatial extents of viscous flow	174
13.7 Viscous flow scaling in hillslope hydrology	175
List of References	181
List of Topics	188
List of Symbols	190
List of Subscripts	192
List of Acronyms and Abbreviations	193
Index	195

Preferential Flow - Stokes Approach to Infiltration and Drainage

*Why does water know
where to flow?
Is the strongest force
dictating the course?
Is the weakest resistance
controlling the distance?
Or is soil hydrology nothing but mental strength
fiddling with mass, time and length?
(P.G., Bolligen October 2010)*

*Summary of a discussion
with Liliana Di Pietro at INRA
upon a lunch time contemplation on a terrace
watching waves and whirls in the river Sorgue
rippling around the old city of Ile-sur-la-Sorgue.
Avignon, June 1996*

1. Introduction

1.1 Synopsis

Infiltration summarizes the transgression of liquid water from above to below ground, and the subsequent movement within it. Infiltration is a process in the terrestrial water cycle that appeals to hydrologists, geologists, and soil scientists alike. Take the annual water balance of the Swiss low-lands as an example, where the average annual precipitation amounts from about 1'000 to 1'200 liters per square meter. About half of it returns as water vapor to the atmosphere via evapo-transpiration and interception, while the remainder keeps seeping until it eventually reaches groundwater, a well or similar surface waters. Even in the rainy climate of the Toggenburg valley in Eastern Switzerland covers the total duration of precipitation less than 7(%)of the

year (Germann, 1980). The major part returning to the atmosphere is due to transpiration through plant leaves during daytime which may last a total of about one third of the year, while underground percolation continues steadily and may last for years. The bulk of seepage typically proceeds anti-cyclic with regard to evapo-transpiration and advances about one to ten vertical meters per year. The corresponding nitrate front advanced about 1 to 2(m) in the English chalk formation according to Wellings and Bell (1980).

However, Fig. 1.1 provides evidence that infiltration fronts may proceed much faster. The figure depicts the results from an infiltration experiment at a site with a perching water table at the depth of about 1.9(m). Water supply was through an artificial pond of 1(m) by 1(m). A pressure transducer was placed just below the antecedent water table underneath the small pond and an access tube was installed at the edge of the pond for recording soil moisture profiles with a neutron-probe. Figure 1.1a shows the time series of the pressure head which first increased at $[T_{w,1} = 1'850(s)]$ after the beginning of ponding, peaked shortly after the cessation of infiltration at about 0.65(m) above the original water level and gradually returned to it at around 26(ks). A second, more gentle but persisting increase started at $[T_{w,2} = 33'800(s)]$. Figure 1.1b shows the profiles of increased soil moisture with respect to its antecedent state. The pronounced rise of pressure head was accompanied with modest soil moisture increases whereas the later modest and persistent increase of the pressure head showed much higher water content increases, particularly near the water table where complete saturation is assumed. The first increase of pressure head is attributed to a fast moving wetting front and the second one to its slower counterpart. The original depth of the water table divided by the time lapsed between the beginning of infiltration and the wetting front hitting the water table produces the average wetting front velocity. The early and late arrival times yield two wetting front velocities with their approximate ratio of 18:1. Numerous similar observations are reported, and comparably fast advancements of wetting fronts we will ascribe here to *preferential infiltration*.

The soil surface represents the interface between above and below ground. Water from above arrives at the surface either in discrete drops, like rain, or as coherent liquid during overland flow, stem flow or ponding. The solid part beneath the surface contains connected voids that permit water to seep through the ground, thus classifying the medium as permeable. Here, the surface water enters abruptly an environment built of the rigid, yet porous matrix whose voids are filled either with water, the wetting fluid, or air, the non-wetting fluid. The two fluids' respective shares of the pore space vary with time, and both carry the bio-chemical signatures of their immediate environment. Huge internal surfaces exist among the solid, liquid and gas phases, and the interplay of gravity, viscosity and surface tension governs flow in intricate patterns.

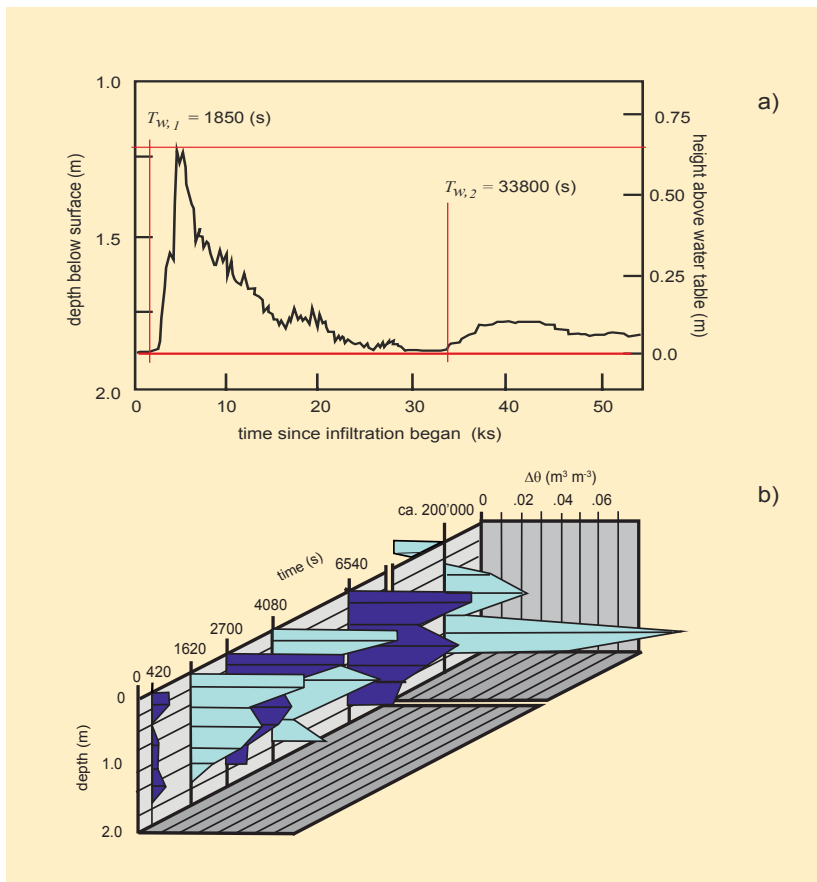


Figure 1.1: Illustration of presumed preferential flow: Reaction of a shallow ground-water table on ponded infiltration.

- a) Reaction of a pressure transducer mounted underneath the antecedent water table. Rapid pressure increase starts at $[T_{w,1} = 1'850(s)]$ after the beginning of infiltration, attaining a peak after approximately 4'800(s) and at approximately 0.65(m) above the antecedent level. The gradual increase starts at $[T_{w,2} = 33'800(s)]$.
 - b) Profiles of water content variations $\Delta\theta$ ($m^3 m^{-3}$) with respect to antecedent conditions, monitored with a neutron probe. Minor increases occurred above the water table after the first pressure increase, while the soil at the same depth was probably saturated during the second and gradual pressure increase.
- The early rapid pressure increase combined with modest water-content increase is attributed to preferential flow. The later slow pressure increase combined with pronounced water-content increase is ascribed to sequential flow.

(Adelphia Experimental Farm, Cook College, Rutgers, The State University of New Jersey.)

There are two major properties to consider when dealing with simultaneous flows of water and air in permeable media. One accentuates the water's tensile strength and subsequently focuses on capillarity. Early concepts go back to Buckingham (1907) whose perception led to the well established Richards (1931) equation on *capillary flow*. The other one pronounces viscosity, thus elevating *viscous flow* to the central theme of the book.

1.2 Soils representing permeable media

Soils are most prominent and, arguably, spatially the most variable representatives of grounds containing well-connected pores. Because of their complex void geometries concepts of infiltration applicable to soils most likely apply also to unconsolidated sediments and fissured rocks.

Hillel (2005), for instance, summarizes the soil properties that are here relevant:

The term 'soil' refers to the weathered and fragmented outer layer of our planet's land surfaces. Formed initially through the physical disintegration and chemical alteration of rocks and minerals by physical and biogeochemical processes, soil is influenced by the activity and accumulated residues of a myriad of diverse forms of life. As it occurs in different geologic and climatic domains, soil is an exceedingly variegated body

He continues:

Another intrinsic attribute of the soil is its sponge-like porosity and its enormous internal surface area. [A] fistful of soil may actually consist of several hectares of active surface, upon which physicochemical processes take place continuously.

And:

Soil also determines the fate of rainfall and snowfall reaching the ground surface - whether the water thus received will flow over the land as runoff, or seep downward to the subterranean reservoir called groundwater, which in turn maintains the steady flow of springs and streams.

Well aware of the extreme abstraction of, and injustice against soils, the interactions between their fabrics and infiltration, soils will be reduced here to some physical parameters and functions, thus consciously neglecting details about pore structure, connectivity, tortuosity, and properties of the internal surfaces, among many other subjects worth our attention. Thus, properties of *permeable media* are here considered distillations from soils, unconsolidated sediments, fissured rocks and other substrates containing well-connected pores.

1.3 Preferential flow

Preferential flow summarizes observations of permeable-media flows that are faster than ordinarily perceived. It suffices at the moment to relate faster flows with the example presented in Fig. 1.1, while Chapter 6 will discuss in details their relations with so-called *ordinary flow*.

Jury (1999) stated clearly that

Preferential flow is no longer a pathological phenomenon found only in Tennessee soil columns; it is manifest in virtually every field where it has been investigated. It might be due to instabilities, geometry, or simply lateral flow and channeling, and it depends strongly on water content and even boundary conditions of the experiments where it is observed. At the present time, we do not even know what soil characteristics to look for other than gapping cracks and crevices.

Preferential flow is a subject of increasing awareness as Gerke et al. (2010) have summarized. Concepts of preferential flow evolved, disappeared, and resurfaced again, resulting in the common denominator that neither Darcy's (1856) law nor the Richards (1931) equation adequately deal with the process. Yet a generally recognized concept of preferential flow is still missing which hints at an epistemic deficiency.

Darcy (1856) was probably the first to systematically quantify flow in water-saturated granular media. He expressed flow in a solid-liquid two-phase system as a macroscopic process with the entire cross section of a permeable medium as reference, regardless of the specific arrangements of grains and voids. Darcy stated that the volume flux density is proportional to the gradient of the hydraulic head while the factor of proportionality, K_{sat} , completely describes the hydraulic property of a permeable medium. This view of treating flow as a process occurring in an entire permeable medium without much concern about its internal structure is referred to as a Darcian approach to flow at the corresponding Darcy scale. (See Sections 6.2 and 6.3 for details.)

In the quest for dealing with flows with time-variable water contents less than saturation Richards (1931) added a continuous gas phase to Darcy's solid-liquid flow system. Capillarity appeared as an additional force that is due to the water's surface tension in the presence of the gas phase and the liquid's affinity to the solid phase. Richards dubbed this kind of flow as *capillary flow*. Richards had to turn Darcy's constant factor of proportionality into a function of the time-variable water content. Both, factor and function of proportionality are deduced from back-calculating specific experimental results. The apparently simple addition of the gas phase increases the number of interfaces and interactions to be dealt with. The Richards equation relies

on sequential flow, meaning that bigger pores have to empty before smaller ones do during drainage, whereas during imbibition smaller voids have to fill before larger ones are allowed to do. (See also Sections 6.4 and 6.5.)

However, already Lawes et al. (1882) observed that

The drainage water of a soil may thus be of two kinds (1) of rainwater that has passed with but little change in composition down the open channels of the soil; or (2) of the water discharged from the pores of a saturated soil.

Their observations contradict the space-averaging flow concepts of Darcy's saturated and Richards' sequential flow. They launched the discussion about preferential flow in macropores as, for instance, a century later Beven and Germann (1982) have reviewed. Further, non-equilibrium flow became a common expression for larger pores conducting water before smaller pores are saturated as Jarvis (2007), among others, explains. Thus, *preferential flow* is also viewed in contrast to Richards' (1931) *sequential flow*.

Two major groups of preferential flows are commonly recognized, macropore flow and finger flow. Macropore flow on one side is considered along fissures, cracks and voids that some authors assume wide enough for not exerting capillary forces onto flow. Finger flow, on the other side, may occur even in homogeneous matrices. It does not require macropores but occurs in zones of higher water contents that are well separated from their dryer surroundings. Experimental evidence demonstrates viscous flow to apply to both groups (Hincapié and Germann, 2010).

Under the exclusion of finger flow, the majority of the approaches to preferential flow adhere to the paradigm of flow in macropores of some sort as a separable domain of the pore space causing non-Richards- or a particular Richards-flow behavior, while sequential capillary flow occurs in the micropore domain with due consideration of flow interactions between the two domains (see, for instance, Gerke et al., 2010). Gerke and van Genuchten (1993) were most likely the first who presented an elaborated dual-porosity concept, while Jarvis' (2007) model MACRO is widely applied to the assessment of preferential flow and transport in field soils. Dual-porosity approaches are commonly loaded with the requirement of an *a priori* definition of the threshold between the two domains, either by direct assessment of the soil structure from tomographic information (see, for instance, Snehota et al., 2010) or by some calibration procedure as, for example, Alaoui et al. (2003) have presented. Further, Watson and Luxmoore (1986) explained preferential flow from pore size distributions derived from in-situ measurements with tension infiltrometers. Moreover, there are numerical approaches based on particular solutions of the Navier-Stokes equation. Among them is the Lattice-Gas Automaton approach according, for example, to

Di Pietro et al. (1993) and to Di Pietro (1996) that presumes the arrangement and dimension of pores. Adaptations of the Navier-Stokes equation have also been applied more directly to 2- and 3-d images of pore structures (Heijns et al., 1995). More recently, radiographic and tomographic information was used to improve models as, for instance, Snehota et al. (2010) have proposed.

However, neither Darcy (1856), nor Buckingham (1907) nor Richards (1931) stressed a priori the separation of pores and presumed flow paths. They rather postulated models that are solidly founded on theoretical principles representing well the processes they have envisioned from experience. They also provided the procedures for the experimental determination of the associated parameters and functions. The three authors serve as role models in the development of this treatise including the appreciation of the respective scales in the studies of permeable media flow. Richards (1931) was particularly clear in the definition of *capillary flow* as will be laid out in Sections 6.4 and 6.5. He implicitly did not exclude approaches that are not primarily focusing on capillarity. The contrary is quite feasible in that theories may cover aspects of flow in permeable media that do not require the definition of particular pore dimensions, and that do not fix the sequence of processes like the separation of Darcy's law from Richards equation based on absence or presence of capillarity. Instead, it is conceivable that elements of both flow processes may occur in the same volume of a permeable medium and even at the same time. More specific, there is no reason to a priori reject the co-existence of viscous flow and capillary flow in permeable media. A thin water film between two glass plates may illustrate the case. Gliding one glass plate tangentially along the other one requires but little effort when compared with the force needed to tear the glass plates apart in the direction perpendicular to their main areal extent. Gliding relates to lubricity (which consequently leads to viscous flow) by letting the clusters of water molecules move rather freely within the film, while tearing the plates apart has to rupture the film which is related with the water's tensile strength. Apart from the scale difference to be considered when thus comparing the tensile strength with the viscous force, just the co-existence of gliding and tearing suggests the co-existence of viscous and tensile behavior within a common range of hydro-mechanical properties.

Lamb's (1932) *Article 330a* quantitatively demonstrates the co-existence of pressure and viscosity from basic hydro-dynamic principles by commenting

The above results, as thus generalized, have an important application in the theory of Lubrication, which was initiated by Osborne Reynolds [1886] in a classical paper.

Therefore, a **dual-process** approach to preferential flow is postulated here in which *capillary flow* in the sense of Richards occurs side-by-side with *viscous flow*. Figure 1.2 illustrates the concept. For example, based on

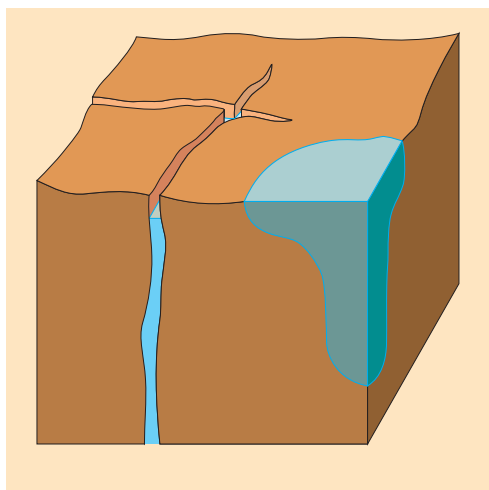


Figure 1.2: The two concepts of preferential flow: macropore flow (on the left) and finger flow (on the right). Macropore flow is thought of following discrete structural voids, whereas hydro-mechanical conditions induce finger flow in more diffuse pore systems. Water may seep from preferential flow paths to the surrounding matrix (brown colors).

There are purposefully no spatial scales attached to the figure; they will result from flow experiments.

infiltration of a solution containing dye and bromide, Germann et al. (1984) demonstrated preferential flow along root channels occurring simultaneously with solute sorption from the channels into the surrounding finer pores.

As an agreeable corollary the postulated dual-process approach does not a priori require the delineation of pore domains but leaves the decision about flow-path geometry to the hydraulic interpretation of measurements.

A closer look at the major flow-controlling forces offers a systematic treatment of preferential flow. Gravity, pressure, capillarity, and viscosity are the sources of the four forces to be considered during infiltration. Gravity is ubiquitous. Water pressure exceeding atmospheric pressure occurs in most cases only in completely water-saturated permeable media like groundwater systems. Thus, positive water pressures are generally excluded in the following considerations unless specifically mentioned. Capillarity occurs when water and air are attracted to the matrix, and the joint fluid interface touches the surface of the solid within a sufficiently short distance. But capillarity is treated here mainly as a state variable. Viscosity is the property of a fluid to resist flow, and it expresses momentum dissipation during motion. The focus on gravity, that adds momentum to, and viscosity, that abstracts momentum from the moving water leads to a kinematic view on infiltration. Viscosity-dominated flow is regarded as the promising concept able to explain numerous observations at scales that are amenable to experimentations in the laboratory as well as in the field.

The evolving approach to preferential infiltration separates the sessile from the mobile water content. The latter is due to a water pulse hitting the surface of the permeable medium. The emerging relationships apply to flow along

paths without requesting their detailed position and geometry. The velocity of flow is a unique function of the film thickness, the mobile water content is the product of the thickness of the water film and its contact length per unit area of the medium, and the volume flux density of preferential infiltration is the product of the mobile water content and the flow velocity. The principles are derived from pore-scale considerations, but decoupling flow velocity from volume flux density permits linear up-scaling from individual paths to much larger units.

1.4 Assumptions and restrictions

Viscosity expresses the ability of a fluid to dissipate momentum per unit area during laminar flow. The coefficients of dynamic viscosity for air and water amount to [$\mu_{air} = 1.8 \times 10^{-5}(\text{Pa s})$] and [$\mu_{HOH} = 10^{-3}(\text{Pa s})$]. Air is thus about 55 times easier to move and its density is about 83 times less than water's density. Air flow is therefore not considered to impact water flow, and air pressure is assumed to equal atmospheric pressure every where in the continuous gas phase of a permeable medium.

Temperature and pressure affect density and viscosity. However, fluid properties are considered constant by assuming normal pressure and temperature. Water and the matrix are presumably incompressible, thus a priori excluding, for instance, the effects of soil compaction during preferential flow.

1.5 Guide to the book

The treatise rests on two pillars. Part I develops the basics leading to the concept of viscous flow applicable to preferential infiltration, including the technique of routing a cascade of input pulses. The contemplations require some tools from physics and mathematics while the step-by-step development facilitates the readers' access even if they are not fully familiar with the tools. Part II rests on the second and equally important pillar featuring the numerous experimental applications illustrating and delineating the theoretical part. The examples are distributed over scales ranging from sand grains with diameters of less than 1(mm) to layers of unconsolidated sand with thicknesses of up to 2(m), hinting at the ability of the approach to bridge some notorious scale gaps in the hydraulics of soils, slopes, and catchments.

Part I Stokes-Flow Applied to Preferential Infiltration introduces in Chapter 2 the basic soil-hydrological concepts and principles of Stokes flow. Chapter 3 extends them to the routing of an input pulse through the medium. The

follow-up chapter links the basics of Stokes flow with the kinematic wave theory, offering an elegant tool for modeling time-variable input rates under the restriction of the special case of macropore flow. Chapter 5 discusses the impact of presumed flow geometries on viscous flow which then is confronted with Darcy's law and Richards equation in Chapter 6. The summary in Chapter 7 spans the bridge to

Part II Viscous Flow Applied to Infiltration and Drainage. Chapter 8 presents experimental protocols and basic data interpretation. Chapters 9 to 11 increase the complexity of viscous flows from the local to the profile and to the system level, while Chapter 12 returns to the flow path level. The concluding Chapter 13 deals with the temporal and spatial scales of viscous flows.

The *Système International* applies throughout. Here, it comprises the basic units of (kg), (m) and (s), and their combinations. Their prefixes (μ), (m), (k), and (M) indicate powers of ten ranging from (-6), (-3), to (3) and (6).

[] brackets are used to optically better separate formulae and similar expressions from the general text,

() parentheses separate units from the text, and

Eq.(.) refers to a particular equation while the digit in front of the dot indicates the chapter of its introduction.

Part I

Stokes-Flow Applied to Preferential Infiltration

Rule I

*We are to admit no more causes
of natural things, than such as are
both true and sufficient to explain
their appearances.*

Rule II

*Therefore to the same natural effects we must,
as far as possible, assign the same causes*

Newton, I. (1729 a)

*The Rules of Reasoning in Philosophy.
Mathematical Principles, Book III.*

2. Fundamentals

2.1 Introduction

In the natural sciences a theory is an abstraction of reality with the advantage of not being bothered by single observations and particular considerations. It is a logical construct of facts that are generally agreed upon by the relevant scientific community. Here, the tools for constructing a model are mathematical procedures that exclude contradiction. On its track from fundamentals to the specific application there are assumptions, constraints and restrictions that shield the evolving theory from reality. However, once considered mature the theory awaits confrontation with reality through experimental testing against the processes it was conceived to deal with.

Newton's (1729a) Rules I and II are best fulfilled when a specific case of flow is uniquely deduced from fundamentals through theory which is referred to as *deductive procedure* in the top-down direction. The universal Navier-Stokes equation

$$\frac{\partial \mathbf{v}}{\partial t} + \mathbf{v} \bullet \nabla \mathbf{v} = -\frac{1}{\rho} \cdot \nabla p + \mathbf{g} + \mathbf{f} \quad (2.1)$$

summarizes fundamentally all the hydro-mechanical cases, where, in Brutsaert's (2005) notation, \mathbf{v} is the velocity vector, ρ represents density, p refers to pressure, \mathbf{g} is the vector of acceleration due to gravity, and \mathbf{f} denotes the frictional force per unit mass, and the nabla-operator ∇ indicates the first derivatives in the three cardinal directions. The advantage of the deductive procedure is its inclusion of all possible types of flow. Then, specific cases follow from restraining the fundamentals, for instance, to incompressible fluids to those

$$\mathbf{f} = \eta \cdot \nabla^2 \mathbf{v} \quad (2.2)$$

applies, where η is the kinematic viscosity. According to José and Saletan (2000) the Navier-Stokes equation, Eq.(2.1), has defied full analytical solution, while Lamb (1932) presents irrotational flow in his *Article 30* which refers to Stokes (1845). Lamb thus derived irrotational flow as a sub-set of the universal Navier-Stokes equation under the constraint that flow be slow enough to allow for the suppression of the inertia terms, as expressed with small Reynolds numbers, which leads to the exclusion of rotational fluid movement. Irrotational flow is commonly referred to as laminar flow, while geophysicists refer to it as *creeping flow*. Here it is labeled *viscous flow* and stands in contrast to Richards' (1931) *capillary flow*.

However, a major disadvantage of deductive procedures is that they require substantial knowledge of physics and mathematics, and risk discouraging those readers who are mainly interested in the applications of the specific relationships that result from the deductive procedure.

The inductive method in the bottom-up direction is the complementary way to arrive at applicable relationships. It starts with supposedly reasonable qualitative descriptions of the system and the process which may lead to logical and quantitative rules. The nature of the rules may vary from being completely empirical to being close to the fundamentals. The advantage of this procedure is its vividness and its comprehensiveness. A major disadvantage lies in the uncertainty of its general applicability. Darcy (1856), for instance, followed the inductive method when generalizing the observed linear relationship between the volume flux density and the hydraulic gradient of flow in sand columns. Also, the author (Germann, 1985) followed an inductive procedure by experimentally determining the coefficients of a kinematic wave approach to rapid infiltration, with, however, minimal reference to hydro-mechanical principles.

Here, preference is given to the inductive derivation of viscous flow applicable to preferential infiltration. However, periodic references to the fundamentals will demonstrate its ultimate link to the Navier-Stokes equation, Eq.(2.1). So as not to encumber the reader with lengthy mathematical derivations of marginal importance to the thrust of the argument, only the references to the relevant studies are provided.

Gravity and viscosity are discussed in Sections 2.2 and 2.3, and the necessary elements of laminar flow are introduced in Section 2.4. Because the condition of low Reynolds numbers, [$Re < 1$], requires flow in films that are so thin that surface tension and capillary forces have to be considered. They will be outlined in Section 2.5.

2.2 Gravity

Newton (1729, b) defined gravity as:

a power ... tending to all bodies, proportional to the several quantities of matter which they contain.

Thus,

the forces by which the primary Planets are continually drawn off from rectilinear motions, and retain'd in their proper orbits, tend to the Sun; and are reciprocally as the squares of the distances of the places of those Planets from the Sun's centre.

This reads in our notation as two bodies with masses m_1 and m_2 attracting one another with the force due to gravity of

$$\mathcal{F}_g = G \cdot \frac{m_1 \cdot m_2}{r^2} \quad (2.3)$$

(N), where $[G = 6.67 \times 10^{-11}(\text{m}^3\text{kg}^{-1}\text{s}^{-2})]$ is the gravitational constant and $r(\text{m})$ is the distance between the centers of the two masses. Inserting our globe's mass and radius, $[m_G = 5.97 \times 10^{24}(\text{kg})]$ and $[R_G = 6.37 \times 10^6(\text{m})]$, into Eq.(2.3) yields acceleration due to gravity as $[g = G m_G R_G^{-2} \approx 9.81(\text{m s}^{-2})]$ that varies across the earth's surface because of the uneven mass distribution. The force emanating from gravitational acceleration is the weight $[\mathcal{F}_G = m g]$.

Permeable media are open systems, thus unconfined, and intensive properties are required. They are usually expressed as quantity per unit volume V of the permeable media and water, and both are considered incompressible. The mass density (usually density) $[\rho = m / V(\text{m}) (\text{kg m}^{-3})]$ and the specific weight $[\gamma = \rho g (\text{N m}^{-3})]$ may serve as examples for intensive properties.

The water potential emerging from gravity is the energy stored per unit volume of water that is required to do the work of lifting it a vertical distance Δz above an arbitrary horizontal reference plane, for instance above a free water table, FTW (Fig. 2.3). Thus, the potential due to gravity is

$$\psi_g = \rho \cdot g \cdot \Delta z \quad (2.4)$$

The hydraulic head is the same work stored per unit weight of water:

$$h_g = \frac{\psi_g \cdot \Delta z}{\rho \cdot g} = \Delta z \quad (2.5)$$

The gradients of potential and head of gravity in the vertical direction are $[\rho g (\text{N m}^{-3})]$ and $[\Delta z / \Delta z (\text{m m}^{-1})]$, respectively. The densities of air and water are about 1.3 and 1'000(kg m^{-3}) under conditions of normal pressure and temperature, leading to the ratio of [1:769]. Thus, the gravitational potential of air is usually ignored in permeable media flow, while ρ expresses the density of water.

2.3 Viscosity

Newton (1729 c) introduced the movement of bodies and the forces acting on them in his three laws of motion, which are still employed in mechanics literature. They are

Law I : *Every body perseveres in its state of rest, or of uniform motion in a right line, unless it is compelled to change that state by forces impress'd thereon.*

Law II: *The alteration of motion is ever proportional to the motive force impressed; and is made in the direction of the right line in which that force is impress'd.*

Law III: *To every action there is always opposed and equal reaction: or the mutual actions of two bodies upon each other are always equal, and directed to contrary parts*

Newton's Laws I & II translate to

$$\mathcal{F} = m \cdot a \quad (2.6)$$

where $a(\text{ms}^{-2})$, Newton's second law of the *alteration of motion*, is acceleration, from which $[\mathcal{F}/m = a]$ follows. Equation (2.6) applies to solid bodies as illustrated by the anecdote of Newton's personal experience in the apple orchard. However, Newton also realized that fluids do generally not obey the two laws of motion but they may follow $[\mathcal{F}/m = v]$ instead, where $v(\text{m s}^{-1})$ represents here average flow velocity. In the quest to subjugate the motion of fluids under the same laws Newton (1729 d) postulated the hypothesis of shear:

The resistance, arising from the want of lubricity in the parts of a fluid, is, caeteris paribus, proportional to the velocity with which the parts of the fluid are separated from each other.

Fluids that adhere to Newton's (1729d) hypothesis of shear are referred to as Newtonian fluids. The resistance that Newton referred to is what is now called *viscosity* which term is derived from *Viscum album*, or Mistletoe, whose sticky berries once furnished the raw material for producing birdlime.

Consider in the following thought-experiment a horizontal water film of thickness $F(\text{m})$ sitting on a horizontal solid surface, while a blade (a giant razor blade if you wish) is floating on top of the film as depicted in Fig. 2.1. The blade's cross-sectional area $A(\text{m}^2)$ is large enough to neglect significant edge effects. The blade moves gently with the velocity $v(F)(\text{m s}^{-1})$ along the film's surface, and \mathcal{F}_p is the pulling force acting in the direction of v . The f -coordinate extends vertically from the supporting surface, where $[f=0]$, to the blade, where $[f=F]$. Horizontal water films (*laminae* in Latin, hence laminar flow) of infinitesimal thinness df are considered to glide

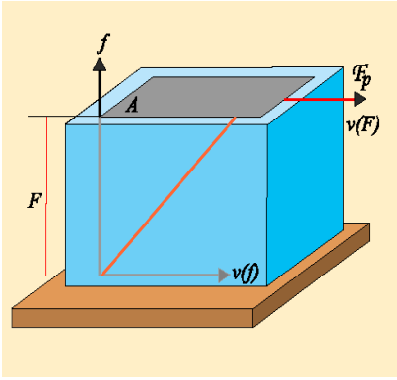


Figure 2.1: Newton's hypothesis of resistance to flow, where $F(m)$ is the thickness of the water film, $f(m)$ is the thickness variable, $A(m^2)$ is the surface area on which the horizontal pulling force $F_p(N)$ acts. This leads to the velocity of the uppermost water layer of $v(F) (m s^{-1})$ while $[0 \leq v(f) \leq v(F)]$.

one over the other. The no-slip condition requires that the laminae next to the two solid surfaces stick to them, thus $[v(0) = 0]$ and $[v(F) = v]$. The blade exerts a shear force onto the water amounting to $[\varphi = F_p/A (N m^{-2})]$. Fluid motion as described in Fig. 2.1 is referred to as Couette (1890)-flow. Under its consideration Newton's (1729 d) hypothesis of shear leads to

$$\varphi(f) = -\eta \cdot \rho \cdot \left. \frac{dv(f)}{df} \right|_f \quad (2.7)$$

$(N m^{-2})$, where $[v(f) (m s^{-1})]$ represents the velocity of the lamina at f , and $[dv(f)/df]$ is the velocity gradient. Dimensional analysis yields $(m^2 s^{-1})$ for η . At the limits we get $[\varphi(0) = 0]$ and $[\varphi(F) = F_p/A]$. Equation (2.7) holds for incompressible liquids. It expresses the dissipation of momentum, $[\rho v(f)]$, at f with η acting as the diffusion coefficient which Maxwell (1866) called the kinematic viscosity (of water in our case). Lamb's (1932) *Art. 328* demonstrates the analogy of Eq.(2.7) with the equation of thermal diffusion. Poiseuille (1846) experimentally determined $[\eta \rho]$ as a function of temperature $\mathcal{T}(^{\circ}C)$, and Helmholtz (1860) cast Poiseuille's data into the following expression:

$$\eta' \cdot \rho' = \frac{0.01779}{1 + 0.03368 \cdot \mathcal{T} + 0.00022099 \cdot \mathcal{T}^2} \quad (2.8)$$

where η' and ρ' are the water's kinematic viscosity and density in the c-g-s system. The frequently applied kinematic viscosity $[\eta = 10^{-6}(m^2 s^{-1})]$ thus appears at $[\mathcal{T} = 12.6(^{\circ}C)]$. In honor of Poiseuille's achievements, the unit of dynamic viscosity, $1(g cm^{-1} s^{-1})$, is called Poise.

José and Saletan (2000) explained that

Viscosity is a property of a fluid that causes relatively moving adjacent parts of the fluid to exert forces on each other, forces that vanish in the

limit when the relative velocity goes to zero.

Therefore, the work done by the shear force also vanishes when the motion ceases and, as a consequence, the shear force has no potential. This notwithstanding, flowing water follows the path of least momentum dissipation or, equivalently, the path of least resistance.

2.4 Elements of Stokes flow

This section develops the expressions from Newton's hypothesis of shear flow to the quantitative treatment of a moving water film with the constant thickness F (m) and the increasing depth $z_w(t)$ (m) to the film's wetting front. This leads to a specific version of Stokes (1845)-flow according to Lamb's (1932) irrotational flow.

Equation (2.7), considering the shear force due to momentum dissipation, is now constrained to the balancing of the weight of the moving water film with the shear force acting within it. The shear, $\varphi(f)$ Eq.(2.7), in the lamina at an arbitrary distance f from the solid wall balances the weight of the remaining film that stretches from f to F such that

$$\rho \cdot g \cdot l \cdot z_w(t) \cdot (F - f) = \eta \cdot \rho \cdot l \cdot z_w(t) \cdot \left. \frac{dv}{df} \right|_f \quad (2.9)$$

(N). The shear force $\varphi(f)$ is due to momentum dissipation onto the vertical area $[l z_w(t)]$, where l (m) is the contact length in the horizontal plane between the mobile water film and the static parts of the system that generally consists of the solid permeable medium and the two fluids, Fig. 2.2.

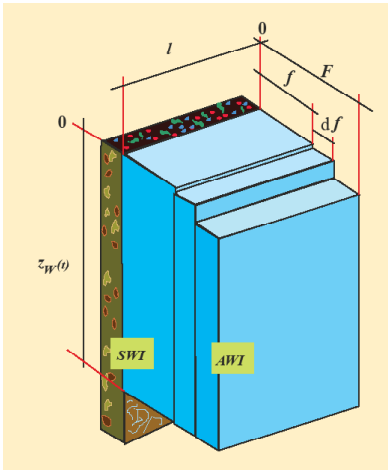


Figure 2.2: Film flow along a vertical plane, where F (m) is the film thickness, f (m) is the thickness variable, df (m) is the thickness of a lamina, $z_w(t)$ (m) is the vertical position of the wetting front as function of time t (s), and l (m) is the length of contact between the moving water film and the resting parts of the permeable medium. *AWI* and *SWI* are the air-water and the solid-water interfaces, respectively.

Integration of Eq.(2.9) from the solid-water interface, *SWI*, where [$v(0) = 0$] (the no-slip condition), to f yields the parabolic velocity profile of

$$v(f) = \frac{g}{\eta} \cdot (F \cdot f - \frac{f^2}{2}) \quad (2.10)$$

(m s^{-1}), while the average velocity of the water film amounts to

$$\bar{v} = \frac{1}{F} \cdot \int_0^F v(f) \cdot df = \frac{g}{3 \cdot \eta} \cdot F^2 \quad (2.11)$$

(m s^{-1}). The velocity in Eq.(2.11) is exclusively related to F and to [$g/(3 \eta)$]. The differential volume flux at f is

$$dQ|_f = (l \cdot v(f) \cdot df) \quad (2.12)$$

($\text{m}^3 \text{s}^{-1}$). Its integration from the *SWI* at [$f=0$] to the air-water interface, *AWI*, at [$f=F$] produces the volume flux of the film as

$$Q(F, l) = \frac{g}{3 \cdot \eta} \cdot l \cdot F^3 \quad (2.13)$$

($\text{m}^3 \text{s}^{-1}$). The mobile water volume per unit depth amounts to

$$W(F, l) = F \cdot l \quad (2.14)$$

(m^2), while the velocity of the wetting shock front follows from the volume balance as

$$v(F) = \frac{Q(F, l)}{W(F, l)} = \frac{g}{3 \cdot \eta} \cdot F^2 \quad (2.15)$$

This equals the average film velocity \bar{v} , Eq.(2.11). Equations (2.7), and (2.9) to (2.15) are based on Newton's hypothesis of shear and Stokes' (1845) flow. They treat laminar film-flow as free-surface flow with an *AWI* and a *SWI*. The latter interface is static and consists of a dominantly solid phase that may be porous and may include stationary fluid portions. Equation (2.15) states that F is the only variable impacting v . This convenient relationship allows for the development of a concept of flow in a permeable medium without *a-priori* considerations of its internal structure. Stokes-flow, summarized with Eqs. (2.13) to (2.15), is valid within the domain of Eq.(2.7) which coincides at the lower limit with the applicability of η to films of Newtonian fluids as thin as 0.01 (μm). Stokes (1845), according to Lamb (1932), set the condition for the upper limit at a low Reynolds number [$Re < 1$]. Lin and Wang (1986),

however, in an attempt to extend the range of the approach's applicability, pushed the limit to the transition from Stokes-flow to unstable flow to $[Re \leq 3]$ by proposing

$$Re = \frac{F \cdot v}{\eta} = \frac{F^3 \cdot g}{3 \cdot \eta^2} = \left(\frac{3 \cdot v^3}{g \cdot \eta} \right)^{1/2} \leq 3 \quad (2.16)$$

Equation (2.16) yields an approximation for the maximum tolerable film thickness of $[F_{max, visc} = 97(\mu m)]$. This still very small maximum film thickness requires that the surface tension and capillary forces be respected in any further analyses.

2.5 Surface tension, capillarity, and water retention

The water's surface tension at the air-water interface, *AWI*, follows from the thought-experiment in Fig. 2.3. A horizontal wire of length l_{wire} (m) and sufficiently narrow diameter dW (m) (ideally several molecules thick) is gently pulled out of the free water table at the vertical position of FWT until the suspended film at the apex of the wire ruptures at the height Δz above the FWT. The water's surface tension is defined as the weight of the film per unit length of the rod at the height of rupture

$$\sigma = (l_{wire} \cdot dW \cdot \Delta z) \cdot \rho \cdot g \cdot \frac{1}{l_{wire}} \quad (2.17)$$

which produces for water $[\sigma = 0.073 \text{ N m}^{-1}]$ and $[dW \Delta z = 7.4 \times 10^{-6}(\text{m}^2)]$.

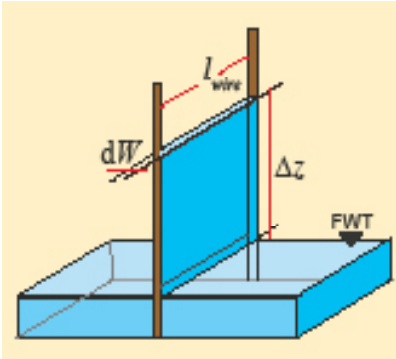


Figure 2.3: The concept of surface tension. FWT indicates the free water table, l_{wire} and dW (m) are the length and diameter of the wire, and Δz (m) is the height above the water table when the film ruptures at the apex of the wire.

The affinity of a fluid pair to a solid surface is expressed with the contact angles α and β ($^\circ$), Fig. 2.4. The wetting fluid is defined by $[0 \leq \alpha \leq 90(^\circ)]$ and the non-wetting fluid by $[90(^\circ) \leq \beta \leq 180(^\circ)]$, where $[\alpha + \beta = 180(^\circ)]$. As a consequence, any two angles $[\alpha, \beta \neq 90(^\circ)]$ will bend the interfacial surface of the two fluids toward the wetting fluid as depicted in Fig. 2.4. The length l_{af} (m) indicates the horizontal distance from the vertical solid wall causing the solid-fluid contact line to where affinity just begins to affect the two fluids' interface by lifting the wetting fluid. As a consequence, any two solid surfaces that are closer than $[2 l_{af}]$ will lift the wetting fluid between them above the FWT. The result of the lifting process is referred to as *capillary rise*. In general, water is assumed to completely wet the solid surface, thus $[\alpha = 0(^\circ)]$.

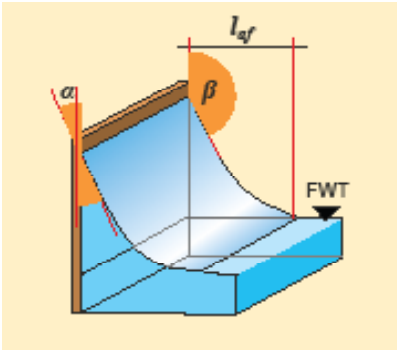


Figure 2.4: Concept of fluid affinity to a solid vertical surface, where $[\alpha \leq 90(^\circ)]$ and $[\beta \geq 90(^\circ)]$ are the contact angles of the wetting and non-wetting fluid with the solid surface. FWT indicates the free water table, and l_{af} is the perpendicular distance from the solid to where affinity begins to pull water above the FWT.

In soil physics, static capillary rise of water in a cylindrical tube is the most popular model leading to the thought-experiment of Fig. 2.5a: A vertical tube with inner radius R (m) stands in a pond. The contact angle is $[\alpha = 0(^\circ)]$ and $[R < l_{af}]$, while $h_{cap,cyl}$ (m) is the resulting rise of the meniscus represented by the height of the bottom of the curved *AWI* above the FWT. This *AWI* forms a half-sphere because $[\alpha = 0(^\circ)]$ is assumed, and it is concave towards the water that pulls down its surface. The weight of the water column is $[F_{g,cyl} = g \rho \pi R^2 h_{cap,cyl}]$, while the surface tension σ along the circumference of $[2 \pi R]$ keeps the water column in place; (the index *cyl* refers to the cylinder).

Thus, the surface tension acting in the rim of the meniscus balances the weight of the water column according to

$$-\pi \cdot g \cdot \rho \cdot R^2 \cdot h_{cap,cyl} = 2 \cdot \pi \cdot R \cdot \sigma \quad (2.18)$$

The left-hand side of Eq.(2.18) is negative because work is required to bring the meniscus back to the reference level, FWT. Rearranging Eq.(2.18) leads to the relationship of

$$h_{cap,cyl} = \frac{-2 \cdot \sigma \cdot \cos(\alpha)}{g \cdot \rho \cdot R} \quad (2.19)$$

where $[\sigma \cos(\alpha)]$ expresses the vertical component of the surface tension. An estimate of the maximum pore radius at the limit of capillarity, $[h_{cap,cyl} \rightarrow 0]$, follows from considering the bottom of the meniscus just to touch the FWT in Fig. 2.5a by substituting $|h_{cap,cyl}|$ with R in Eq.(2.19). Solving for R_{max} yields

$$R_{max, cap} = \sqrt{\frac{2 \cdot \sigma}{\rho \cdot g}} = 3.9(\text{mm}) \quad (2.20)$$

Similarly, balancing the weight $[F_G = g \rho F l h_{cap,F}]$ of the water film between two parallel and vertical walls, Fig. 2.5b, with the corresponding surface tension of $[2 l \sigma \cos(\alpha)]$ yields the relationship between aperture F and capillary head $h_{cap,F}$ acting in the film as

$$h_{cap,F} = \frac{-2 \cdot \sigma \cdot \cos(\alpha)}{F \cdot \rho \cdot g} \quad (2.21)$$

where the index F refers to the film between the parallel plates.

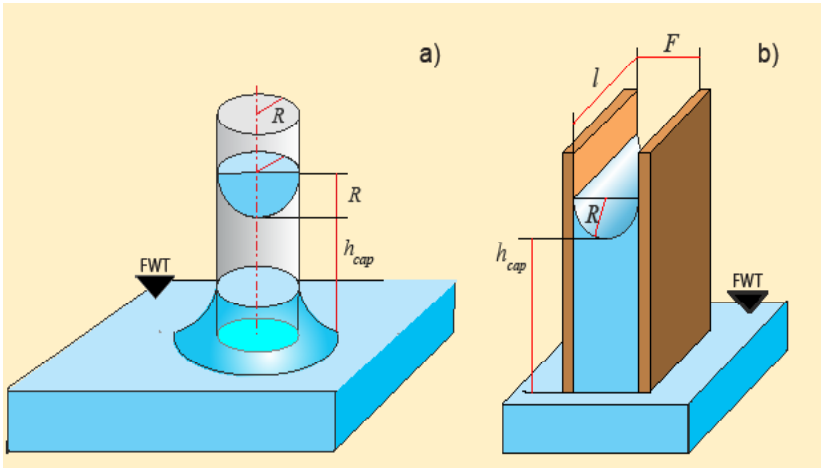


Figure 2.5: Capillary rise

- a) in a cylinder with radius R (m), and the meniscus of the same radius, while h_{cap} (m) is the capillary rise of the meniscus above the free water table FWT;
- b) between two parallel plates, with the film thickness F (m) that equals the distance between the plates, and the contact length l (m).

Similar to the derivation of Eq.(2.20), the widest aperture just able to exert capillarity amounts to

$$F_{\max, \text{cap}} = \sqrt{\frac{4 \cdot \sigma}{\rho \cdot g}} = 5.5(\text{mm}) \quad (2.22)$$

Both, $R_{\max, \text{cap}}$ and $F_{\max, \text{cap}}$ resulting from Eqs.(2.20) and (2.22) are forty to sixty times thicker than $F_{\max, \text{visc}}$ emerging from Eq.(2.16) ff., thus justifying the consideration of surface tension and capillarity.

The capillary head h_{cap} expresses the work per unit weight of water that the system, consisting of the fluid pair and either the cylinder or the two parallel plates, has performed to lift water to the height h_{cap} above the FWT (Figs. 2.5a,b). That work is stored as capillary energy per unit weight of water. Work is required to bring water back to the FWT, hence, $[h_{\text{cap}} < 0]$, and the surface tension is a force having potential. The reference level for capillary potential energy is the FWT, which is conventionally set to zero. The water pressure at the FWT is equal to the atmospheric pressure, thus atmospheric pressure becomes also a reference. Because the meniscus is concave towards the wetting fluid, this indicates that h_{cap} is less than atmospheric pressure. This is consistent with $[h_{\text{cap}} < 0]$ and the statement that work is required to bring water back to the reference level, either to the FWT or to atmospheric pressure. Capillary potential ψ_{cap} (Pa) is the same energy that is contained in the water at height h_{cap} but expressed per unit volume,

$$\psi_{\text{cap}} = h_{\text{cap}} \cdot \rho \cdot g \quad (2.23)$$

Lamb's (1932) *Art. 265* provides a more general approach to capillarity:

... the common surface of two fluids which do not mix, behaves as if it were in a state of uniform tension, the stress between two adjacent portions of the surface, estimated at per unit length of the common boundary-line, depending only on the nature of the two fluids and on the temperature.

This leads to

$$p_1 - p_2 = \psi_{\text{cap}} = \sigma \cdot \left(\frac{1}{R_{\max}} + \frac{1}{R_{\min}} \right) \quad (2.24)$$

where p_1 and p_2 (Pa) are the pressures close to the surface on the two sides of the meniscus, while R_{\max} and R_{\min} express here the longest and shortest radii (the principle radii) of the curvature at a point on the meniscus.

The water retention curve of a particular porous medium is defined as $h_{cap}(\theta)$, where θ ($\text{m}^3 \text{ m}^{-3}$) refers to the total volumetric water content in a permeable medium that may vary within $[0 \leq \theta \leq \varepsilon (\text{m}^3 \text{ m}^{-3})]$ while the upper limit at ε represents the medium's porosity (i.e., volume of pores per total volume of the permeable medium). Figure 2.6 illustrates an example of a water retention curve. A porous medium is considered air-dry if $[\theta = 0]$ and saturated if $[\theta = \varepsilon]$. The water retention curve mathematically separates the air-filled pore space from the water-filled pore space in relation to h_{cap} . Figure (2.5a) suggests a relationship between the water volume in the cylinder and the corresponding capillary head. Solving Eq.(2.19) for R , while calculating the water volume in the cylinder with it, yields the volume of water content in relation

$$V(h_{cap}) = \frac{4}{h_{cap}} \cdot \pi \cdot \left(\frac{\sigma \cdot \cos(\alpha)}{\rho \cdot g} \right)^2 \quad (2.25)$$

If a soil is conceptualized as a bundle of capillary tubes of varying radii, then $[V(h_{cap}) = d\theta/d(h_{cap})]$, and an approximate relationship $\theta(h_{cap})$ emerges as

$$\frac{d\theta}{dh_{cap}} \approx \frac{1}{h_{cap}} \quad (2.26)$$

Integration of Eq.(2.26) may describe a section of the water retention curve between $\theta(h_{cap,lo})$ and $\theta(h_{cap,up})$ as

$$\theta(h_{cap,lo}) = \theta(h_{cap,up}) - \Pi(h_{cap}) \cdot \ln \left(\frac{h_{cap,up}}{h_{cap,lo}} \right) \quad (2.27)$$

where the function $\Pi(h_{cap})$ expresses a frequency distribution of the menisci in the range from $[h_{cap,up}]$ to $[h_{cap,lo}]$ and the inherent physical constants are the same as in Eq.(2.25). The generalized presentation of a retention curve, Eqs. (2.25) to (2.27), may illustrate the common application of logarithmic scales of h_{cap} or ψ_{cap} against the linear scale of θ . However, major deviations from the theoretical relationship, Eq.(2.27), are to be expected in real permeable media.

The specific water capacity of a porous medium is defined as

$$C(\theta) = C(h_{cap}) = \left. \frac{\Delta \theta}{\Delta h_{cap}} \right|_{\theta, h_{cap}} \quad (2.28)$$

(m^{-1}) and expresses the change of volumetric water content per unit of the capillary head.

The physical definitions of the essential parameters θ , h_{cap} , and ψ_{cap} require a sufficiently sized volume of the permeable medium to contain all the necessary properties, yet the volume has to be small enough to permit their spatial continuity. Such an ideal volume is called a *representative elementary volume, REV*. All the considerations in this section 2.5 are based on static soil-water relationships. Their applications to water flow require infinitesimally small temporal changes of θ and h_{cap} .

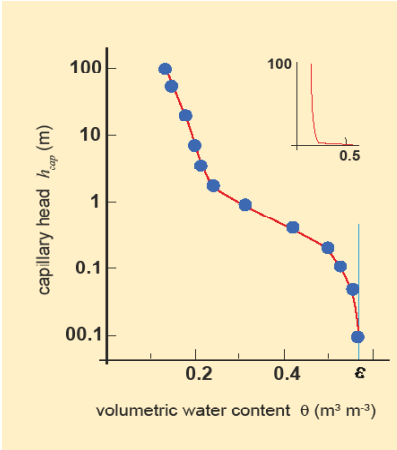


Figure 2.6: Soil-water retention curve: Capillary head h_{cap} (m) as function of volumetric water content θ ($\text{m}^3 \text{m}^{-3}$). Note the logarithmic scale of h_{cap} in the main figure and the linear scale in the inset. Porosity ϵ in this example amounts to 0.56 ($\text{m}^3 \text{m}^{-3}$). The soil was a coarse-textured sandy loam, and θ (h_{cap}) was determined with a pressure-plate apparatus (Richard et al., 1978).

3. The water-content wave, *WCW*

3.1 Introduction

This chapter discusses the routing of one rectangular water pulse across a permeable medium under the consideration of Stokes (1845) flow, Section 2.4. The pulse $P(q_s, T_B, T_E)$ is completely defined by the constant volume flux density q_s (m s^{-1}), and by the times T_B and T_E , when it hits the surface and when it ceases. At the moment of penetrating the medium at T_B , the pulse transforms into a water-content wave *WCW* that envelops the mobile water content $w(z, t)$ as function of time and depth of the permeable medium, while w_s refers to the mobile water content that initially evolves from q_s . The index S refers to the parameters' origin at the surface. Stokes-flow adapted to infiltration into permeable media is henceforth referred to as *viscous permeable-media flow* or, under the considerations presented here, as ***viscous flow*** for short. Figure 3.1 depicts an entire *WCW*.

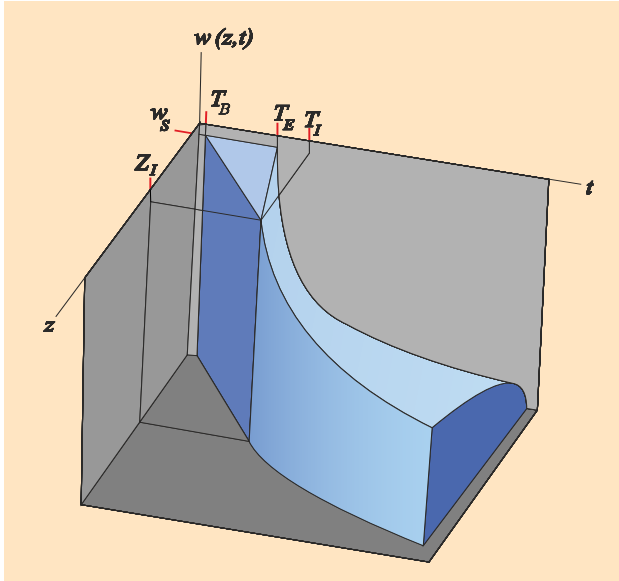


Figure 3.1: Schematic representation of a water-content wave *WCW*, where the $w(z, t)$ -axis represents the mobile water content, t and z are the axes of time and depth; w_s indicates the mobile water content that follows from q_s ; T_B and T_E (s) are the beginning and ending times of the water pulse $P(q_s, T_B, T_E)$ that hits the surface at $[z = 0]$; T_I and Z_I indicate time and depth of the wetting front intercepting the draining front. The line from $w_s(0, T_B)$ to $w_s(Z_I, T_I)$ represents the position of the wetting front, $z_w(t)$, while the line from $w_s(0, T_E)$ to $w_s(Z_I, T_I)$ gives the position of the draining front, $z_d(t)$. The wetting front continues beyond $[t > T_I]$ and $[z > Z_I]$ as curve along time and depth.

The following conditions apply to this chapter:

- (i) All flow arriving at the surface continues as *WCW*, no ponding occurs.
- (ii) Conditions of flow prevail along the flow paths during the existence of the *WCW*. (This condition does not mandatorily require a homogeneous pore system).
- (iii) The *WCW* neither loses nor gains water.
- (iv) There is no viscous flow in the permeable medium prior to the arrival of the pulse.

Some of the four conditions will, however, have to be relaxed when viscous flow is applied to variable input rates and experimental data. As a consequence, the volume V_{WCW} (m) per coross-sectional area A (m²) contained in the pulse $P(q_s, T_B, T_E)$ continues as *WCW*, thus

$$V_{WCW} = q_s \cdot (T_E - T_B) \quad (3.1)$$

3.2 Adaptation of Stokes-flow to infiltration

Adaptation of Stokes flow to viscous flow relates the volume flow Q and the mobile water volume W , Eqs.(2.13) and (2.14), to the cross-sectional area A of the permeable medium. Thus, the early stage of the *WCW*'s volume flux density becomes

$$q_s = \frac{Q}{A} = F^3 \cdot L \cdot \frac{g}{3 \cdot \eta} \quad (3.2)$$

(m s⁻¹), where $[L = \Sigma l / A \text{ (m m}^{-2}\text{)}]$, Fig.2.2. Further, the mobile water content related to q_s is

$$w_s = F \cdot L \quad (3.3)$$

(m³m⁻³), where L also expresses the vertical area $[z_w(t) \Sigma l]$ per volume $[z_w(t) A]$ of the medium onto which momentum dissipates, thus

$$L = \frac{z_w(t) \cdot \sum_A l}{z_w(t) \cdot A} \quad (3.4)$$

(m²m⁻³). The depth $z_w(t)$ (m) is the position of the discontinuous wetting shock front during $[t > T_B]$ that is defined as $[w(-z_w) = w_s]$ and $[w(+z_w) = 0]$. Subsequently, $v(w_s)$ and $q(w_s)$ are similarly discontinuous. The velocity of the wetting front remains according to Eq.(2.15) while the wave

velocity

$$c = \frac{d q_s}{d w_s} = F^2 \cdot \frac{g}{\eta} = 3 \cdot v \quad (3.5)$$

(m s⁻¹) is the velocity of any alteration of q (i.e., celerity). Thus, a *WCW* in a permeable medium is completely characterized by the pulse $P(q_s, T_B, T_E)$, the specific contact length L and the film thickness F . The latter two parameters are assumed to be established at T_B when the *WCW* spontaneously forms as reaction to a particular $P(q_s, T_B, T_E)$ hitting a particular porous medium. Condition (ii) in Section 3.1 requires $L(q_s)$ to remain constant over time and depth during the existence of a *WCW*.

3.3 Draining front and trailing wave

Figure 3.1 depicts a *WCW* as the spatio-temporal variation of $w(z, t)$. Its entire domain covers the reaction to $P(q_s, T_B, T_E)$ in a particular permeable medium. The cessation of input to the surface at $[t = T_E]$ cuts off flow, and the thickness of the water film at $[z = 0]$ instantaneously collapses from F to 0 while V_{WCW} , Eq.(3.1), remains. The sudden cut-off at T_E releases the rear ends of all the laminae at $[z = 0]$, Fig. 2.2, while the laminae themselves continue to glide one over the other. The rear end of the lamina at F represents the draining front that moves the fastest with the wave velocity c , Eq.(3.5), and whose position is

$$z_D(t) = c \cdot (t - T_E) \quad (3.6)$$

Under consideration of Eq.(3.5) the wetting front $z_w(t)$ eventually intercepts the draining front $z_D(t)$ at depth

$$Z_I = v \cdot (t - T_B) = c \cdot (t - T_E) = \frac{c}{2} \cdot (T_E - T_B) \quad (3.7)$$

and at time

$$T_I = T_B + \frac{Z_I}{v} = T_E + \frac{Z_I}{c} = \frac{1}{2} \cdot (3 \cdot T_E - T_B) \quad (3.8)$$

It should be noted that T_I depends exclusively on the duration of the pulse $[T_E - T_B]$. In particular, T_I is independent of depth, velocity, and volume flux density.

The following leads to the shape of the trailing wave, $w(z, t)$, during $[T_E \leq t \leq T_I]$. The water film starts to physically disintegrate beyond the line from $w_s(0, T_E)$ to $w_s(Z_I, T_I)$, Fig. 3.1. This is reflected mathematically in the reversing of integration which describes the formation of the collapsing trailing wave. (Integration across all laminae led to Eqs.(2.10) and (2.13), which deal with the propagation of the water film). A lamina at the arbitrary distance f carries the volume flux density $[dq]$ and the water content $[L \, df]$. From volume balance requirements follows the velocity of its rear end:

$$c_{RE}(f) = \left. \frac{dq}{df} \right|_f \cdot \frac{1}{L} = \frac{z_{RE}(f)}{t(z_{RE}) - T_I} \quad (3.9)$$

where $z_{RE}(f)$ (m) is the position of the rear end of the lamina at f at time $t(z_{RE})$. Upon inserting the first derivative from the equivalent of Eq.(3.2),

$$\frac{dq}{df} = \frac{g}{\eta} \cdot L \cdot f^2 \quad (3.10)$$

into Eq. (3.5) we get

$$c_{RE}(f) = \frac{z_{RE}(f)}{(t - T_E)} = \frac{g}{\eta} \cdot f^2 \quad (3.11)$$

Rearranging the central and right-hand parts of Eq.(3.11) and solving for f leads to the temporal position of the film thickness,

$$F_{RE}(z, t) = \left(\frac{\eta}{g} \right)^{1/2} z^{1/2} (t - T_E)^{-1/2} \quad (3.12)$$

(m). Its multiplication with L provides the spatio-temporal distribution of the mobile water content of the *WCW* during $[T_E \leq t \leq T_I]$ as

$$w(z, t) = L \cdot \left(\frac{\eta}{g} \right)^{1/2} z^{1/2} (t - T_E)^{-1/2} \quad (3.13)$$

After $[t > T_I]$ and beyond $[z > Z_I]$ the *WCW* loses the plateau and becomes crested, the draining front disappears, and $v(z, t)$ decreases with time and depth. The shape of the profile of mobile water according to Eq.(3.13) remains over the entire depth range extending from the surface to the wetting front, $[0 \leq z \leq z_w(t)]$, in particular also during $[t \geq T_I]$. The depth integral of $w(z, t)$ at any time $[t \geq T_I]$, according to Eqs.(3.1) and (3.13) is:

$$V_{WCW} = \left(\frac{\eta}{g} \right)^{1/2} \cdot L \cdot (t - T_E)^{-1/2} \cdot \int_0^{z_w(t)} z^{1/2} \, dz \quad (3.14)$$

Solving Eq.(3.14) for $z_w(t)$ yields the temporal position of the wetting front as

$$z_w(t) = \left(\frac{3 \cdot V_{WCW}}{2 \cdot L} \right)^{2/3} \cdot \left(\frac{g}{\eta} \right)^{1/3} \cdot (t - T_E)^{1/3} \quad (3.15)$$

The first derivative of Eq.(3.15) produces the velocity of the wetting front as

$$v(t)|_{z_w} = \left(\frac{V_{WCW}}{2 \cdot L} \right)^{2/3} \cdot \left(\frac{g}{3 \cdot \eta} \right)^{1/3} \cdot (t - T_E)^{-2/3} \quad (3.16)$$

Inserting $z_w(t)$ from Eq.(3.15) into Eq.(3.13) yields the mobile water content at the wetting front as

$$w(t)|_{z_w} = \left(\frac{\eta}{g} \right)^{1/3} \cdot \left(\frac{3 \cdot V_{WCW}}{2} \right)^{1/3} \cdot (t - T_E)^{-1/3} \cdot L^{2/3} \quad (3.17)$$

Multiplication of Eq.(3.16) with Eq.(3.17) produces the volume flux density at the wetting front as

$$q(t)|_{z_w} = \frac{V_{WCW}}{2 \cdot (t - T_E)} \quad (3.18)$$

The simple expressions for the velocities of the draining and wetting fronts favor the separate treatments of the temporal and the spatial functions of $w(z,t)$ and $q(z,t)$. The advantage will be extensively explored in Sections 3.4 and 3.5 which present the depth and time functions of mobile water contents with the goal of rendering operational Eqs.(3.1) to (3.18).

3.4 Profiles of mobile water content, $w(z,\tau)$

The section considers profiles of mobile water contents $w(z,\tau)$ at times τ_i [$1 \leq i \leq 3$], within the three intervals of $[T_B \leq \tau_i \leq T_E]$, $[T_E \leq \tau_i \leq T_I]$, and $[T_I \leq \tau_i < \infty]$.

(i) $T_B \leq \tau_i \leq T_E$: Position of the wetting front, mobile water content, and volume flux density are

$$z_w(\tau_1) = \frac{g}{3 \cdot \eta} \cdot F^2 \cdot (\tau_1 - T_B) \quad (3.19)$$

$$w(z, \tau_1) = L \cdot F = w_s \quad (3.20)$$

$$q(z, \tau_1) = \frac{g}{3 \cdot \eta} \cdot F^3 \cdot L = q_s \quad (3.21)$$

Thus, piston flow occurs during infiltration, $[T_B \leq \tau_1 \leq T_E]$.

- (ii) $T_E \leq \tau_2 \leq T_I$: The position of the wetting front is the same as in Eq.(3.19) while that of the draining front follows from Eq.(3.6) as

$$z_D(\tau_2) = \frac{g}{\eta} \cdot F^2 \cdot (\tau_2 - T_E) \quad (3.22)$$

Between $[0 \leq z \leq z_D(\tau)]$ the trailing wave evolves as with Eq.(3.13) as

$$w(z, \tau_2) = L \cdot \left(\frac{\eta}{g} \right)^{1/2} \cdot z^{1/2} (\tau_2 - T_E)^{-1/2} \quad (3.23)$$

The mobile water content remains at w_s between $[z_D(\tau) \leq z \leq z_w(\tau)]$ according to Eq.(3.20), and piston flow prevails according to Eq.(3.21).

- (iii) $T_I \leq \tau_3 < \infty$: Velocity, mobile water content, and volume flux density at the wetting front follow from Eqs.(3.16) to (3.18), while the profile $w(z, t)$ follows from Eq.(3.23).

Figure 3.2 illustrates the profiles of mobile water content at four typical times. The physics and mathematics of viscous flow permit the separation of temporal relationships from their spatial counterparts. This particular property circumvents the necessity of solving partial differential equations, while exclusively dealing with ordinary differential equations results in a set of analytical expressions which are easy to solve.

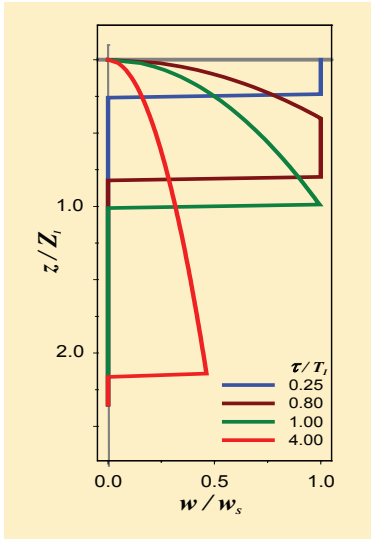


Figure 3.2: Profiles of relative mobile water content (w/w_s) as functions of relative depth (z/Z_l) at four relative times (τ/T_l).

3.5 Time series of mobile water contents $w(\zeta, t)$

Time series of mobile water contents $w(\zeta, t)$ at the three depth ranges ζ_i [$1 \leq i \leq 3$] of $[0 \leq \zeta_i < Z_l]$, $[\zeta_2 = Z_l]$ and $[\zeta_3 \geq Z_l]$ are now considered.

(i) $0 \leq \zeta_i < Z_l$: The arrival times of the wetting and draining fronts at ζ_i are

$$t_w(\zeta_1) = T_B + \frac{3 \cdot \eta}{g} \cdot F^{-2} \cdot \zeta_1 \quad (3.24)$$

$$t_D(\zeta_1) = T_E + \frac{\eta}{g} \cdot F^{-2} \cdot \zeta_1 \quad (3.25)$$

while the mobile water content assumes the following values during the respective time intervals:

$$0 \leq t \leq t_w(\zeta_1) \quad w(\zeta_1, t) = 0 \quad (3.26)$$

$$t_w(\zeta_1) \leq t \leq t_D(\zeta_1) \quad w(\zeta_1, t) = L \cdot F = w_s \quad (3.27)$$

$$t \geq t_D(\zeta_1) \quad w(\zeta_1, t) = L \cdot F \cdot \left(\frac{t_D(\zeta_1) - T_E}{t - T_E} \right)^{1/2} \quad (3.28)$$

Equation (3.28) results from solving Eq.(3.25) for ζ_i , and substituting with it the depth z in Eq.(3.23).

- (ii) $\zeta_2 = Z_I$: At depth of front interception and after $[t \geq T_I]$ the mobile water content becomes

$$w(\zeta_2, t) = L \cdot F \cdot \left(\frac{T_E - T_B}{2 \cdot (t - T_E)} \right)^{1/2} \quad (3.29)$$

Equation (3.29) results from replacing $t_D(\zeta_i)$ in Eq.(3.28) with T_I , Eq.(3.8).

- (iii) $\zeta_3 \geq Z_I$: Solving Eq.(3.15) for t yields the arrival time of the wetting front at ζ_3 as

$$t_W(\zeta_3) = T_E + \frac{4}{9} \cdot \frac{\eta}{g} \cdot \left(\frac{L}{V_{mob}} \right)^2 \cdot \zeta_3^3 \quad (3.30)$$

Inserting Eq.(3.30) into Eq.(3.13) yields the mobile water content at the crest as

$$w_{crest}(\zeta_3) = \frac{3}{2} \cdot V_{mob} \cdot \frac{1}{\zeta_3} \quad (3.31)$$

and the mobile water content as a function of time becomes

$$0 \leq t \leq t_W(\zeta_3) \quad w(\zeta_3, t) = 0 \quad (3.32)$$

$$t \geq t_W(\zeta_3) \quad w(\zeta_3, t) = \frac{3}{2} \cdot V_{mob} \cdot \frac{1}{\zeta_3} \cdot \left(\frac{t_W(\zeta_3) - T_E}{t - T_E} \right)^{1/2} \quad (3.33)$$

Figure 3.3 illustrates four time series of $w(\zeta_i, t)$ at four different relative depths $[\zeta_i/Z_I]$. The physics and mathematics of viscous flow permit the separation of spatial relationships from their temporal counterparts. This particular property circumvents the necessity of solving partial differential equations. Exclusive dealing with ordinary differential equations results in a set of comfortably solvable analytical expressions. The following chapter enhances the effect by introducing the method of characteristics as powerful mathematical tool for dealing with viscous flow.

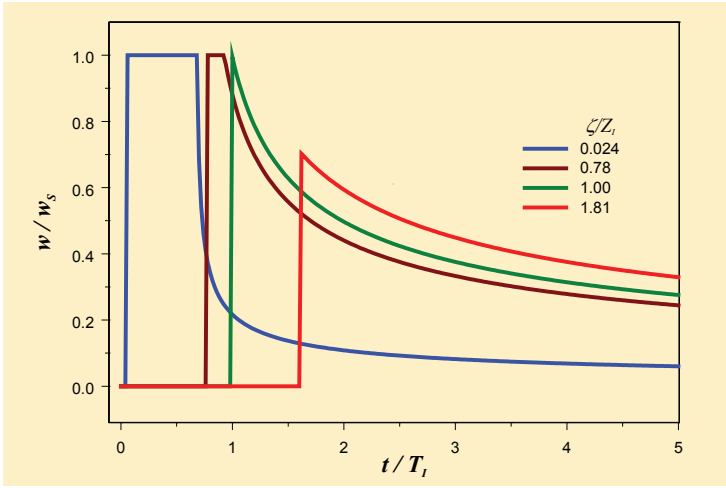


Figure 3.3: Time series of relative mobile water content, (w/w_s) as functions of relative time (t/T_i) at four relative depths (ζ/Z_i) .

3.6 Initial and boundary conditions (IC and BC)

The input pulse $P(q_s, T_b, T_e)$ initiates the water content wave WCW at the surface. But no flow occurs prior to infiltration within the permeable medium, leading to the IC of $[w(z, t) = 0]$ and $[q(z, t) = 0]$ for $[t \leq T_b]$ and $[0 \leq z \leq \infty]$.

Figure 2.2 suggests the inspection of boundaries that belong to the following five categories of BC:

- (i) *The vertical soil-water interface (SWI)* is a zero-flux boundary.
- (ii) *The air-water interface (AWI) opposite the SWI* is also a zero-flux boundary, but its shape responds to the input rate at the upper boundary. The *AWI* is parallel to the solid surface at distance F during $[T_b \leq t \leq T_e]$. When input ceases at $[t = T_e]$ the water content at the surface snaps from $[w = w_s]$ back to $[w = 0]$, while the cessation causes the film to smoothly contract and to form a trailing wave. The smooth contraction is due to viscosity and tensile strength. Equations (3.20) and (3.23) express mathematically the shape of the *AWI*.
- (iii) *The two vertical sides of the WCW* form an *AWI* each and are also zero-flux boundaries. In principle, capillarity according to Eq.(2.19) or Eq.(2.23) has to be considered. From $[F_{max, vis_c} = 97(\mu m)]$, Eq.(2.16), follows under consideration of Eq.(2.21) that $[h_{cap}(F_{max}) = -0.15(m)]$. However, the effect of capillarity on viscous flow is ignored because the film thickness F is orders of magnitudes tinier than the entire surface

area of $[L A]$ onto which momentum dissipates.

(iv) *The upper boundary* at $z = 0$ receives water according to $P(q_s, T_B, T_E)$,

$$t \leq T_B \text{ and } t \geq T_E : \quad q(0, t) = 0 \quad (3.34)$$

$$T_B \leq t \leq T_E : \quad q(0, t) = q_s \quad (3.35)$$

under the condition that the permeable medium accepts all the input rate and no ponding occurs. The experimentally controlled volume flux density qualifies for a Neumann-type boundary condition. The abrupt initiation at $[t = T_B]$ lets the mobile water content jump from 0 to $[w(q_s) = L F = w_s]$. Cueto-Felgueroso and Juanes (2009) suggest reverse capillary rise (i.e., a suspended capillary fringe) to occur between the surface of a permeable medium and the depth z_{cap} , where non-capillary flow (finger flow in my view) gets started. Following their notion suggests that films of a *WCW* might be suspended due to capillarity whenever $[F < 5.5(\text{mm})]$, Eq.(2.22). An estimate of the depth range, z_{cap} , of capillary suspension follows from balancing the weight of the static film with the surface tension

$$\sigma \cdot \cos(\alpha) \cdot L = \rho \cdot g \cdot L \cdot F \cdot z_w(t) \quad (3.36)$$

Inserting $v(F)$ from Eq.(2.15) into Eq.(3.36) yields at the limit of $[z_w(t) = z_{cap}]$

$$z_{cap} = v^{-1/2} \cdot \frac{\sigma \cdot \cos(\alpha)}{\rho \cdot \sqrt{3 \cdot g \cdot \eta}} = 0.0134 \cdot v^{-1/2} (\text{m}^{3/2} \text{s}^{-1/2}) \quad (3.37)$$

The depth z_{cap} indicates the position of the wetting front of a particular *WCW* where it starts to leave the static water-content formation according to the retention curve, for instance, to Eq.(2.27).

(v) *The moving wetting shock* front forms the *WCW*'s lower boundary at $z_w(t)$. It is released at the surface due to the sudden appearance at T_B of the mobile water content w_s . The wetting shock front has to overcome the water's surface tension at the triple contact line of solid-water-air. Because momentum dissipation is considered to balance the weight of the *WCW*, Eq.(2.9), kinetic energy per cross-sectional area is thought to provide the necessary force for overcoming surface tension.

There are two tracks of investigating the kinetic energy at the limit of the

surface tension at the lower *AWI*. The kinetic energy of either the entire *WCW* with velocity v or of the outermost lamina moving with the wave velocity c may overcome the surface tension. Under consideration of v and Eq.(2.15) the specific kinetic energy [$E_{kin}(v)$ (N m⁻¹)] per cross-sectional area of the water film [$F l$] amounts to

$$E_{kin}(v) = \frac{L \cdot F \cdot Z_{char} \cdot \rho \cdot v^2}{2 \cdot L \cdot F} = \frac{F^4}{2} \cdot \frac{g^2}{9 \cdot \eta^2} \cdot Z_{char} \cdot \rho \geq \sigma \quad (3.38)$$

(N m⁻¹), where Z_{char} is a characteristic length.

In view of Eq.(2.18), the adaptation of Eq.(3.38) to free-surface film flow, it follows that

$$\sigma = Z_{char} \cdot \rho \cdot g \cdot F \quad (3.39)$$

Setting Eq.(3.38) equal to Eq.(3.39) and solving for F leads to the minimum film thickness of [$F_{min}(v) = 122(\mu\text{m})$] required to push further the wetting front against surface tension.

From considering $E_{kin}(c)$ of the outermost lamina of the *WCW* and observing similar procedures leading to $F_{min}(v)$ yield for the lamina [$df l$] the specific kinetic energy per cross-sectional area of

$$E_{kin}(c) = \frac{L \cdot df \cdot Z_{char} \cdot \rho \cdot c^2}{2 \cdot L \cdot df} = \frac{F^4}{2} \cdot \frac{g^2}{\eta^2} \cdot Z_{char} \cdot \rho \geq \sigma \quad (3.40)$$

(N m⁻¹). Setting Eq.(3.40) equal to Eq.(3.39) yields [$F_{min}(c) = 59(\mu\text{m})$].

In conclusion, F_{min} , either as function of v or c , appears in the range of viscous-flow film thicknesses. Therefore, it seems plausible that *WCWs* are able to break-up the surface tension at the wetting fronts. However, further investigations are required, both theoretical and experimental, to furnish evidence to these preliminary findings.

4. Routing input pulses as kinematic waves

4.1 Introduction

The previous chapter introduced the concept of an evolving water content wave, WCW , caused by one rectangular input pulse $P(q_s, T_B, T_E)$. However, water flows to permeable media usually vary with time, basically requiring solutions to the two problems of volume flux density to increase, $[q_{s,i-1} < q_{s,i}]$, and volume flux density to decrease, $[q_{s,i-1} > q_{s,i}]$. The splitting of an arbitrary input function $q_s(0, t)$ into a series of N ($0 < i \leq N$) rectangular pulses $P_i(q_{s_i}, T_{B_i}, T_{E_i})$ is referred to as *input cascading*, which allows for the generalization of the upper boundary condition of viscous flow. Besides practical considerations there is no upper limit to N because viscous flow itself is based on the progression of an infinite number of infinitesimally thin laminae. (Actually, a single pulse can be viewed as a cascade of laminae with identical volume flux densities.) The lower limit of N depends on the desired accuracy of approaching $q_s(0, t)$. There is also a practical aspect to input cascading because meteorological services frequently publish precipitation records as series of rectangular pulses.

This chapter draws heavily from Lighthill and Witham (1955a,b) who developed the kinematic-wave theory applicable to flood movement in long rivers and to traffic flow on long crowded roads. The theory is restricted to one-dimensional flow and it requires a functional relationship between the volume flux density q , the concentration term w , and the position, z in our case, within the respective system. Wooding (1965) introduced kinematic-wave theory to the topic of catchment hydrology, and Germann (1985) employed it to data that were obtained from sprinkling-drainage experiments performed with a porous block of polyester-consolidated sand as permeable medium.

Chapter 3 developed the hydro-mechanical relationships that link viscous flow directly with the kinematic-wave theory, thus turning the latter into a valuable mathematical tool for input cascading. The mathematical construct of kinematic-wave theory fits well to viscous flow by simply fixing to 3 the exponent in the water-content-flux relationship. The accompanying method of determining the characteristics and the trajectories of the wetting front also visualizes the spatio-temporal distributions of volume flux densities and of mobile water contents.

4.2 Kinematic wave theory

The wave property follows from the equation of continuity alone, therefore the appropriate adjective *kinematic*. The equation of continuity

$$\frac{\partial w}{\partial t} + \frac{\partial q}{\partial z} = 0 \quad (4.1)$$

states that the water volume w per unit volume of the permeable medium over a short depth element ∂z changes at a rate equal to the difference $[\partial q / \partial z]$ between inflow and outflow. Further, assuming the volume flux density in the permeable medium as

$$q = q(z, w) \quad (4.2)$$

the wave velocity becomes

$$c = \left. \frac{\partial q}{\partial w} \right|_z = c(z, w) \quad (4.3)$$

This is the slope of $q(w)$ at z , and compares well with Eq.(3.5). The combination of Eq.(4.1) with Eq.(4.3) results in

$$\frac{\partial q}{\partial t} + c \cdot \frac{\partial q}{\partial z} = 0 \quad (4.4)$$

Equation (4.4) has one system of *characteristics* $[dz = c dt]$, while q remains constant along each of them. The mean velocity of the flow is

$$v = \frac{q}{w} = \frac{z_w(t)}{t} \quad (4.5)$$

and the wave velocity becomes

$$c = \frac{d}{dw}(v \cdot w) = v + w \cdot \frac{dv}{dw} = \left. \frac{dz}{dt} \right|_w \quad (4.6)$$

Equations (4.5) and (4.6) compare well with Eqs.(2.15) and (3.5). Thus, $[c > v]$ if $[\partial v / \partial w > 0]$ as in viscous flow, while $[c < v]$ if $[\partial v / \partial w < 0]$ as in traffic flow.

Similarly to *WCWs* (p.26), kinematic waves are not dispersive and they move as shocks. They form discontinuities when a faster wave overtakes a slower one. Let c_j be the velocity of the shock front (the index J indicates the jump), while q_1 and w_1 are the values ahead, and q_2 and w_2 the values behind the shock front such that $[q_2 > q_1]$ and $[w_2 > w_1]$. Volume balance requires that

flow crossing the shock front per unit time be either $[q_1 - c_J w_1]$ or $[q_2 - c_J w_2]$, resulting in the velocity of the shock as

$$c_J = \frac{q_2 - q_1}{w_2 - w_1} \quad (4.7)$$

Figure 4.1 illustrates the function $q(w)$ on which the jump-velocity c_J , Eq.(4.7), appears as the slope of the chord from $q(w_1)$ to $q(w_2)$, line (6). The chord represents the transition of the states of the shock wave, both behind and to the front of it. The chord also demonstrates that $[c_J > v_1]$ and $[c_J > v_2]$, while $[v_1 < v_2]$.

The application of kinematic-wave theory to viscous flow is based on the following three considerations:

- (i) *On the constraint of $[dL/dq = 0]$* : The restriction is based on the unlimited reaction of $F(q)$ on q -variations, on the condition that any lateral expansions or contractions of films are excluded. The consequences of the restrictions will be discussed in Chapter 6. Viscous flow along macropores is considered an example of the constraint, therefore $[dL/dq = 0]$ is further referred to as the *macropore flow restriction*.

- (ii) *On the equivalence with viscous flow*: The conductance

$$b = \frac{g}{3 \cdot \eta \cdot L^2} \quad (4.8)$$

(m s⁻¹), scales the basic relationships according to

$$q = b \cdot w^3 \quad (4.9)$$

$$c = \frac{dq}{dw} = 3 \cdot b \cdot w^2 \quad (4.10)$$

$$v = \frac{q}{w} = b \cdot w^2 \quad (4.11)$$

- (iii) *On the algebraic relationship of $(i^3 - j^3)/(i - j) = (i^2 + ij + j^2)$* : The velocity of the shock, Eq.(4.7), becomes

$$c_J = b \cdot (w_2^2 + w_2 \cdot w_1 + w_1^2) \quad (4.12)$$

Figure 4.1 illustrates the definitions for viscous flow.

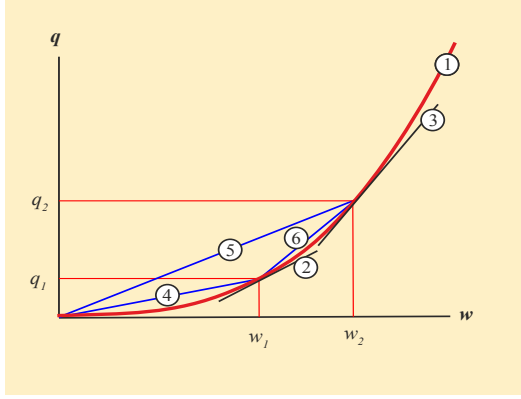


Figure 4.1: Velocities of two waves, of their wetting fronts, and of the jump.

- (1): Volume flux density as function of mobile water content, $q(w)$, Eq.(4.9)
- (2) and (3): The slopes of the tangents, Eq.(4.10), represent the wave velocities, c_1 and c_2 , of the two WCW 's that are represented with $q_1(w_1)$ and $q_2(w_2)$
- (4) and (5): The slopes of the chords are $[q/w]$, Eq.(4.11), and represent the wetting shock front velocities, v_1 and v_2 , of the two WCW 's
- (6): The slope of the chord represents the jump velocity c_j , Eq.(4.7).

Regardless of the actual position on $q(w)$, the sequence of the steepness in decreasing order is always from (3) to (6) to (2), as well as from (6) to (5) to (4).

4. 3 Propagation of a single pulse

The special case of $[q_2 = w_2 = 0]$, Eq.(4.7), is now considered. It produces a single input pulse $P(q_s, T_B, T_E)$ releasing at time T_B at the surface $[z = 0]$ a WCW that is due to the pulse's volume flux density q_s and the structure of the permeable medium that is expressed with the specific contact length L , resulting in a specific conductance b , Eq.4.8.

The wetting shock front of the WCW moves with the constant velocity v , Eq.(4.11), whose position is $[z_w(t) = v(t - T_B)]$. Each lamina moves with the wave velocity $[c = 3v]$, Eq.(4.10). The trajectory of the wetting shock front, line (1) in Fig.4.2, intercepts continuously the characteristics of the laminae. The abrupt cessation of input at time T_E releases the last lamina moving with c , and its rear end is referred to as the draining front with a time-dependent position of $z_D(t)$. The wetting shock front will eventually intercept the draining front at depth

$$Z_I = \frac{c}{2} \cdot (T_E - T_B) \quad (4.13)$$

which results from equating $[T_B + Z_I/v = T_E + Z_I/c]$.

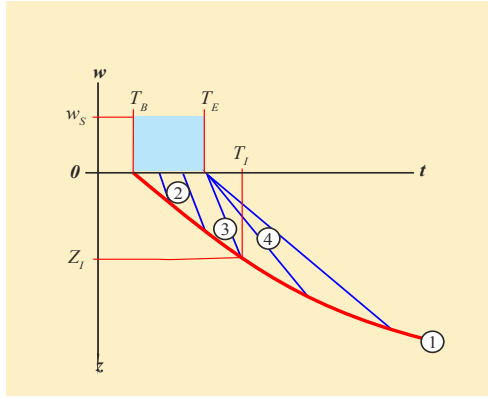


Figure 4.2: Characteristics of a single *WCW*, where w_S , T_B , and T_E are the amplitude and times of its beginning and ending; Z_I and T_I are depth and time of the wetting front, $z_w(t)$, intercepting the characteristics of the draining front, $z_D(t)$.

- (1) Depth $z_w(t)$ of the wetting front as function of time during $[T_B \leq t \leq T_I]$, Eq.(4.5), and during $[t \geq T_I]$ Eq.(4.20)
- (2) Two characteristics of the *WCW*, Eqs.(4.6), (4.10)
- (3) Characteristics of the draining front, $z_D(t)$ Eq.(4.6); lines (2) and (3) are parallels.
- (4) Two spreading characteristics of the trailing wave, Eq.(4.15), with the same origin at T_E .

Further, the time of interception amounts to

$$T_I = \frac{1}{2} \cdot (3 \cdot T_E - T_B) \quad (4.14)$$

At T_E the rear ends of the laminae glide one over the other with the innermost not moving at all due to the no-slip condition, while the rear ends of all the other laminae reduce their wave velocities the closer they are at the *SWI* due to the decreasing mobile water content. The straight line (3) in Fig. 4.2 is the trajectory of the draining front, while the lines (4) depict two arbitrary representatives of all the rear-end trajectories forming the trailing wave. One slope of the ensemble represents the wave velocity $c(w_{RE})$ of the lamina that envelops the mobile water content w_{RE} . The complete trailing wave results from the variation of w_{RE} in the range of $[w \geq w_{RE} \geq 0]$, where $[w = (q/b)^{1/3}]$ is according to Eq.(4.9). Thus, an arbitrary lamina's rear end follows a trajectory of $z_{RE}(t)$ with the wave velocity of

$$c_{RE} = \frac{z_{RE}(t)}{(t - T_E)} = 3 \cdot b \cdot w_{RE}^2 \quad (4.15)$$

The wetting front moves with velocity v until T_I . After that it continues to intercept the trajectories of the laminae but it moves decelerated due to their

spreading at T_E as depicted by the two exemplary lines (4) in Fig. 4.2. The arrival time at depth ζ within $[0 < \zeta \leq z_D(t) \leq Z_I]$ of the rear end of the lamina enveloping w_{RE} is

$$t(w_{RE}, \zeta) = T_E + \frac{\zeta}{c(w_{RE})} = T_E + \frac{\zeta}{3 \cdot b \cdot w_{RE}^2} \quad (4.16)$$

From equating the left and right hand sides of Eq.(4.16) it follows that the general depth-time distribution of mobile water of any collapsing film after the cessation of input becomes

$$w_{RE}(\zeta, t) = \left(\frac{\zeta}{3 \cdot b \cdot (t(w_{RE}, \zeta) - T_E)} \right)^{1/2} \quad (4.17)$$

Substituting ζ in Eq.(4.17) with $[z_D(t) = (t - T_E) c(w)]$ results in the temporal variation of w at the draining front depth $[0 < z_D(t) \leq Z_I]$ after its passing $z_D(t)$ during $[t \geq t_D(z)]$

$$w(z_D, t) = w \cdot \left(\frac{t_D(z) - T_E}{t - T_E} \right)^{1/2} \quad (4.18)$$

where $t_D(z)$ is the arrival time of the draining front at z_D .

The wetting front velocity decelerates at time T_I when it starts to intercept the rear ends of laminae moving slower than the draining front. The depth-time distribution of mobile water, Eq.(4.18) persists during $[T_E \leq t \leq \infty]$ and the total volume of the pulse, $[V_{mob} = q_S (T_E - T_B)]$, remains. This leads to the following continuity equation:

$$V_{mob} = \int_0^{z_W(t)} w(z, t) dz \quad (4.19)$$

Inserting Eq.(4.18) into Eq.(4.19) and solving for $z_W(t)$ yields the temporal position of the decelerating wetting shock front during $[T_I \leq t < \infty]$ as

$$z_W(t) = c \cdot \left(\frac{T_E - T_B}{2} \right)^{2/3} \cdot (t - T_E)^{1/3} \quad (4.20)$$

It is worth noting that the wetting shock front decelerates at Z_I and T_I from $[z_W(t) \propto t]$, Eq.(4.5), to $[z_W(t) \propto t^{1/3}]$, Eq.(4.20). The substitution of ζ in Eq.(4.17) with the right hand side of Eq.(4.20) under consideration of

Eq.(4.10) yields the mobile water content at the wetting front as function of time as

$$w(t) = w \cdot \left(\frac{T_E - T_B}{2 \cdot (t - T_E)} \right)^{1/3} \quad (4.21)$$

while $[t \geq T_i]$.

The above derivations, Eqs.(4.1) to (4.21), are based on kinematic-wave theory as Lighthill and Witham (1955) presented. On various occasions the derivations in this chapter coincide with Stokes flow, Chapter 2, and viscous flow, Chapter 3, under the macropore flow restriction. The coincidences support the kinematic-wave theory's valid representation of viscous flow. Section 4.4 inspects the interception function while Sections 4.5 and 4.6 extend kinematic-wave theory to decreasing and increasing jumps. The two kinds of jumps present the necessary building blocks to apply viscous flow to input cascades under the restriction of macropore flow.

4.4 The interception function

Depth Z_i and time T_i of front interception indicate the point on the wetting front position where the front above it moving with constant v smoothly starts to decelerate, thus moving according to Eq.(4.20). Smooth transition requires that the position functions of the early wetting front, $[t < T_i]$, Eq.(4.5), always be a tangent to the position function of the later wetting front, $[t > T_i]$, Eq.(4.20), and that the point of contact in general be $Z_i(T_B, T_E)$, Eq.(4.13), of any pulse $P(q_s, T_B, T_E)$.

Thus, the first derivative of Eq.(4.20) yields

$$\frac{dz_w(t)}{dt} = \frac{c}{3} \cdot (t - T_E)^{-2/3} \cdot \left(\frac{T_E - T_B}{2} \right)^{2/3} \quad (4.22)$$

Substituting t in Eq.(4.22) with T_i from Eq.(4.14) amounts to

$$\left. \frac{dz_w}{dt} \right|_{T_i} = \frac{c}{3} = v = \frac{z_w(t)}{t - T_B} \quad (4.23)$$

The right-hand part of Eq.(4.23) presents a straight line in the z - t -diagram of characteristics which originates at $[z = 0]$ and $[t = T_B]$, having a slope of v and is a tangent to the function of Eq.(4.20) whenever $[T_E > T_B]$. The limit of

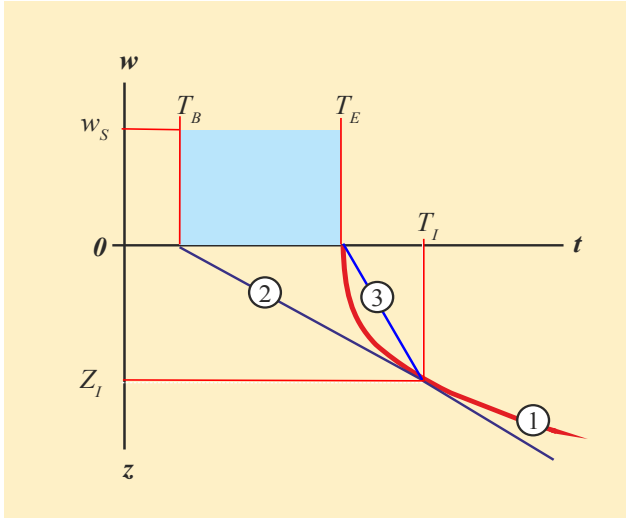


Figure 4.3: General position of (Z_I, T_I) with respect to $z_w(t)$ and $z_D(t)$

- (1) $z_w(t)$ during $[T_E \leq t < \infty]$, Eq.(4.20), the **interception function**
- (2) $z_w(t)$ during $[T_B \leq t \leq T_I]$, touching (1) at (Z_I/T_I) , Eqs.(4.13) and (4.14)
- (3) $[z_D(t) = c(t - T_E)]$ during $[T_E \leq t \leq T_I]$, Eq.(4.10)

$[T_E = T_B = T_I]$ represents the hypothetical pulse of infinitely short duration while the wetting shock front would move with infinite velocity similar to an explosion (see Fig. 4.3 for details). Thus, Eq.(4.20) expresses the position of the wetting shock front after $[t \geq T_I]$ of any pulse $P(q_S, T_B, T_E)$, regardless of its finite duration. Generally, and serendipitously for modeling, Eq.(4.20) applies to any $[t > T_E]$. Thus, Eq.(4.20) is further referred to as the *interception function*.

4.5 Propagation of a decreasing jump

The following presents the sequence of two input pulses, $P_1(q_{S,1}, T_{B,1}, T_{E,1})$ and $P_2(q_{S,2}, T_{B,2}, T_{E,2})$, one running behind the other one, where $[q_{S,1} > q_{S,2}]$ and $[T_{E,1} = T_{B,2}]$, further referred to as a decreasing jump. The indices 1 and 2 refer to WCW_1 and WCW_2 .

During the interval $[T_{B,1} \leq t \leq T_{I,1}]$ the WCW_1 behaves similarly to the individual WCW with

$$T_{I,1} = \frac{1}{2} \cdot (3 \cdot T_{E,1} - T_{B,1}) \quad (4.24)$$

and

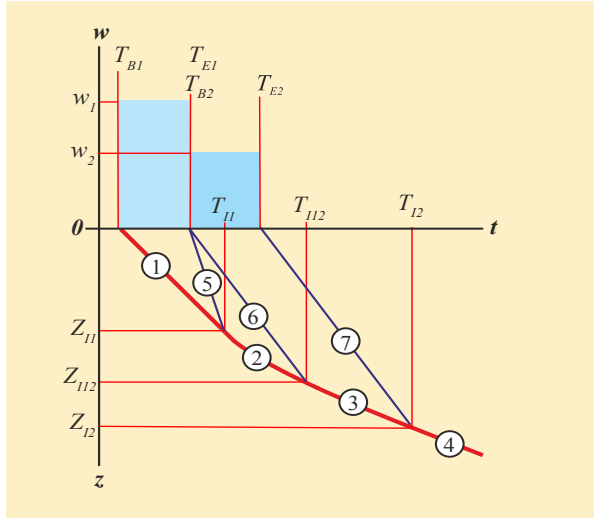


Figure 4.4: Wetting front and characteristics of a slower WCW following a faster WCW

- (1) Wetting front from WCW_1 , Eq.(4.5).
 - (2) Wetting front during the slow-down (spreading characteristics), Eq.(4.26).
 - (3) Wetting front from WCW_2 moving with constant velocity v_2 , Eq.(4.5).
 - (4) Wetting front from WCW_2 moving with decreasing velocity, Eq.(4.34).
 - (5) Last characteristic of WCW_1 , characteristic of its draining front, Eq.(4.10).
 - (6) First characteristic of the WCW_2 , Eq.(4.10).
 - (7) Last characteristic of the WCW_2 i.e., characteristic of its draining front, Eq.(4.10).
- Lines (6) and (7) are parallels.

$T_{B,1}$, $T_{E,2}$, $T_{B,2}$, and $T_{E,2}$: Beginnings and endings of P_1 and P_2 .

$T_{I,1}$ and $Z_{I,1}$: Time and depth of wetting front from WCW_1 , line (1), intercepting characteristic of draining front, line (5), Eqs.(4.13) and (4.14).

$T_{I,1-2}$ and $Z_{I,1-2}$: Time and depth of wetting front from WCW_1 , line (2), intercepting first characteristic of WCW_2 , line (6), Eqs.(4.28) and (4.29).

$T_{I,2}$ and $Z_{I,2}$: Time and depth of wetting front from WCW_2 , line (3), intercepting characteristic of draining front, line (7), Eqs.(4.32) and (4.33).

$$Z_{I,1} = v_1 \cdot (T_{I,1} - T_{B,1}) \quad (4.25)$$

The mobile water content during $[T_{B,1} \leq t \leq T_{I,1}]$ amounts to $[w(t) = w_1]$. Again, the characteristics start spreading at $T_{E,1}$, however, only within the range of $[w_1 \geq w_{RE} \geq w_2]$. The time $T_{I,1-2}$ indicates the wetting front intercepting the first lamina from WCW_2 . In accord with Eq.(4.20) the wetting front position during $[T_{I,1} \leq t \leq T_{I,1-2}]$ is

$$z_W(t) = c_1 \cdot \left(\frac{T_{E,1} - T_{B,1}}{2} \right)^{2/3} \cdot (t - T_{E,1})^{1/3} \quad (4.26)$$

After the application of the same principles that led to Eq.(4.21) the mobile water content during $[T_{I,1} \leq t \leq T_{I,1-2}]$ amounts to

$$w(t) = w_1 \cdot \left(\frac{T_{E,1} - T_{B,1}}{2 \cdot (t - T_{E,1})} \right)^{1/3} \quad (4.27)$$

The wetting front characteristic, Eq.(4.26), intercepts the characteristic of the first lamina of WCW_2 , $[c_2(t - T_{E,1})]$, at the time

$$T_{I,1-2} = T_{E,1} + \left(\frac{c_1}{c_2} \right)^{3/2} \cdot \left(\frac{T_{E,1} - T_{B,1}}{2} \right) \quad (4.28)$$

and depth

$$Z_{I,1-2} = c_1^{3/2} \cdot c_2^{-1/2} \cdot \left(\frac{T_{E,1} - T_{B,1}}{2} \right) \quad (4.29)$$

During the interval of $[T_{I,1-2} \leq t \leq T_{I,2}]$ the wetting front position is

$$z_w(t) = v_2 \cdot (t - T_{aB,2}) \quad (4.30)$$

where

$$T_{aB,2} = T_{I,1-2} - \frac{Z_{I,1-2}}{v_2} \quad (4.31)$$

is the apparent beginning of the wetting front at the surface, accounting for the retardation due to the spreading of the characteristics at $T_{E,1}$ and that itself is due to $[q_{s,2} < q_{s,1}]$. Upon equating the wetting front depth, Eq.(4.26) with the characteristic of the draining front of the WCW_2 , the time of the wetting front intercepting the draining front of WCW_2 is

$$T_{I,2} = \frac{1}{2} \cdot \left(\frac{Z_{I,1-2}}{v_2} - T_{I,1-2} + 3 \cdot T_{E,2} \right) \quad (4.32)$$

while the corresponding depth becomes

$$Z_{I,2} = Z_{I,1-2} + v_2 \cdot (T_{I,2} - T_{I,1-2}) \quad (4.33)$$

The mobile water content during $[T_{I,1-2} \leq t \leq T_{I,2}]$ is $[w(t) = w_2]$. Beyond $Z_{I,2}$ and after $T_{I,2}$ the wetting front position is

$$z_w(t) = c_2 \cdot \left(\frac{T_{E,2} - T_{aB,2}}{2} \right)^{2/3} \cdot (t - T_{E,2})^{1/3} \quad (4.34)$$

Upon the application of the same principles that led to Eq.(4.21) the mobile water content during the period of $[t \geq T_{l,2}]$ amounts to

$$w(t) = w_2 \cdot \left(\frac{T_{E,2} - T_{aB,2}}{2 \cdot (t - T_{E,2})} \right)^{1/3} \quad (4.35)$$

Figure 4.1 schematically presents in the $q(w)$ -diagram the gradual transition when a faster pulse reduces to a slower one. Consider the slopes of lines (5) and (3) as the velocities of the wetting front and the faster wave, and the slopes of lines (2) and (4) as the velocities of the slower wave and its wetting front. Spreading of the characteristics at time $T_{E,1}$ in Fig.4.4 corresponds to the reduction of the slopes from line(3) to line (2) along line (1).

4. 6 Propagation of an increasing jump

The section presents the sequence of two input pulses, $P_1(q_{s,1}, T_{B,1}, T_{E,1})$ and $P_2(q_{s,2}, T_{B,2}, T_{E,2})$ that follow one another, where $[q_{s,1} < q_{s,2}]$ and $[T_{E,1} = T_{B,2}]$.

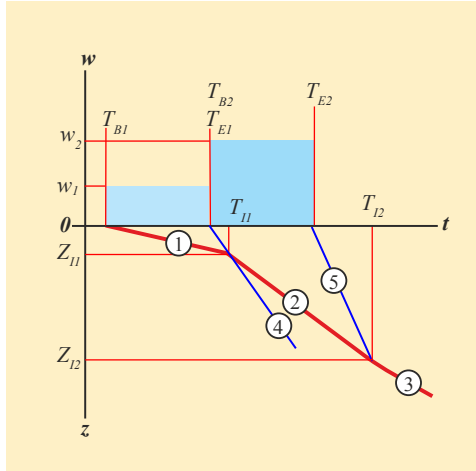


Figure 4.5: Wetting front and characteristics of a faster WCW_1 following a slower WCW_2

(1), (2): Wetting front depths as functions of time of WCW_1 and WCW_2 , Eq.(4.11)

(3) Wetting front depth of WCW_2 after $[t > T_{l,2}]$, Eq.(4.41)

(4) Characteristic of the jump, Eqs.(4.7) and (4.12)

(5) Characteristic of the draining front of WCW_2 , Eqs.(4.6) and (4.10)

$T_{B,1}$, $T_{E,1}$, $T_{B,2}$, and $T_{E,2}$: Beginnings and endings of P_1 and P_2 .

$T_{l,1}$ and $Z_{l,1}$: Time and depth of the wetting front of WCW_1 (1) intercepting the characteristic of the shock front (4), Eqs.(4.36) and (4.37).

$T_{l,2}$ and $Z_{l,2}$: Time and depth of the wetting front from WCW_2 (2) intercepting the characteristic of draining front (5), Eqs.(4.39) and (4.40).

During the interval $[T_{B,l} \leq t \leq T_{l,l}]$ the WCW_1 behaves similarly to a single WCW , however, the steeper characteristic of the jump with slope of $c_{J,l-2}$ replaces the draining front characteristic of WCW_l . Time and depth of the wetting front intercepting the jump are

$$T_{l,1} = \frac{T_{B,2} \cdot c_{J,l-2} - T_{B,1} \cdot v_1}{c_{J,l-2} - v_1} \quad (4.36)$$

$$Z_{l,1} = v_1 \cdot (T_{l,1} - T_{B,1}) \quad (4.37)$$

The mobile water content during $[T_{B,l} \leq t \leq T_{l,l}]$ is $[w(t) = w_l]$. Routing the wetting front position from the known depth and time of interception at $[Z_{l,1}]$ and $[T_{l,1}]$ with the velocity v_2 of WCW_2 , Eq.(4.5), leads during $[T_{l,1} \leq t \leq T_{l,2}]$ to

$$z_w(t) = Z_{l,1} + (t - T_{l,1}) \cdot v_2 \quad (4.38)$$

while the mobile water content during the same period amounts to $[w(t) = w_2]$.

Depth and time $Z_{l,2}$ and $T_{l,2}$ of the wetting front of WCW_2 intercepting its draining front results from equating Eq.(4.32) with the characteristic of WCW_2 , Eq.(4.3), vis

$$T_{l,2} = \frac{1}{2} \cdot \left(\frac{Z_{l,1}}{v_2} + 3 \cdot T_{B,2} - T_{l,1} \right) \quad (4.39)$$

$$Z_{l,2} = Z_{l,1} + (T_{l,2} - T_{l,1}) \cdot v_2 \quad (4.40)$$

After interception, $[t \geq T_{l,2}]$, the wetting front depth is in accord with Eq.(4.20)

$$z_w(t) = c_2 \cdot \left(\frac{T_{E,2} - T_{aB,2}}{2} \right)^{2/3} \cdot (t - T_{E,2})^{1/3} \quad (4.41)$$

where

$$T_{aB,2} = T_{l,1} - \frac{Z_{l,1}}{v_2} \quad (4.42)$$

is the apparent beginning time of WCW_2 , which accounts for the accelerating

effect of $[c_{j,l-2} > v_2]$ which, in turn, is due to $[q_2 > q_1]$. After the faster WCW_2 has swallowed the slower WCW_1 at $Z_{l,l}$ and $T_{l,l}$, WCW_1 completely loses its identity and viscous flow moves according to the conditions of WCW_2 . The mobile water content after $[t \geq T_{l,2}]$ amounts to

$$w(t) = w_2 \cdot \left(\frac{T_{E,2} - T_{aB,2}}{2 \cdot (t - T_{E,2})} \right)^{1/3} \quad (4.43)$$

Figure 4.1 schematically presents in the $q(w)$ -diagram the abrupt jump when a faster pulse chases a slower one. Consider the slopes of lines (4) and (2) as the velocities of the wetting front and the slower wave, the slope of line (6) as the jump velocity, and the slopes of lines (3) and (5) as the velocities of the faster wave and its wetting front.

4.7 Superposition of kinematic waves

Under the condition that the $WCWs$ neither gain water, for instance, from joining paths nor lose it by capillary sorption into smaller and previously air-filled pores, Sections 4.5 and 4.6 presented the routing of jumps due to the sequence of either decreasing or increasing pulses according to the theory of kinematic waves. The wetting front depths and the mobile water contents as functions of time at those depths were derived for each segment of an either constant, increasing or decreasing wetting front velocity.

A new WCW forms whenever a faster one swallows a slower one. Both original $WCWs$ lose their identity and the emerging one will dominate flow. Equation (4.17) describes the temporal decay of a collapsing film's mobile water content w after its arrival at depth z at time $t_D(z)$ with respect to the cessation of input at time T_E . The expression generally applies to any kinematic wave that evolves without restrictions. Generalization is achieved by waiving the specific depth such that

$$w(t) = w_0 \cdot \left(\frac{t(w_0) - T_E}{t - T_E} \right)^{1/2} \quad (4.44)$$

where w_0 is the mobile water content at time $[t(w_0) > T_E]$ of a wave that ceased at the surface at T_E . The corresponding reduction of the volume flux density follows from the combination of Eq.(4.44) with Eq.(4.8), which amounts to

$$q(t) = q_0 \cdot \left(\frac{t(q_0) - T_E}{t - T_E} \right)^{3/2} \quad (4.45)$$

Both decay processes, Eqs.(4.44) and (4.45), depend only on the amount of the decaying property, w_0 or q_0 , at the beginning of the local decay at $t(w_0)$ or $t(q_0)$, and on the time lapsed since the input ceased at T_E . Both decay processes are independent of depth. Once a new mobile water content and the corresponding volume flux density have emerged due to superposition their temporal decay is expressed by Eqs.(4.44) and (4.45) under consideration of the corresponding times $t(w_0)$ or $t(q_0)$, and T_E .

4.8 Kinematic waves that include a sink term

Germann and Beven (1985) added a sink term s (s^{-1}) (r in the original publication) to the kinematic wave theory that expresses water abstraction from the *WCW* into the surrounding air-filled pores due, for instance, to capillarity. The rate of water abstraction was considered proportionate to w ,

$$\frac{dw}{dt} = -s \cdot w(t) \quad (4.46)$$

which leads to the balance equation of

$$\frac{\partial q}{\partial t} + c \cdot \frac{\partial q}{\partial z} + c \cdot s \cdot w(t) = 0 \quad (4.47)$$

The maximum depth where the *WCW* ultimately ceases due to complete abstraction of the input into the pores that exert capillarity becomes

$$Z^* = q_s^{2/3} \frac{3}{2 \cdot s} \cdot b^{1/3} = \frac{c}{2 \cdot s} \quad (4.48)$$

The depth Z^* evolves as a scaling factor for all other basic relationships. The analytical expressions were worked out and they applied reasonably well to drainage flow from a block of an undisturbed soil. However, the approach failed entirely when applied to the water-content version of viscous flow. (P. Sieber, unpublished internal report). Thus, the sink-function approach, Eqs.(4.46) to (4.48) is considered unfit to handle water abstraction from a *WCW*.

4.9 Summary

The chapter demonstrates agreement between the two theoretical approaches to gravity-driven and viscosity controlled flow in permeable media, viscous flow in Chapter 3 and flow according to the kinematic wave theory. From viscous flow follows the constraint to 3 of the exponent in Eq.(4.9) and the macropore-flow constraint as the only two restrictions in the application of the purely mathematical kinematic wave theory of Lighthill and Witham (1955) to physical viscous flow. It is therefore concluded that kinematic wave theory is a complete analogue to viscous flow under the macropore flow restriction [$dL/dq = 0$]. From this it follows that the related method of characteristics correctly extends viscous flow as a valid concept for routing any series of input pulses of any arbitrary finite duration, as the discussion of Eqs.(4.22) and (4.23) demonstrates.

The analytical expressions are well suited for the estimation of either $w(z,t)$ or $q(z,t)$ as response to any series of rectangular input pulses $P_j(q_{S,j}, T_{B,j}, T_{E,j})$, [$1 \leq j \leq N$] of finite duration. However, general modeling a sequence of pulses with [$N > 2$] requires careful book-keeping of the respective wetting fronts in view of superposition.

5. Geometries of flow

5.1 Introduction

So far, viscous flow was presented as free-surface flow, featuring films that move between an *AWI* and a *SWI*. Chapters 2 to 4 applied free-surface flow to permeable media thus implying a restrictive decision on the flow geometry. However, the real flow geometries are but poorly known, they are most likely complicated, and may vary strongly between media. In order to get a better handle on the impact of flow geometry on viscous flow, Chapter 5 discusses in addition to free-surface flow the three flow geometries of: *Plane Poiseuille flow*, *pP*, between two parallel plates; *Hagen-Poiseuille flow*, *HP*, along a vertical cylinder; and *corner flow*, *Co*, along a vertical corner according to Tuller and Or (2001). The chapter then concludes with the comparison of the flow coefficients from the four geometries.

Plane-Poiseuille flow between two parallel plates may present flow in water-filled fissures and cracks, while the aperture between the plates adequately describes the geometry. Flow in a water-filled cylindrical pipe is probably the widest known application of viscous flow that is ascribed to Poiseuille (1846) and Hagen, where the cylinder radius is the parameter to be considered. Colbeck (1974) described flow along the outer walls of solid cylinders that conceptualize units of isothermal snow. Colbeck's approach is a variant of the Hagen-Poiseuille approach and is not pursued further because flow around vertical cylinders hardly applies to any other features but to isothermal snow. Flow along a vertical corner according to Tuller and Or (2001) includes surface tension at the curved *AWI* while the angle of the corner and the radius of the *AWI* determine the contact length of the *SWI*.

Alluding to open channel flow, the hydraulic radius, rh_{pm} , of the permeable medium facilitates comparison among the four flow geometries. It is defined as

$$rh_{pm} = \frac{w}{L} \quad (5.1)$$

(m), and represents the cross-section of the flow path per total length of the wetted perimeter, both parameters per cross-sectional area A of the permeable medium. The hydraulic radius of a permeable medium is a measure of the distance of momentum dissipation towards the *SWI*. As an example, the hydraulic radius of free-surface flow amounts to $[rh_{fs} = F]$.

5.2 Flow between two parallel walls - plane-Poiseuille flow (pP)

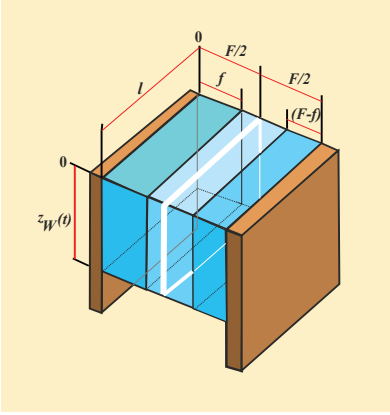


Figure 5.1: Plane-Poiseuille flow (pP). Definition of films flowing between two parallel and vertical walls. The aperture $F(m)$ is the distance between the walls, $f(m)$ is the thickness variable in the range of $[0 \leq f \leq F]$, $z_w(t)$ is the vertical position of the wetting front, and l indicates one half of the contact length per unit of the cross-sectional area A between the mobile water and the sessile parts of the porous medium.

Figure 5.1 depicts plane-Poiseuille flow. Consider two parallel and vertical walls with free-surface flow along the two inclined faces. Let the two film thicknesses increase due to, for instance, increased q_s , until the two $AWTs$ collapse and flow continues as a single cohesive water film between the two walls. Further increase of q_s would lead to perched water at the top of the two plates with subsequent pressure build up. Previous premises, however, exclude positive pressures from considerations. Figure 5.1 suggests symmetry, thus $[dv/df \geq 0]$ in the range of $[0 \leq f \leq F/2]$, $[dv/df = 0]$ at $F/2$, and $[dv/df \leq 0]$ in the range of $[F/2 \leq f \leq F]$, where $[v(0) = v(F) = 0]$. These conditions and the considerations that led to Eqs.(2.9) to (2.15) produce the velocity profile across the water film, volume flux, volume flux density, mobile water content, wetting front velocity, and hydraulic radius as

$$v(f) = \frac{g}{2 \cdot \eta} \cdot (F \cdot f - f^2) \quad (5.2)$$

$$Q(F) = \frac{2 \cdot g}{3 \cdot \eta} \cdot l \cdot \left(\frac{F}{2} \right)^3 = \frac{g}{12 \cdot \eta} \cdot l \cdot F^3 \quad (5.3)$$

$$q_{pP} = \frac{Q(F)}{A} = \frac{g}{24 \cdot \eta} \cdot L_{pP} \cdot F_{pP}^3 \quad (5.4)$$

$$w_{pP} = \frac{F_{pP} \cdot L_{pP}}{2} \quad (5.5)$$

$$v_{pP} = \frac{q_{pP}}{w_{pP}} = \frac{g}{12 \cdot \eta} \cdot F_{pP}^2 \quad (5.6)$$

$$rh_{pP} = \frac{w_{pP}}{L_{pP}} = \frac{F_{pP}}{2} \quad (5.7)$$

Equation (5.3) is identical with Lamb's (1932) Eq.(4) in *Art. 330*, if his dynamic viscosity is replaced with kinematic viscosity [$\eta = \mu / \rho$], and his pressure gradient [$\partial p / \partial y$] is replaced with [$\rho_{HOH} g$] because flow is here exclusively gravity-driven. The identity demonstrates that the bottom-up approach followed here leads to the same result as Lamb's (1932) fundamental deduction.

In accord with the derivations of Eq.(3.37), the depth of a plane-Poiseuille *WCW* at which it starts to leave the static water-content formation amounts to [$z_{cap} = \nu^{1/2} 0.0165(m^{3/2} s^{1/2})$].

5.3 Flow along a vertical cylinder - Hagen-Poiseuille flow (HP)

Figure 5.2 illustrates the concept and the parameters of Hagen-Poiseuille (Poiseuille, 1846) flow along the inner wall of a vertical cylinder. The diameters of the cylinder and the air-filled lumen are [$2 R$] and [$2 R'$], the corresponding film thickness amounts to [$F = R - R'$], and r is the thickness variable.

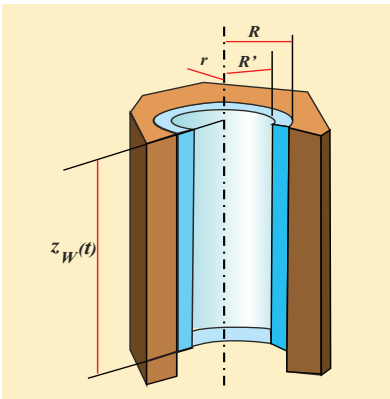


Figure 5.2: Hagen-Poiseuille flow (HP). Definitions of film flow along the inner side of a cylindrical tube, where R (m) is the radius of the tube and R' (m) is the radius of the air-filled lumen.

The force balance, Eq.(2.9), transmutes to

$$\pi \cdot (r^2 - R'^2) \cdot z_w(t) \cdot \rho \cdot g = 2 \cdot \pi \cdot r \cdot z_w(t) \cdot \eta \cdot \rho \cdot \left. \frac{dv}{dr} \right|_r \quad (5.8)$$

The non-slip condition, $[v(R) = 0]$, and integration from r to R , yield the velocity profile as

$$v(r) = \frac{g}{2 \cdot \eta} \cdot \left[\frac{R^2 - r^2}{2} - R'^2 \cdot \ln\left(\frac{r}{R}\right) \right] \quad (5.9)$$

The differential volume flow at r is

$$dQ|_r = 2 \cdot \pi \cdot r \cdot v(r) \cdot dr \quad (5.10)$$

Integration of Eq.(5.10) from R to R' yields the volume flow in the cylindrical film as

$$Q(R, R') = \frac{\pi \cdot g}{\eta} \cdot \left[\frac{R^4}{8} + \frac{R'^4}{8} + \frac{R'^4}{2} \cdot \left(\ln \frac{R'}{R} - \frac{1}{2} \right) \right] \quad (5.11)$$

Zero-flow results when $[R' = R]$, while well-known Hagen-Poiseuille flow emerges in a water-filled cylinder when $[R' = 0]$:

$$Q(R) = \frac{\pi \cdot g}{8 \cdot \eta} \cdot R^4 \quad (5.12)$$

Again, Eq.(5.12) is identical with Lamb's(1932) Eq.(4), Art. 331, when taking into consideration that his pressure gradient $[(p_1 - p_2) / \Delta l]$ is replaced here with $[\rho_{HOH} g]$ (only gravity-driven flow), and $[\eta = \mu / \rho]$. The identity supports once more that the bottom-up derivation followed here leads to the same result as Lamb's (1932) fundamental deduction in which he also notes that

The formula (4) [here Eq.5.12] contains exactly the laws found experimentally by Poiseuille [1846] in his researches on the flow of water through capillary tubes ...

The specific contact area onto which momentum dissipates during Hagen-Poiseuille flow amounts to $[L_{HP} = (2 N \pi R z_w(t)) / (A z_w(t)) \text{ (m}^1\text{)}]$, and we get

$$q_{HP}(R) = \frac{g}{16 \cdot \eta} \cdot L_{HP} \cdot R^3 \quad (5.13)$$

where N is the number of cylindrical tubes with equal radii R per A . Further, the mobile water content, the wetting front velocity and the hydraulic radius amount to

$$w_{HP} = \frac{1}{2} \cdot L_{HP} \cdot R \quad (5.14)$$

$$v_{HP} = \frac{g}{8 \cdot \eta} \cdot R^2 \quad (5.15)$$

$$rh_{HP} = \frac{R^2 \cdot \pi}{2 \cdot R \cdot \pi} = \frac{R}{2} \quad (5.16)$$

In accord with the derivations of Eq.(3.37), the depth of a Hagen-Poiseuille WCW at which it starts to leave the static water-content formation amounts to $[z_{cap} = v^{1/2} \cdot 0.019(\text{m}^{3/2} \text{ s}^{-1/2})]$.

5.4 Corner-flow (Co)

Vertical rills and furrows belong to the fourth flow geometry. Figure 5.3 depicts vertical corner-flow that Tuller and Or (2001) captured with the corner angle γ ($^\circ$) of the SWI and the radius R of the curved AWI .

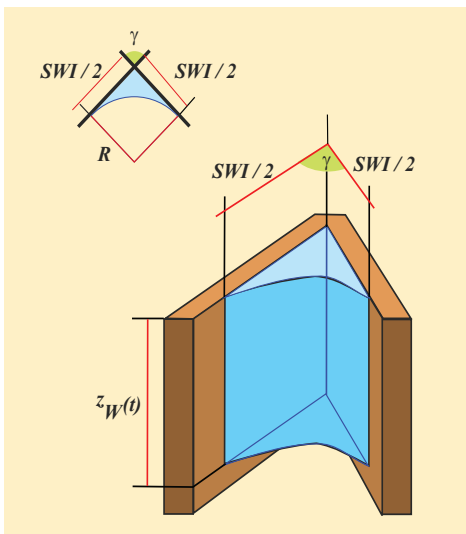


Figure 5.3: Corner flow (Co) definitions: γ ($^\circ$) indicates the angle of the corner, $[SWI/2 \text{ (m)}]$ is the tangent length to the meniscus with radius $R \text{ (m)}$.

The contact length l (m) is related with the radius R (m) of the meniscus according to

$$R = \frac{l}{2} \cdot \text{tg}(\gamma/2) \quad (5.17)$$

However, integration of the force balance requires a numerical procedure according to Ransohoff and Radke(1988), who expressed the average flow velocity in our notation as

$$v(l, \gamma) = R^2 \cdot \frac{g}{\eta \cdot \Phi(\gamma)} \quad (5.18)$$

Tuller and Or (2001) cast the results of the numerical investigation, Eq.(5.18), into the exponential function of

$$\Phi(\gamma) = \exp\left(\frac{u_1 + u_2 \cdot \gamma}{1 + u_3 \cdot \gamma}\right) \quad (5.19)$$

Their regression analysis yielded the coefficients of $[u_1 = 2.124]$, $[u_2 = 0.00783]$, and of $[u_3 = -0.00415]$, with the coefficient of determination of $[\mathcal{R}^2 = 0.995]$ between the model, Eq.(5.19), and the numerical results of Ransohoff and Radke (1988). Equation (5.19) applies to the range of $[10^\circ \leq \gamma \leq 150^\circ]$.

The *SWI* and *AWI* confine an area of $[(R \cdot l)/2 - R^2 \cdot \pi \cdot (180^\circ - \gamma) / 360^\circ]$. Recognizing that

$$l = 2 \cdot R \cdot \text{ctg}(\gamma/2) \quad (5.20)$$

leads to the mobile water content of $[N/A]$ corners of

$$w_{Co} = R^2 \cdot \frac{N}{A} \cdot \left[\text{ctg}(\gamma/2) - \pi \cdot \left(\frac{180^\circ - \gamma}{360^\circ} \right) \right] \quad (5.21)$$

From Eq.(5.18) it follows that

$$R = v^{1/2} \cdot \left(\frac{g}{\eta} \right)^{-1/2} \cdot \Phi(\gamma)^{1/2} \quad (5.22)$$

and from Eq.(5.20) that

$$R = \frac{L}{2} \cdot \frac{A}{N} \cdot \text{tg}(\gamma/2) \quad (5.23)$$

Inserting one R from Eq.(5.22) and one R from Eq.(5.23) into Eq.(5.21), while solving for L , leads to

$$L_{Co} = 2 \cdot v^{-1/2} \cdot w \cdot \left(\frac{g}{\eta} \right)^{1/2} \cdot \Phi(\gamma)^{-1/2} \cdot \left[1 - \text{tg}(\gamma/2) \cdot \pi \cdot \left(\frac{180^\circ - \gamma}{360^\circ} \right) \right]^{-1} \quad (5.24)$$

where $[L_{Co} = l N/A \text{ (m}^{-1}\text{)}]$ is the total contact length per A of $[N/A]$ water-conducting corners. The volume flux density of (N/A) corners and the hydraulic radius amount to

$$q_{Co} = v_{Co} \cdot w_{Co} = v_{Co}^2 \cdot \left(\frac{g}{\eta} \right)^{-1} \cdot \Phi(\gamma) \cdot \frac{N}{A} \cdot \left[\text{ctg}(\gamma/2) - \pi \cdot \left(\frac{180^\circ - \gamma}{360^\circ} \right) \right] \quad (5.25)$$

$$rh_{Co} = \frac{w_{Co}}{L_{Co}} = v_{Co}^{1/2} \cdot \left(\frac{g}{\eta} \right)^{-1/2} \cdot \frac{\Phi(\gamma)^{1/2}}{2} \cdot \left[1 - \text{tg}(\gamma/2) \cdot \pi \cdot \left(\frac{180^\circ - \gamma}{360^\circ} \right) \right] \quad (5.26)$$

5.5 Impact of the presumed flow geometries on viscous flow

The velocity v_w of the wetting front, the water content w_s and the duration of input $(T_E - T_B)$ completely determine a WCW . The resulting L and F or the corresponding radius R are now compared during $[T_B \leq t \leq T_I]$ among the four geometries of viscous flow. Corner angles of $[\gamma = 45, 90, \text{ and } 135^\circ]$ are assumed in corner flow.

The parameter L scales according to

$$S_L = w_s \cdot v_w^{-1/2} \cdot \left(\frac{g}{\eta} \right)^{1/2} \quad (5.27)$$

(m^{-1}), while the parameters rh and F or R scale with

$$S_{rh} = S_F = S_R = v_W^{1/2} \cdot \left(\frac{g}{\eta} \right)^{-1/2} \quad (5.28)$$

(m). Table 5.1 lists the scaling coefficients of the four flow geometries. The function $[\Phi(\gamma)]$, Eq.(5.19), summarizes the numerical analysis of Ransohoff and Radke (1988). Because its physical meaning is not obvious the coefficient $[\Phi(\gamma)]^{1/2}$ of corner flow is difficult to rank among the corresponding coefficients of the other three flow geometries. Besides scaling R of corner flow, however, all other coefficients are within a factor of 5.5, whereas the variations of the coefficients of the three canonical flow geometries, free-surface, plane-Poiseuille, and Hagen-Poiseuille flow, are each less than 2. Likewise, the suspended capillary fringe varies within [1:1.4], Tab. 5.2. Thus, the decision regarding the most suitable flow geometry seems not to be crucial when compared with all the other necessary assumptions and restrictions encountered when applying viscous flow to preferential infiltration.

Table 5.1: Coefficients of the four presumed geometries of viscous flow in permeable media

approach	L / S_L	F / S_F or R / S_R	rh / S_{rh}
(1) free-surface, fs	0.577	1.732	1.732
(2) plane Poiseuille, pP	0.577	3.464	1.732
(3) Hagen-Poiseuille, HP	0.707	2.828	1.414
max./min. (1) to (3)	1.73	1.63	1.41
(4.1) corner- $\gamma = 45(^{\circ})$	0.61	5.58	1.17
(4.2) corner- $\gamma = 90(^{\circ})$	0.45	9.56	1.03
(4.3) corner- $\gamma = 135(^{\circ})$	0.24	37.22	0.97
max./min. (1) to (4.3)	2.95	21.5	1.79

approach	$z_{cap} v^{1/2}$ (m ^{3/2} s ^{-1/2})
(1) free-surface, fs	0.0134
(2) plane Poiseuille, pP	0.0165
(3) Hagen-Poiseuille, HP	0.0190

Table 5.2: Depth of capillary fringe z_{cap} in relation to the presumed flow geometry, derivation of Eq.(3.37)

5.6 Dominance of viscosity

In view of the above considerations, the proposition of Lin and Wang (1986), Eq.(2.16), leads to

$$\mathcal{Re} = \frac{F \cdot \bar{v}}{\eta} = \frac{rh \cdot v}{\eta} \leq 3 \quad (5.29)$$

It includes the hydraulic radius rh of the respective flow geometry and the wetting front velocity. Table 5.3 summarizes for the three canonical flow geometries the maximum wetting front velocities, and film thicknesses or radii at $[\mathcal{Re} = 3]$. Table 5.3 also includes the capillary heads, h_{cap} , that result from applying Eqs.(2.19) or (2.21) to either F or R . The analysis demonstrates that the requirement of stable film flow confines viscous flow completely to capillarity, while flows faster than v_{max} are not stable and require special caution in their interpretation.

Table 5.3: Maxima of wetting front velocities and film thicknesses, including the associated capillary heads at the threshold of stable viscous flow, $\mathcal{Re} = 3$, Eq.(5.29)

approach	v_{max} (mm s ⁻¹)	F_{max} or R_{max} (μm)	$h_{cap}(v_{max})$ (m)
(1) fs	31	97	-0.15
(2) pP	39	154	-0.10
(3) HP	35	170	-0.18

Figure 5.4 presents \mathcal{Re} of free-surface flow as a function of either F or v in order to shed some light on the sensitivity of relaxing the Stokes (1845)-restriction of $[\mathcal{Re} \leq 1]$ and the Lin-and-Wang (1986)-restriction of $[\mathcal{Re} \leq 3]$. Thus,

$$\mathcal{Re}_{fs} = \frac{F^3 \cdot g}{3 \cdot \eta^2} = v^{3/2} \cdot \left(\frac{3}{\eta \cdot g} \right)^{1/2} \quad (5.30)$$

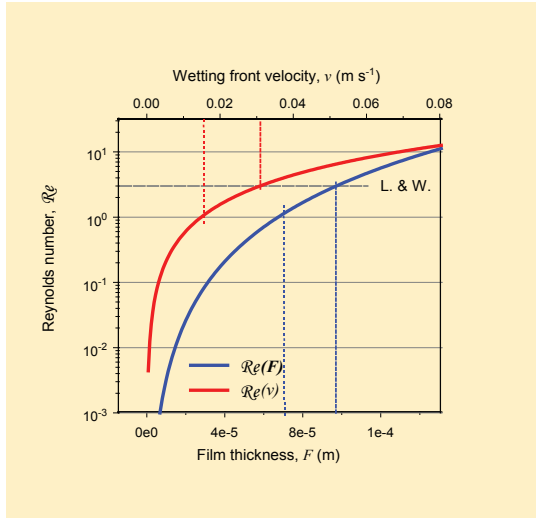


Figure 5.4 Reynolds number Re for free-surface flow as function of film thickness, F , and wetting front velocity, v . The grey dashed line L. & W. indicates [$Re = 3$] that Lin and Wang (1986) considered as threshold between stable and unstable flows. The vertical lines indicate v_{max} and F_{max} according to Tab. 5.3 and their counterparts at [$Re = 1$]

6. Darcy's law and the Richards equation in view of viscous flow

6.1 Introduction

Darcy's (1856) law and the Richards (1931) equation are the two most widely applied concepts of flow in porous media, the former in completely saturated and the latter in partially water-saturated systems. After briefly introducing Darcy's law and the Richards equation their relationships with viscous flow will be explored. In addition, the juxtapositions shed light on the notorious discussion about field capacity and offer a hydrodynamic explanation of hysteresis in the soil-hydrological functions.

6.2 Saturated permeable media - Darcy's (1856) law

This section introduces Darcy's (1856) law, which is most likely the first quantitative approach to flow in permeable media. While modernizing the public water supply system of Dijon, the capital of Burgundy, France, Darcy turned to the optimization of filtration tanks. He - actually his assistant Ritter - filled various mixtures of gravel and sand into steel cylinders in the search for the optimal filter material. The cylinders were 3.5(m) high and had inner diameters of 0.35(m). Figure 6.1 is a copy from Darcy (1856) that illustrates well the endeavor. Each cylinder was sealed at the top and at the bottom, and the faucet at the bottom drained into a squared reservoir of 1(m) by 1(m). Two mercury manometers were mounted into the cylinder wall, one each at the heights of the inlet and the faucet, respectively. Water was conducted from the city hospital's water supply directly to the top. Occasional failures in the water supply system led to interruptions of the experiments and were meticulously reported.

From numerous experiments Darcy found empirically that the volume ΔV (m³) of water that passed the faucet during the time interval of Δt (s) was proportional to the entire cross-sectional area [$A = 0.0962$ (m²)] of the cylinder, to the time interval Δt , to the difference ΔH (m) of the heads in the two mercury manometers, and inversely proportional to the distance Δl (m) between the manometers, thus

$$\Delta V \propto \frac{A \cdot \Delta t \cdot \Delta H}{\Delta l} \quad (6.1)$$

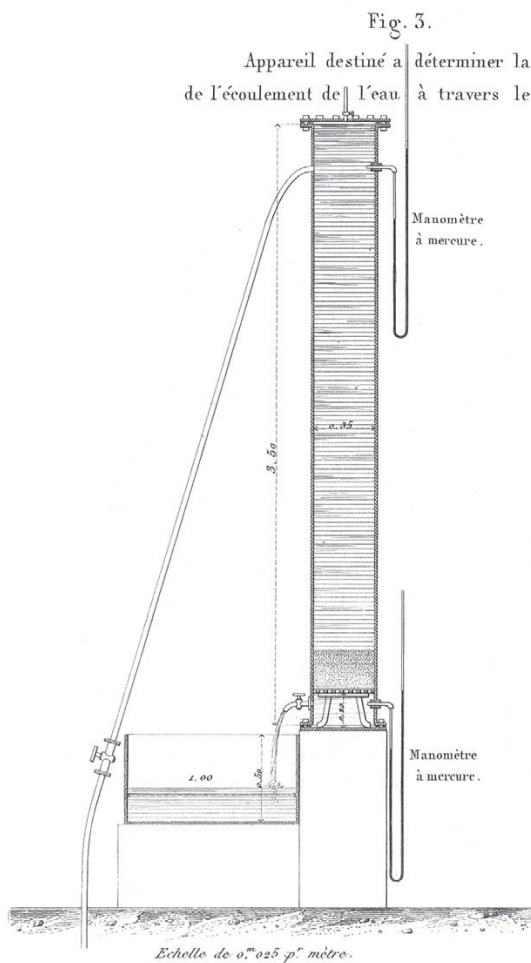


Figure 6.1: Appareil destiné à déterminer la loi de l'écoulement de l'eau à travers le sable: Darcy's apparatus dedicated to the determination of the water's flow law across the sand (Darcy, 1856).

Recognizing the volume flux density

$$q = \frac{\Delta V}{A \cdot \Delta t} \quad (6.2)$$

leads to the common notation of Darcy's law

$$q = -K \cdot \frac{\Delta H}{\Delta l} \quad (6.3)$$

where Darcy's *facteur de proportionnalité* (factor of proportionality) K (m s^{-1}) was transformed into the hydraulic conductivity at saturation, K_{sat} , of a particular flow system consisting of a permeable medium that is completely saturated with water. The direction of q is along the decreasing hydraulic gradient, $(\Delta H / \Delta l)$, which is expressed in the minus sign in Eq. (6.3). Darcy's one-dimensional experiments were conducted only in vertical cylinders but there are no restrictions to expand the law to other directions and to three dimensions.

The hydraulic head is the sum of the two heads that originate from gravity and pressure:

$$H = h_G + h_p \quad (6.4)$$

The gravitational head is $[h_G = \Delta z]$ according to Eq.(2.5), while the gradient emanating from it amounts to $[\Delta z / \Delta z = 1]$. The pressure head h_p (m) is due to any additional pressure acting on the liquid according to Fig. 6.1. The condition $[h_p > 0]$ requires $[\theta = \varepsilon]$ because $[\theta < \varepsilon]$ permits θ to temporarily increase with increasing h_p , expressing a kind of a two-fluid elasticity in a soil-water-air system. The hydraulic gradient resulting from the pressure head is $[h_p / \Delta z]$. Therefore, vertical flow in a saturated permeable medium that is not subject to external pressure, $[h_p = 0]$, is

$$|q| = K_{sat} \quad (6.5)$$

Darcy's (1856) mercury manometers are now scrutinized. Figure 6.2 depicts one of the two mercury manometers whose recorded pressure is

$$P_M = g \cdot [\Delta z_a \cdot (\rho_{Hg} - \rho_{H_2O}) + \Delta z_b \cdot \rho_{Hg}] \quad (6.6)$$

(Pa), where Δz_a and Δz_b refer to the heights of the water column in the manometer below the outlet's level and of the mercury column above it, $[\rho_{Hg} = 13'534(\text{kg m}^{-3})]$ and $[\rho_{H_2O} = 1'000(\text{kg m}^{-3})]$ are the respective densities of mercury and water. The hydraulic head H (m) amounts to

$$H = \frac{P_M}{\rho_{H_2O} \cdot g} = (\Delta z_a + \Delta z_b) \cdot \frac{\rho_{Hg}}{\rho_{H_2O}} - \Delta z_a \quad (6.7)$$

Equation (6.7) demonstrates the strong impact of ρ_{Hg} on Darcy's pressure recording device, which markedly reduces its sensitivity. Nonetheless, the linearity of Eq.(6.3) is generally undisputed which implies that the hydraulic conductivity at saturation is independent of the hydraulic gradient, thus $[dK_{sat} / d(\Delta H / \Delta l) = 0]$.

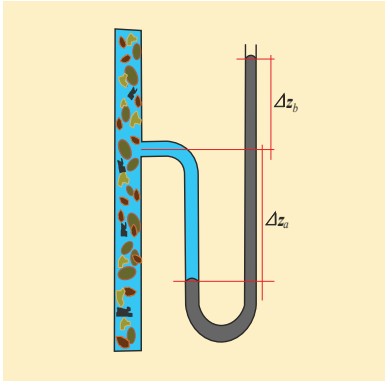


Figure 6.2: Set-up of a mercury manometer used in Darcy's (1856) experiments, Eqs.(6.6) and (6.7).

6.3 Darcy's law and viscous flow

The comparison of Darcy's law with viscous flow begins at the joint limit of either approach where the two conditions common to both approaches are

- (i) complete water saturation $[\theta = \varepsilon]$ that envelops the maximum mobile water content, w_{max} ;
- (ii) absence of additional pressure, leaving gravity as the only source of flow-driving force, hence $[h_p = 0]$, $[\Delta H/\Delta z = 1]$, and $[|q| = K_{sat}]$, Eq.(6.5).

Thus, comparing Eq.(6.3) with Eq.(5.4) (plane-Poiseuille flow) under consideration of Eq.(6.5) leads to the hydraulic conductivity at saturation as

$$K_{sat} = q_{v,max} = (F^3 \cdot L)_{max} \cdot \frac{g}{24 \cdot \eta} \quad (6.8)$$

where $q_{v,max}$ represents the maximum volume flux density of viscous flow. Equation (6.8) defines K_{sat} in terms of viscous flow and, ultimately, of Stokes (1845) flow.

The extension of Eq.(6.8) into the realm of Darcy-flow, $[q > q_{v,max}]$, where $[h_p = p/(\rho g) > 0]$, $[\theta_{max} = \varepsilon]$, and $[h_{cap} = 0]$, brings us to the question of whether $[(F^3 L)_{max}]$ is independent of h_p . The addition of the pressure gradient to the driving force on the left-hand side of Eq.(2.9) and replacing the kinematic viscosity with the dynamic viscosity, $[\mu = \rho \eta]$ on its right-hand side produces

$$\left(\rho \cdot g + \frac{\Delta p}{\Delta z} \right) \cdot l \cdot z_w(t) \cdot (F - f) = \mu \cdot l \cdot z_w(t) \cdot \frac{dv}{df} \bigg|_f \quad (6.9)$$

Applying a similar procedure to Eq.(6.9) to that which produced Eq.(5.6) yields

$$v(h_p) = \frac{(\rho \cdot g + \Delta p / \Delta z)}{12 \cdot \mu} \cdot F^2 = \frac{g \cdot (1 + \Delta h_p / \Delta z)}{12 \cdot \eta} \cdot F^2 \quad (6.10)$$

Equation (6.10) demonstrates that the linear increase of v with increasing h_p is possible only if $[dF/dh_p = 0]$. Further,

$$q(h_p) = v(h_p) \cdot w_{\max} \quad (6.11)$$

Again, this is only plausible if $[dw_{\max}/dh_p = 0]$ at $[\theta = \varepsilon]$. If Darcy's law, Eq.(6.3), and Eq.(6.10) apply then $[d\theta/dh_p = dw_{\max}/dh_p = 0]$ and, ultimately, $[dL/dh_p = 0]$. Equation (6.10) is consistent with Eq.(5.6) at the limit of $[h_p = \Delta h_p / \Delta z = 0]$. This demonstrates that unsaturated viscous flow seamlessly glides over to Darcy-type flow when $[h_p \geq 0]$. However, this paragraph reinterprets Darcy's law rather than proving it. The alternative of h_p not only impacting v but either F or L , or F and L , while $[w_{\max} = (F^3 L)_{\max}]$ has to remain constant, is highly improbable in view of the various dimensionalities of F and L in the relationships of $[w \propto (F^1 L^1)]$, $[v \propto (F^2 L^0)]$, and $[q \propto (F^3 L^1)]$, Eqs.(5.5), (5.6) and (5.4).

There are reports on non-linearity in Darcy's law. Swartzendruber (2005), for instance, presents examples from flows in clay-rich soils. Because L also represents the surface area per unit volume of the medium onto which momentum dissipates, L may respond to h_p in non-structured and clay-rich materials mainly due to the enormous internal surface area.

The extension of Eq.(6.8) into the range of $[\theta < \varepsilon]$, $[h_c < 0]$ and $[h_p = 0]$ due to $[q < q_{\max}]$ leads to the three theoretical cases of

- (i) $[F(q) < F(q_{v,\max})]$ and $[L(q) < L(q_{v,\max})]$;
- (ii) $[F(q) < F(q_{v,\max})]$ and $[dL/dq = 0]$, macropore flow restriction;
- (iii) $[dF/dq = 0]$ and $[L(q) < L(q_{v,\max})]$.

Case (i) applies in general to viscous flow, while the determination of the empirical relationships of $v(q)$ and $w(q)$ awaits experimentation.

Case (ii) implies macropore flow restriction, assuming that the flow paths carrying $q_{v,\max}$ at K_{sat} are the same and only paths which carry any viscous flow when $[q \leq q_{v,\max}]$. The restriction is the base for the unconditioned application of the kinematic wave theory, Section 4.2, to any variation of input pulses. Because F is the only parameter left to react upon q -variations during $[T_B \leq t \leq T_E]$ under macropore flow restriction any input rate $[q \leq q_{\max}]$, L_{\max} will scale free-surface flow, Eqs.(2.15), (3.2), and (3.3) in the following way

$$F(q) = \left(\frac{3 \cdot q \cdot \eta}{g \cdot L_{max}} \right)^{1/3} \quad (6.12)$$

Further, the wetting front velocity and mobile water content are related to $[q \leq q_{max}]$ as follows

$$v(q) = \left(\frac{q}{L_{max}} \right)^{2/3} \cdot \left(\frac{g}{3 \cdot \eta} \right)^{1/3} \quad (6.13)$$

and

$$w(q) = \left(\frac{3 \cdot q \cdot \eta}{g} \right)^{1/3} \cdot (L_{max})^{2/3} \quad (6.14)$$

On the one hand, the macropore flow restriction rigorously excludes from flow conduction all the pores that are not considered macropores able to carry F_{max} . On the other hand, the restriction would allow F_{max} and L_{max} to be deduced from K_{sat} on the assumption that w_{max} or $v(K_{sat})$ are known from additional measurements. Moreover, if $[dL/dq = 0]$ then $[w(q) = v/q]$ for the entire permitted q -range of viscous flow.

Case (iii) is discarded because it contradicts Eqs. (2.13) to (2.15).

Whether preference will go to *Case(i)* or to *Case(ii)* awaits rigorous experimentation. The applicability of *Case(ii)* would let viscous flow in the unsaturated zone elegantly benefit from Darcy's (1856) Law including the countless world-wide collections of K_{sat} .

6.4 Partially saturated permeable media - Richards (1931) equation

The apparently simple addition of the gas phase to flow in permeable media increases the number of interactions in Darcy's law from one to four, viz, three due to the pair-wise interactions between the three phases and one from the triple interaction among all three phases. The replacement of h_p in Eq.(6.4) with h_{cap} from Eqs.(2.19) or (2.21) provides a way of adapting Darcy's (1856) law to partially saturated porous media. However, this apparently simple adaptation bears severe physical consequences. The pressure head h_p in Darcy's law is due to a boundary condition in mono-fluid systems while $h_{cap}(\theta)$ is due to the local interactions among the solid, liquid, and gas phases as outlined in Section 2.5.

According to Jury et al. (1991) Buckingham's (1907) modification of Darcy's law reads for vertical flow in the notation used here as

$$q = -K(h_{cap}) \cdot \frac{\partial H}{\partial z} = -K(h_{cap}) \cdot \left(\frac{\partial h_{cap}}{\partial z} + 1 \right) \quad (6.15)$$

where $K(h_{cap})$, replacing K in Eq.(6.3), is now a function of the capillary head or, via $h_{cap}(\theta)$, Eq. (2.27), a function of the water content, $K(\theta)$. For clarity reasons, the subscript *sat* is added to K in Eq.(6.3), thus $[K_{sat} \geq K(h_{cap})]$. Further, the capillary head h_{cap} in Eq.(6.15) replaces the pressure head h_p in Eq.(6.4). This part of the modification is the fundamental deviation from Darcy's law because $[h_p > 0]$ in Eq.(6.4) acts independently on the boundaries of the permeable medium, whereas $[h_{cap} < 0]$ in Eq.(6.15) acts exclusively in its interior as $h_{cap}(\theta)$ whenever $[\theta < \varepsilon]$. Partial derivatives are required because K , h_{cap} , and θ are transient functions of both, space and time. A transient process as outlined here expressively requires mass-balance constraints. This is in contrast to Darcy's law that applies to steady flow. Thus, the adaptation of Darcy's law to flow in unsaturated permeable media leads to Richards' second-order partial differential equation, Eq.(6.17).

Richards' (1931) definition of capillary flow will now be briefly introduced. The remainder of Section 6.4 adheres to his notations to maintain the closest possible identity with his considerations. The reader is asked to bear in mind the apparent confusion of notations and abbreviations in this section with the other parts of the book. Richards mastered the physical consequences of switching from h_p to h_{cap} by introducing a set of assumptions and by focusing on the potentials of capillarity and gravity (ψ and ϕ in his notation) that are expressed with the dimension of ($\text{cm}^2 \text{ s}^{-2}$) as energy per unit mass of water in the system of centimeter-gram-second that physicists prefer. He stated that

When the conditions for equilibrium under gravity ... are fulfilled, the velocity and acceleration of the capillary liquid are everywhere zero and Eq.(5) becomes,

$$\nabla(\phi + \psi) = 0 \quad (6.16)$$

*which means that the force arising from the pressure gradient just balances gravity. If this condition does not obtain there will be a resultant water-moving force and in general there will be **capillary flow**. (Richards, 1931).*

He used the term pressure for the capillary potential $[\psi_{cap} \leq 0]$ according to Eq.(2.23), and the considerations lead to the original Richards

differential equation for the general case of capillary flow,

$$K \left(\frac{\partial^2 \psi}{\partial x^2} + \frac{\partial^2 \psi}{\partial y^2} + \frac{\partial^2 \psi}{\partial z^2} \right) + \frac{\partial K}{\partial x} \frac{\partial \psi}{\partial x} + \frac{\partial K}{\partial y} \frac{\partial \psi}{\partial y} + \frac{\partial K}{\partial z} \frac{\partial \psi}{\partial z} + g \frac{\partial K}{\partial z} = -\rho_s \cdot A \cdot \frac{\partial \psi}{\partial t} \quad (6.17)$$

Further,

If from experimental data, K and A can be expressed as functions of the capillary potential, the ψ is the only variable occurring in the equation. Either ψ or θ may be used as the dependent variable and q , K , and A may be expressed in terms of either one. It seems that ψ will be the easier variable to use when experimentally investigating the nature of K . If ψ is a single valued function of θ , the choice is simply a matter of mathematical expedience. (Richards, 1931)

In Richards' notations are [$A = d\theta/d\psi$ ($\text{cm}^2 \text{ s}^{-1}$)] the capillary capacity of the medium [the equivalent of the specific water capacity, Eq.(2.28) (P.G.)], θ ($\text{cm}^3 \text{ g}^{-1}$) volume of water per gram of dry medium, ρ_s (g cm^{-3}) weight of the dry medium in unit volume, and ψ (erg/gram). Further, ϕ and ψ correspond with h_G and h_{cap} , respectively, and his factor of proportionality K assumes the unit of (s). From the division of both sides of Eq. (6.17) follows the diffusivity as

$$D(\psi) = K(\psi) / [A(\psi) \cdot \rho_s] \quad (6.18)$$

with the dimension of the diffusion coefficient, ($\text{cm}^2 \text{ s}^{-1}$). Thus, the moderate modification of the original Richards equation according to Eq.(6.18) expresses the diffusion of capillary potential (Richards' ψ), while gravity is separately treated with $g \cdot (\partial K / \partial z) / (A(\psi) \cdot \rho_s)$.

Richards (1931) introduced three basic assumptions:

(i) *Capillary potential is a single valued and continuous function of θ :*

The assumption implies that any temporal variation of θ is instantaneously equilibrated by the corresponding alteration of h_{cap} , and vice versa. Any deviation of this behavior is dubbed non-equilibrium flow as, for instance, Jarvis (2007) explains. Moreover, wetting and drying of a porous medium must follow the retention curve, i.e. Fig. 2.6, in that during imbibition smaller pores fill with water before larger pores are allowed to carry it, and larger pores drain before smaller ones may do so. The condition requires sequential wetting and drying of a porous medium (see, for instance, Sposito, 1986). Thus, Richards' capillary flow is sequential in nature.

(ii) *The variables K and A may be expressed in terms of either ψ or θ :* The assumption requires continuous functions of $K(\psi)$ or $K(\theta)$, and $A(\psi)$ or $A(\theta)$, which subsequently rely on sequential flow.

(iii) *Isotropy, $K(z) = K(x,y)$:* There is no distinction in the conductivity functions between gravity-dominated and purely capillarity-driven flow.

6.5 Richards equation and viscous flow

The question if expressions similar to Eq.(6.17) may satisfactorily deal with preferential flow boils down to the adequacy of the three Richards-assumptions to realistically deal with gravity-dominated infiltration and drainage. Whereas K_{sat} is obviously related with viscous flow, Eq. (6.8), no equivalent relationship was found linking $K(z)$ simultaneously with capillary- and viscous-flow. Most of the numerous experimental procedures to estimate the parameters of the $[K-\psi-\theta]$ -relationships are designed such that they *a priori* fulfill the Richards-assumptions. Therefore, the relationships are here classified as empirical constructs that are useful in their own rights.

The Richards (1931) equation, Eq.(6.17), bears the great advantage over viscous flow that it accommodates flow in all directions. In particular, it envelops capillary rise of water from wetter to dryer horizons including flow from groundwater against gravity towards the root zone. The evolution of the local flow direction is governed by the spatial distribution of the water content, the hydraulic conductivity, and the action of sinks, such as roots. Thus, it is able to account for the internal redistribution of soil moisture for long periods after the last infiltration event. For that reason it is the foundation for the numerous applications used to assess soil water availability mainly in horticulture as well as in dry-land and irrigation agriculture.

Equations (6.17) and (6.18) express the diffusion of capillary potential with the variable diffusion coefficient, $D(\psi)$. Thus, wetting fronts advance in proportion to the square root of time, $[z_w(t) \propto t^{1/2}]$, according, for instance, to Philip (1969). Yet, wetting fronts in viscous flow advance proportionate to $[z_w(t) \propto t]$ and to $[z_w(t) \propto t^{1/3}]$ in the ranges of $[z_w(t) < Z_I]$ and $[z_w(t) > Z_I]$, respectively, as Eqs.(3.19) and (3.15) demonstrate. There are also interesting comparisons at the operational level. The h_{cap} -limit due to $[\mathcal{R}_e \leq 3]$ of $[-0.15 \geq h_{cap} \geq -0.18(\text{m})]$ in Tab. 5.3 suggests that the realms of capillary flow and viscous flow overlap. This is in analogy to Lamb's (1932) *Article 330a*, where he postulated that viscous flow applies to $[h_p > 0]$. Moreover, if viscous flow is a valid representation of preferential flow any assumption of its exclusive occurrence in voids that do not exert capillarity has to be discarded. Further, viscous flow in the range of $[0 \geq h_{cap} \geq -0.15(\text{m})]$ is considered unstable, leading to wavy flow, and eventually to a *WCW*'s collapse to water-bridges according to Gezehegy and Or (2005). Actually, hysteresis during capillary flow at higher capillary heads according, for instance, to Dane and Lenhard (2005) is presumably due to instabilities during viscous flow.

In current notation Richards' (1931) diffusivity, Equation (6.18), is $[D(h_{cap}) = K(h_{cap})/C(h_{cap}) \text{ (m}^2 \text{ s}^{-1})]$, where the specific water capacity $C(h_{cap})$ is according to Eq.(2.28). Under consideration of $[w = (FL)/2]$ and assuming that Eq. (6.8) basically also applies to viscous flow in non-saturated porous

media, it follows that

$$D(h_{cap}) = \frac{K(h_{cap})}{C(h_{cap})} = \frac{g \cdot F^2 \cdot w}{12 \cdot \eta} \cdot \frac{\Delta h_{cap}}{\Delta \theta} \quad (6.19)$$

According to Germann et al. (1997), the following assumes that $[D(h_{cap}) = \eta]$ represents the threshold between the realm of exclusive capillary flow and the realm, where capillary flow and viscous flow co-exist. The application of typical values of $[w = 0.05(\text{m}^3 \text{ m}^{-3})]$ (see Chapters 8 ff.) and of $[\Delta \theta / \Delta h_{cap} \approx 0.5(\text{m}^{-1})]$ (see, for instance, Richard and Lüscher, 1987, for a broad collection of $C(h_{\phi})$ -data) yields $[F_{thresh} \approx 5(\mu\text{m})]$ and $[h_{cap}(F_{thresh}) \approx -3(\text{m})]$, Eq.(2.21). The ambiguous application of so-called “typical values” and the crude assumptions and restrictions applied to Eq.(6.19) produce an approximate capillary head that coincides with the limit of *Field Capacity FC* according to Veihmeyer and Hendrickson (1949). Various authors set $[h_{cap}(FC) \approx -1/3(\text{bar}) = -3.4(\text{m})]$ as, for instance, Hillel (1998) broadly discussed. Thus, Veihmeyer and Hendrickson’s (1949) fast drainage of originally saturated soils is explicable with viscous flow that ceases at about $[D(h_{cap}) \approx \eta]$.

The definition of the hydraulic functions $\theta(h_{cap})$ and $K(\theta)$ require a representative elementary volume, *REV*, that has to be small enough to be amenable to the mathematical derivatives of the Richards equation, Eq.(6.17), yet large enough to include all the necessary volume-averaged properties. Moreover, transitions among *REV*s have to be smooth such that $h_{cap}(x,y,z)$, $K(x,y,z)$ and $\theta(x,y,z)$ are continuously defined. In contrast, viscous flow only requires for the definition of the mobile water content, w , the same yet arbitrary cross-sectional area A used in the definition of the specific contact length, L . The arbitrary areal extent of A becomes adjustable to the specific problem at hand. It permits discontinuities of hydraulic properties in the directions perpendicular to flow, while the discontinuous wetting shock front is an inherent viscous-flow property.

6.6 Capillary number, Ca , and Bond number, Bo

The dimensionless capillary number, Ca , and Bond number, Bo , place within a broader hydrodynamic context the thresholds of the domineering forces acting in a particular flow regime. The capillary number

$$Ca = \frac{\eta \cdot \rho \cdot v}{\sigma} \quad (6.20)$$

relates the capillary with the viscous force. Replacing v in Eq.(6.20) with

$F(v)$, Eq.(2.15), yields the Bond number as

$$Bo = \frac{\rho \cdot g}{\sigma} \cdot F(v) \quad (6.21)$$

which weighs the gravitational force with the capillary force. Their upper limits are set at $[\mathcal{R}\ell = 3]$, Eq.(2.16), where $[\nu = 3.1 \times 10^{-2}(\text{m s}^{-1})]$ and $[F = 97(\mu\text{m})]$, yielding $[Ca_{\max} = 4.2 \times 10^{-4}]$ and $[Bo_{\max} = 1.3 \times 10^{-3}]$. Their lower limits follow, for instance, from Germann and alHagrey (2008) (see also *Case II.1* in Part II), where $[\nu = 3.3 \times 10^{-5}(\text{m s}^{-1})]$ and $[F = 3.2(\mu\text{m})]$. The corresponding minima found so far from well documented viscous flow are at $[Ca_{\min} = 4.5 \times 10^{-7}]$ and $[Bo_{\min} = 1.4 \times 10^{-6}]$. Thus, any flow regime with Ca and Bo exceeding the minima bears the possibility of gravity driven and viscosity controlled flow i.e., viscous flow. On the one hand, Friedman's (1999) typical values for capillary flow in porous media in the vicinity of $[Ca = Bo \approx 10^{-5}]$ deserve a closer look at the postulated capillary-flow regime. On the other hand, the overlapping ranges may indicate the simultaneous co-existence of capillary and viscous flow.

6.7 Domains of flow in permeable media

The juxtaposition of Darcy's law and Richards equation on one hand with and viscous flow on the other hand results in three domains of permeable-media flow with respect to the film thickness and the viscous force. The three domains are:

- (i) $F < \approx 5(\mu\text{m})$: The tensile strength in the water is strong and capillarity dominates flow. This is the domain of exclusive sequential capillary flow in the sense of the Richards equation.
- (ii) $5 < \approx F < \approx 200(\mu\text{m})$: The tensile strength is weak enough to allow for the co-existence of capillary flow and viscous flow. This is the domain of laminar viscous flow that follows from Stokes's principles of irrotational flow according to Chapter 2.
- (iii) $F > \approx 200(\mu\text{m})$: The tensile strength is feeble, flow becomes unstable, and water-bridges may form according to Ghezzehei and Or (2005).

The conditions for capillary flow and Darcy-flow are $[\theta < \varepsilon]$ and $[\theta = \varepsilon]$, respectively. Thus, preferential flow may also occur in the Darcy-domain where, however, features of unstable flow may increasingly impact the process. This may obscure the applicability of Darcy's law, and capillary potentials of about $[-0.2 \leq h_{\text{cap}} \leq 0]$ may cover the range of severe hysteresis in the $[\theta-h_{\text{cap}}-K(\theta)]$ -relationships.

The two transitions between the three domains follow at the lower end from the dissipation of capillary potential alone vs. its joint dissipation with momentum, while the transition from stable laminar to unstable flow leads to the delineation at the upper end. Her, it is proposed that the transitions approximately occur from domain (i) to (ii) at $[D = \eta]$ and from domain (ii) to (iii) at $[\mathcal{R}e = 3]$, respectively.

7. Part I Conclusion

7.1 Achievements

Chapters 2 and 3 provided a bottom-up approach to preferential infiltration. The theory rests on the assumption that gravity exclusively drives steady vertical flow while viscosity prevents its acceleration. The two parameters of film thickness F and of contact length L per cross-sectional area A were developed, where F depends exclusively on the flow velocity of the film and L represents the vertical area per unit volume of the permeable medium where momentum is dissipated. The greater is L the higher is the density of flow paths. The two parameters F and L are adequate to route a water content wave WCW caused by $P(q_s, T_B, T_E)$.

Chapter 4 linked viscous-flow to kinematic wave theory, which provides for the routing of sequences of variable pulses. Chapter 5 investigates the relationships among the four presumed geometrical shapes of the flow paths - free-surface flow, plane-Poiseuille flow, Hagen-Poiseuille flow, and corner flow. The chapter concluded that the differences among the four flow geometries are of minor importance vis-à-vis the real but poorly known flow path geometries in natural permeable media.

From the numerous links with irrotational Stokes (1845, 1851)-flow according to Lamb (1932) the following restrictions on viscous flow emerged:

- (i) incompressible wetting fluid;
- (ii) no slip at the solid-water interface, SWI ;
- (iii) small Reynolds number, $[Re \leq 3]$.

The conditions resulted in films so thin that capillary forces presumably acting in them require experimental attention.

Further restrictions emerge from the viscous-flow derivations:

- (iv) Rigid permeable media;
- (v) Neuman boundary condition of no-ponding during infiltration;
- (vi) macropore-flow for the unrestricted applicability of kinematic wave theory.

The dimensional analysis in Chapter 6 revealed that positive pressure on the liquid affects only the flow velocity. Therefore, the macropore-flow restriction applies to the realm of Darcy's (1856) law, which provides an opportunity to also apply Dirichlet boundary conditions to viscous flow. The somewhat daring assumption that Richards (1931)-diffusivity may also be applied to momentum dissipation if $[D > \eta]$ leads to the three domains of permeable

media flow that are governed by either strong, weak, or feeble viscous forces. Moreover, viscous flow is documented for so far unexpectedly low capillary- and bond-numbers.

Viscous flow requires only that the identical but otherwise arbitrary extent of the cross-sectional area A be defined for both, the mobile water content w and the specific contact length L . As A may be arbitrarily defined this provides an easy way to deal with viscous flow in any spatial extent of a permeable medium. On one hand, A 's arbitrariness circumvents the need for pedo-transfer functions and similar approaches for crossing the various limits among presumed spatial scales. On the other hand, the arbitrariness may obscure the underlying physical relationships when A increases. The decision regarding the size of A is analogous to the decision to define the areal extent of a hydrological catchment in the investigation of precipitation-runoff relationships. The smaller the catchment area the closer one presumably gets to the physics of the processes, mainly by reducing spatial variability. However, the reduction of the area ultimately means that one deals only with flow routing in individual channels, but loses sight of important processes such as evapo-transpiration, infiltration, and run-off to the channels.

The parameters ν and F depend exclusively on one another, and both are independent of θ . The wetting front velocity is directly related with the wave velocity c that is considered to strongly relate with the propagation of water-borne signals like tracer pulses. Moreover, L becomes a bulk measure of the flow path geometry. For instance, in non-structured porous media, L is supposed to be highly correlated with texture, increasing with decreasing average particle sizes. But L , also expressing the vertical area per unit volume of soil through which momentum dissipates, is presumably correlated with the exchange of water, particles, heat and ions between the mobile water and the stationary parts of the permeable system.

The separation of ν from L is well-founded in viscous-flow principles. Its systematic investigation may open new vistas on permeable-media flow and transport. The separability of ν from L also severs flow from weakly founded relationships of parameters and functions with the sessile water content as, for instance, Richards' (1931) sequential flow requires.

7.2 Preview of Part II

Part I, *Stokes-flow and Preferential Infiltration* resulted in numerous hypotheses founded on first hydro-dynamic principles, which may be experimentally tested. Purposefully, no data were introduced, with the exception of typical values to illustrate particular issues. The limitations emerged solely due to the strict application of hydro-dynamical principles. Thus, the derivation of the viscous-flow approach was not restricted by *ifs* and *buts* from specific experience or belief.

The chapters in Part II *Applications of Viscous Flow to Infiltration and Drainage* introduce experimental aspects. Most of the data presented there originate from master's theses and doctoral dissertations carried out under my guidance, mainly because few other data sources exist. This circumstance exposes one to the criticism that the data have been purposefully selected, resulting in experimental bias in favor of the postulated theory and approach. However, a great part of the experiments have passed scrutiny in renowned peer-reviewed journals.

The analyses in Part II are restricted to various hews of one-dimensional water flow in permeable media including a discussion about bending of flow from the vertical to the lateral direction in hill-slope soils. Abstraction of water from the mobile to the sessile part is scrutinized but the corresponding exchange of matter and heat is left to further investigations.

Part II

Viscous Flow Applied to Infiltration and Drainage

*The proof of the pudding
lies in its eating*

English proverb

8. Experimental protocol, data acquisition and interpretation

8.1 Introduction

In this chapter the protocols of experimental data acquisition are introduced, followed by the interpretation of the temporal variations of drainage flow and water contents. Data acquisition serves at a minimum the following purposes:

- to test the applicability of the viscous-flow approach to infiltration and drainage;
- to explore the limits of viscous flow due to inappropriate conditions;
- to investigate flow systems and specific relationships;
- to parameterize infiltration and drainage;
- to predict infiltration and drainage after due calibration.

Viscous flow, as developed in Part I, provides a priori the functional relationships of approaching preferential flow, while only the parameters F and L in the context of $P(q_s, T_B, T_E)$ need to be determined through optimization procedures. Moreover, the spatial evolution of a WCW at various time steps is separable from its temporal evolution at various depths as Sections 3.4 and 3.5 demonstrated. Thus, optimization is relatively easy and the goodness-of-fit can be judged simply by graphically comparing viscous flow performance with data. However, one pair of F and L is due to both, P and the medium's specific reaction on it. Thus, ambiguity is to be expected in that variations of input pulses applied to the same medium may produce various pairs of F - and L -parameters. Conversely, the same F - and L -parameters derived in various permeable media only characterize similar $WCWs$.

Wetting fronts of $WCWs$ and kinematic waves move as cohesive shocks, and both are not diffusive. The scales of a WCW depend on L , F , and the duration $[T_E - T_B]$ of P . The WCW 's spatio-temporal scaling pivots around time and depth of front-interception, thus

$$T_I = \frac{1}{2} \cdot (3 \cdot T_E - T_B) \quad (3.8)$$

depends entirely on the duration of the pulse, while

$$Z_I = \frac{c}{2} \cdot (T_E - T_B) = \frac{F^2 \cdot g}{2 \cdot \eta} \cdot (T_E - T_B) \quad (3.7)$$

depends also on F , which is established when P at the surface transforms to the WCW .

The amplitude of either w_F or $q_{dr,max}$ covers the quantitative aspect of the *WCW* which requires L :

$$w_F = L \cdot F \quad (3.3)$$

$$q_{dr} = F^3 \cdot L \cdot \frac{g}{3 \cdot \eta} \quad (3.2)$$

The subscripts dr and F refer to *drainage* and *front*.

Neither spatial nor temporal scaling seem suited for the classification of *WCWs* and, consequently, four levels of complexity are introduced instead:

- (i) *Procedures at the flow-path level* conform to the processes which, so far, served primarily the development of the basic relationships. Techniques of quantitative imaging are continuously and rapidly improving in both spatial and temporal resolutions to the extent that we will soon be enabled to directly research processes at the water-film scale of 10(μ m) and less. Anderson and Hopmans (2013), for instance, summarize the current state of the art.
- (ii) *Procedures at the local level* comprise a large number of similar flows appearing as a macroscopic time series of either volumetric water content $\theta(Z_{meas}, t)$ or drainage flow $q(Z_{meas}, t)$ at a particular depth Z_{meas} of measurements in a permeable medium. Both of these time series are local expressions of a water content wave $WCW(z, t)$ which is exclusively due to a well-defined pulse $P(q_s, T_B, T_E)$. The specific contact length L is the parameter required for up-scaling from the flow-path to the local level where typically *WCWs* are accessible to experimentation. Numerous examples derived at this level will illustrate the applicability of viscous flow.
- (iii) *Procedures at the profile level* include at least two depths of observation in a permeable medium, permitting us to reproduce a spatio-temporal section of an entire *WCW*. The wetting front velocity v , and thus the film thickness F are the parameters linking processes at the local with those at the profile level.
- (iv) *Procedures at the system level* include the simultaneous recording of at least one $\theta(Z_{meas}, t)$ and of drainage flow $q(Z_{dr}, t)$, thus permitting the most complete possible testing of the viscous flow approach with balance calculations.

The experimental determination of the two parameters F and L of a specific permeable medium that are due to $P(q_s, T_B, T_E)$ requires flux-controlled input (a Neuman boundary-condition). Moreover, for clarity of presentation, data acquisition and analyses are restricted here to the depth range between

surface and front interception, that is $[Z_{meas} < Z_I]$. In principle, the restriction does not jeopardize the experimental calibration of permeable media over greater depths because $[T_E - T_B]$ of experimental fixing of P such that $[Z_{meas} < Z(T_I)]$ always results according to Eq.(3.8). Thus, the design of the experiment becomes adjustable to the system's requirements. However, more practical constraints may limit the duration of P , for instance, the maximum available supply of sprinkling water.

Once the viscous-flow parameters for a particular system are known, and under the premise that the parameters remain valid, neither depth nor time is limited in modeling input pulses.

Editorial note: The following introduces **Topic $n.m$** and **Case $n.m$** . *Topic* provides the link between particular theoretical considerations presented in Chapters 2 to 6 and subsequent data handling. *Case* describes the acquisition of a particular set of data to discuss the *Topic* with. The numbers n and m refer to the chapter and serial numbering within the chapter. Further, Figs. 3.1 to 3.3 may provide guidance.

8.2 Experimental protocol

Under consideration of $P(q_s, T_B, T_E)$ and the depth-limitation of $[Z_{meas} < Z_I]$, the experimental determination of F and L relies on Eqs.(3.2) to (3.5), and one pair of the following three data sets:

- (i) Amplitude $w_F(Z_{meas})$ of the water content wave WCW at any one depth $[Z_{meas} < Z_I]$.
- (ii) Maximum volume flux density $q_{dr,max}(Z_{meas})$ of the water content wave WCW .
- (iii) Wetting front velocity v_F or draining front celerity c_D .

The following combinations exhaustively cover the three possible cases for designing specific experimental protocols:

Combination I if the experiment produces q_{dr} and v_F [or c_D with $v_F = c_D/3$],

$$F = \sqrt{\frac{3 \cdot \eta \cdot v_F}{g}} \quad L = q_{dr,max} \cdot \sqrt{\frac{g}{3 \cdot \eta \cdot v_F^3}} \quad (8.1), (8.2)$$

Combination II if the experiment produces w_F and v_F [or c_D with $v_F = c_D/3$],

$$F = \sqrt{\frac{3 \cdot \eta \cdot v_F}{g}} \quad L = w_F \cdot \sqrt{\frac{g}{3 \cdot \eta \cdot v_F}} \quad (8.1), (8.3)$$

Combination III if the experiment produces w_F and $q_{dr,max}$,

$$F = \sqrt{\frac{3 \cdot \eta \cdot q_{dr,max}}{g \cdot w_F}} \quad L = \sqrt{\frac{g \cdot w_F^3}{3 \cdot \eta \cdot q_{dr,max}}} \quad (8.4), (8.5)$$

Combination III is most likely redundant. It will be demonstrated that v_F is a by-product of matching viscous flow to the time series of either $\theta(Z,t)$ or $q(Z,t)$. Because both series are reactions on $P(q_s, T_B, T_E)$ that are recorded at preset depths Z_{meas} in the flow system it follows that

$$v_F = \frac{Z_{meas}}{t_W(Z_{meas}) - T_B} \quad (8.6)$$

where $t_W(Z_{meas})$ is the time of first significant increase of either w_F or q_{dr} at Z_{meas} , the depth of measurement.

8.3 Estimation of F and L from drainage flow, $q(Z,t)$

Recording of unobstructed drainage flow due to $P(q_s, T_B, T_E)$ requires water-saturation of the permeable medium at least near the outlet. Early experiments had to rely on flux measurements because neither instrumentation nor theory was then available to adequately record and interpret temporal water content variations. For instance, Germann (1985) collected drainage from a polyester-consolidated block of sand, while Levy and Germann (1988) determined drainage flow and bromide concentrations due to input variations from a block of an isolated and undisturbed soil. Likewise, Germann et al. (1986) assessed drainage flow in situ by sprinkling on an isolated soil block of 2.6(m) by 2.3(m) that was 0.7(m) deep. The inclined and stony forest soil was underlain with glacial till, which facilitated the recording of drainage flow in the down-slope trough. Moreover, Fig. 1.1 stimulated the investigation of water-table rises due to infiltration in the ante-TDR era. On the other hand, the analysis of drainage in the meaning of viscous flow allows for obvious assessment of the wetting front arrival. Thus, precedence is given here to the analysis of flow variations rather than of water-content variations which will follow in Section 8.4.

Topic 8.1: *Determination of F and L from transient drainage flow.* Matching viscous flow to the entire sequence of drainage is based on Eqs.(3.24) to (3.28). From Eqs.(3.24) and (3.25)

$$t_W(\zeta_1) = T_B + \frac{3 \cdot \eta}{g} \cdot F^{-2} \cdot \zeta_1 \quad (3.24)$$

$$t_D(\zeta_1) = T_E + \frac{\eta}{g} \cdot F^{-2} \cdot \zeta_1 \quad (3.25)$$

follows

$$t_D(Z_{meas}) = T_E + \frac{1}{3} \cdot [t_W(Z_{meas}) - T_B] \quad (8.7)$$

Thus, equations

$$0 \leq t \leq t_W(Z_{meas}) \quad w(Z_{meas}, t) = 0 \quad (3.26)$$

$$t_W(Z_{meas}) \leq t \leq t_D(Z_{meas}) \quad w(Z_{meas}, t) = L \cdot F = w_F \quad (3.27)$$

$$t \geq t_D(Z_{meas}) \quad w(Z_{meas}, t) = L \cdot F \cdot \left(\frac{t_D(Z_{meas}) - T_E}{t - T_E} \right)^{1/2} \quad (3.28)$$

completely describe a water-content time series at Z_{meas} . They have to be converted to accommodate drainage flow $q_{dr}(Z_{meas}, t)$. Conversion relies on

$$q = w^3 \cdot \frac{g}{3 \cdot \eta \cdot L^2} \quad (4.9)$$

leading to

$$0 \leq t \leq t_W(Z_{meas}) \quad q_{dr}(Z_{meas}, t) = 0 \quad (8.8)$$

$$t_W(Z_{meas}) \leq t \leq t_D(Z_{meas}) \quad q_{dr}(Z_{meas}, t) = q_S \quad (8.9)$$

$$t \geq t_D(Z_{meas}) \quad q_{dr}(Z_{meas}, t) = q_S \cdot \left(\frac{t_D(Z_{meas}) - T_E}{t - T_E} \right)^{3/2} \quad (8.10)$$

A pulse $P(q_s, T_B, T_E)$ produces a WCW , while $t_w(Z_{meas})$ is deduced from drainage flow and $[q_{dr,max}(Z_{meas}) = q_s]$ is assumed. The wetting front velocity and the arrival time of the draining front follow from the application of Eqs.(8.6) and (8.7), the mobile water content amounts to $[w_F = q_{dr,max}/v_F]$ and the parameters F and L are calculated with Eqs.(8.1) and (8.2). The procedure leaves the arrival time of the wetting front, $t_w(Z_{meas})$, as the only free parameter to vary to best match viscous flow to the data.

Case 8.1 *Ohashi's (1988) sprinkler-drainage experiment in a column of a reconstituted soil:* A PVC-pipe with a depth $[Z_{meas} = 0.20(\text{m})]$ and an inner diameter of $[\varnothing = 0.145(\text{m})]$ was filled with a mixture of 87(%) sand and 13(%) clay. Bulk density and porosity of the soil were $[\rho_b = 1.66(\text{Mg m}^{-3})]$ and $[\varepsilon = 0.37(\text{m}^3 \text{m}^{-3})]$. Five vertical and artificial macropores with diameters of 6(mm) were supposed to carry distinct macropore flows, Figs. 8.1 and 8.2. Figure 8.3 illustrates reasonable matching of viscous flow to Ohashi's drainage data, while Tab.8.1 summarizes the results.

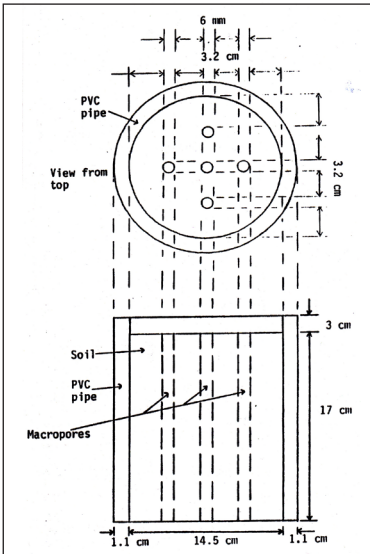


Figure 8.1, Case 8.1: Scheme of artificial macropores in a column of reconstituted soil. (Ohashi, 1988)

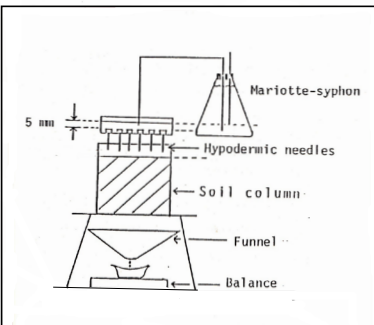


Figure 8.2, Case 8.1: Set-up of Ohashi's (1988) column experiments.

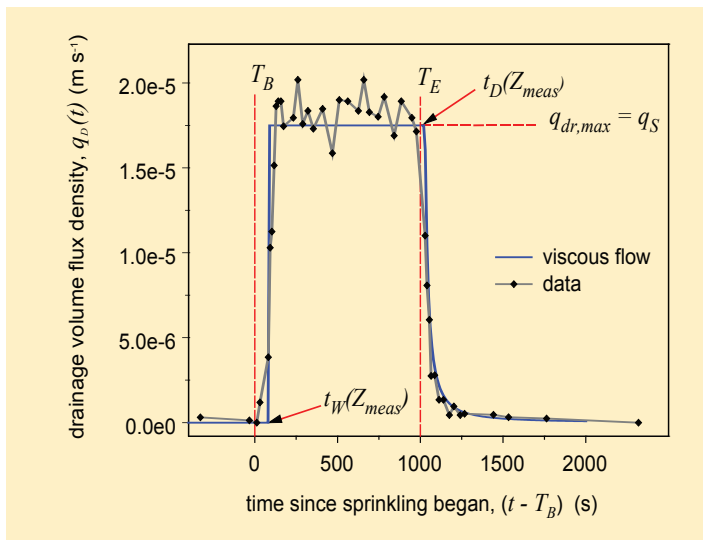


Figure 8.3, Topic 8.1: Viscous flow approach to drainage data (Ohashi, 1988). T_B and T_E indicate the beginning and ending of sprinkling, $t_W(Z_{meas})$ and $t_D(Z_{meas})$ are the arrival times of the wetting and draining fronts at the bottom of the column, $q_{dr,max}$ is the volume flux density of sprinkling and during supposedly steady drainage flow.

Table 8.1, Topic 8.1 : Boundary condition, optimization of $[t_W(Z_{meas}) - T_B]$, of matching viscous flow to Ohashi's data.

parameter	unit	amount	source
$q_S (= q_{dr,max})$	$m s^{-1}$	1.75×10^{-5}	experimental boundary condition
$T_E - T_B$	s	1'000	
$t_W(Z_{meas}) - T_B$	s	85	optimization
v_F	$m s^{-1}$	2.4×10^{-3}	Eq.(8.6)
$t_D(Z_{meas}) - T_B$	s	1'028	Eq.(8.7)
w_F	$m^3 m^{-3}$	0.0073	$q_{dr,max} / v_F$
F	μm	27	Eq.(8.1)
L	m^{-1}	270	Eq.(8.2)

Topic 8.2: *Flow path dimensions and viscous flow:* It is interesting that L , representing the vertical surface area per unit volume of the sample onto which momentum dissipates, is about 47 times greater than the total area per sample volume of the inner walls of the five artificial macropores. Also, L is about 10 times larger than the inner wall of the cylinder per unit sample volume. Moreover, F is about 220 times slimmer than the diameters of the artificial macropores. The three juxtapositions suggest that, according to viscous flow, neither the artificial macropores nor gaps between soil sample and cylinder mantle greatly impacted viscous flow.

8.4 Estimation of F and L from a water-content time series, $\theta(Z,t)$

On a visit to our lab in the early 1990's Vijay P. Singh suggested that the kinematic wave theory should apply equally well to both, the q - and the w -version of infiltration-drainage processes. Subsequently Germann (2001) compared the frequency distributions of F and L derived from 50 w -experiments with those derived from 12 q -versions. It was found that the viscous flow approach applies to both versions. The paramount advantage of applying viscous flow to water-content measurements is that it significantly expands the realm of experimental investigations. Moreover, flux measurements always require a water-saturated region containing the potential of interfering with the process in the unsaturated domain of the permeable medium. Since the 1980's TDR-equipment (Hillel, 1998) has evolved to precision and temporal resolutions that permit adequate *in-situ* determination of $\theta(Z_{meas}, t)$ -series.

Topic 8.3: *Determination of L and F from the measured θ_{init} and θ_{max} at depth Z_{meas} , while optimizing $t_w(Z_{meas})$:* Referring to Fig. 3.3, and to Eqs.(3.24) to (3.28) in *Topic 8.1*, viscous flow assumes an instantaneous increase from θ_{init} to θ_{max} , steady-state during $[t_w(Z_{meas}) \leq t \leq t_D(Z_{meas})]$, and a trailing wave after $[t > t_D(Z_{meas})]$. The wetting front velocity follows from Eq.(8.6), and the amplitude of the WCW is from data, $[w_F(Z_{meas}) = \theta_{max} - \theta_{init}]$. The arrival time of the draining front follows from Eq.(8.7) and may serve to validate matching. Figure 8.4 illustrates the parameters required in the procedure of determining F and L from $\theta(Z_{meas}, t)$.

Case 8.2: *Determination of $\theta(Z,t)$ in a column of an undisturbed forest soil.* The data presented in Fig. 8.4 were recorded from sprinkling on a column of an undisturbed forest soil from the site Bantiger near Bern (Germann et al., 2007), Fig. 8.5. The column was prepared by driving a cylinder made of stainless-steel sheet-metal 0.4(m) deep into the ground. The cylinder had an inner diameter of 0.4(m), a length of 0.5(m), and the wall was 3(mm) thick. In the laboratory the column was placed on a metal grid permitting free

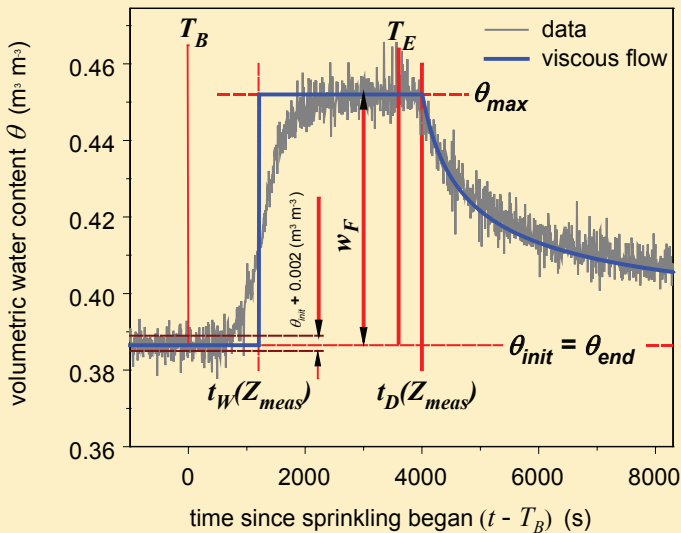


Figure 8.4, Topic 8.2: Matching viscous flow to data (Germann et al., 2007) by taking θ_{init} and θ_{max} from the data and optimizing $t_W(Z_{meas})$. The wave's amplitude is $[w_F = \theta_{max} - \theta_{init}]$, while θ_{init} and θ_{end} are the volumetric water contents prior to sprinkling and a long time after its cessation. The range $[\theta \pm 0.002(\text{m}^3 \text{m}^{-3})]$ indicates the frequently reported precision of TDR-moisture measurements.

drainage. The edge of the soil surface was sealed against the cylinder wall with bentonite. Paired TDR-wave guides with stainless-steel rods of 6(mm) in diameter, 50(mm) apart, and 0.15(m) long were horizontally inserted at depths of 0.1 and 0.2(m). Calibration was according to Roth et al. (1990).

The data discussed here were retrieved from Run 3 at depth $[Z_{meas} = 0.1(\text{m})]$. Equation (3.28) represents the trailing wave of viscous flow and it serves as an ocular objective function in the assessment of goodness-of-fit. Table 8.2 summarizes the parameters and results.

The trailing wave and the arrival of the draining front match the data well. However, the gradual arrival of the measured wetting front differs markedly from viscous flow expectation, and the deviation is much more pronounced than in drainage flow, *Case 8.1* and Fig. 8.3. *Topic 8.2* produced a 'reasonable average' of the wetting front's arrival time but still requires explanation.

Table 8.2, *Topic 8.2:* Boundary condition, optimization of $[t_W(Z_{meas}) - T_B]$, and results of matching viscous flow to the Bantiger data.

parameter	unit	amount	source
q_S	m s^{-1}	1.26×10^{-5}	experimental boundary condition
$T_E - T_B$	s	3'600	
$w_F = \theta_{max} - \theta_{init}$	$\text{m}^3 \text{m}^{-3}$	0.065	from data
$t_W(Z_{meas}) - T_B$	s	1'200	optimization
v_F	m s^{-1}	8.3×10^{-5}	Eq.(8.6)
$t_D(Z_{meas}) - T_B$	s	4'000	Eq.(8.7)
steady $q_{dr,max}$	m s^{-1}	5.4×10^{-6}	$v_F \times w_F$
$q_{dr,max} / q_S$	--	0.43	
F	μm	5.0	Eq.(8.1)
L	m^{-1}	12'875	Eq.(8.3)

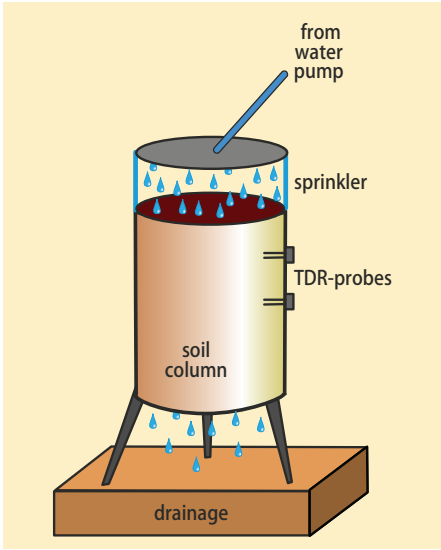


Figure 8.5, *Case 8.2:* Schematic representation of an instrumented column of an undisturbed forest soil. (Germann et al., 2007)

8.5 Summary

Chapter 8 builds a bridge from theoretical considerations of viscous flow in permeable media to their experimental implementations. First, after providing the theoretical base of applying viscous flow to drainage, *Topic 8.1* successfully matched theory to data by taking the maximum drainage rate as equal to the constant input rate while using the arrival time of the wetting front, $t_w(Z_{meas})$, as the only matching parameter. The sizes of F and L hint at the required widths and extents of preferential flow paths to accommodate preferential flow. As discussed in *Topic 8.2*, the resulting two viscous-flow parameters do not necessarily reflect the generally perceived dimensions of preferential-flow paths. Second, *Topic 8.3* matched viscous flow to the temporal variation of $\theta(Z_{meas}, t)$, where the WCW 's amplitude was taken from data and $t_w(Z_{meas})$ served again as the only matching parameter.

However, viscous flow does not predict a gradual increase of $\theta(Z_{meas}, t)$. The discussion of the discrepancy between theory and observation will resurface at all procedure-levels and eventually will shed light on the relationship between viscous flow and capillarity. The examples were purposefully selected to most clearly illustrate how the data may be interpreted adhering to viscous flow. The following chapters will extend the procedures to numerous other cases and to the various levels.

Chapters 9 to 12 follow the not-so logical order of local, profile, system, and flow path level. The discussions of processes at the flow-path level, however, are experimentally the least obvious, and they have to build on the background presented in the previous three chapters.

9. Procedures at the local level

9.1 Introduction

Based on Part I and Chapter 8 this chapter presents procedures of estimating the parameters F and L from data measured at the local-level. The procedures require the pulse $P(T_B, T_E, q_S)$ and one time series of either $q(Z_{meas}, t)$ or $\theta(Z_{meas}, t)$, where Z_{meas} is the one depth of data recording. The examples chosen are far from exhaustive but should suffice to demonstrate both the versatility and the limitations of viscous flow applications.

9.2 Wetting front arrival

Topic 9.1: *Estimating $t_W(Z_{meas})$ from the increasing limb of $\theta(Z_{meas}, t)$:* In search of the most objective procedure for determining the wetting front velocities of a great number of $\theta(Z_{meas}, t)$ -series, Germann and Hensel (2006) proposed an empirical procedure for estimating $t_W(Z_{meas})$. They repeatedly observed quasi-linear increases of water contents during time periods that were sufficiently long to be analyzed with linear regressions. The backward extension of the linear regression to the cut with θ_{init} produced the expected arrival time of the wetting front.

The procedure automatically fixes $t_D(Z_{meas})$ according to Eq.(8.7). Ocular matching of viscous flow to the data was achieved by varying θ_{max} until the modeled and measured trailing waves showed the closest agreement. Figure 9.1 demonstrates the procedure for deriving $t_W(Z_{meas})$ and it presents the results from applying *Topic 9.1* to the data in *Case 8.2*, while Tab. 9.1 compiles the parameters and the results.

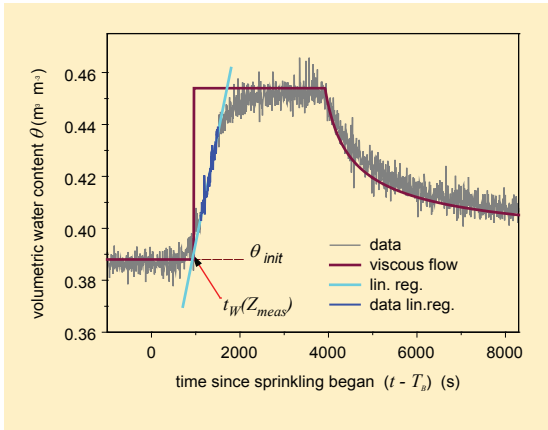


Figure 9.1, Topic 9.1: Matching viscous flow to *Case-8.2* data by fixing $t_W(Z_{meas})$ through the extension of the linear regression, optimizing θ_{max} and taking θ_{init} from data. The linear regression of the increasing limb of $\theta(Z, t)$ yielded $R^2 = 0.933$ with 65 data points (63 d.f.)

The computational procedure of *Topic 9.1* leading to $t_W(Z_{meas})$ seems to eliminate the uncertainty of estimating the arrival time during the gradual early increase of the water content. However, it remains a complete empirical observation until a satisfactory explanation for the linear water content increases can be developed. The comparison of Tab. 8.2 with Tab. 9.1 illustrates the sensitivity of the parameters when applying various methods of matching viscous flow to data. Despite the difference in the estimated arrival times $[t_W(Z_{meas}) - T_B]$ of 304(s), F increased by just 16(%) while L declines by 6(%).

Table 9.1, Topic 9.1: Boundary condition, predetermination of $[t_W(Z_{meas}) - T_B]$, optimization of θ_{max} , and results of matching viscous flow to the Case-8.2 data

parameter	unit	amount	Source
q_s	$m\ s^{-1}$	1.26×10^{-5}	experimental boundary condition
$T_E - T_B$	s	3'600	
$t_W(Z_{meas}) - T_B$	s	896	lin. regr.
v_F	$m\ s^{-1}$	1.12×10^{-4}	Eq.(8.6)
$w_F = \theta_{max} - \theta_{init}$	$m^3\ m^{-3}$	0.071	optimization
$t_D(Z_{meas}) - T_B$	s	3'900	Eq.(8.7)
$q_F = v_F\ w_F$	$m\ s^{-1}$	7.9×10^{-6}	Eq.(2.12)
q_F/q_s	--	0.63	
L	m^{-1}	12'153	Eq.(8.3)
F	μm	5.8	Eq.(8.1)
$h_{cap}(F)$	m	-2.6	Eq.(2.21)

9.3 Rivulet approach

While investigating the gradual increase of $\theta(Z,t)$ from θ_{init} to θ_{max} , Germann et al. (2007) conceptualized a *WCW* as a superposition of N_R rivulets, indexed $[1 \leq j \leq N_R]$. Each of the rivulets is released at T_B but their wetting fronts arrive successively delayed at Z_{meas} , such that $[t_W(Z_{meas})_{j-1} < t_W(Z_{meas})_j < t_W(Z_{meas})_{j+1}]$. Thus, velocities, film thicknesses, and specific contact lengths vary among rivulets.

Topic 9.2: Determination and superposition of a WCW's rivulets: The time period of the increasing limb, $[\Delta t = t(\theta_{\max}) - t_w(Z_{\text{meas}})]$, is divided into N_R equal periods of $[\Delta t/N_R]$, where $t(\theta_{\max})$ is the time of $\theta(Z_{\text{meas}}, t)$ attaining its maximum. Further, $[\theta_0 = \theta_{\text{init}}]$ and the times of the wetting front arrivals are $[t_{w,j} = t_w(Z_{\text{meas}}) + (j-1) \Delta t/N_R]$. In accord with *Topic 9.1*, $[w_{F,j} = s_j \Delta t/N_R]$, where s_j is the slope of the linear regression of $\theta(Z_{\text{meas}}, t)$ -data within the time interval from $t_{w,j-1}$ to $t_{w,j}$.

Equations (3.24) to (3.28) and (8.7) are now applied to each rivulet. Rivulet j at depth Z_{meas} is completely determined by the data with $t_{w,j}$, $t_{w,j+1}$, and $w_{F,j}$. The superposition of all rivulets yields the final WCW. The comparison of the data with the trailing wave emanating from superimposing all rivulets serves as a measure for the goodness-of-fit and it ultimately demonstrates the plausibility of the rivulet-procedure. The trailing wave resulting from superposition thus serves as an objective function for the assessment of the procedure.

Figure 9.2 displays the results of $[N_R = 5, 10, 20]$ rivulets applied to *Case 8.2*. The variations of increasing rivulet limbs augmented with expanding N_R , and $[s_j < 0]$ occurred occasionally. However, there is hardly any discernible difference between the three resulting trailing waves. Extended numerical experimentation led Germann et al. (2007) to conclude that $[N_R \approx 10]$ suffices to match trailing waves. Table 9.2 lists the relevant parameters for $N_R = 5$.

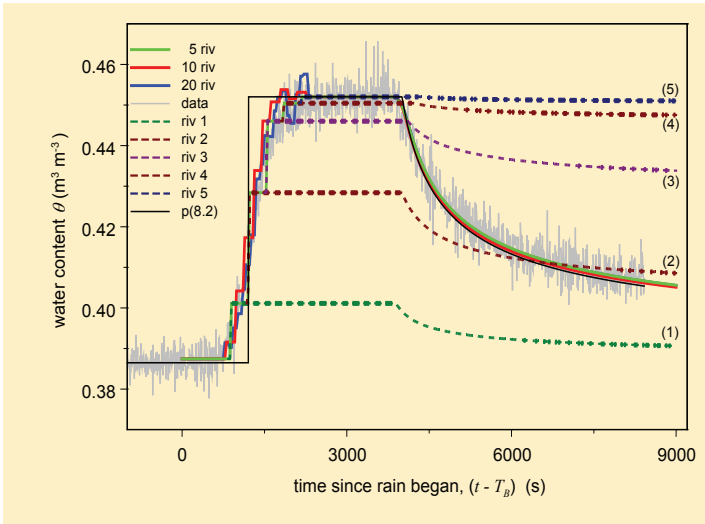


Figure 9.2, Topic 9.2: Rivulet approach to the data of *Case 8.2*. The lines *5 riv*, *10 riv*, and *20 riv* refer to the number of rivulets applied, *riv1* to *riv5* indicate the successive rivulets that were superimposed to form the wave *5 riv*. The line *p(8.2)* is the same as in *Topic 8.2*, Fig. 8.2.

Table 9.2, *Topic 9.2:* Parameters of the 5-Rivulet approach to the data of **Case 8.2.**

parameter	unit	rivulet					source
		1	2	3	4	5	
q_s	m s^{-1}	1.26×10^{-5}					experiment
$T_E - T_B$	s	3600					
$t_{Wj}(Z_{meas}) - T_B$	s	726	1'049	1'372	1'694	2'017	from data
v_{Fj}	$\text{m s}^{-1} \times 10^{-5}$	14.0	9.4	7.3	5.9	5.0	Eq.(8.11)
w_{Fj}	$\text{m}^3 \text{m}^{-3}$	0.014	0.027	0.018	0.004	0.002	lin. regr.
$t_{Dj}(Z_{meas}) - T_B$	s	3'842	3'950	4'057	4'165	4272	Eq.(8.12)
q_{Fj}	$\text{m s}^{-1} \times 10^{-7}$	19.0	26.0	13.0	2.6	0.8	$v_F \ w_F$
q_{Fj} / qS	--	0.151	0.208	0.103	0.021	0.007	
L_j	m^{-1}	2'106	5'048	3'738	1'044	395	Eq.(8.8)
F_j	μm	6.5	5.4	4.7	4.2	3.9	Eq.(8.6)
$h_{cap}(F_j)$	m	-2.2	-2.8	-3.2	-3.6	-3.8	Eq.(2.21)

Topic 9.2 provides a tool for the objective investigation of gradually increasing *WCW* limbs. However, the procedure still does not explain the occurrence of gradual increase, and two lines of interpretation are here offered. The slopes are either due to separate flow paths extending from the surface to Z_{meas} that produce sub-waves with a variety of film thicknesses and front velocities or the slopes are due to local variations. Investigations at the profile and system levels are required to further discuss the issue, and a third line of interpretation will be offered in *Topic 12.6*, Section 12.4.

As a side effect, the topic implicitly demonstrates the robustness of the trailing wave with respect to the various approaches to the interpretation of increasing limbs. The procedure may eventually help to test hypotheses regarding the physics of increasing limbs, once we are in a position to formulate them.

9.4 Water abstraction from a *WCW*

Topic 8.2 employs the special *Case 8.2* with $[\theta_{init} = \theta_{end}]$. The case was intentionally selected for the purpose of clarity when introducing viscous flow experimentation. However, in most cases the end-water contents are

substantially higher than the initial water contents, which effect is referred to as *water-content divergence*, [$\theta_{div} = \theta_{end} - \theta_{init} > 0$]. θ_{end} is considered attained at a long time after the cessation of input when $\theta(t)$ decreases very slowly when compared with the time shortly after the arrival of the draining front. The consideration coincides with Veihmeyer and Hendrikson's (1949) concept of *Field Capacity*, *FC*, who thought of it as an invariable soil property (see also discussion in Section. 6.5), whereas Kutilek and Germann (2009) demonstrated that only in about half of the 96 repeated infiltration experiments were the end-water contents within [$\theta_{end} \pm 0.002(\text{m}^3\text{m}^{-3})$], while the *FC* of the remaining cases cannot be considered as constant.

The effect of divergence is experimentally reducible by pre-wetting the soil. To do this, experiments were typically run three times with about one-day intervals between the runs. While the $\theta(Z,t)$ -series of the second runs usually differ markedly from those of the first runs, they are in most cases not distinguishable from those of the third runs. Case-by-case assessments are, however, required. The vertical extent of the control volume sensed by TDR-equipment is approximately equal to the horizontal distance between two parallel wave-guides, which amounts to 50(mm) in our cases. Assuming [$v_F = 10^{-4}(\text{m s}^{-1})$], this yields an approximate residence time of the *WCW* within the control volume of 500(s), thus allowing sufficient time for substantial water abstraction from the wave due to capillarity. Therefore, only a part of the entire flow of a *WCW*, which was carried to the control volume drains after running through it. So far, *WCW*-divergence has not been included in the viscous flow approach and its effect will be demonstrated now.

Topic 9.3: *Viscous flow matching under conditions of [$\theta_{div} > 0$] compared with [$\theta_{div} = 0$]:* Estimation of θ_{end} was done by simultaneous optimizing it with $t_w(Z_{meas})$. The trailing wave is used as the objective function when assessing the matching of viscous-flow to the data.

Case 9.1: *Preferential flow underneath Miscanthus sinensis.* The data used to demonstrate the effects of water-content divergence are based on the work of Jäggi (2001) who investigated the effect on infiltration of a 7-year old plantation of *Miscanthus sinensis* ('China reed') in comparison with infiltration in the same soil under crop rotation. She demonstrated an increased depth of infiltration under *Miscanthus*, which was most likely the result of the roots of the perennial plants penetrating deeper than those of annual crops, thus presumably providing preferential-flow paths to greater depths. Five TDR-probes were horizontally installed *in situ* at the depths of [$Z_j = 0.1, 0.2, 0.3, 0.4, \text{ and } 0.5(\text{m})$] below a tractor rut.

Figure 9.3 depicts the $\theta(Z_j,t)$ -series monitored at [$Z_j = 0.3(\text{m})$]; [$\theta_{div} = 0.016(\text{m}^3 \text{m}^{-3})$] and θ_{max} are taken from the data, while $t_w(Z_j)$ and θ_{end}

were simultaneously optimized by matching based on *Topic 9.3*. The figure includes the results of both matching procedures, *Topics 8.2* and *9.3*, and it clearly demonstrates the need for considering θ_{div} . Table 9.3 lists comparatively the results of both matching procedures. That the conclusion of *Topic 8.2* is incorrect notwithstanding, the comparisons of F and L demonstrate from a formalistic point of view that the water film gets thinner and the contact area wider when divergence is not taken into consideration. As a consequence, L from the imbibing section $[\theta_{max} - \theta_{init}]$ exceeds L from the draining section $[\theta_{max} - \theta_{end}]$: they will henceforth be referred to as L_{im} and L_{dr} .

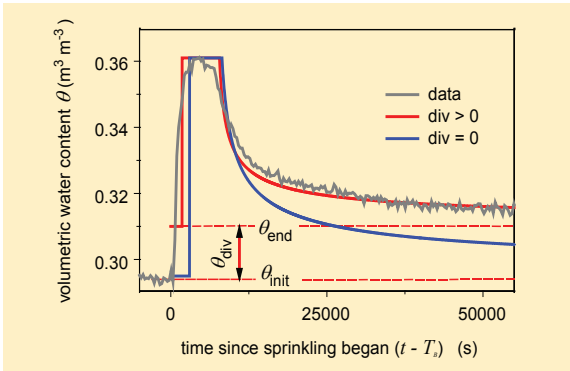


Figure 9.3, Topic 9.3: Comparison between matching *Case-9.1* data with either *Topic 9.3*, $[\theta_{div} > 0]$, or *Topic 8.2*, $[\theta_{div} = 0]$.

Table 9.3, Topic 9.3: Comparison between matching *Case-9.1* data with either *Topic 9.3*, $[\theta_{div} > 0]$, or *Topic 8.2*, $[\theta_{div} = 0]$.

parameter	unit	Topic 9.3 $\theta_{div} > 0$	Topic 8.2 $\theta_{div} = 0$	source
q_S	m s ⁻¹	1.39 x 10 ⁻⁵		experiment
$T_E - T_B$	s	7200		
$t_W(Z_j) - T_B$	s	1'800	3'000	optimization
v_F	m s ⁻¹	1.67 x 10 ⁻⁴	1.00 x 10 ⁻⁴	Eq.(8.11)
w_F	m ³ m ⁻³	0.051	0.066	optimization
θ_{div}	m ³ m ⁻³	0.0163	0.0	optimization
$t_D(Z_j) - T_B$	s	7'800	8'200	Eq.(8.12)
q_F	m s ⁻¹	8.5 x 10 ⁻⁶	6.6 x 10 ⁻⁶	$v_F \ w_F$
q_F/q_S	--	0.61	0.47	
L_{im}	m ⁻¹	11'930	11'930	Eq.(8.8)
L_{dr}	m ⁻¹	7'100	11'930	Eq.(8.8)
F	μm	7.1	5.5	Eq.(8.6)
$h_{cap}(F)$	m	-2.1	-2.7	Eq.(2.21)

Despite the research interest in the local water distribution during infiltration, we must interrupt our interpretation of capillary-driven abstraction from *WCWs*. The poorly definable TDR-control volume has no sharp edges because physics demands a gradually decreasing influence on the TDR-signal with increasing distance from the wave-guides. Moreover, the antenna-properties of the wave-guides may also depend on the water content itself and on other local soil properties. Alternative methods of monitoring $\theta(z,t)$ may provide information which more clearly explains water abstraction from a *WCW*.

9.5 Restricted drainage flow

Soil horizons result from soil-forming processes such as clay and silt accumulations at profile depths forming B_r -horizons, thus reducing hydraulic conductivity at large and restrict preferential flow in particular. In Chapter 10 preferential flow restriction at the profile level will be discussed. The process will however be described here with the temporal constraint of drainage flow from a weighing lysimeter which, in all likelihood, is the result of too narrow an orifice. Germann's (2001) comparison of 50 w -versions with 12 q -versions mentioned in Section 8.4 included an additional series of 16 drainage flows from the Rietholzbach weighing lysimeter, whose F - and L -parameters were significantly outside the frequency distributions of the other 62 cases. Subsequent investigations revealed that drainage flow more accurately followed a linear-reservoir approach at the beginning of flow recession, and only later did the viscous flow approach satisfactorily represent the data.

Topic 9.4: *Linear-reservoir approach to drainage flow.* The linear-reservoir approach is based on the notion that, during a limited period since the onset of drainage, the water will perch due to reduced drainage. The perched water table with unknown height above the restraining layer is assumed to drain like a linear reservoir, while viscous flow is assumed to apply to drainage once perching has ceased. Under the assumption that the water table height is proportional to the volume of perched water the following relationship emerges

$$q(Z_j, t) = q(Z_j, t_0) \cdot e^{-\lambda \cdot (t - t_0)} \quad (9.1)$$

where $\lambda(\text{s}^{-1})$ is the effective reservoir constant of the constraint-flow system, and $q(Z_j, t_0)$ and $q(Z_j, t)$ (m s^{-1}) are the volume flux densities of drainage at times t_0 and at t , respectively. The recession limb of viscous flow, Eq.(8.10), can be transformed to

$$q(Z_j, t) = q(Z_j, t_0) \cdot \left(\frac{t_0 - T_E}{t - T_E} \right)^{3/2} \quad (9.2)$$

which is of a structure similar to Eq.(9.1) in that estimates of both parameters, λ and T_E , require two data points each, while the goodness-of-fit is assessed using linear regressions of modeled flow vs. data.

Case 9.2: *Drainage flow from the weighing Rietholzbach lysimeter.* Figure 9.4 presents a schematic cut across the weighing Rietholzbach lysimeter while Fig. 9.5 depicts drainage flow, covering 55(h) from February 2, 13:00(h) to February 4, 20:00(h), 1979 (Seneviratne et al., 2012; Germann, 1980). Irregular precipitation produced smooth drainage flow that was matched with the dual-process of *Topic 9.4*, Eqs.(9.1) and (9.2). The two pairs of diamonds in Fig. 9.5 mark the data points required to estimate λ and T_E , respectively, yielding $[\lambda = 5.86 \times 10^{-5}(\text{s}^{-1})]$ and $[T_E = 18'000(\text{s})]$.

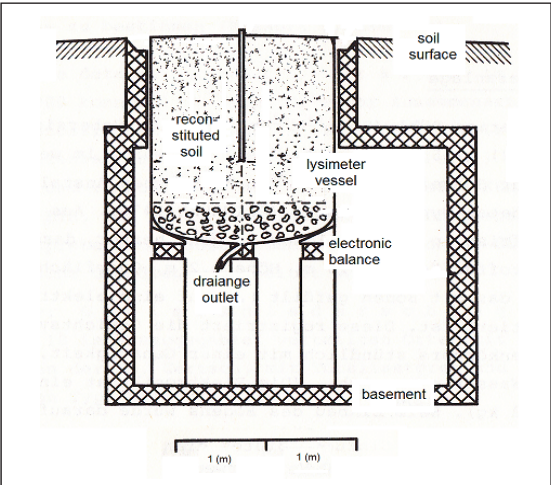


Figure 9.4, Case 9.2: Scheme of the Rietholzbach lysimeter (after Germann, 1980)

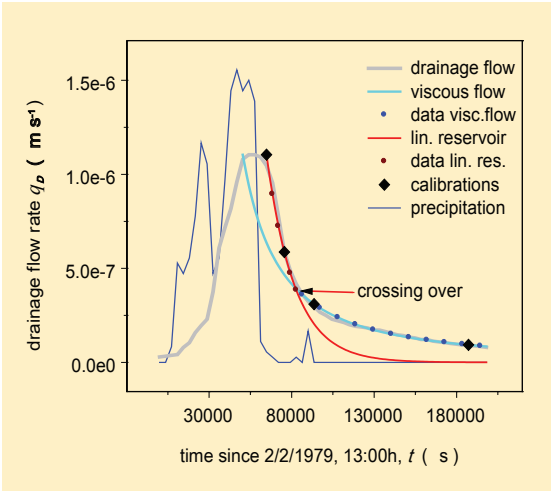


Figure 9.5, Topic 9.4: Drainage from the Rietholzbach lysimeter. Red and cyan lines refer to the earlier linear-reservoir approach and the later viscous-flow approach. The two pairs of diamonds indicate the data points used to calculate λ and T_E .

The approaches were checked against data, producing $[\mathcal{R}_{lin}^2 = 0.98]$ and $[\mathcal{R}_{vis}^2 = 0.99]$. A minor intrusion of one approach into the realm of the other one reduced both \mathcal{R}^2 -values markedly. Thus, the linear-reservoir approach seems plausible when hampered drainage leads to temporarily perched water tables. Moreover, the analysis provides an example for the transition from saturated Darcy-flow, in which water pressure exceeds atmospheric pressure, to viscous flow, in which water pressure equals atmospheric pressure, i.e. $(dq/dt)_{lin} > (dq/dt)_{vis}$.

Topic 9.5: *Darcy-flow vs. viscous flow*: Figure 9.5 suggests more rapid decline of drainage during early linear-reservoir flow in comparison with later viscous flow. Enhanced decline during perching is due to additional hydrostatic pressure acting on flow. The following assess the transition from linear-reservoir to viscous flow. Under the assumptions of t_0 and the slopes at t_0 being equal in both Eqs.(9.1) and (9.2) one gets

$$\lambda_{trans} = \frac{3}{2 \cdot (t_0 - T_E)} \quad (9.3)$$

The inclusion of the resulting exponent $[\lambda_{trans} = 4.63 \times 10^{-5}(\text{s}^{-1})]$ into Eq.(9.1) produces a function of drainage decline which matches the one of Eq. (9.2) in the range of $[q(t)/q(t_0) \geq 0.5]$ with $[\mathcal{R}^2(\lambda_{trans}) = 0.99]$ and an intercept of $[I(\lambda_{trans}) = -0.173]$. Thus, any exponent $[\lambda > \lambda_{trans}]$ in linear-eservior flow, Eq.(9.1), suggests drainage under the regime of hydrostatic pressure alias Darcy-flow.

Similar considerations may also apply to soil profiles just above layers of distinctly reduced hydraulic conductivity like compacted glacial tills, the typical B_r-horizons in loess-derived soils or, as Lange et al. (2011) have shown in poorly permeable Stagnogleys. However, both parameters, λ and T_E , are purely computational constructs in this case. Although hydraulic considerations led to Eqs.(9.1) and (9.2), the reverse argumentation, that λ and T_E are of physical significance, requires separate discussion and independent assessments not provided in this section, and the two parameters are therefore considered as *computational parameters*.

9.6 Minimal interval length for analyzing $q(z,t)$ and $\theta(z,t)$

The complete *WCW* represented in Fig. 3.1 indicates asymptotic approaches of the water contents and the volume flux densities to the final values of $[d\theta_{end}/dt, q_{end} \rightarrow 0]$. From a practical point of view, an analysis can be terminated when the respective temporal decreases become less than the significant differences measured with the technique at hand. Figure 8.4, for instance, suggests that changes of less than $0.002(\text{m}^3\text{m}^{-3})$ are not significantly

discernible with the TDR-technique. However, viscous flow allows for a more rigorous assessment. A measure for the time interval necessary to investigate the series of $q(Z,t)$ to the desired completeness is proposed below.

Topic 9.6: *Interval length required to cover the significant part of $q(Z,t)$:* The total volume contained in $P(q_s, T_B, T_E)$ eventually passing at $[Z < Z_l]$ as an unimpeded WCW amounts to

$$V_{WCW} = q_s \cdot (T_E - T_B) \quad (3.1)$$

while the volume $V(Z,t)$ having passed Z at any given time $[t_D(Z) < t < \infty]$ follows from the sum of integrating Eq.(8.9) from $t_w(Z)$ to $t_D(Z)$ and of integrating Eq.(8.10) from $t_D(Z)$ to t , yielding

$$V(Z,t) = q_s \cdot \left(3 \cdot t_D(Z) - 2 \cdot T_E - t_w(Z) - 2 \cdot \frac{(t_D(Z) - T_E)^{3/2}}{(t - T_E)^{1/2}} \right) \quad (9.4)$$

The time-integral in Eq.(9.4),

$$T_{\text{int}}(Z) = 3 \cdot t_D(Z) - 2 \cdot T_E - t_w(Z) - 2 \cdot \frac{(t_D(Z) - T_E)^{3/2}}{(t - T_E)^{1/2}} \quad (9.5)$$

accounts for the depth-related delay of the drained water volume. It converges at the surface to

$$T_{\text{int}}(0) = T_E - T_B \quad (9.6)$$

where $[t_w(0) = t = T_B]$ and $[t_D(0) = T_E]$, and where Eq.(9.4) reduces to Eq.(3.1).

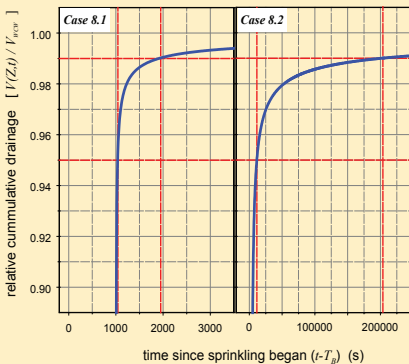


Figure 9.6, Topic 9.6: Relative cumulative drainage, Eq.(9.3), applied to the Case 8.1- and Case 8.2-data.

The ratio $[V(Z,t)/V_{WCW}]$ serves as a measure for deciding the termination time $[t_{term} - T_E]$ for analyzing $q(Z,t)$. Accordingly, Eq.(9.4) also applies to $\theta(Z,t)$ -series with $[\theta_{div} > 0]$ once $F(Z)$ and $L(Z)$ have been determined and q_s is replaced by $[q(Z) = F(Z)^3 L(Z) 3g/\eta]$. Figure 9.6 depicts the thresholds at 0.95 and 0.99 of cumulative drainage flow from *Case 8.1* and *Case 8.2*.

The 0.95-thresholds were attained at 1'042(s) and 11'600(s), respectively, while the 0.99-thresholds were attained at 1'950(s) and 203'800(s). The examples demonstrate the wide variety among the cases. Moreover, *Case 8.2* shows that the temporal extension has to increase from 11'600 to 203'800(s), that is by a factor of 17.5, to increase the relative cumulative drainage volume from 0.95 to 0.99.

9.7 Relationship of $v_F(q)$

Mathematical combinations of basic viscous-flow expressions lead to secondary relationships amenable to experimental testing. Such a windfall as elucidated here is essentially the relationship of v_F vs. q . For instance, *WCW*-routing with kinematic-wave theory as described in Chapter 4 relies on substantiated knowledge of $v_F(q_s)$.

Topic 9.7: *Investigation of v_F vs. q_s :* From Eq.(6.13) it follows that

$$v_F(q, L) = q^{2/3} \cdot L^{-2/3} \cdot \left(\frac{g}{3 \cdot \eta} \right)^{1/3} \quad (9.7)$$

Of particular interest is the function of $v_F(q_s)$, which would predict the propagation of any input pulse $P(q_s, T_B, T_E)$ after due calibration, ideally with the requirement of just one pulse. Thus, the expression

$$v_F(q_s) = q_s^{2/3} \cdot L^{-2/3} \cdot \left(\frac{g}{3 \cdot \eta} \right)^{1/3} \quad (9.8)$$

applies generally to a specific permeable medium within the bounds of viscous flow under the macropore restriction of $[dL/dq = 0]$, Sections 4.2 and 6.3. Otherwise, $L(q_s)$ needs to be included which, most probably, would require simultaneous calibration of the triple parameter set of v - q - L in an expression similar to Eq.(9.7).

Case 9.3: Shizowa and Fujimaki (2004) provide experimental support for the applicability of Eq. (9.8). They recorded the wetting front velocities due to two rates of infiltration into a 9-mm thick vertical layer of glass beads having diameters of 0.2(mm). The input rates were $[q_{s,1} = 4.5 \times 10^{-5}(\text{m s}^{-1})]$ and $[q_{s,2} = 1.5 \times 10^{-6}(\text{m s}^{-1})]$, while the observed wetting front velocities

amounted to $[v_{F1} = 2 \times 10^{-4}(\text{m s}^{-1})]$ and $[v_{F2} = 2 \times 10^{-5}(\text{m s}^{-1})]$. The ratios are $[(q_{s,1}/q_{s,2}) = 30]$ and $[(v_{F1}/v_{F2}) = 10]$. Under the assumption of $[dL/dq = 0]$, scaling is expected at $[(v_{F1}/v_{F2}) = (q_{s,1}/q_{s,2})^{2/3}]$ that is $[30^{2/3} = 9.65]$. Thus the observations deviated only by 3.5% from expectation.

Case 9.4: Hincapié and Germann (2009b) determined v_F at the 0.28-m depth in a column of undisturbed forest soil as response to the four input rates of $[q_s = 1.4, 2.8, 5.6, 11.1 \times 10^{-6}(\text{m s}^{-1})]$ i.e., $[q_s' = 5, 10, 20, 40(\text{mm h}^{-1})]$. The wetting front velocities of the averages of 7 experimental runs each amounted to $[\overline{v_F} = 7.3, 9.7, 12, 25 \times 10^{-4}(\text{m s}^{-1})]$. Figure 9.7 summarizes the results. The regression with the logarithmic version of Eq.(9.8) applied to the four data points produced $[L = 181(\text{m}^{-1})]$. The velocities score in the upper 10(%) of the frequency distribution of v of Hincapié and Germann (2009a) while L is one of the shortest found so far. The four data points in Fig. 9.7 are scattered considerably around the regression line but their positions are within $[\overline{L} / 1.4 \leq \overline{L} \leq 1.4 \times \overline{L}]$. The uncertainty in the data of Hincapié and Germann (2009a) does not permit to generalize the macropore flow restriction of $[dL/dq = 0]$ for a given permeable medium. Such generalization could be used as an indicator for flow of variable q along the same paths. The relationship of Eq.(9.8) notwithstanding, this should encourage further experimentation.

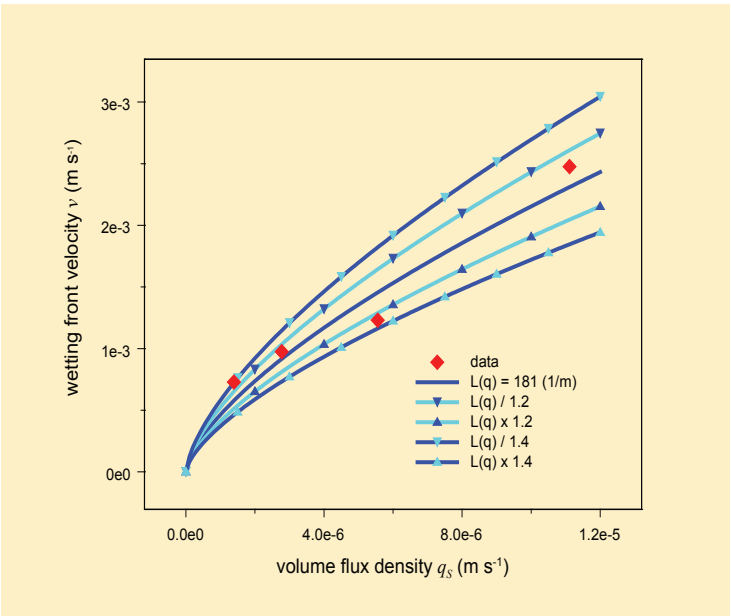


Figure 9.7, Topic 9.7: Wetting front velocity, v , as function of the input rate, q_s , Eq.(9.8). $[L(q) = 181(\text{m}^{-1})]$ results from regression to the four data points. (Data from Hincapié and Germann, 2009b)

9.8 Viscous flow in fissured rocks

Flow along cracks and fissures in consolidated sediments and solid rock formations are frequently blamed for the rapid water-borne transportation of harmful liquids and colloids like bacteria and virus. The section explores the applicability of viscous flow to fissured rocks.

Topic 9.8 *Viscous flow in fissured rocks*: Fissures and cracks in rocks are prototypes of preferential flow paths, and viscous flow is assumed to apply.

Case 9.5: *Presumed viscous flow in English chalk formations*. In the chalk formations of England the depth to the groundwater level is typically between 10 and 50(m). Studies of the $^{18}\text{O}/^{16}\text{O}$ -ratios of pore waters in the 1970's revealed a downward velocity of about 1(m) per year of the water-balances' annual surplus. Thus, the time the pore-water remained in the chalk was in the order of a decade. However, local ground-water users occasionally complained about bad odors in the water supply system within weeks following liquid manure applications. Reeves (1979) estimated wetting front velocities between 1 and 100(m d^{-1}). He suggested mechanisms of rapid flow and transport across chalk formations which are similar to the dual-flow proposition of Lawes et al. (1882) for soils, however, over depths out pacing by far the typical soil profile.

Case 9.6: *Tracer-front velocity in crystalline rocks*. In the region of Aguilles Rouges and Mt. Blanc, in the three-corner region where France, Italy and Switzerland meet, Dubois (1991) applied uranine and eosine tracers about 1'800(m) above the car-tunnel connecting Chamonix (France) with Courmayeur (Italy). Within 108 days following injection he found tracers in the seep to the car-tunnel. This amounts to an average velocity of the tracer front of 16.7(m d^{-1}). Translated to viscous flow, Dubois' observations lead to $[v_F = 1.9 \times 10^{-4}(\text{m s}^{-1})]$, $[F(v_F) = 7.6(\mu\text{m})]$ and $[h_{cap}(F) = -1.9(\text{m})]$ when assuming momentum dissipation to instantaneously consume gravitational acceleration. The viscous-flow parameters in crystalline rocks score well among those reported here so far.

Case 9.7: *Infiltration into Jurassic limestone*. Close to the surface the Jurassic lime formations are frequently broken into squared rocks that remain in the original setting but leave numerous fissures between them. Into the wall of a former quarry near the pass of Marchairuz in the Swiss Jura mountains Alaoui (1998) carved a horizontal slit 0.5(m) below the rim and inserted a sheet-metal plate of 0.5(m) by 1.0(m) to collected drainage which was diverted to a calibrated cylinder in which the water level was automatically recorded. Water was applied to the soil surface through the sprayer of a hand-held

watering can while the beginning and ending of the applications were synchronized with the recording system. Figure 9.8 displays the data of three infiltration-drainage experiments and the corresponding viscous-flow matching in accord with Section 8.4. Table 9.4 summarizes the parameters. Data matching appears reasonable and the range of F indicates laminar flow. Not surprisingly, the range of $[10.9 \leq L \leq 98.5(\text{m}^{-1})]$ covers the shortest specific contact lengths found so far, but the results of the preliminary study do not allow further interpretations.

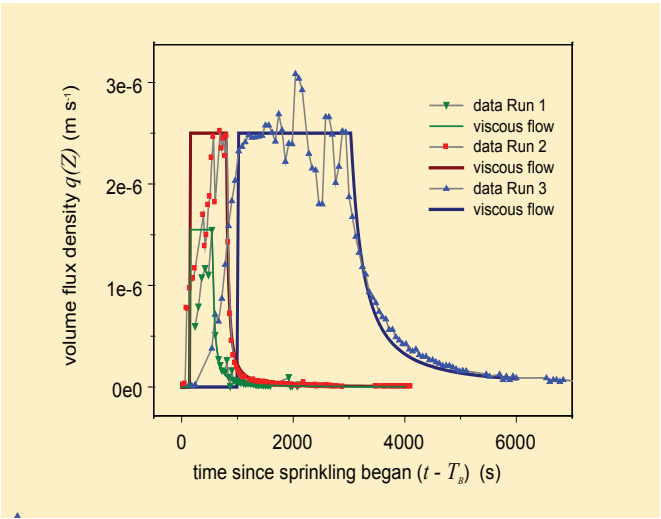


Figure 9.8, *Topic 9.8, Case 9.7:* Viscous-flow matching to three infiltration runs into fissured lime stone in the Swiss Jura mountains.

Table 9.4, *Topic 9.8:* Viscous-flow parameters applied to and resulting from matching the three infiltrations displayed in Fig. 9.8.

parameter	dimension	Run 1	Run 2	Run 3
$q_s \times 10^{-6}$	m s^{-1}	1.5	2.5	2.5
q_s	mm h^{-1}	5.4	9.0	9.0
$T_E - T_B$	s	500	750	2700
L	m^{-1}	14.6	10.9	98.5
$v_F \times 10^{-3}$	m s^{-1}	3.3	5.5	1.3
F	μm	32	41	20
$h_{cap}(F)$	m	-0.47	-0.36	-0.74

9.9 Summary

Various hues of viscous-flow matching to data evolved from Chapter 9. They demonstrate both the versatility and limitations of the approach. A set of expressions has emerged suited to the systematic characterization of time series of either $\theta(Z,t)$ or $q(Z,t)$. Figure 9.9 provides the relevant parameters. The tools thus prepared will now be used for the exploration of viscous flow at the more complex levels of profiles and systems before their application to the most intricate flow-path level.

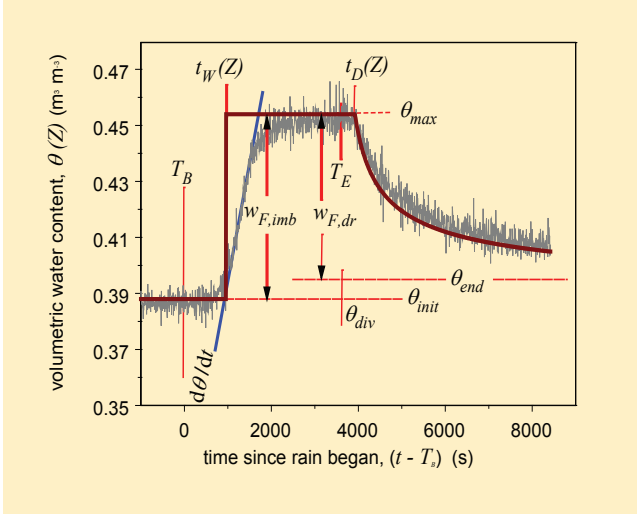


Figure 9.9: Expressions and parameters used to characterize a $\theta(Z,t)$ -time series in the context of viscous flow.

a) Measured water contents:

θ_{init} prior to infiltration, $[t < T_B]$;

θ_{end} at long time when drainage has practically ceased;

θ_{max} maximum prior to the begin recession;

$[\theta_{div} = \theta_{end} - \theta_{init}]$ divergence due to capillary abstraction from the WCV;

$d\theta/dt$ slope of increasing $\theta(Z,t)$.

b) Interpreted water contents:

$[w_{F,im} = \theta_{max} - \theta_{init}]$ during imbibition

$[w_{F,dr} = \theta_{max} - \theta_{end}]$ during drainage.

c) Times:

T_B beginning of water input;

T_E end of input;

$t_W(Z)$ arrival time of the wetting front at depth Z ;

$t_D(Z)$ arrival time of draining front at Z .

10. Procedures at the profile level

10.1 Introduction

Chapters 8 and 9 introduced experimental aspects of local viscous-flow procedures including some of the effects of omnipresent capillarity. The cases relied on the two unambiguous features of viscous flow: rapid increase and concave decrease of water content due to an infiltrating pulse. Moreover, the beginning of decrease is related to the beginning of increase if infiltration lasts long enough, while the input pulse $P(q_s, T_B, T_E)$ together with F and L completely parameterize a WCW . More complete impressions of the WCW -evolution are expected from profile-level procedures. Horizons and other spatially variable soil properties may, however, obscure vertical viscous flow, while realistic boundary and initial conditions may lead to further restrictions.

10.2 Evolution of a WCW

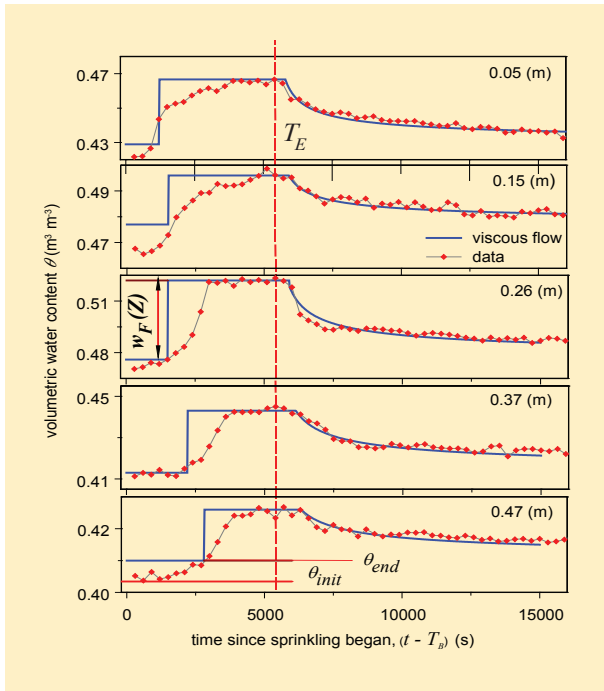


Figure 10.1, Topic 10.1: Matching the time series $\theta(Z, t)$ with viscous flow at depths $[Z_j = 0.05, 0.15, 0.26, 0.37, 0.47(\text{m})]$. Rate and duration of sprinkling were $[q_s = 2.1 \times 10^{-5}(\text{m s}^{-1})]$ and $[(T_E - T_B) = 5'400(\text{s})]$. The amplitudes decrease with depth. θ -scales vary among plots. Data from Schütz (2002).

Topic 10.1: *Evolution of a WCW from in-situ infiltration experiments.*

Case 10.1: *Simultaneous determination of $\theta(Z_j, t)$ at five depths in an arable soil.* The information presented here is from Schütz (2002) who described the impact of various tillage techniques on infiltration. The data represent the response to sprinkling on an arable soil with a plow layer extending from the surface to the 0.26-m depth, a blocky structure and the texture of a sandy loam. From a trench wall TDR-wave guides were horizontally installed at $[Z_j = 0.05, 0.15, 0.26, 0.37, 0.47(\text{m})]$. $P(q_s, T_B, T_E)$ was due to sprinkling with $[q_s = 2.1 \times 10^{-5}(\text{m s}^{-1})]$ and $[(T_E - T_B) = 5'400(\text{s})]$. The time interval between TDR-recordings was $[\Delta t = 300(\text{s})]$. Figure 10.1 presents the data and viscous-flow matching to each $\theta(Z_j, t)$ -series, *Topic 9.3*. Table 10.1 lists the parameters. At all depths was $[t_D(Z_j) < T_l = 8'100(\text{s})]$, thus $[Z_j < Z_l]$. Both, θ_{init} and θ_{max} indicate high degrees of water saturation with noticeable variations with depth. They and w_F attain the maximum at the 0.26-m depth which is at the transition from the plow layer to the B-horizon.

Table 10.1, Topic 10.1: Parameters of matching time series $\theta(Z_j, t)$ with viscous flow at depths $[Z_j = 0.05, 0.16, 0.26, 0.37, 0.47(\text{m})]$. Sprinkling was with $[q_s = 2.1 \times 10^{-5}(\text{m s}^{-1})]$, $[(T_E - T_B) = 5'400(\text{s})]$ and the total volume of $[V = 0.11(\text{m})]$

parameter	units	depths Z_j					source
		0.05	0.15	0.26	0.37	0.47	
		m	m	m	m	m	
$\theta_{init}(Z_j)$	$\text{m}^3 \text{ m}^{-3}$	0.417	0.464	0.468	0.411	0.403	data
$\theta_{max}(Z_j)$	$\text{m}^3 \text{ m}^{-3}$	0.467	0.499	0.523	0.445	0.427	
$t_W(Z_j)$	s	1'200	1'500	1'500	2'200	2'800	optimiza- tion, calibration
$\theta_{end}(Z_j)$	$\text{m}^3 \text{ m}^{-3}$	0.429	0.477	0.476	0.413	0.410	
$\theta_{max}(Z_j)$	$\text{m}^3 \text{ m}^{-3}$	0.467	0.496	0.522	0.443	0.426	model calcula- tions
$w_F(Z_j)$	$\text{m}^3 \text{ m}^{-3}$	0.038	0.019	0.046	0.030	0.016	
$t_D(Z_j)$	s	5'800	6'000	5'900	6'133	6'333	
$v_F(Z_j)$	$\text{m s}^{-1} \times 10^{-4}$	0.42	1.0	1.73	1.68	1.68	
$F(Z_j)$	μm	3.6	5.5	7.3	7.2	7.2	
$L(Z_j)$	m^{-1}	15'710	3'440	6'318	4'183	2'233	
$q_F(Z_j)$	$\text{m s}^{-1} \times 10^{-6}$	1.6	1.9	8.0	5.1	2.7	
$q_F(Z_j) / q_s$	----	0.07	0.1	0.38	0.24	0.13	

Bold-italic numbers indicate approximate constant values across horizons.

Neither in the data nor in the parameters of the upper three levels at $[Z_j = 0.05, 0.15, 0.26(\text{m})]$ is it possible to discern any clear patterns. This is probably due to too long Δt -intervals vis-à-vis the heterogeneity of the plow layer. However, the three wetting front velocities at the lower three levels $[Z_j = 0.26, 0.37, 0.47(\text{m})]$ deviate only by about $[\pm 1.5(\%)]$ from the average of $[\bar{v} = 1.7 \times 10^{-4}(\text{m s}^{-1})]$. Thus, a constant wetting front velocity must be considered for these depths. Water moving with a constant velocity confirms the basic assumption that viscosity balances gravity, Eq.(2.9). As a consequence, the film thickness $F(Z_j)$ remains constant. The decreasing $w_F(Z_j)$ and $q_F(Z_j)$ vis-à-vis constant $v(Z_j)$ and $F(Z_j)$ indicate flow paths of similar quality that were gradually blocked between the 0.26- and the 0.47-m depth. In addition, $[(\theta_{end} > \theta_{init})_j]$ indicates that some of the arriving flow became stuck within the individual TDR-control volumes and was no longer available for further drainage. However, capillary abstraction from the *WCW* has not significantly thinned F and has not substantially reduced v_F . Thus, the reduction of $w_F(Z_j)$ and $q_F(Z_j)$ is mainly due to the decrease of $L(z)$. Referring to Eqs.(9.4) and (9.5), total water abstraction as function of z amounts to

$$\frac{dV}{dz} = \frac{g}{3 \cdot \eta} \cdot \overline{F^3} \cdot \frac{dL(z)}{dz} \cdot \overline{T_{int}} \quad (10.1)$$

where $[\overline{T_{int}}]$ is the average of $T_{int}(Z)$ at the three depths when inserting $[t = 10^9 (\text{s})]$ into Eq.(9.5). The linear regression of $L(z)$, Tab. 10.1, produces the slope of $[dL/dz = -1.95 \times 10^4(\text{m}^{-2})]$ with $[\mathcal{R}^2 = 1.0]$. Inserting $[dL/dz]$ into Eq.(10.1) indicates that the *WCW* would be exhausted at the depth of 0.59(m) if the flow properties of the 0.26- to 0.47-m depth range were to remain beyond the 0.47-m depth.

10.3 Viscous flow initiation in dry soil

Viscous flow assumes weak tensile strength of the mobile water as described in Sections 6.5 and 6.6. In dry soils capillarity opposes viscous flow mainly by increasing tensile strength and by abstracting water from the *WCW* up to its complete annihilation. Ignoring shrinking and swelling clays, at least three scenarios are conceivable that would lead to the required weak tensile strength:

- (i) A few wide paths carry most of the viscous flow with small areas exposed to water-sorbing while modest water abstraction does not severely hamper the *WCW*. This scenario leans towards flow in macropores as it is generally perceived in the literature. It is expressed with relatively small L -parameters.
- (ii) Viscous flow is along numerous narrow paths imbedded in a matrix of low hydraulic conductivity due to low antecedent water content. This

type of flow is represented with relatively large L -parameters, such as are found in well-structured loams and sandy loams. Nonetheless, spreading of the WCW across the wide internal surface area may substantially decelerate the wetting front.

- (iii) Viscous flow occurs in diffuse pores, for example, in fine but poorly structured sands. Any increase of low antecedent water contents up to the permitted level of viscous flow is mostly governed by slow capillary flow, therefore the initiation of viscous flow gets delayed despite an intermediate extent of L .

In summary, the impact of antecedent water content on the initiation of viscous flow seems to increase from scenario (i) to (iii). However, initiation of viscous flow may follow any of the above combinations - or none of them at all. This undetermined situation demands further experimentation.

If Z_j lies deeper in the profile than the depth of the investigation, two patterns of $\theta(Z, t)$ -series will indicate viscous flow:

- (i) Rapid increase of soil moisture at $t_w(Z)$ and
- (ii) its concave decrease starting at $[t_D(Z) = T_E + 1/2 (T_E - T_B)]$.

The combined patterns suggest that the data sets warrant a full viscous-flow analysis, while pattern (i) alone only allows for the estimation of v_F and, subsequently, of F .

Topic 10.2: *Empirical assessment of viscous-flow initiation based on in-situ infiltration.*

Case 10.2: *Infiltration into a loam-textured Chernozem (Mollisol) at low antecedent water content.* Five consecutive runs of ponded-infiltration into a Chernozem of fluvial deposits from the Danube river near Bratislava (Slovakia) serve here as an example. The average texture was a loam with 20(%_w) clay, 47(%_w) silt, and 33(%_w) sand. At intervals of approximately one day 27(L) of water were added to a basin of 1(m) by 1(m) situated above the wave guides. Severe ponding was avoided through controlled pouring with a hand-held watering can. The time lapsed for complete infiltration was from 1'630 to 10'500(s). Further information can be found in Mdaghri Alaoui et al. (1997). Figure 10.2 represents the results from Runs 1 to 5, featuring the time series of $\theta(Z_j, t)$ at the five depths of horizontally installed TDR-wave guides at $[Z_j = 0.1, 0.3, 0.5, 0.7, 0.9(\text{m})]$.

In July of 1995 the water content of the loam soil under a corn crop dropped to $[\theta_{init} < 0.36(\text{m}^3 \text{ m}^{-3})]$. While Run 1 increased the water content only at the uppermost wave guides, Runs 2 to 5 produced viscous flow patterns at consecutive depths with the corresponding delays. The last infiltration experiment barely but nevertheless significantly increased the water contents at the 0.7- and 0.9-m depths.

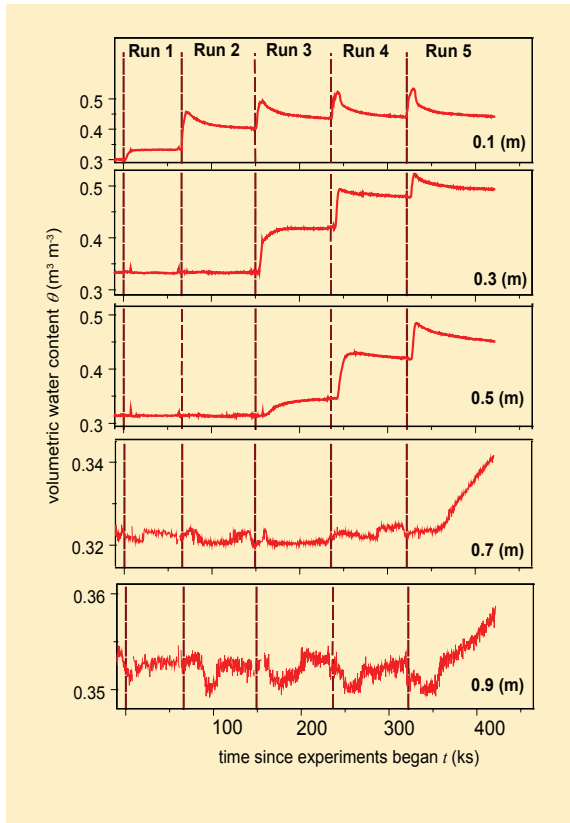


Figure 10.2, Case 10.2: Water content variations $\theta(Z,t)$ as the result of five consecutive infiltrations, Run 1 to 5, into a Chernozem near Bratislava (Slovakia) at depths $[Z_j = 0.1, 0.3, 0.5, 0.7, 0.9(\text{m})]$. θ -scales vary among plots.

Three $\theta(Z,t)$ -shapes are discernible:

- (i) No reaction at all, which indicates that the wetting front has not arrived at Z , such as at $[Z > 0.1(\text{m})]$ during Runs 1 and 2.
- (ii) An early steep and bulging increase changing to a subsequent moderate persisting increase that may level off at a constant water content i.e., depths 0.3 and 0.5(m), Run 3.
- (iii) An early steep increase, that may or may not attain a constant water content, and that is followed by a concave decrease i.e., depth 0.1(m), Runs 2 to 5.

Only shape (iii) is attributable to viscous flow, whereas shapes (i) and (ii) indicate complete or substantial capillary abstraction from a WCW that does not allow any water to drain according to viscous flow.

Table 10.2 lists a θ_{init} that gradually increased with progressing infiltration runs. *Case 10.2* suggests that a minimal water content of about $0.30(\text{m}^3 \text{ m}^{-3})$ is required before significant viscous flow appears. In accord with Germann (1976) the range of antecedent capillary heads is estimated at $[-7 \leq h_{cap} \leq -20(\text{m})]$.

Table 10.2, Topic 10.2: Initial water contents, θ_{init} , durations of infiltrations, $[T_E - T_B]$, and average infiltration rates, q_s of the five infiltration runs.

depth Z_j (m)	initial water contents, θ_{init} ($\text{m}^3 \text{ m}^{-3}$)				
	Run 1	Run 2	Run 3	Run 4	Run 5
0.1	0.300	<i>0.334</i>	<i>0.405</i>	<i>0.439</i>	<i>0.457</i>
0.3	0.333	0.335	0.335	0.421	0.479
0.5	0.315	0.315	0.318	0.348	<i>0.418</i>
0.7	0.323	0.323	0.323	0.323	0.325
0.9	0.353	0.353	0.353	0.352	0.351
duration $T_E - T_B$ (s)	1'630	4'800	7'440	10'500	9'300
average rate $q_s \times 10^{-6}$ (m s^{-1})	16.5	5.6	3.6	2.6	2.9

Bold numbers: determination only of $t_w(Z)$

Bold italic numbers: determination of both, $t_w(Z)$ and w_F

The wetting-front arrival times yield velocities v_F , Tab. 10.3. With the exception of the 0.1-m depth, they were estimated from the differences between the arrival times at the lower TDR-wave guide minus the arrival times at the adjacent upper one. The film thicknesses F , Eq.(2.15), are compiled in Tab. 10.4. The capillary potentials acting in the water films are calculated according to Eq.(2.21) and are within the range of $[-1.7 \geq h_{cap}(F) \geq -6.5(\text{m})]$.

Table 10.3, Topic 10.2: Wetting front velocities v_F between depths of TDR-recordings

depth range (Z_{j-1}, Z_j) (m)	average velocity of wetting front, v_F , between depths ($\times 10^{-5} \text{ m s}^{-1}$)				
	Run 1	Run 2	Run 3	Run 4	Run 5
0.0 to 0.1	4.7	<i>27.8</i>	<i>11.1</i>	<i>7.9</i>	<i>7.9</i>
0.1 to 0.3			5.5	4.7	<i>4.8</i>
0.3 to 0.5			2.1	9.5	<i>9.5</i>
0.5 to 0.9					1.7

The six available *WCW*-amplitudes are comparatively high with [$w_s \geq 0.08(\text{m}^3 \text{ m}^{-3})$], Tab. 10.5. However, the accompanying contact lengths [$L > 10'000(\text{m}^{-1})$], Tab. 10.6, indicate densely distributed flow paths in an otherwise poorly structured permeable medium. The findings are in accord with the relatively thin water films, the majority with [$F < 10(\mu\text{m})$], Tab. 10.4.

Table 10.4, *Topic 10.2:* Film thicknesses *F* between depths of TDR-recordings

depth range (Z_{j-1}, Z_j) (m)	filmthickness <i>F</i> (μm)				
	Run 1	Run 2	Run 3	Run 4	Run 5
0.0 to 0.1	3.6	9.2	5.8	4.9	4.9
0.1 to 0.3			4.1	3.7	3.8
0.3 to 0.5			2.4	5.4	5.4
0.5 to 0.9					2.3

depth Z_j (m)	amplitudes w_F of the <i>WCW</i> s ($\text{m}^3 \text{ m}^{-3}$)			
	Run 2	Run 3	Run 4	Run 5
0.1	0.121	0.083	0.082	0.080
0.3				0.044
0.5				0.065

Table 10.5,
Topic 10.2:
Amplitudes
 w_F of the
*WCW*s

depth Z_j (m)	specific contact length <i>L</i> (m ⁻¹)			
	Run 2	Run 3	Run 4	Run 5
0.1	13'150	14'310	14'640	16'330
0.3				11'580
0.5				12'040

Table 10.6,
Topic 10.2:
Contact
lengths *L*

Table 10.7 lists the six volume flux densities, q_F , according to Eq.(3.2), the hydraulic conductivities at saturation, K_{sat} , and the average infiltration rates, q_S . With the exception of q_F of Run 2 at the 0.1-m depth all other viscous-flow estimates of q_F are below or within the range of K_{sat} of Mdaghri-Alaoui et al. (1997), demonstrating consistency of viscous flow with the Darcy (1856)-concept. There are at least three reasons for the exceptional [$q_F > q_S$] during Run 2 at the 0.1-m depth:

- (i) The TDR-probe was placed too close to the soil surface;
- (ii) uneven application of infiltration with the hand-held watering can;
- (iii) finger flow.

However, to determine the cause for [$q_F > q_S$] requires an improved experimental protocol.

Table 10.7, Topic 10.2: Volume flux densities $q(z)$, Eq.(3.2); F and L from Tables 10.4 and 10.6.

depth Z_j (m)	K_{sat}		volume flux densities at the wetting fronts $q_F \times 10^{-6}(\text{m s}^{-1})$			
	average ($\times 10^{-6} \text{ m s}^{-1}$)	CV (%)	Run 2	Run 3	Run 4	Run 5
0.0 $q_F = q_S$	---	---	5.6	3.6	2.6	2.9
0.1	8	200	33.5	9.1	5.6	6.3
0.3	7	140				2.1
0.5	4	170				6.2

Case 10.3: Infiltration into a silty clay-loam: From sites in Catalonia (Spain), Vadilonga et al. (2008) reported infiltration into a silty clay-loam with clay-, silt-, and sand-fractions of 39, 50, 11(%_w), and the parameters [$\theta_{init} = 0.355(\text{m}^3 \text{ m}^{-3})$], [$q_S = 1.5 \times 10^{-5}(\text{m s}^{-1})$] and [$(T_E - T_B) = 36'00(\text{s})$]. At the 0.21-m depth the experiment produced [$F = 8.5(\mu\text{m})$] and [$L = 7'600(\text{m}^{-1})$].

The initial water content is comparable with the contents listed in *Case 10.2* Tab. 10.2 but the infiltration rate exceeds the rates compiled in Tab. 10.7 by factors from 3 to 6. Here it is speculated that the higher clay-percentage at the Spanish site compared with the Slovak site, 39(%_w) vs. 20(%_w), indicates a system that contains fewer but better structured flow paths, whereas the higher sand-percentage at the Slovak site, 33(%_w) vs. 11(%_w), suggests a more diffuse path system. A comparison of the contact lengths supports the hypothesis of higher clay contents promoting and stabilizing preferential-flow paths. The Slovak site with the lower clay content produced [$11'600 \leq L \leq 16'300(\text{m}^{-1})$].

The suggested relationship between texture on one hand and the L - and F - parameters on the other hand, mainly in view of viscous-flow initiation in dry soils, is here considered a stimulus for further experimental research rather than a generalizable fact. Nevertheless, in the context of controlled infiltration and the subsequent monitoring of temporal water-content variations, L and F emerge as promising parameters that are well suited for the functional quantification of viscous-flow paths.

10.4 Viscous flow restrictions at interfaces

The complete evolution of a WCW assumes homogeneous paths wide enough not to hamper viscous flow, while the properties of the embedding matrix may vary. However, three main features disturb paths of preferential flow:

- (i) Compacted horizons, for instance B_T -horizons related with clay accumulations, as indicated in Section 9.5;
- (ii) interface to the atmosphere, for instance, at the bottom of a soil column draining freely;
- (iii) abrupt changes of flow-path widths.

Topic 10.3: *Viscous-flow restriction due to a compacted layer.* It is reasonable to assume that a compacted soil horizon will also hamper viscous flow such that it is observable at the profile level. The most prominent indication of distortion is the absence of viscous flow within and underneath a compacted horizon, whereas viscous flow is well detectable between the compacted horizon and the soil surface. More subtle indications of hampered viscous flow are expected from the distortion of θ -time series immediately above the compacted horizon.

Case 10.4: *Sprinkler infiltration into a Eutric Cambisol with a B_T -horizon:* The soil discussed here was an arable Eutric Cambisol at the Rütli-Experimental Farm (Zollikofen, Switzerland) with a compacted B_T -horizon between the depths of 0.8 and 1.1(m).

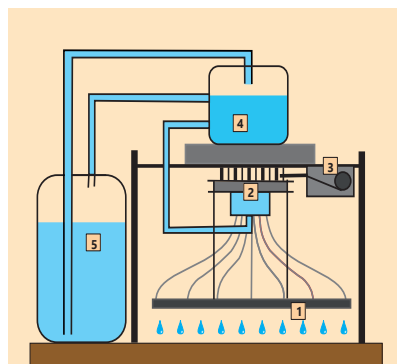


Figure 10.3, Case 10.4: Schematic representation of a in-situ applicable sprinkler device. (1) sheet metal of 1(m) x 1(m), keeping 100 nozzles in place; (2) manifold, diverting water to the 100 nozzles; (3) gear moving (1) in the x - and y - directions such that it takes more than 600(s) for one nozzle to drip on the same spot; (4) constant-level reservoir; (5) tank supplying water via pump to (4). After Schütz (2002).

At depths 0.1, 0.4, 0.8, 1.0(m) were $[\rho_b = 1.40, 1.45, 1.57, 1.65(\text{Mg m}^{-3})]$. Five wave guides were mounted at $[Z_j = 0.15, 0.35, 0.55, 0.75, 0.95, 1.05(\text{m})]$ horizontally. At each of three consecutive days the soil was sprinkler irrigated with $[q_s = 2.8 \times 10^{-5}(\text{m s}^{-1})]$ and $[(T_E - T_B) = 4'500(\text{s})]$. The sprinkler is presented in Fig. 10.3, and more details are available in Germann et al. (2002a).

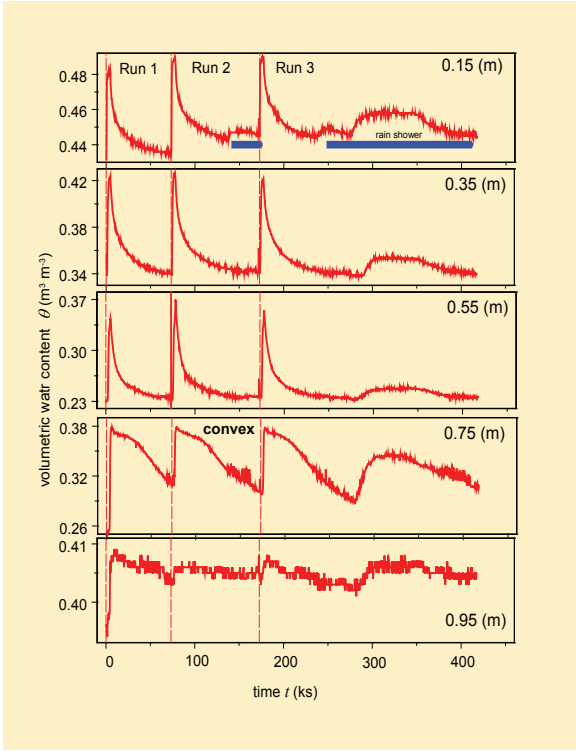


Figure 10.4, Case 10.4: Infiltration in a soil with a compacted B_T -horizon at the 0.8-m depth. The blue bars indicate rain showers. θ -scales vary among plots.

The results are summarized in Figure 10.4. Water-content recording was extended into the fourth day. Showers of unknown intensities and durations occurred in the afternoons of day 2, 3, and 4. The $\theta(Z_j, t)$ -series from the upper three horizons feature typical concave trailing waves, whereas the trailing waves at the 0.75-m depth are convex, and the time series at 0.95(m) hardly show any significant infiltration reactions. The convex trailing waves closely above the compacted soil horizon indicate water congestion due to restrained vertical drainage. Lateral drainage may occur along the compacted horizon but it was considerably slower than vertical flow. The barely significant water content variations at the 0.95-m depth confirm viscous-flow restrictions in the B_T -horizon.

The shapes of the drainage phases at the 0.75-m depth are convex in all three runs. However, only the time series of Run 1 is suitable for quantitative interpretation because the θ -increases during Runs 2 and 3 started before WCW s of the previous runs had completely drained to constant θ_{end} . In Tab. 10.8 the F - and L -parameter of the upper four TDR-levels are compiled: F decreases moderately with depth while L increases by a factor of more than 3, clearly indicating a significant increase of the specific contact area. The moderate decrease of $F(z)$ is interpreted as an early indication of the B_1 -horizon whereas the substantial increase of $L(z)$ is taken as a measure of water accumulation. Slow lateral drainage, as indicated by the convex shapes of $\theta(0.75, t)$ in Fig. 10.4, is an experimental artifact due to the limited sprinkler area of 1(m) by 1(m). Rain-infiltration that occurs at a much wider areal extent is supposed to drain substantially slower along the entire B_1 -horizon.

Table 10.8, Topic 10.4: F and L of Run 1

depth Z_j (m)	specific contact length L (m ⁻¹)	film thickness F (μ m)	wetting front velocity $v_F \times 10^{-4}$ (m s ⁻¹)
0.15	4'100	12.4	5.0
0.35	7'900	10.9	3.9
0.55	12'700	9.0	2.6
0.75	13'100	9.8	3.1

Further interpretation of L demands caution when water congestion is presumed. So far, L is strictly related to the mobile water content of a WCW , Eqs.(3.2) to (3.5). However, a flow-restricting horizon may increase the water content above it through neither capillarity nor increasing the density of flow paths but simply through perching, thus, leading to an apparent increase of L with depth. Therefore, it is reasonable to interpret [$dL/dz > 0$] as the most likely result of viscous-flow restriction but further interpretations without additional information are here avoided.

Topic 10.4 *Viscous-flow restriction due to a capillary fringe.* The film thicknesses reported so far are in the range of [$2.3 \leq F \leq 27(\mu\text{m})$] and, according to Eq.(2.21), the corresponding capillary heads amount to [$-6.5 \leq h_{cap} \leq -0.55(\text{m})$]. At the interface of the permeable medium to the atmosphere viscous flow has to overcome capillary tension, resulting in the formation of a capillary fringe.

Case 10. 5 *Neutron radiographs of finger-flow*. Neutron radiography is a powerful tool for the dynamic recording of 2-dimensional water-content distributions at time intervals and with precision adequate for viscous-flow analyses. However, a strong enough neutron source requires an elementary-particle accelerator and the dedicated infrastructure as, for instance, provided with the NEUTRA-facility run at the Paul-Scherrer Institute (Villigen, Switzerland). The set-up is shown in Fig. 10.5. Lehmann et al. (2005) provide more technical details, while the data are from Hincapié's (2008) dissertation. Hincapié and Germann (2010) investigated spatio-temporal distributions of water contents during finger-flow in a box with two horizontal extents of 0.2 and 0.05(m), and a vertical extent of 0.4(m). The facility produces pixels extending 0.272(mm) in the vertical and horizontal directions resulting in a areal minimal resolution of 0.074(mm²). Hincapié and Germann (2009) report reproducibility of water content measurements within less than [$\pm 2(\%)$] of the entire signal. The box was filled with quartz-sand sieved to particle diameters between 0.2 and 0.5(mm). Pixel and particle diameters are thus of the same order of magnitude.

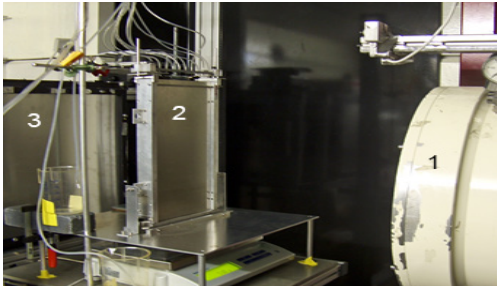


Figure 10.5, Case 10.5: View of NEUTRA set-up: (1) Neutron source; (2) sand box with sprinkler on top; (3) Detector (CCD-camera).
Courtesy: Ingrid Hincapié.

Figure 10.6 shows two radiographs recorded at 225 and 1'125(s) after the beginning of infiltration in air-dry sand. Total volume of [$V_{tot} = 20(\text{mm})$] was sprinkled during [$(T_E - T_B) = 600(\text{s})$]. The capillary fringes at both the upper and lower edges of the box extend about 47(mm) into the sample.

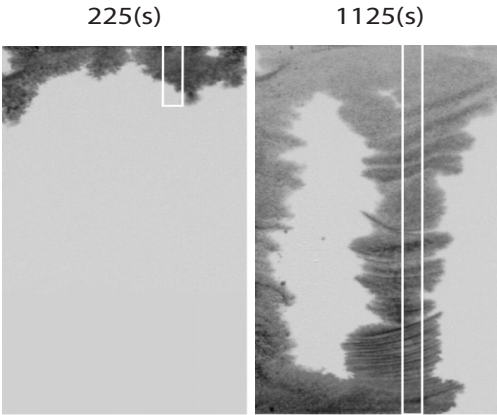


Figure 10.6: Case 10.5, Topic 10.4 Radiographs at 225 and 1'125(s) after beginning of sprinkling. The white rectangles indicate the region selected for further investigations, Fig. 10.8. (Hincapié and Germann, 2009b).

Under the assumption that the heights of the capillary fringes express the capillary heads [$h_{cap} = -0.047(\text{m})$], from Eq.(2.21) it follows that film thickness in the static fringes of [$F_f = 320(\mu\text{m})$] should be 10 to 100 times thicker than the films from viscous flow encountered so far.

Topic 10.5: *Viscous flow alterations due to abrupt changes in the viscous-flow paths.* Consider two contrasting layers both capable of carrying a viscous volume flux of $Q(\text{m}^3 \text{ s}^{-1})$. The viscous-flow properties are F_{up} and L_{up} in the upper layer, and F_{lo} and L_{lo} in the lower layer, while their ratios are [$n_F = F_{up}/F_{lo}$] and [$n_L = L_{up}/L_{lo}$]. Further, given a cross-sectional area A that is sufficiently wide, then from

$$q_s = \frac{Q}{A} = F^3 \cdot L \cdot \frac{g}{3 \cdot \eta} \quad (3.2)$$

follow

$$\frac{L_{up}}{L_{lo}} = n_F^3 \quad (10.2)$$

and

$$\frac{F_{up}}{F_{lo}} = n_L^{1/3} \quad (10.3)$$

Therefore, abrupt increases of F vs. z , as expected in coarse grained materials overlain by finer grained materials, should lead to marked reductions of L across the material interface in the order of n_F^{-3} . This is considered one of the reasons leading to the formation of finger-flow. In contrast, changes of L across the interface are presumably of minor importance on F and on v_F . Such purely theoretical reasoning allows us to develop experimental procedures that might explain the formation of finger flow.

10.5 Viscous flow and finger flow

This section describes viscous flow during finger flow. Although the section does not focus on finger flow per se it provides some tools for further investigating the phenomenon in unsaturated porous media. The presumed dominance of F over L as presented in the previous *Topics 10.1* and *10.5*. They suggest tangential forces co-evolve with finger-flow, which then protect the flow structure against the lateral capillary pull away from the preferentially wetted volume. Moreover, Selker et al. (1992) reported constant wetting front

velocities during finger flow, which link well the force balance equation, Eq.(2.9) with finger flow. The following topics investigate various viscous-flow aspects of finger flow based on *Case 10.5*.

Topic 10.6: Wetting front velocity during finger flow. The depth-variation of the wetting front velocity v_F of a *WCW* is a prominent feature at the profile level. It is a measure of the homogeneity of viscous-flow expressed in the depth-variation of the film thickness F .

Case 10.5 (continued): The 2-d distribution of bulk density ρ_b of the packed sand was recorded with γ -ray absorption that is part of the NEUTRA equipment. Figure 10.7 summarizes ρ_b -averages in layers that were 3 mm thick and extended horizontally across the entire sand box. A decreasing trend and enormous scatter with depth are well discernible. The scatter is mirrored in the 2-d water content distributions in Figs. 10.6 and 10.8. Averages and variations within one standard deviation of bulk density and porosity were $[\rho_b = 1.505 \pm 0.216(\text{kg m}^{-3})]$ and $[\varepsilon = 0.43 \pm 0.08(\text{m}^3\text{m}^{-3})]$. The uneven loading of the sand box is suspected of some impact on viscous flow.

Intensity and duration of sprinkler irrigation were $[q_s = 3.3 \times 10^{-5}(\text{m s}^{-1})]$ and $[(T_E - T_B) = 600(\text{s})]$, amounting to $[V_{tot} = 20(\text{mm})]$. Figure 10.8 illustrates 2-d distributions of $\theta(x,z,t)$ at $[T_k = 300, 600, 2'000(\text{s})]$ after the beginning of infiltration. Evidently, fingers and capillary fringes form before 300(s) and after 600(s), respectively. To avoid capillary fringe effects the viscous-flow analyses concentrate down to the 0.22-m depth in the computationally isolated prism with the horizontal dimensions of $[A = 5(\text{mm}) \times 30(\text{mm})]$ as depicted in Figs. 10.6 and 10.8. The region selected for further investigation is completely embedded in the highly water-saturated finger-flow volume.

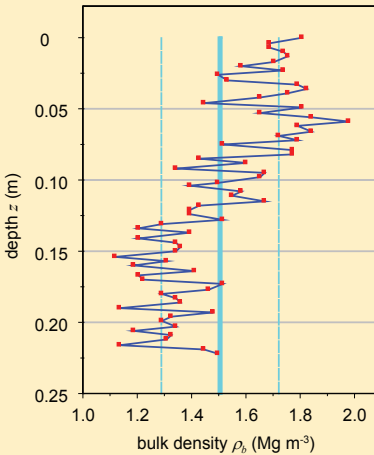


Figure 10.7, Topic 10.6: Bulk density, $\rho_b(z)$. Each point represents an average of layers that are 3 (mm) i.e., 11 to 12 NEUTRA-pixels thick. The horizontal gray lines at $[Z = 0.05, 0.1, 0.15, 0.2(\text{m})]$ depict depths of $\theta(Z,t)$ -analyses, while the vertical solid and dashed cyan lines indicate average ρ_b , and $\pm 1(\text{stdv})$.

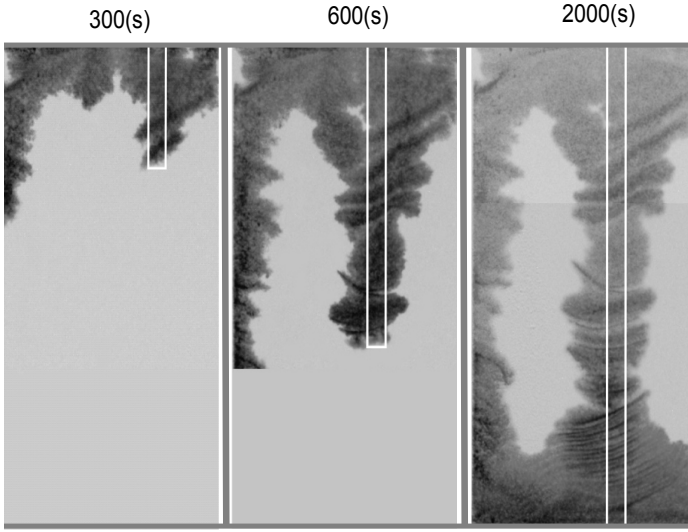


Figure 10.8, Case 10.5: 2-d distribution of volumetric water contents at times $[T_k = 300, 600, 2'000(\text{s})]$ after the beginning of infiltration. Drainage started shortly after 600(s) and the capillary fringe evolved between 600 and 2'000(s). The white rectangle delineates the prism selected for the analyses of finger flow. The intensities of the gray-black shades are proportional to the water content.

Figure 10.9 shows the arrival times $[t_w(z) - T_B]$ of the wetting front at 16 depths, $z_w(t)$. Llinear regression yielded with $[\mathcal{R}^2 = 0.99]$ a slope of $[v_F = 4.37 \times 10^{-4}(\text{m s}^{-1})]$, an intercept indicating retardation of $[ret = 79(\text{s})]$, and the constant film thickness of $[F = 11.6(\mu\text{m})]$, Eq.(2.15).

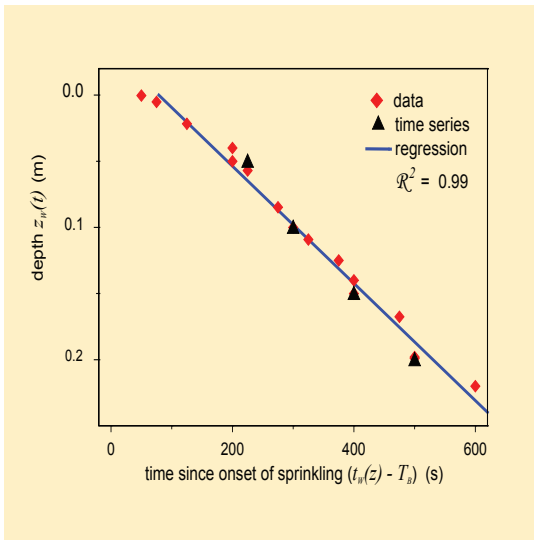


Figure 10.9, Topic 10. 6: Linear regression of wetting front depth $z_w(t)$ vs. arrival time, $(t_w(z) - T_B)$. The triangles indicate the depths of time-series that are further analyzed.

The linearity indicates constant v_F in the range from the surface to the 0.22-m depth, supporting the notion of viscosity balancing gravity, Eq.(2.9). Moreover, constant $v_F(z)$ and $F(z)$ demonstrate they are independent of $\rho_b(z)$ and $\varepsilon(z)$, although both latter parameters vary strongly and show systematic trends with depth. Thus, the suspicion raised in the previous section of density- and porosity-variations impacting viscous flow is here disregarded.

Topic 10.7: Analyses of $\theta(t, Z_j)$ -time series at various depths Z_j provides local-level information to be incorporated in the wider context of viscous flow at the profile level.

Case 10.5 (continued): Four $\theta(Z, t)$ -time series are here analyzed at depths $[Z_j = 0.05, 0.1, 0.15, 0.2(\text{m})]$. The spatial resolution of NEUTRA permits the investigation of horizontal layers that are only 1 pixel thick with a control volume of $[V_{\text{ctrl}} = (30 \times 5 \times 0.272)(\text{mm}^3) = 41(\text{mm}^3)]$. Moreover, the wetting front arrived at the lowest level considered at $[t_w(0.2) = 0.2(\text{m})/v_F = 458(\text{s})]$ which is less than $[(T_E - T_B) = 600(\text{s})]$ and $[T_I = T_B + 3/2 \times (T_E - T_B) = 900(\text{s})]$. Therefore, Eqs.(3.24) to (3.28) suffice for the complete analyses of the time series. Figure 10.10 illustrates the data and viscous-flow matching according to Topic 9.3. Marked breaks of water content increases indicate the arrival of the wetting front at all depths with the weakest indication

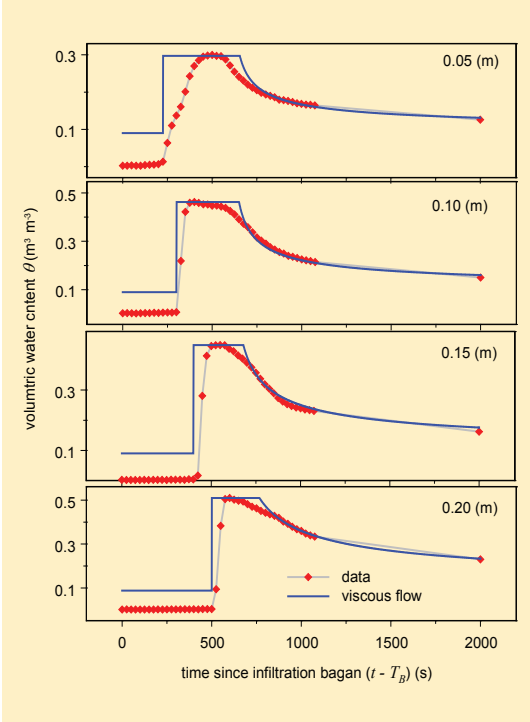


Figure 10.10, Case 10.5, Topic 10.7: $\theta(Z, t)$ -series and viscous-flow matching at depths of $[Z_j = 0.05, 0.1, 0.15, 0.2(\text{m})]$. Mind the different θ -scales.

at 0.05(m). The sand was air-dry prior to infiltration, thus $[\theta_{init}=0]$ while matching required $[\theta_{end}=0.09(\text{m}^3\text{m}^{-3})]$ at all four depths. Table 10.9 lists two contact lengths for each time series, the first evolved from the increasing imbibition limb and the second was deduced from the decreasing drainage limb, using $[L_{im} = (\theta_{max} - \theta_{init})/F]$ and $[L_{dr} = (\theta_{max} - \theta_{end})/F]$, respectively. Because $F(z)$ is constant the ratio of $[(L_{im}-L_{dr})/L_{im}]$ indicates the reduction of contact length between the water entering and the water leaving the control volume. The comparatively high L -values are due to the focus on water contents within the domain of highly water-saturated finger-flow. This is in contrast to the previous cases, in those cross-sectional areas A coincide with the horizontal extent of the control volumes of the TDR-wave guides which include both, flow-active and flow-passive zones. Despite the thinness of the control volume of just 1 pixel of 0.272(mm) the water contents still increase gradually. This is in contrast to the abrupt and discontinuous increase expected from the theory and indicated by the blue lines in Fig. 10.10. Thus, the gradual water-content increases are considered to be primarily due to the horizontal variations of preferential flow. However, the variations have to be within small depth increments because otherwise no overall constant $v_F(z)$ could have evolved.

Time series of $\theta(Z,t)$ allow for the estimation of fluxes $[q(Z) = v_F L(Z) F]$ across $[A_F = (5 \times 30)(\text{mm}^2)]$ at depths Z_j according to Eqs.(8.8) to (8.10). Flux integrations over a time interval according to Eq.(9.4) yield the volume V_F that has crossed A_F during the respective time interval. In Tab. 10.10 the volumes V_F that resulted from integration from the beginning of sprinkling at T_B to the respective times T_k are presented. The local volumes V_F per cross-sectional area of the finger that exceed the total volume sprinkled at the surface $[V_F(Z) > V_{tot} = 20(\text{mm})]$ are due to the reduced actual cross-sectional area of finger flow with respect to the total cross-sectional area of the sand box that

Table 10.9, Topic 10.7: Specific contact lengths of imbibition and draining limbs, L_{im} and L_{dr} , and the relative reduction during the passing of the *WCW* through the control volume.

depth Z_j (mm)	L_{im} (m ⁻¹)	L_{dr} (m ⁻¹)	$(L_{im} - L_{dr}) / L_{im}$
50	25'730	17'940	0.30
100	40'010	32'220	0.20
150	38'840	31'050	0.20
200	44'090	36'480	0.17
average	37'170	29'420	
stdv	6'885	6'931	

was sprinkled at. The effect is dubbed here as flow-funneling that amounts at 2'000(s) to $[2.7 \leq V_F(Z)/V_{tot} \leq 4.6]$ as listed in Tab. 10.10, column (6).

Table 10.10, Topic 10.7: Computed volumes $V_F(Z_j)$ of fluxes, Eq.(9.4), that have passed the cross-sectional area $[A = 30 \times 5(\text{mm}^2)]$ at depths $[Z_j = 0.05, 0.1, 0.15, 0.2(\text{m})]$ from T_B to $[(T_k - T_B) = 150, 350, 800, 2'000(\text{s})]$, columns (2) to (5); the ratios of the volumes $[V_F(Z_j)/V_F(0)]$ from 0 to 2'000(s) are listed in column (6), and column (7) contains the differences between columns (5) and (4).

depth Z_j (m)	volumes of fluxes $V_F(Z_j)$ (mm) that have crossed A at Z_j during $(T_k - T_B)$				$V_F(Z_j)/$ $V_F(0)$	$V_F(Z_j) \Big _{2000}$ $- V_F(Z_j) \Big _{800}$
	0 to 150 (s)	0 to 350 (s)	0 to 800 (s)	0 to 2'000 (s)	0 to 2'000 (s)	(5)-(4) (mm)
(1)	(2)	(3)	(4)	(5)	(6)	(7)
0.0	5.0	11.7	20.0	20.0	1.0	0
0.05	4.6	30.6	51.4	53.2	2.7	1.8
0.10	0	24.5	82.3	91.8	4.6	9.5
0.15	0	1.0	66.9	83.8	4.2	16.9
0.20	0	0	61.1	91.5	4.6	30.4

Topic 10.8: Water-content profiles, $\theta(z, T_k)$ at specific times T_k : Equations (3.19) to (3.23) and Fig. 3.2 provide the theoretical base for the investigation.

Case 10.5 (continued): Extending from the surface to $[z = 0.22(\text{m})]$, the case provides four water-content profiles at times $[T_k = 150, 350, 800, 2'000(\text{s})]$. They are distilled from NEUTRA-data in the prism shown in Fig. 10.8, covering a cross-sectional area of $[A_F = (5 \times 30)(\text{mm}^2)]$. Figures 10.6 to 10.8 suggest substantial variations of $\theta(z, T_k)$ that are mitigated through water content averages across layers of 3(mm) thickness i.e., in control volumes of $[V_{contr} = 450(\text{mm}^3)]$. The averaging procedure yields water content profiles that are supported at 68 depths. Viscous-flow is matched to the four profiles according to Eqs.(3.19) to (3.23). Table 10.11 compiles the water volumes $[V_s(0 - Z_j)]$ that are stored in the depth ranges from 0 to Z_j at the times T_k . Figure 10.11 summarizes the results of matching water content profiles with viscous flow. Retardation $[ret = 79(\text{s})]$, Topic (10.6), was applied in the matching of imbibition at times $[T_k = 150, 350(\text{s})]$, while $[\theta_{end} = 0.09(\text{m}^3\text{m}^{-3})]$, Topic (10.7), was considered in matching drainage at $[T_k = 800, 2'000(\text{s})]$. The figures also feature the standard deviations of the data with respect to viscous flow, which amounted to 0.042 and

0.028(m³m⁻³) at 800 and 2'000(s), respectively. Viscous-flow simulations are extended far beyond the depth of the sand box to illustrate the entire, in the lower part completely theoretical, *WCW*-profiles. The model parameters were [$F = 11.6(\mu\text{m})$] and [$L(T_k) = 850, 12'000, 34'000, 20'000(\text{m}^{-1})$]. The variation of $L(T_k)$ from 850 to 12'000(m⁻¹) is most likely due to formation of the finger, indicating a local increase of water content due to funneling. The variations of L from 12'000 to 34'000 and back to 20'000(m⁻¹) may indicate capillary break-through at the bottom. However, the need of more detailed research is suggested, for instance, by including lateral extents of the finger as function of time and depth. Averages and standard deviations of all four $L(T_k)$ amount to 16'710 and 12'080(m⁻¹), while those of the three latter profiles are 22'000 and 9'090(m⁻¹). The stark differences of $L(T_k)$ to L_{im} and L_{dr} listed in Tab. 10.9 require further investigation.

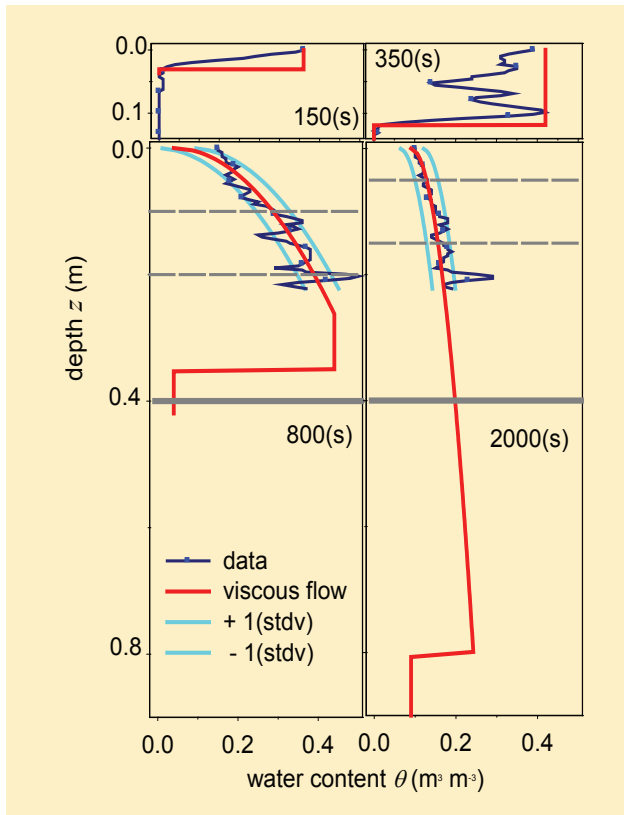


Figure 10.11, Case 10.5, Topic 10.8: Measured profiles of $\theta(z,t)$ at times [$T_k = 150, 350, 800, 2'000(\text{s})$] and viscous flow matching. The cyan lines indicate a range of [$\pm 1(\text{stdv})$] of the data around viscous flow matching. The standard deviations amount to 0.042 and 0.028(m³m⁻³) at 800 and 2'000(s). The solid gray line marks the bottom of the sand box at 0.4(m), and the dashed lines indicate depths of the $\theta(z,t)$ -analyses at [$Z_j = 0.05, 0.1, 0.15, 0.2(\text{m})$].

time T_k (s)	volumes $V_s(0-Z_j)$ (mm) of water stored at times T_k in the depth range of			
	0 to 0.05 (m)	0 to 0.10 (m)	0 to 0.15 (m)	0 to 0.2 (m)
(1)	(2)	(3)	(4)	(5)
150	4.7	4.8	4.8	4.8
350	15.4	30.3	32.9	32.9
800	9.2	20.7	37.4	56.0
2'000	6.0	12.7	21.3	30.4
$V_s(0-Z_j) \big _{2000}$	-3.2	-8.0	-16.1	-25.6
$-V_s(0-Z_j) \big _{800}$				

Table 10.11, Topic 10.8: Measured water volumes $V_s(0-Z_j)$ stored from the surface to $[Z_j = 0.05, 0.1, 0.15, 0.2 \text{ (m)}]$ at times $[T_k = 150, 350, 800, 2'000 \text{ (s)}]$, columns (2) to (5).

Topic 10.9: Water balance of finger flow: Attempts to close the water balance are most revealing in the assessment of a hydrological procedure's applicability. Here, the term procedure includes at least the following aspects:

- (i) The theoretical base which is one-dimensional viscous-flow in this case. In the literature this kind of base is often referred to as model;
- (ii) the spatial definition of the system considered, i.e., the prism in this case;
- (iii) the mode of the theoretical base's application to the data, which might be quite involved and may include numerical codes;
- (iv) the acquisition of data adequate to both, the theoretical base and the system;
- (v) the objective criteria applied to assess the applicability of (i) to (iv). Here, the objective criterion is the precision obtained when closing the water balance.

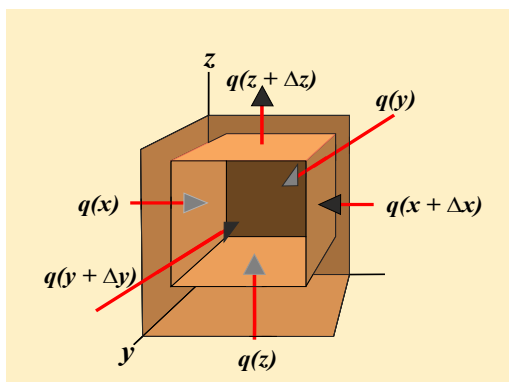


Figure 10.12 Topic 10.9: Scheme of the volume balance elements.

The basics of water balance computations are now introduced. A cubical control volume with the dimensions of $[\Delta x, \Delta y, \Delta z]$ is given. It is positioned in the 3-d Cartesian coordinate system with the orthogonal x -, y -, and z -axis as depicted in Fig. 10.12. Time t , considered the 4th dimension, is captured on the separate t -axis. The difference of the water volume within the control volume between time $[t + \Delta t]$ and time t due to the differences in the volume flux densities across the surfaces at $[x + \Delta x]$ and x , $[y + \Delta y]$ and y , and $[z + \Delta z]$ and z amounts to

$$\Delta V_x = -\Delta y \cdot \Delta z \cdot \Delta t \cdot [q(x + \Delta x) - q(x)] \quad (10.4a)$$

$$\Delta V_y = -\Delta x \cdot \Delta z \cdot \Delta t \cdot [q(y + \Delta y) - q(y)] \quad (10.4b)$$

$$\Delta V_z = -\Delta x \cdot \Delta y \cdot \Delta t \cdot [q(z + \Delta z) - q(z)] \quad (10.4c)$$

The summation of Eq.(10.4a) to (10.4c) divided by the control volume and the time interval Δt yields

$$\frac{\Delta V_x + \Delta V_y + \Delta V_z}{\Delta x \cdot \Delta y \cdot \Delta z \cdot \Delta t} = - \left[\frac{\Delta q_x}{\Delta x} + \frac{\Delta q_y}{\Delta y} + \frac{\Delta q_z}{\Delta z} \right] \quad (10.5)$$

where $[\Delta q_x = q(x+\Delta x)-q(x)]$ etc. Both, time interval and spatial differences are now considered infinitely small and it follows that

$$\frac{d\theta}{dt} = -\nabla q \quad (10.6)$$

The nabla operator ∇ stands for the sum of the partial derivatives in all three dimensions that evolve from the right hand side of Eq.(10.5). Here the following should be noted regarding the signs: Fluxes are positive in the positive directions of the axis, differences result from subtracting the value of the point closer to the origin from the one farther apart, and a water content increase is only possible when the sum of the six volume flux densities across the control volume decreases, and vice versa, hence the minus signs in Eqs. (10.4) to (10.6).

The application of Eq.(10.6) to finite volumes and time intervals requires integration over a specific time interval of the volume flux densities at the six boundaries and integration of the water contents over the volume under consideration at the beginning and at the end of the specified time interval.

Case 10.5 (continued) The application of Eq.(10.6) to the prism studied during finger-flow in *Case 10.5* requires the following two restrictions:

- (i) Lateral fluxes across the vertical boundaries of the prism are negligible, and $[\Delta q_x = \Delta q_y = 0]$ is assumed.

- (ii) The only time-interval with known volume flux density across the surface of the prism i.e., $[q(0) = 0]$, lasts from $[T_3 = 800(\text{s})]$ to $[T_4 = 2'000(\text{s})]$.

Uncertainties due to variable cross-sectional areas of infiltration, such as the funneling effect according to Tab. 10.10, exclude earlier time intervals from volume balance calculations with this simple approach. Therefore,

$$\sum_0^{Z_j} \theta \Delta z \Big|_{t=2000} - \sum_0^{Z_j} \theta \Delta z \Big|_{t=800} = - \int_{800}^{2000} q(Z_j) dt - \int_{800}^{2000} q(0) dt \quad (10.7)$$

where $[Z_j = 0.05, 0.10, 0.15, 0.20(\text{m})]$. The differences of the water contents' sums on the left hand side of Eq.(10.5) are listed in the last line of Tab.10.11, while the first integral on the right hand side corresponds to column (7) in Tab. 10.10, and the second integral on the right hand side of Eq.(10.7) is zero. Table 10.12 rearranges the items of the previous two tables and presents the balance calculations, which ideally should close according to Eq.(10.7). Tables 10.12 and 10.13 use the following notations:

$$\Delta V_s = \sum_0^{Z_j} \theta \Delta z \Big|_{t=2000} - \sum_0^{Z_j} \theta \Delta z \Big|_{t=800} \quad (10.8)$$

and

$$\Delta V_F = - \int_{800}^{2000} q(Z_j) dt - \int_{800}^{2000} q(0) dt \quad (10.9)$$

Table 10.12, Case 10.5, Topic 10.9: Water balance elements. Columns (2) and (3) list the volumes of fluxes, $V_F(Z_j)$, col. (4) their differences ΔV_F at Z_j ; col. (5) and (6) list the volumes of storage, $V_s(0-Z_j)$, col.(7) their differences ΔV_s .

depth Z_j (m)	volumes $V_F(Z_j)$ (mm) col.(4) and (5), Tab. 10.10, that have passed at Z_j from $[T_B = 0]$ to		ΔV_F at Z_j , column (3) - (2) (mm)	volumes $V_s(0-Z_j)$ (mm) last three lines Tab. 10.11, that have been stored down to Z_j at times		ΔV_s , column (6) - (5) (mm)
	$T_k = 800$ (s)	$T_k = 2'000$ (s)		$T_k = 800$ (s)	$T_k = 2'000$ (s)	
(1)	(2)	(3)	(4)	(5)	(6)	(7)
0.05	51.4	53.2	1.8	9.2	6.0	- 3.2
0.10	82.3	91.8	9.5	20.7	12.7	- 8.0
0.15	66.9	83.8	16.9	37.4	21.3	- 16.1
0.20	61.1	91.5	30.4	56.0	30.4	- 25.6

There are considerable deviations between the volumes of flow, ΔV_F , and the volumes of storage, ΔV_S . The latter are taken as independent references because no viscous flow impacts their calculations in contrast to the computed ΔV_F -values. Because both calculations depend on the same NEUTRA-data, the bias due to water-content recording is supposed to equally affect both sides of the balance, Eq. (10.7), thus the NEUTRA-bias is supposed to cancel out in these considerations. Further, $[\Delta q_y \approx 0]$ is assumed when the y -direction is taken perpendicular to the front and back walls of the sand box, which are just 5(mm) apart, and lateral flow, $[\Delta q_x \neq 0]$, is presumed. The deviations are listed in Tab. 10.13.

At the 0.05-m depth the computed flux volume ΔV_F is 1.4(mm) less than the change of the storage volume ΔV_S leading to a relative deviation of -44(%). This is most likely due to funnel flow from the surface to this depth, which has contributed to ΔV_S but which is not adequately picked up by drainage across this depth as Figs. (10.6) and (10.8) suggest. On the other hand, ΔV_F exceeds ΔV_S at the three lower depths by 5 to 19(%). This hints at systematic overestimations of viscous-flow rates. It is conceivable that vertical drainage of the entire finger occurs preferentially through its center part while the peripheral finger volumes not covered by the prism also drain laterally as the horizontal structures in Fig. 10.8 let suggest. However, the apparent bias deserves further attention, for instance, by varying the prism's cross-sectional area A when re-calculating the water balance. This type of analysis should also include the local variations of $\rho_b(z)$ (Fig. 10.7, *Topic 10.6*).

A closer look at the estimation of F and L may open an additional track for further investigation, particularly in view of the L -variations in *Topic 10.8*.

Table 10.13, Topic 10.9: Water balance deviations $[\Delta V_F(Z_j)+\Delta V_S(0-Z_j)=0]$. Col. (2) absolute deviations, col.(4) + col. (7) in Tab. 10.12; col. (3) relative deviations with reference to the water contents measured with NEUTRA, col. (7) in Tab.10.12.

depth Z_j (m)	deviations from Eqs.(10.5), (10.6) $[\Delta V_F(Z_j)+\Delta V_S(0-Z_j) = 0]$	
	absolute col. [(4) + (7)] from Tab.10.12 (mm)	relative col. [(4) + (7)]/(7) from Tab. 10.12 (--)
(1)	(2)	(3)
0.05	-1.4	-0.44
0.10	1.5	0.19
0.15	0.8	0.05
0.20	4.8	0.19

Nevertheless, the fundamental water balance, Eq.(10.6), which serves as objective function and the fulfilling of the accompanying objective criterion of its closing within less than 20(%) based on viscous-flow estimates applied to layers that were just 0.27(mm) thick, is viewed as experimental support of the promising approach.

10.6 Viscous-flow and dye staining

The time-depth relationship of the wetting front in viscous flow offers a tool for crude estimates of F from static dye patterns. The only parameters required are T_B , T_E , and the depth $z_w(t)$ of the dye front. If digging is fast enough, such that $[(t - T_B) < (T_I - T_B)]$, Eq.(3.8), then $[v_F = z_w(t)/(t - T_B)]$. If digging to the wetting front lasts longer, such that $[(t - T_B) > (T_I - T_B)]$, it follows from Eq.(4.19) that

$$v_F = \frac{z_w(t)}{3} \cdot \left(\frac{T_E - T_B}{2} \right)^{-2/3} \cdot (t - T_E)^{-1/3} \quad (10.10)$$

Using Eq.(2.15), from v_F follows F , which may relate to the transport of colloids and microbes (Germann et al., 1987, 2002b). However, estimates of L and q require additional information about the mobile water content w , Eqs. (8.1) to (8.5).

10.7 Summary

Chapter 10 explicates aspects of viscous flow at the profile level, which implies primarily a vertical sequence of local $\theta(t, Z)$ -time analyses. Matching of viscous flow with $\theta(t, Z)$ -time series appears successful in the cases presented although a rigorous assessment of the goodness-of-fit is still required.

The wetting front velocity, v_F , emerges as a parameter that links the local procedures with the profile level and simultaneously leads directly to the film thickness, F . Constant $v_F(z)$ and $F(z)$ indicate the evolution of cohesive WCW s as *Topics 10.1* and *10.6* demonstrate. The physical properties of permeable media like texture, ρ_b , and porosity ε , seem to have minor impact on $v_F(z)$ and $F(z)$, as demonstrated in *Topic 10.6* and in view of Figs. 10.6 to 10.8.

Moreover, constant v_F below the plow-layer in *Topic 10.1* indicates little variation of the flow-path geometry. But $L(z)$ decreasing with depth presumes the paths' continuous reduction with depth per unit volume of the entire medium. Viscous-flow logic excludes from explanation any substantial water abstraction from the WCW into the surrounding matrix because it would reduce F and v_F with depth. The only alternate explanation left is the reduction of similar flow paths that carry flow with the same constant F .

However, *Topic 10.3* demonstrates the opposite effect. A compacted layer in a soil profile completely blocked viscous flow as the water-content time series immediately above and below the layer indicate. Though considered primarily an experimental effect, a capillary fringe at the bottom of a permeable medium may interrupt viscous flow, as discussed in *Topic 10.4*.

From the juxtaposition of the *Topics 10.3* and *10.4* on one side with *Topics 10.1* and *10.6* on the other side, it may be concluded that structure is an additional but not always a mandatory property impacting viscous flow. Both, F and L evolve as parameters that completely characterize the hydrodynamics of the flow paths under the imposed initial and boundary conditions.

The depth z_{cap} , Section 3.5, Eq.(3.37), suggests the importance of the wetting-front position where it leaves the static capillary formation behind. However, estimations in *Topics 10.1* and *10.2* rend z_{cap} as negligible and the issue is not considered any further.

The initial water content of the matrix may be an important factor in the formation of *WCWs* as *Topic 10.2* with *Case 10.2* document. However, the initiation of typical viscous flow in *Topic 10.2* with *Case 10.3* and *Topics 10.6* to *10.9* seem much less affected by the initial water content, which is indicated by the decrease of L from the imbibition- to the drainage-state, Tab. 10. 9.

Matching water content profiles, $\theta(z, T)$ at specific times T with viscous flow is more involved than matching the $\theta(t, Z)$ -time series at specific depths. This is mainly due to the enormous scatter of the water content data with depth, Fig. 10.7. Nevertheless, the marked spatial variations complicate the analyses of water content profiles. The lack of data, experimental attention, and experience then become evident.

The successful water balance calculation of finger flow, *Topic 10.9*, opens a further track for viscous-flow applications. The flux integrations, based on water-content measurements in a 0.27(mm) thick sand layer, matched within at most 19(%) the water content variations in the isolated column of finger flow with lengths between 0.05 and 0.2(m). The thickness-to-length ratios in the range of 1:180 to 1:740 emphasize the filigree geometry of viscous-flow calculations that are applicable to the process scale in the range of single sand grains. On the other hand, wetting front velocities that are constant over considerable depth ranges are strong indicators for viscous-flow applicability from flow-path to system-levels without breaks in scale. Further investigation of viscous flow is required before it can be classified as a scale-independent process, although *scale-tolerance* seems here to be adequate.

Scale tolerance of viscous flow requires as the dimension of its representative spatial element REV_{visc} . Figures 2.2, and 5.1 to 5.3 suggest the local film thickness as a spatial unit in which momentum dissipation balances gravity. From the theoretical considerations and the experimental topics presented so far a REV_{visc} may extend horizontally from about 1 to 150(μ m) and vertically

to the minimum thickness of water content measurements, which may be as thin as 0.272(mm) when working with NEUTRA. Film thickness and the dimension of the instrument's control volume suffice to deal with the conductive i.e., motion-related component of viscous flow. Its capacitive i.e., storage-related component depends on the contact length L per unit of the purposefully defined cross-sectional area A of the medium. For instance, comparing *Topic 10.1* with *Topics 10.6* to *10.9* demonstrates the versatility and the restrictions of adjusting A for the investigation of particular processes and instrumental settings.

On the one hand, the minimum extent of A in *Topic 10.1* is strongly related to the horizontal dimensions of the control volume a TDR-wave guide occupies. Thus, only the ensemble of flow is recorded if the horizontal dimensions of the flow structures, like finger-flow, are considerably smaller than those of the control volume. Processes occurring in smaller volumes than the instrument's control volume have to be inferred from additional considerations. For instance, Germann et al. (2007) and Hincapié and Germann (2009) interpreted gradual increases of $\theta(Z,t)$ -time series as superpositions of rivulets. (See also Section 9.3.)

On the other hand, in the investigation of finger flow, *Topics 10.6* to *10.9*, the maximum extent of [$A = 30(\text{mm}) \times 5(\text{mm}) = 150(\text{mm}^2)$] was selected such that it is completely placed within one wetted finger. However, the volume balance calculations presumed [$Aq_x \neq 0$], which contradicts the simplifying assumption of 1-d viscous flow. Therefore, the consideration of the other two dimensions is required. Figure 10.10 shows gradual increases of water contents in the control volume of [$A \times 0.272(\text{mm}) = 41(\text{mm}^3)$], indicating substantial scatter of the wetting-front arrival even across a small A . The separation of motion from storage (v_f is only related to F , while w_s is the product of F and L) frees viscous flow from back-feeding the flow-driving force that results from transient flow. But the advantage of separating conductive properties from capacitive properties has its price: Viscous flow is purely gravity driven and excludes a priori capillary flow in the sense of Richards (1931), Sections 6.4 and 6.5.

11. Procedures at the system level

11.1 Introduction

System-level investigations consider data from volume flux density $q(Z,t)$ at some depth Z that were simultaneously collected with the associated temporal water-content variations at the profile level. The basic procedures applied at the system level include at least those introduced in *Topics 8.1, 8.2, 9.1, and 10.9*. The film thicknesses encountered so far suggest that the capillary heads acting on mobile water are to consider. Therefore, capillary-fringe effects are expected to interfere with free viscous flow in the vicinity of the interface to the atmosphere as presented, for instance, in *Topics 9.4, 10.3, and 10.4*. Notwithstanding the fundamental limitation imposed by the capillary fringe, the parameters from matching viscous flow to $[\theta(Z_j,t) \ (j = 1, N)]$ will be compared with those from matching $q(Z_{N+1},t)$. This chapter is based on the various viscous-flow aspects encountered so far, which need to be developed here only beyond the previous derivations that have been presented. The discussions pivot around data collected more than a decade ago from an infiltration-drainage experiment in the Kiel sand tank.

The data lend themselves to the exploration, at least in relative terms, of the impacts of $h_{cap}(Z_j)$ and θ_{init} on viscous flow. The parameters $L_{im}(Z_j)$, $L_{dr}(Z_j)$, the slope $[d\theta(Z_j)/dt]$ of the increasing limb, and the divergence $[\theta_{div}(Z_j) = \theta(Z_j)_{end} - \theta(Z_j)_{init}]$ characterize $\theta(Z_j,t)$ -time series at the local level, while over-all constant v_F and F suggest relationships among them across the system. The presumed relationship will be explored statistically.

11.2 The Kiel sand tank

Case 11.1: In 1996 al Hagrey et al. (1999) constructed a full-scale sand tank prototype that was more than 2(m) deep with a surface area of 2(m) by 5(m), Fig. 11.1. The tank was uniformly filled with sand in the texture range of 63 to 630(μm) such that a build-up of structural pores was avoided. Average porosity, and particle and bulk densities amounted to $[\varepsilon = 0.47]$, $[\rho_p = 2.76(\text{Mg m}^{-3})]$, and $[\rho_b = 1.47(\text{Mg m}^{-3})]$, while hydraulic conductivity at saturation was $[K_{sat} = 1.27 \times 10^{-4}(\text{m s}^{-1})]$. Two columns of tensiometers, and one column of TDR-probes were installed equally spaced at nine depths ranging from 0.2 to 1.8(m) below the surface. Among other instrumentation were two antennae of a ground-penetrating radar device, GPR, with operating frequencies of 500 and 900(MHz) which were installed horizontally. Twelve collectors at the bottom of the tank sampled drainage flow, which poured into five troughs. Collectors and troughs were embedded in a 0.2(m) thick gravel

layer that supported the 2(m) thick sand profile. In this chapter the data from the first infiltration experiment are further explored in the context of viscous flow (Germann and al Hagrey, 2008). The surface was sprinkled at in 1997 with an intensity of [$q_s = 4.33 \times 10^{-6}(\text{m s}^{-1})$] from 9 June, 12:50(h) to 10 June, 05:07(h), thus [$(T_E - T_B) = 58'620(\text{s})$] and [$V_{input} = 0.254(\text{m}^3\text{m}^{-2})$]. Sprinkling ended 720(s) after first drainage occurred. Therefore, time and depth beyond T_l and Z_l need not to be considered. Data collection lasted until 16 June, 06:19(h) i.e., 581'340(s), when the total drainage volume amounted to [$V_{tot} = 0.175(\text{m}^3 \text{m}^{-2})$]. However, the analyses are restricted here to 320'000(s), and the total drainage collected to the end of this analyses was $0.158(\text{m}^3\text{m}^{-2})$, equivalent to 91(%) of V_{tot} .

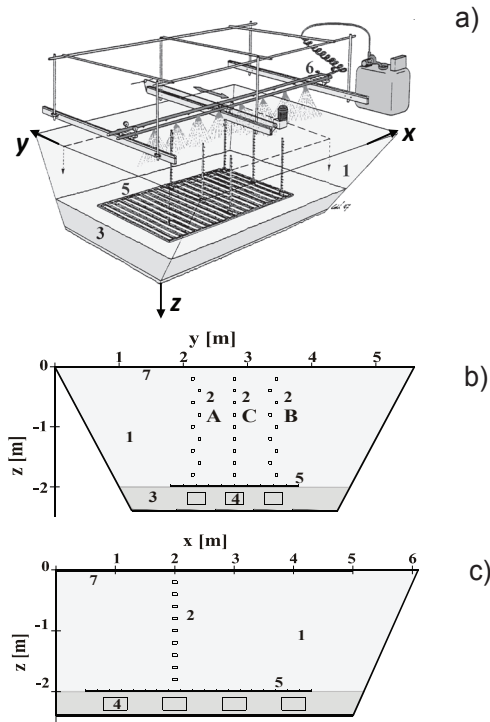


Figure 11.1, Case 11.1: Overview of the experimental set-up of the full-scale model in (a) block diagram, (b) sections yz at $[x = 2(\text{m})]$, and (c) xz at $[y = 2.8(\text{m})]$. (1) sand, (2) tensiometers, TDR sensors (profiles A, B, C), (3) filtered-gravel horizon, (4) bottom drain, (5) electrode grid, (6) irrigation system, (7) surface profile of electrodes or radar antenna. (al Hagrey et al., 1996, with permission).

11.3 Viscous flow matching to the data

Figure 11.2 presents the data: Water-content time series at nine depths, $[\theta(Z_j, t) \ (1 \leq j \leq N = 9)]$, and cumulative drainage, $V(Z, t)(m)$ collected at $[Z_{N+1} = 2.0(m)]$.

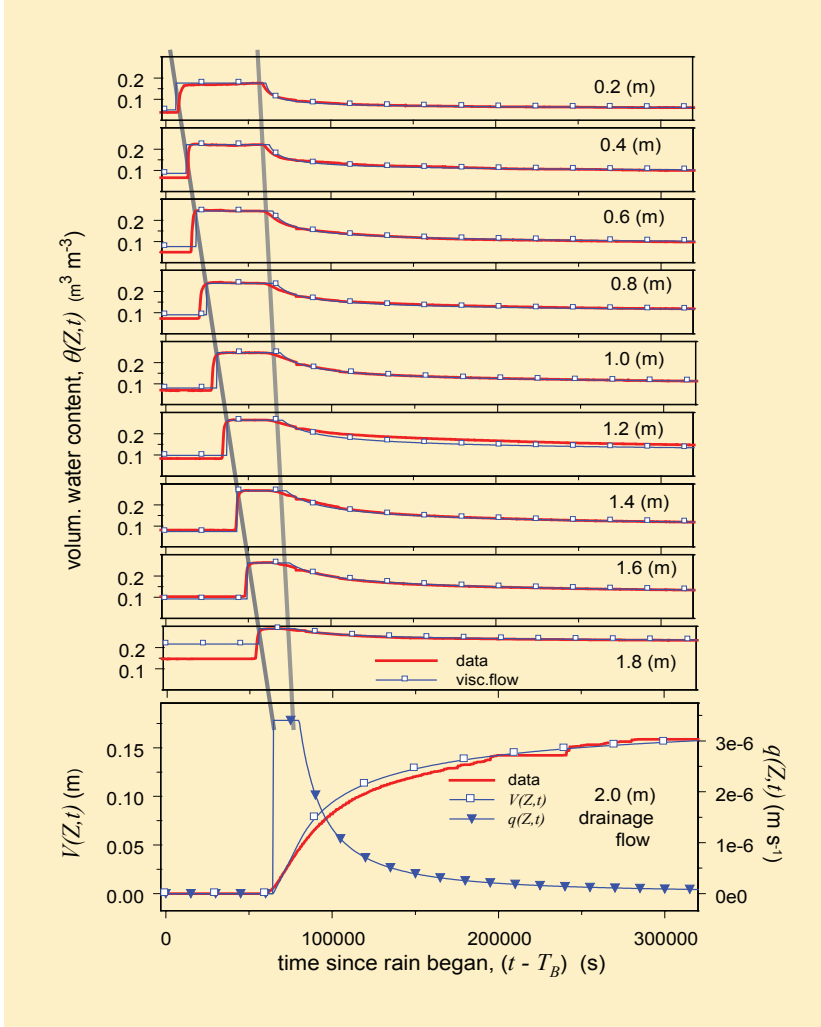


Figure 11.2, Case 11.1, Topic 11.3: Time series of TDR-water contents $\theta(Z_j, t)$ ($m^3 m^{-3}$) at nine depths and cumulative drainage $V(Z, t)(m)$ in the Kiel-sand tank. The blue lines with square symbols illustrate viscous-flow matching to the data, *Topics 11.2 and 11.3*. The volume flux density $[q(Z, t) = dV(Z, t)/dt]$ of drainage follows from the first derivative of $V(Z, t)$, Eq.(11.1), depicted in the lowest panel by the blue line with the triangles, *Topic 11.3*. The two gray lines across depth allude to the constant velocities of the wetting and draining fronts, Fig.11.3.

Topic 11.1: *Wetting front velocity v_F and film thickness F :* Figure 11.3 shows time and depth of the first water content increases that were recorded with the two GPR antennae, 18 tensiometers and nine TDR-probes. (One additional point each originates from T_B at the surface). The figure includes the three linear regressions whose parameters are listed in Tab. 11.1. They are highly significant with [$\mathcal{R}^2_{(GPR, hcap, TDR),z} = 0.99$]. However, the delay in GPR-data was about [$\Delta t = 9'500(s)$] compared with the TDR- and tensiometer-data. The GPR-delay will be discussed in *Topic 11.10*. From the constant wetting front velocity [$v_F = 3.35 \times 10^{-5}(m\ s^{-1})$] follow [$c_F = 1.005 \times 10^{-4}(m\ s^{-1})$], [$F(v_F) = 3.2(\mu m)$], and [$h_{cap}(F) = -4.7(m)$], Eq.2.21. These parameters will be applied when further analyzing *Case 11.1*.

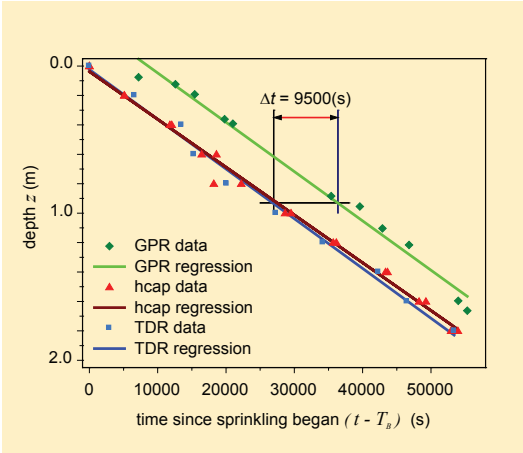


Figure 11.3, Topic 11.1: Regressions of depth vs. first recorded indication of water content increases based on GPR-, tensiometer-, and TDR-data. Wetting front velocities are [$v_F = dz_w/dt\ (m\ s^{-1})$]. The delay between the regressions of TDR- and tensiometer-readings versus GPR-readings amounts to [$\Delta t = 9'500(s)$], *Topic 11.10* and Fig. 11.6.

Table 11.1, Topic 11.1: Linear regressions of first wetting arrivals

parameter	first water content increase recorded with		
	GPR-antennae	tensiometers	TDR-probes
slope ($m\ s^{-1}$) (v_F)	3.35×10^{-5}	3.25×10^{-5}	3.38×10^{-5}
intercept (m)	-0.288	0.037	0.024
\mathcal{R}^2	0.99	0.99	0.99
N	11	20	10

Topic 11.2 *Matching profile-level $\theta(Z_j,t)$ with viscous flow:* From v_F follow arrival times [$t_w(Z_j) = Z_j/v_F$] and [$t_D(Z_j) = T_E + Z_j/c_F$], while $\theta_{end,j}$ advances to the local-level matching parameter. Further, [$L_{dr,j} = (\theta_{max,j} - \theta_{end,j})/F$] is in the range of [$2.3 \times 10^4 \leq L_{dr,j} \leq 6.1 \times 10^4(m^{-1})$]. Figure 11.2 also features viscous-flow matching with the $\theta(Z_j,t)$ -data.

Topic 11.3: *Matching cumulative drainage flow $V(Z_{N+P}, t)$ with viscous flow:* In accord with Eq.(9.4), cumulative flow as a function of time at $[Z = 2.0(\text{m})]$ is

$$V(Z, t) = F^3 \cdot L_v \cdot \frac{g}{3 \cdot \eta} \cdot \left(3 \cdot t_D(Z) - 2 \cdot T_E - t_W(Z) - 2 \cdot \frac{(t_D(Z) - T_E)^{3/2}}{(t - T_E)^{1/2}} \right) \quad (11.1)$$

where optimization of the only matching parameter yielded $[L_v = 3.3 \times 10^4(\text{m}^{-1})]$. However, best matching was achieved when the arrival of the wetting front was computationally delayed by $3'000(\text{s})$. Omission of the delay led to overestimation of matched $V(Z, t)$ at earlier times and its underestimation at later times, where further variations of L_v improved matching only marginally. Viewed from the viscous-flow concept the delay is probably due to the various horizontal fluxes in the drainage system occurring before cumulative flow was recorded at the outlet. The lowest panel of Fig. 11.2 depicts $V(Z, t)$ -matching and the back-calculated drainage flow $[q(Z, t) = d(V(Z, t)/dt)]$. It is interesting to note that the contact length of cumulative drainage lies within $[L_{dr}(1.8\text{m}) < L_v(2.0\text{m}) < L_{im}(1.8\text{m})]$ as depicted in Fig. 11.5, *Topic 11.4*. Viscous flow thus represents reasonably well the entire *WCW* at the system level. The supportive results encourage detailed discussions of measured *WCW*-features with viscous-flow arguments.

11.4 Spatial structures of viscous flow

During unhampered viscous flow a measured $\theta(t)$ -time series at depth Z_j is sufficiently characterized by the arrival time of the wetting front, $t_w(Z_j)$, the slope of the increasing water content $(d\theta/dt)(Z_j)$, and the initial, maximum, and final water contents, θ_{init} , θ_{max} , and θ_{end} . Simple relationships lead to v_F , w_F , L_{im} , and L_{dr} . Constant v_F with depth, as found in *Case 11.1*, implies that also F remains constant which indicates a cohesive *WCW*. Here the spatial structures of the parameters that characterize viscous-flow are explored.

Case 11.1. (continued): The initial conditions of capillary heads and water contents set the stage for further analyzing infiltration. The topics below illustrate the *IC*'s impact on viscous flow.

Topic 11.4: *Initial $\theta_{init}(Z_j)$ and $h_{cap,init}(Z_j)$ vs. depth:* Figure 11.4 depicts the depth-distributions of the *IC*; $h_{cap,init,A}(Z_j)$ and $h_{cap,init,B}(Z_j)$ refer to the tensiometer recordings in columns A and B, Fig. 11.1, while $h_{cap,init,A+B}$ represents their amalgamation. Hydrostatic initial conditions are achieved when the capillary head-gradient compensates the gravity gradient, $[dh_{cap}/dz = -dh_G/dz = -1]$, as indicated in Eq.(6.16) (Richards, 1931) and

with the slanted dashed gray line in Fig. 11.4. Hydrostatic conditions prevail between the 1.4- and the 1.8-m depths as shown with the rectangle in Fig. 11.4. The systematic deviations of $h_{cap,init}(Z_j)$ from hydrostatic distribution between the 1.4-m depth and the surface, in particular the prominent deviation at the 0.4-m depth, are due to infiltration of unexpected rain of undisclosed duration and intensity during packing. On the one hand, the deviations from hydrostatic IC do not allow for an unambiguous initiation of the experiment. On the other hand, the deviations lend themselves to the testing of viscous-flow against one set of realistic initial conditions. Nature rarely provides ideal initial conditions.

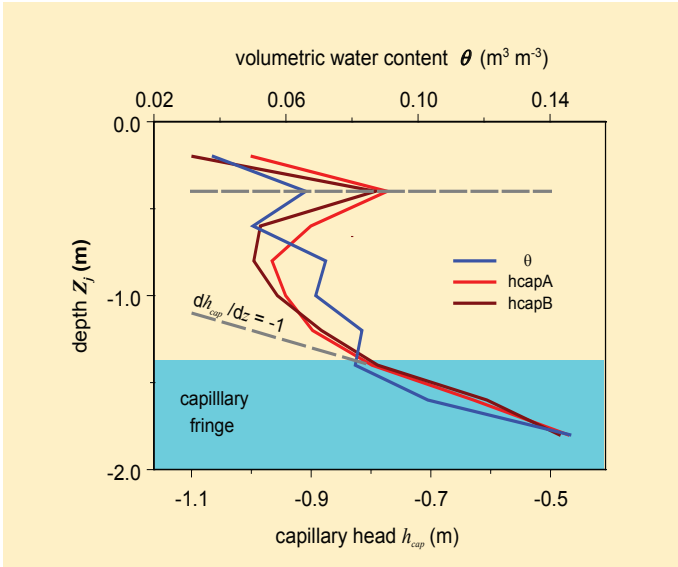


Figure 11.4, *Topic 11.4:* Volumetric water content θ_{init} (m^3m^{-3}) and capillary heads $h_{cap,init}$ (m) vs. depth prior to infiltration. The horizontal gray dashed line at the 0.4-m depth points to deviations due to rain during sand-tank packing. The slanted gray dashed line shows the capillary gradient at hydrostatic conditions and the light-blue rectangle indicates the hydrostatic capillary fringe prior to infiltration.

Also to be taken into account is that $[h_{cap}(F) = -4.7(\text{m})]$ is considerably inferior to the minimum of $[h_{cap,init} = -1.1(\text{m})]$, the consequences of which are discussed in *Topic 11.9*. The hydrostatic depth range from 1.4 to 1.8(m) coincides with the capillary fringe. Hence, linear correlations and regressions in the following analyses of parameters vs. depth are only applied to the range of 0.2 to 1.4(m), yielding just 5 degrees of freedom (d.f.). The two positive correlation coefficients according to Tab. 11.2 amount to $[\mathcal{R}_{\theta,init,z} = 0.83]$, which is significant at the 1(%)-error threshold, and $[\mathcal{R}_{h_{cap,init},A+B,z} = 0.41]$, which is not significant despite the higher number of d.f., but both, $\theta_{init}(Z_j)$ and $h_{cap,init}(Z_j)$ increase with depth.

Topic 11.5: *Spatial structure of $L_{im}(Z_j)$ and $L_{dr}(Z_j)$:* L represents the surface area per unit volume of the permeable medium onto which momentum dissipates (Fig. 2.2). If v_F is constant with depth then L is also a measure of the mobile water content [$w_F(Z_j, t) = F(v_F) L(Z_j)$] during [$t_w(Z_j) \leq t \leq t_D(Z_j)$]. Decreasing L with depth in *Topic 10.1* assumed a decreasing extent of similar viscous flow paths, while *Topic 10.4* discussed the restriction expected when capillary fringes interfere with unhampered viscous flow. Both topics illustrate L -variations with depth, albeit with a constant v_F . In addition, from *Topic 9.3* it follows that [$L_{im} > L_{dr}$] as a consequence of water content divergence [$\theta_{div} = \theta_{end} - \theta_{init} > 0$]. Thus, the following discussion considers L_{im} and L_{dr} separately. Figure 11.5 shows both contact lengths increasing with depth. The trend reverses at the 1.4-m depth which is ascribed to the capillary-fringe effect, which coincides with the results in *Topic 11.4*, Fig.11.4. The impact is plausible vis-à-vis [$F = 3.1(\mu\text{m})$] and [$h_{cap}(F) = -4.7(\text{m})$].

Table 11.2 lists the statistically significant and positive linear correlation coefficients of L_{im} and L_{dr} vs. [Z_j ($j = 1.. 7$)] with [$\mathcal{R}_{im,z} = 0.71$] and [$\mathcal{R}_{dr,z} = 0.88$], while [$dL_{im}/dz = 1.5 \times 10^4(\text{m}^{-2})$] and [$dL_{dr}/dz = 1.0 \times 10^4(\text{m}^{-2})$]. The correlations with considerable [$\mathcal{R} < |1|$] leave margins for alternate interpretations of $L_{im}(Z_j)$ and $L_{dr}(Z_j)$. Notwithstanding the uncertainties arising from the fringe, it is worth noting that L_v , calculated by independently matching viscous flow with cumulative drainage, *Topic 11.3*, lies within [$L_{im}(1.8\text{m}) > L_v(2.0\text{m}) > L_{dr}(1.8\text{m})$]. The numerical order suggests a functional decrease of L from imbibition to drainage. However, additional theoretical and experimental investigations are required to substantiate the process behind the observed order.

parameter	$\mathcal{R}_{par,z}$	d.f.	topic
θ_{init}	0.83 ^{*)}	5	11.4
$h_{c,init,A+B}$	0.41	12	11.4
L_{im}	0.71 ^{*)}	5	11.5
L_{dr}	0.88 ^{*)}	5	11.5
θ_{div}	-0.58	5	11.6
$d\theta/dt$	-0.37	5	11.7

Table 11.2, Topics 11.4, 11.5: Coefficients of linear correlations $\mathcal{R}_{par,z}$ of viscous-flow parameters vs. depths [$Z_j = 0.2 ..1.4(\text{m})$].

^{*)} and ^{**) indicate significance at the 5(%)- and 1(%)-error limit of the one-sided test, and d.f. is degrees of freedom.}

Topic 11.6: *Spatial structure of θ_{div} :* Under the premise of constant v_F water content divergence amounts to $[\theta_{div}(Z_j) = F(L_{im}(Z_j) - L_{dr}(Z_j))]$. The correlation of θ_{div} with depth in the 0- to 1.4-m range yields an insignificant but negative $[\mathcal{R}_{div,z} = -0.58]$. The two converging regression lines in Fig.11.5 illustrate the decrease of $\theta_{div}(Z_j)$ with depth.

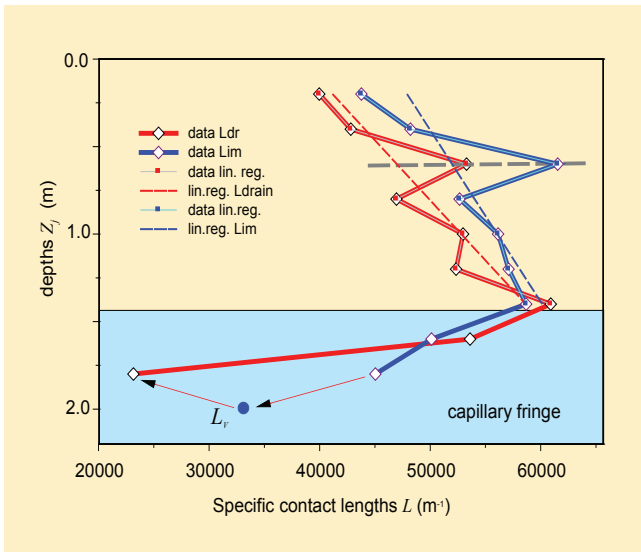


Figure 11.5, *Topics 11.5, 11.6:* Specific contact lengths vs. depth, $L_{im}(Z_j)$ and $L_{dr}(Z_j)$, showing data and linear regressions applied to the upper seven levels. The grey dashed line indicates the strongest deviations from the general trend at the 0.6-m depth. Note that $[L_{im}(1.8\text{ m}) > L_v(2.0\text{ m}) > L_{dr}(1.8\text{ m})]$, while the arrows to and from L_v suggest a sequence worth further investigation.

Topic 11.7: *Spatial structure of the slopes $(d\theta/dt)(Z_j)$ of imbibition limbs:* Topic 8.2 introduces the gradual temporal water content increase during the passing of a *WCW* that contradicts pure viscous-flow expectations. Topic 10.7 presents similar observations from sand layers that were only 0.27(mm) thick. The gradual increase is thought to be due to local flow-path variations at such short vertical distances that the still constant v_F emerges at the profile level. The following analysis alludes to the frequently observed sections with linear water content increases as shown in Fig.9.1, Topic 9.1.

The depth variations of the increasing linear $[(d\theta/dt)(Z_j)]$ -sections of the nine $\theta(Z_j,t)$ -time series, Fig. 11.2, will now be analyzed. Their linear correlation with depth yields $[\mathcal{R} = -0.37]$ which is not significant. On the one hand, this indicates their decrease with depth. On the other hand, the weak correlation indicates that the flow-path variations within the ensemble of the tiny streams composing the *WCW* are weakly correlated over distances distinctly longer than the spacing of the TDR-wave guides which is 0.2(m) in Case 11.1. The

results support the notion of a spatio-temporal cohesive *WCW* in the sense of viscous flow that persists over a distance of 2(m). Thus, a *WCW* is indeed a hydrodynamic entity rather than just a random assemblage of individual flow paths each with its own characteristics that conveniently show some local viscous-flow properties.

Table 11.3, Topic 11.8: Coefficients of linear correlations \mathcal{R} between initial capillary heads $h_{cap,init\ A,B}$ and initial water content θ_{init} vs. viscous-flow parameters.

viscous-flow parameter	Coefficient \mathcal{R} of linear correlation with			
	$h_{cap,init,A}$	$h_{cap,init,B}$	$h_{cap,init,A+B}$	θ_{init}
θ_{init}	0.50	0.75 ^{*)}	0.63 ^{*)}	1.00 ^{**)}
L_{im}	0.24	0.32	0.28	0.44
L_{dr}	0.35	0.47	0.41	0.57
θ_{div}	-0.32	-0.43	-0.37	-0.41
$d\theta/dt$	0.77 ^{*)}	0.67 ^{*)}	0.69 ^{**)}	0.26
d.f.	5	5	12	5

^{*)} and ^{**)} significance at the 5(%)- and 1(%)-error limit, respectively, of the one-sided test.

Topic 11.8: Impacts of $h_{cap,init}(Z_j)$ and $\theta_{init}(Z_j)$ on the viscous-flow parameters: Table 11.3 lists the coefficients \mathcal{R} of correlating various viscous-flow parameters with initial capillary heads $h_{cap,init,A}$, $h_{cap,init,B}$, and $h_{cap,init\ A+B}$. Again, the correlation calculations considered only the 0.2- to 1.4-m depths to avoid capillary fringe effects.

All the correlations support the expected trends, however, not very strongly. Decreasing L_{im} , L_{dr} , and $d\theta/dt$ with decreasing $h_{cap,init}$ demonstrate that water abstraction from the *WCW* is due to local capillary gradients, though neither in a statistically significant nor physically viscous-flow disturbing way as, for instance, constant $v_F(Z_j)$ clearly demonstrates. The decrease of θ_{div} with increasing $h_{cap,init}$ supports the other statements as the gradients of h_{cap} get stronger along more negative $h_{cap,init}$, leading to increased abstraction and diversion. However, water abstraction θ_{div} from the *WCW* is weakly correlated with $h_{cap,init}$ in *Case 11.1*, but with only minor effects on viscous flow as *Case 10.2* suggests.

All the examples demonstrate that, on one hand, viscous flow affects the capillary heads. On the other hand capillary heads do not drive viscous flow, *Case 11.1*, but they may induce abstractions that are strong enough

to completely annihilate viscous flow. *Case 11.1* demonstrates for a sandy substrate that viscous flow at the system level dominates over local processes like water abstraction due to capillary gradients. The result is in contrast to *Case 10.2*, which dealt with infiltration in a poorly structured loam-textured Chernozem, when capillarity completely absorbed water from the first of five consecutive infiltration runs, but with only a gradual emergence of viscous flow. The contrasting results of the two cases hint at the effect of texture on viscous flow in the absence of structural pores. The initial conditions seemed to have little effect on viscous flow in a structured silty clay-loam, as reported in *Case 10.3*. It is concluded that the effects of both structure and texture need to be considered when a priori assessing a soil's susceptibility to viscous flow.

Topic 11.9: *Delay of GPR-readings:* Figure 11.3 shows a delay of $[\Delta t = 9'500(s)]$ in the wetting-front arrivals determined from GPR-data with respect to the wetting-front arrivals from tensiometer- and TDR-measurements. The delay is also marked on the h_{cap} -time series at the 0.6-m depth in Fig. 11.6, suggesting that h_{cap} has to attain a certain steady state before the GPR-measurements can record maximum soil moisture. The delay thus suggests an impact by the surface tension of the water on the GPR-signal in addition to the impact of the water content.

11.5 Capillary heads h_{cap}

The capillary head h_{cap} , Section 2.5, is an important property of water in unsaturated permeable media. The approximate range of film thicknesses $[1 \leq F \leq 100(\mu m)]$ encountered so far suggest viscous flow under the influence of some capillary head in the range of $[-7.4 \leq h_{cap}(F) \leq -0.074(m)]$ that cannot be ignored. Moreover, Richards (1931), Section 6.4, Eqs.6.15 and 6.16, elevates the gradient of h_{cap} to the major driving force of capillary flow.

Topic 11.10: *Capillary heads h_{cap} during viscous flow*

Case 11.1 (continued) offers the opportunity to study tensiometer-monitored h_{cap} during viscous-flow infiltration. Figure 11.6 depicts time series of $h_{cap}(Z_j, t)$ at $[Z_j = 0.2, 0.6, 1.0, 1.4, 1.8(m)]$. Their shapes are strikingly similar to $\theta(Z_j, t)$ as, for instance, the upper panels of Fig.11.2 demonstrate: The sharp increases represent the arrivals of the h_{cap} -pressure front which coincides with the first arrivals of the wetting shock front. The coincidence supports the early advancement of the WCW prior to T_i and also the basic assumption of a discontinuous wetting front leading to Eqs.(2.15) and (4.5). Moreover, the $h_{cap}(Z_j, t)$ -series evolve during $[t_w(Z_j) \leq t \leq t_D(Z_j)]$ to steady state at about $[h_{cap}(w) \approx -0.25(m)]$, indicating a connection of the WCW and atmospheric pressure. Finally, the concave declines approach asymptotically the terminal heads of $h_{cap}(\theta)$. Further interpretation similar to the $\theta(Z_j, t)$ -time series as,

for instance, introduced in *Topic 9.6* and Fig. 9.6, is not pursued because the corresponding theoretical base is lacking at the present.

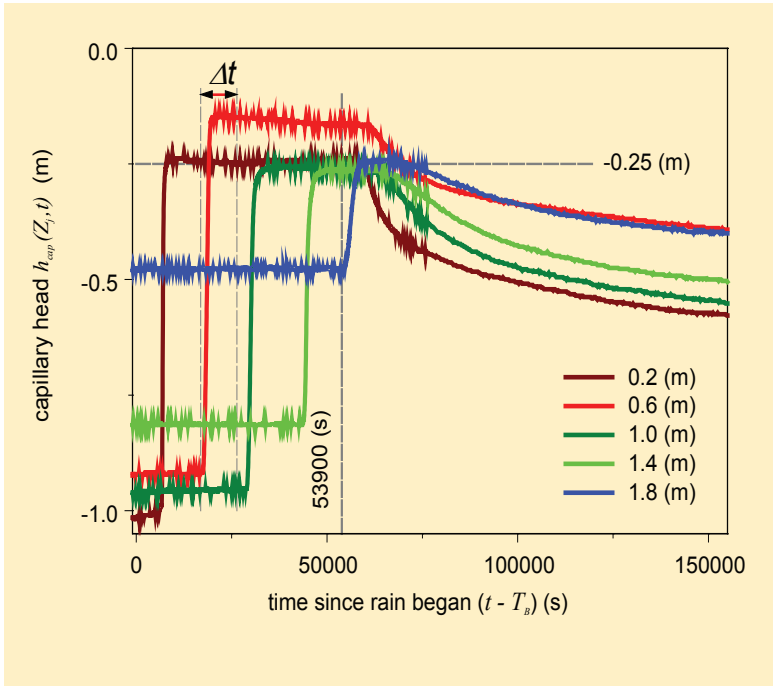


Figure 11.6, Topics 11.9, 11.10: Time series of capillary head $h_{cap}(Z_j, t)$ at depths of $[Z_j = 0.2, 0.6, 1.0, 1.4, 1.8(\text{m})]$. Also shown are the end time of the h_{cap} -profiles at 53'900(s) and the encountered plateaus at $[h_{cap}(w) = -0.25(\text{m})]$, Fig. 11.7; $[\Delta t = 9'500(\text{s})]$ indicates the delay of GPR-regression with respect to TDR- and h_{cap} -regressions of first water content increases, Fig. 11.3.

The arrival times of first h_{cap} -increases vs. depth were already presented in Fig. 11.3, and the linear-regression coefficients in Tab. 11.1 show close agreement between $t_w(Z_j)$ and the arrival times of the h_{cap} -fronts. Figure 11.7 illustrates h_{cap} -profiles

- (i) prior to infiltration, profile (1), representing the initial state of $h_{cap}(Z_j)$;
- (ii) at 53'900(s), profile (2), before input was interrupted at 58'620(s) referred to as final state of $h_{cap}(Z_j)$; and
- (iii) at 26'000(s), profile (3), as a state representing transitions.

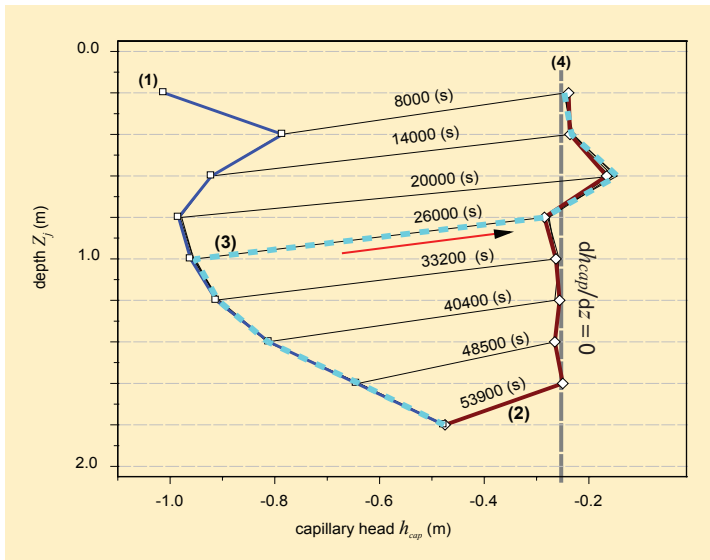


Figure 11.7, Topic 11.10: Profiles of capillary heads, $h_{cap}(z, T_k)$ at times $[T_k = 8'000, 14'000, 20'000, 26'000, 33'200, 40'400, 48'500, 53'900(\text{s})]$.

Profile (1), solid blue line: $[h_{cap,init} = h_{cap}(\theta)]$ at $[t < T_B]$;

Profile (2), solid red line: $h_{cap}(z)$ at $[t = 53'900(\text{s})]$;

Profile (3), cyan dashed line: $h_{cap}(z)$ at $[t = 26'000(\text{s})]$. The arrow points in the direction of snapping during the passing of the wetting front.

Profile (4), vertical gray dashed line, indicates $[dh_{cap}/dz = 0]$ at $[h_{cap}(w) = -0.25(\text{m})]$.

(See also Figs. 11.4 and 11.6 for comparison.)

Profile (3) gives the impression of h_{cap} -snapping from the initial $h_{cap}(\theta)$ to the final state $h_{cap}(w)$ during the passing of the WCW 's wetting front in the time frame of $[t_w(Z_j) \leq t \leq t_w(Z_{j+1})]$. The fast transitions do not support sequential flow when smaller pores have to gradually fill before larger ones may conduct water. Moreover, with the exception of the 0.6-m depth, profile (2) suggests $[dh_{cap}/dz = 0]$ at $[h_{cap}(Z_j) \approx -0.25(\text{m})]$ indicating the cessation of vertical capillary flow behind the wetting front during $[t_w(Z_j) \leq t \leq t_D(Z_j)]$. The capillary gradient of $[dh_{cap}/dz = 0]$ strongly, though only by its absence, supports the basic assumption that ubiquitous gravity exclusively drives viscous flow, Fig. 2.2 and Eq.(2.9). Although $[h_{cap}(Z_j) \approx -0.25(\text{m}) < 0]$ is less than zero, it is quasi-constant with depth. Also, compare with Eq.(6.16).

The heads $h_{cap}(Z_j)$ measured behind the wetting front of the passing WCW differ markedly from the one presumably acting in the water film of $[h_{cap}(F) = -4.7(\text{m})]$. The latter seems to turn into a state variable of the film apparently with little effect on its motion. Concepts such as saturation overshoot according to Di Carlo (2004) and dynamic potentials, such as Hassanizadeh et al. (2002) have proposed, might here come to mind.

11.6 Summary

After due calibration viscous flow at the system level matched well with the infiltration- and drainage-data recorded in the Kiel sand tank. Observed constant v_F vs. depth results in a constant F at the system level, while $L(Z_j)$ appeared as the only free parameter capable of matching viscous flow with the temporal variations of both, $\theta(Z_j, t)$ and $q(Z_{N+1}, t)$ at the local level. In addition, analyses of imbibition and drainage require separate matching due to water abstraction from the *WCW*. The depth-distribution of initial h_{cap} strongly indicates a capillary fringe below the 1.4-m depth whose effect on viscous flow presently remains shrouded, while the intriguing sequence of $[L_{dr} < L_v < L_{im}]$ suggests a functional transition. Despite the non-stationary *ICs*, $h_{cap}(Z_j)$ snapped to a narrow range of $[-0.25 < h_{cap}(Z_j) < -0.2(\text{m})]$ in the intervals of $[t_w(Z_j) < t < t_D(Z_j)]$, clearly demonstrating that viscous flow overrides capillary flow during infiltration.

The role of h_{cap} in the *WCW* during viscous flow remains obscure. On one hand, from v_F results $[h_{cap}(v_F) = -4.7(\text{m})]$. On the other hand, $h_{cap}(Z_j)$ is much closer to the atmospheric pressure but still negative behind the wetting front, including in the capillary fringe. Moreover, $[h_{cap}(F) < h_{cap}(Z_j)]$ indicates independence of the two potentials, while $[h_{cap}(Z_j) < 0]$ leads to speculations about dynamic effects in the $h_{cap}(\theta)$ -relationship as, for instance, Hassanizadeh et al. (2002) have suggested. In general, the discussions demonstrate the need of including h_{cap} -measurements in future studies of viscous flow.

On one hand, the slopes $d\theta/dt$ of the increasing limbs of $\theta(Z_j, t)$ are positively and significantly correlated with $h_{cap, init}$ (Tab.11.3), meaning that the slopes get flatter with stronger capillary gradients. This is in accord with the negative but insignificant correlation of θ_{div} vs. $h_{cap, init}$. On the other hand, the slopes decrease with depth (Tab. 11.2), though statistically not significantly. Taken alone, this fact hints at flow paths with individual film thicknesses that persist over distances longer than the spacing of the TDR-probes of 0.2(m). However, the data and the analyses cannot settle the apparent controversy. Both arguments seem valid: increasing abstraction from the *WCW* due to increasing capillary gradients as well as flow paths with individual wetting front velocities persisting over a considerable depth range. Topic 10.7 supports the argument of the dominant local abstraction in that the gradual increase of $\theta(Z_j, t)$ occurs even in a sand layer that is just 0.27(mm) thick. However, the observations of Selker et al. (1992) favor the individual-path argument. From an infiltration experiment in a 0.5(m) wide sand box they reported wetting front velocities of five individual fingers in the range of $[3.1 \leq v_F \leq 4.4 \times 10^{-3}(\text{m s}^{-1})]$.

$[\mathcal{R}_{h_{cap,init}, \theta_{init}} = 0.5, 0.75, 0.63]$ are the results of the correlations of $h_{cap,init,A,B}$ vs. θ_{init} , *Topic 11.8*. They depend on the tensiometer data included in the statistical analyses listed in Tab. 11.3. The correlations represent sections of retention curves $h_{cap}(\theta)$, Section 2.5, and are considered not very strong, thus ultimately not very useful, at the system scale. The retention curves are pivotal in the Richards (1931) equation, Eq. (6.16), but appear here to be only of local applicability. Schmalz et al. (2003) modeled with the Richards-equation based HYDRUS-2D code the same infiltration and drainage data as presented in *Case 11.1*. In view of the discussions in Sections 6.4 and 6.5, their conclusion is not surprising that

None of the simulation approaches studied reproduced both the measured water balance and the observed flow behavior exactly.

12. Procedures at the flow-path level

12.1 Introduction

So far, local procedures, as described Chapters 8 and 9, present the smallest units of viscous-flow application to permeable media. Typical lengths of both, the instrumentations and the permeable media, to which the basics were applied in Chapters 8 to 11 range from $3 \times 10^{-4}(\text{m})$, *Case 10.5*, to $2(\text{m})$, *Case 11.1*. However, the theoretical base, Chapters 2 to 5, conforms to film thicknesses in the range of about $[2 \times 10^{-6} \leq F \leq 10^{-4}(\text{m})]$. Generally, there is no direct benefit in comparing process scales with system scales but their ratios ranging from $[1:3]$ to $[1:10^6]$, as encountered here, deserve further attention. The flow geometries discussed in Chapter 5 were treated in a rather simplistic way. Only corner-flow according to Tuller and Or (2001), and as presented in Section 5.4, points vaguely at this lacuna lying between theory and reality, to be crossed once methods become available for routine investigations of flow at the pore scale. The presumed lacuna notwithstanding, approaches are available for the assessment of the plausibility of viscous-flow at the pore scale. However, plausibility demonstrates at its best the absence of contradictions between observation and approach but by no means is it proof of viscous-flow's general applicability to permeable-media flow.

Section 12.2 demonstrates superposition of kinematic waves with an unusual liquid. Section 12.3 assesses the plausibility of viscous-flow's spatial dimensions in non-structured permeable media, while flow between the *AWI* and *SWI* is scrutinized in Section 12.4, and the considerations offered in Section 12.5 attempt to establish the relationships between viscous flow and the various capillary heads encountered so far.

12.2 Superposition of kinematic waves - Lorin's candle

Superposition of kinematic waves produces a composite kinematic wave that is amenable to the same rules as introduced in Chapters 3 and 4, and demonstrated with the trailing waves in Section 9.2. The following topic concentrates on the shape of a composite kinematic wave after T_l .

Topic 12.1: *Applicability of viscous flow to superimposed kinematic waves:*

The expression

$$w(z, \tau_2) = \left(\frac{\eta}{g} \right)^{1/2} \cdot L \cdot z^{1/2} (\tau_2 - T_E)^{-1/2} \quad (3.23)$$

represents the *WCW*-profile at times $[t > T_l]$ which also applies to superimposed kinematic waves, Section 4.7.

Case 12.1: *Lorin's hand-drawn candle:* I received from my grandson Lorin a hand-drawn candle, Fig. 12.1a. He proudly told me how he drowned the wick in a bath of liquid wax, pulled it out of the puddle, and let it drain before its submergence in cold water. Using differently colored wax, he repeated the procedure time and again until he thought the accumulated layers thick enough to qualify for grandpa's candle. Actually, young Lorin sculptured with wax a cylindrical equivalent of a kinematic wave by superimposing numerous viscous layers before their hardening. Each time he pulled the candle-to-be out of the wax-baths the newly acquired layer released a draining front at the top, eventually forming the rotational equivalent of the vertical mass distribution as Figs. 3.2 and 10.11 illustrate.

Reduction of Eq.(3.23) to the candle's radius $RC(z)$ with respect to its length z leads to

$$RC(z) = WX \cdot (z_0 - z)^{1/2} \quad (12.1)$$

where z_0 (m) is an arbitrary reference level and WX ($\text{m}^{1/2}$) lumps together all the coefficients and parameters not considered in detail, thus WX and z_0 are the two unknowns in the description of the candle's shape. The two points on its surface selected for calculating the two unknowns WX and z_0 are

$$\begin{aligned} RC(z_1) &= 4.25(\text{mm}) \quad \text{at} \quad z_1 = 140(\text{mm}) \\ RC(z_2) &= 8.40(\text{mm}) \quad \text{at} \quad z_2 = 80(\text{mm}) \end{aligned}$$

The two expressions resulting from applying Eq.(12.1) to the data yield $[WX = 0.935(\text{mm}^{1/2})]$ and $[z_0 = 160.6(\text{mm})]$. The linear regression of $RC(z)$ vs. $z^{1/2}$ applied to a total of seven $RC(z_j)$ -data pairs representing the candle's surface yields $[\mathcal{R}^2 = 0.984]$ which is considered a comfortable confirmation of matching Eq.(12.1) to the surface of Lorin's candle as Fig. 12.1b demonstrates.

The quality of matching depends on the data as well as on the underpinned model assumptions. Two types of uncertainties evolve:

- (i) model validity
- (ii) data reliability that is due to adherence to the experimental protocol and instrument precision.

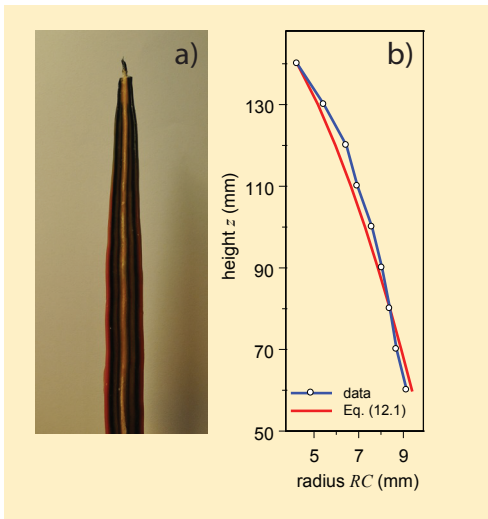


Figure 12.1, Topic 12.1:
Superposition of kinematic waves

a: Cut along Lorin's candle showing the wick and five layers of wax in red, dark blue, olive, dark blue, and yellow (there were many more fine laminae within the same colored layer).

b: Radius of Lorin's candle vs. length, data and results of applying Eq.12.1. Scale in the vertical differs from the horizontal.

Improvement of model validity basically falls in two approaches. The first approach embraces the inclusion in the analysis of as many thinkable basic processes followed by a gradual elimination of those showing lesser impacts on the particular data set. The other approach adds empirical parameters to the basic relationship with subsequent repetition of the smoothing procedure until the approach matches the data within preset limits. Today's computational facilities support both approaches, resulting in either conceptual, perceptual or empirical models.

Improvement of data reliability typically clings to the increase of the number of data, resulting in highly over-determined sets of equations that call for statistical smoothing like regression procedures. In conclusion, the simple analysis indicates that Eq.(12.1), based on Eq.(3.23), explains reasonably well the shape of Lorin's candle. However, there is guarantee of neither the equation's a priori applicability to any other hand-drawn candle nor of proving superposition of *WCWs*.

12.3 Plausibility of v_F and L in unconsolidated sands

Preferential flow is frequently associated with soil macropores. Beven and Germann (2013) question the presumed mandatory relationship between macropores and preferential flow as, for instance, Beven and Germann (1982) had earlier put forward. Similarly, *Case 8.1* demonstrates that the artificial macropores did not carry substantial viscous flow.

Visible macropores in permeable media are at least 0.1(mm) wide. They thus qualify as paths for preferential flow in the sense of viscous flow with

$[F < 0.12(\text{mm})]$. However, the plausibility of the parameter's extent has to be demonstrated during viscous flow in non-consolidated sands and similar permeable media when those macropores are purposefully absent as in the *Cases 10.5* and *11.1*. Likewise, specific contact lengths exceeding about $[L > 50(\text{m m}^{-2})]$ do not necessarily correspond to the common perception of soil macropores, which suggests these should be scrutinized.

Topic 12.2: *Theoretical assessment of viscous flow dimensions with a glass-bead model:* Equal spheres with radius $R(\text{m})$ are to represent the particles in the model-medium, where spheres are packed in a simple-cubic arrangement. Figure 12.2 depicts an areal unit in a horizontal cut across the medium whose constant porosity amounts to

$$\varepsilon = 1 - \frac{1}{8 \cdot R^3} \cdot \frac{4 \cdot R^3 \pi}{3} = 1 - \frac{\pi}{6} = 0.476 \quad (12.2)$$

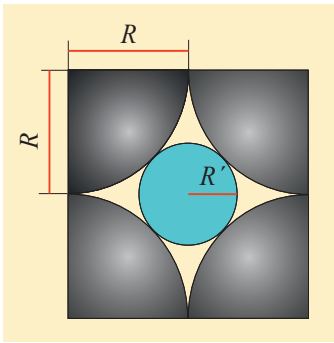


Figure 12.2, *Topic 12.2:* Horizontal areal unit of simple-cubic packing of spheres with radii R and the inscribed vertical cylinder with radius R' .

The largest cylinders fitting vertically between the spheres shall represent the paths of viscous flow. According to Fig.12.2 their radii are

$$R' = R \cdot (\sqrt{2} - 1) \quad (12.3)$$

and their number per cross-sectional area amounts to

$$N_{cyl} = \frac{1}{4 \cdot R^2} \quad (12.4)$$

(m^{-2}) . Like ε , the mobile water content in all cylinders is independent of R and amounts to

$$w_{cyl} = N_{cyl} \cdot R'^2 \cdot \pi = \frac{\pi}{4} \cdot (3 - 2 \cdot \sqrt{2}) = 0.135 \quad (12.5)$$

The specific contact length of the paths per unit area results from

$$L(R) = N_{cyl} \cdot 2 \cdot \pi \cdot R' = \frac{\pi}{2 \cdot R} \cdot (\sqrt{2} - 1) \quad (12.6)$$

The combination of Eqs.(5.15) with (12.3) yields the wetting front velocity within a cylinder as

$$v_F(R) = (3 - 2 \cdot \sqrt{2}) \cdot \frac{R^2 \cdot g}{8 \cdot \eta} \quad (12.7)$$

Figure 12.3 depicts Eqs.(12.6) and (12.7) on logarithmic scales. The figure includes the minima and maxima of all v_F and $L(w)$ reported in Chapters 8 to 11.

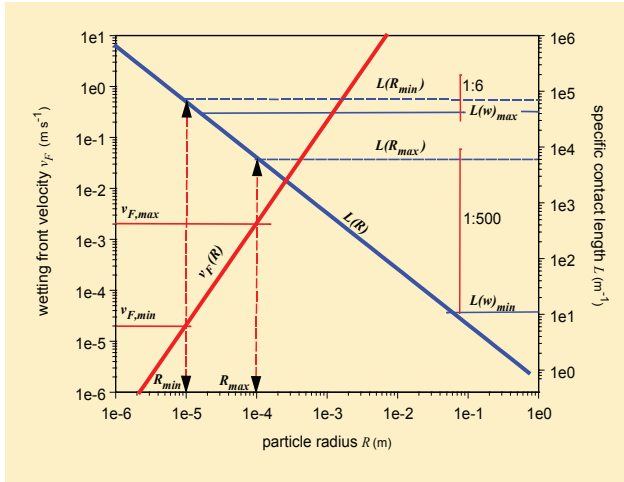


Figure 12.3, Topic 12.2: Illustration of $L(R)$ and $v_F(R)$, Eqs.(12.6) and (12.7); $v_{F,max}$, $v_{F,min}$, $L(w)_{max}$, and $L(w)_{min}$ follow from data presented in Chapters 8 to 11; the arrows indicate estimates $L(R_{max})$ and $L(R_{min})$ that correspond to $v_{F,max}$ and $v_{F,min}$. The ratios of $L(w)$ to $L(R)$ of 1:6 and 1:500 are indicated.

The figure also presents the steps taken in the plausibility assessment:

- (i) estimation of $R(v_F)$, yielding R_{min} and R_{max}
- (ii) estimation of $L(R_{min})$ and $L(R_{max})$ as the two dashed arrows indicate.

From $[L(w)_{max} / L(R_{min}) = 1/6]$ and $[L(w)_{min} / L(R_{max}) = 1/500]$, and based on the assumptions implied in the model it is concluded that:

- (i) Spherical particles with radii as small as $[R_{min} = 10^{-5}(\text{m})]$, which are particles of the silt fraction, may retain textural voids between them that are wide enough to carry viscous flow.

- (ii) Not all possible flow paths in the model were occupied during viscous flow because $[L(w)_{max} < L(R_{min})]$. Mass Balance requires a concentration of flow paths which points towards the formation of finger flow.

Note the tendency of flow path concentration, like finger flow, to increase with increasing radii of the modeled particles, which the decrease of the L -ratios from 1/6 to 1/500 suggests. This demonstrates once again that ‘macropores’ as commonly understood are not required for the evolution of viscous flow in permeable media.

Case 9.3 (continued): *Support from infiltration into artificial permeable media:* As mentioned, Shizowa and Fujimaki (2004) performed infiltration experiments in porous media made of glass beads with radii of $10^{-4}(\text{m})$. From their reported wetting front velocities of $[v_{F1} = 2 \times 10^{-4}(\text{m s}^{-1})]$ and $[v_{F2} = 2 \times 10^{-5}(\text{m s}^{-1})]$ follow $[F(v_1) = 8 \times 10^{-6}(\text{m})]$ and $[F(v_2) = 2.5 \times 10^{-6}(\text{m})]$. According to Eq.(12.3) the radii of the theoretical paths were $4 \times 10^{-5}(\text{m})$ which easily carry viscous flow with the estimated film thicknesses if packing is assumed similar to Fig. 12.2.

Topic 12.3: *Tortuosity* deals with the deviation of the flow path geometry from straight vertical lines as presumed, for instance, in Fig. 12.2. Hillel (1998) defines

ξ , the tortuosity factor, is an empirical parameter smaller than unity, expressing the ratio of the straight-line length of a soil sample to the average roundabout path length through the water filled pores .

Case 10.5 (continued): *Tortuosity during finger flow:* Hincapié and Germann (2010), while assessing the plausibility of $L(w)$ in isolated finger flow, replaced in their estimates the largest and smallest sand particles with ideal spheres with diameters of 0.2 and 0.5(mm). They further calculated the specific surface areas of the spheres per unit volume of the packed sand at the average bulk density as well as at its two limits of $[\pm 1(\text{stdv})]$, Fig. 10.7. The specific surface areas varied from 1.5 to $1.9 \times 10^4(\text{m}^{-1})$ in the smaller spheres and within 5.8 to $7.8 \times 10^3(\text{m}^{-1})$ in the larger spheres. The contact lengths listed in Tab. 10.9, in the ranges of $[25'000 < L_{im}(w) < 44'000(\text{m}^{-1})]$ and of $[18'000 < L_{dr}(w) < 36'500(\text{m}^{-1})]$ thus exceed the surface areas of the idealized spheres by factors of between 2 and 4. Notwithstanding the discrepancy, v_F was constant (Fig. 10.9), which indicates force balance during flow. On the one hand, the lower sand-box boundary may have interfered with viscous flow, indicating too short boxes for proper viscous-flow applications (see Topic 10.8 and Fig.10.11). On the other hand, the surfaces of irregular sand particles might be much larger than those of the evenly shaped idealized spheres, thus locally increasing the area of momentum dissipation.

However, Fig. 12.3 and Eqs. (12.2.) to (12.7), resulting in $[L(w) < L(R)]$, suggest a concentration of flow paths in that not all available surfaces onto those momentum may dissipate are actively involved during viscous flow under the auspice of v_F . Thus, there were no need for tortuosity during viscous flow. Actually, finger-flow seems to present the opposite of tortuosity when A embraces numerous fingers and the spaces not occupied by viscous flow between the fingers.

In conclusion, the limited availability of surface areas onto those momentum dissipates during finger-flow and constant v_F hint at a high degree of water saturation within the finger. Moreover, the method of determining L results in the actual surface area onto which momentum dissipates, regardless of tortuosity. At any rate, the currently unresolved importance of tortuosity during viscous flow calls for further experimentation under particular attention to the scales of pores and fingers.

12.4 Viscous flow between *SWI* and *AWI*

Vertical solid-water- and air-water-interfaces, *SWI* and *AWI*, type-(i) and type-(ii) *BCs* in Section 3.6, are now considered. A channel narrower than the critical width of 5.5(mm) exerts a surface tension on the mobile water according to Eq.(2.22). Similarly, a film which is thinner than the critical width is subject to surface tension. Capillary flow assumes a strong relationship between surface tension and the total water content in a *REV*, hence leading to the retention function of $h_{cap}(\theta)$ as, for instance, Eq.(2.27) may represent. But viscous flow ignores the impact of surface tension on the mobile water despite the various indications of $h_{cap}(F)$, $h_{cap}(\theta)$, and $h_{cap}(w)$. They call for a thorough discussion.

Flow along walls of typical macropores that are wide enough not to exert capillarity onto the moving water might be less frequent than generally expected as *Toipic 8.2* demonstrates. Corner flow according to Tuller and Or (2001), and as discussed in Section 5.4, probably represents more realistically viscous flow as surface tension is combined with other dimensions of the flow path. The assumed relationship of $h_{cap}(w)$ may depend on the tensile strength of an *AWI*. For instance, it seems feasible to consider vertical *AWIs* sheathing finger-flow, thus leading to a flow structure bearing the chance of better explaining *WCWs*' shapes, which so-far are poorly defined.

Topic 12.4: *Surface tension in the AWI.* Equation (2.10) arguably assumes unlimited parabolic increase of the lamina-velocity $v(f)$ at distance f from the *SWI* in the direction of the *AWI*, where $[v(0) = 0]$ and $[v(F) \propto F^2]$ are assumed within the margins of $[2 \leq F < \approx 100(\mu\text{m})]$.

Case 12.2: Particle tracking in a micro channel. By confocal microscopy Lazouskaya et al. (2006) tracked the transport of fluorescent latex microspheres with diameters of $1.1\text{ }\mu\text{m}$ in a rectangular channel that was 0.5 mm wide. Figure 12.4 depicts the particle velocity with respect to the distance from the *SWI* in the longitudinal center-plane of the micro channel. The figure includes the velocity profile of plane-Poiseuille flow, Eq. 5.2, which was matched to the data. First, the data confirm the non-slip condition of $[v(0) = 0]$ at the *SWI* that is required in the integration leading to the velocity profile, Eq. (2.10). Second, flow at the *AWI* is similarly constrained as at the *SWI* which results in a second non-slip boundary. Moreover, the tendency of an *AWI* to confine flow like a *SWI* increases with decreasing channel width and film thickness (Zheng et al., 2012). Thus, the assumption of films in the thickness range of $[1 < F < 100(\mu\text{m})]$ to move as plane-Poiseuille flows according to Eqs.(5.2) to (5.7) appears reasonable regardless of their respective restrictions, either by two *SWIs* or by one *SWI* and one *AWI*. The statement in Section 5.5, that
.. the decision on the most suitable flow geometry seems not crucial vis-à-vis all the other assumptions and restrictions necessary to apply viscous flow to preferential infiltration ..

takes an unexpected twist in that the generalization of *Case 12.2* eliminates a priori free-surface flow from representing permeable media flow along rough surfaces with roughness lengths in the order of F . Consequently, lateral *AWI*-boundaries of a *WCW*, type-(iii) *BC* in Section 3.6, are hardly relevant during most viscous flows. This leads to a striking consequence. Let us assume, for instance in a soil profile, that the walls of either side of a fissure carry plane-Poiseuille flow, both confined by an *AWI* and *SWI*, while the fissure gets narrower with depth, Fig. 12.5. It is conceivable that the two facing films collapse onto one another when the width of the path becomes $2F$ at the

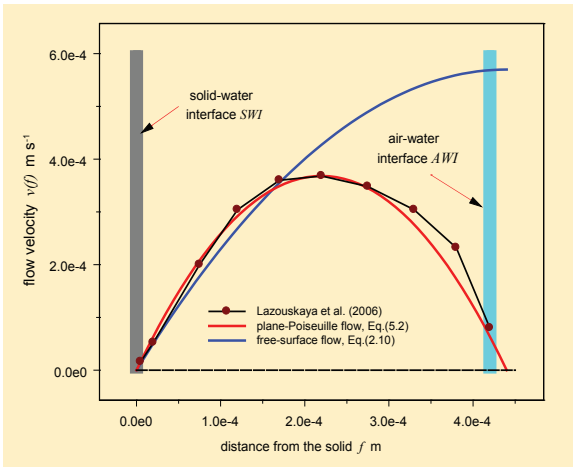


Figure 12.4, *Topic 12.4:* Velocity distribution in a $0.5(\text{mm})$ wide micro-channel with respect to the distance from the *SWI* in the longitudinal center-plane (Lazouskaya et al. 2006).

throat. This produces a plane-Poiseuille flow that is now confined by two *SWI* but whose film is twice as thick as before the collapse.

Topic 12.5: *Throat effect of plane-Poiseuille flow:* $P(q_s, T_B, T_E)$ initiates a *WCW* at the surface that is defined with the emerging F and L . Referring to Fig. 12.5 and to Eqs.(5.4) to (5.6), the following three expressions represent plane-Poiseuille flow moving in two films along the facing fissure-walls before their collapse above the throat (index *up*):

$$w_{up} = L \cdot F \quad (12.8)$$

$$v_{F,up} = F^2 \cdot \frac{g}{12 \cdot \eta} \quad (12.9)$$

$$q_{up} = F^3 \cdot L \cdot \frac{g}{12 \cdot \eta} \quad (12.10)$$

Bellow the throat (index *lo*) and after the collapse of the two films on one another plane-Poiseuille flow transmutes to a single film according to

$$w_{lo} = L \cdot F \quad (12.11)$$

$$v_{F,lo} = F^2 \cdot \frac{g}{3 \cdot \eta} \quad (12.12)$$

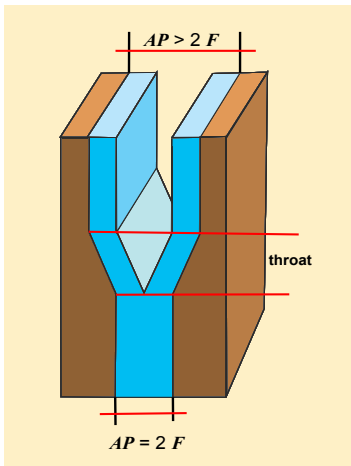


Figure 12.5: *Topic 12.5:*
Throat effect - fissure with
an aperture AP narrowing
at the throat from
 $[AP > 2F]$ to $[AP = 2F]$.

$$q_{lo} = F^3 \cdot L \cdot \frac{g}{3 \cdot \eta} \quad (12.13)$$

Thus, $[w_{lo} = w_{up}]$, while velocity and volume flux density accelerate at the throat according to the transformations of Eqs.(12.9) and (12.10) to Eqs. (12.12) and (12.13), respectively, resulting in $[v_{F,lo} = 4 v_{F,up}]$ and $[q_{lo} = 4 q_{up}]$. The additional force available for the acceleration, Eq.(2.6), is due to the reduction of momentum dissipation (a kind of lubrication), Eqs.(2.9) and (2.15). From volume-balance considerations this kind of acceleration is only possible when the cross-sectional area of flow per unit of the medium's cross-sectional area reduces by a factor of four from above to below the throat, consequently leading to the formation of finger-flow. The phenomenon is dubbed as the *throat effect* of viscous flow and it illustrates a counter intuitive case of narrower paths accelerating flow without additional pressure build-up.

Topic 12.6: *Throat effect at the profile level:* In the upper soil horizons a vertical distribution of throats is expected. There might be some fissures with apertures of $[AP \approx 2F]$ close to the surface at $[\zeta \approx 0]$ and similar throats of other paths that are close to $[\zeta \approx Z]$, while most throats will be located between, $[0 < \zeta < Z]$. The arrival time of a wetting front at Z with respect to the throat's position at depths ζ amounts to

$$t_w(\zeta)|_Z = T_B + \frac{3 \cdot Z \cdot \eta}{F^2 \cdot g} \cdot \left(3 \cdot \frac{\zeta}{Z} + 1 \right) \quad (12.14)$$

Inserting the maximum and minimum, $[\zeta = Z]$ and $[\zeta = 0]$, into Eq.(12.14) and solving for T_w yields

$$t_{w,max}|_Z = \kappa \cdot t_{w,min}|_Z - (\kappa - 1) \cdot T_B \quad (12.15)$$

where $[\kappa = 4]$ represents the maximum arrival time with respect to the first arrival $T_{w,min}$ of the wetting front at Z . (See Fig. 9.9 that illustrates $t_{w,min}$ and $t_{w,max}$). If the throats are evenly distributed within $[0 \leq \zeta \leq Z]$ the water content $\theta(Z,t)$ increases linearly during the interval of $[t_{w,min}(Z) \leq t \leq t_{w,max}(Z)]$ as, for instance, *Topic 9.1* with *Case 8.2* suggests at least during part of the time interval. The deepest position of the last throat at $[0 \leq \zeta/Z \leq 1]$ leads to the generalization of Eq.(12.15) with the corresponding variation of κ within $[1 \leq \kappa \leq 4]$. Thus, any relationship according to Eq.(12.15) with $[1 < \kappa \leq 4]$ may include throat effects. Notwithstanding the simplified view of Fig. 12.5, *Case 12.2* may shed some light on the depth distribution of the throat effect. Pressure build-up has been ignored so far (and will here not be treated further). However, flow in $[AP < 2F]$ will perch water above the throat leading to a positive pressure and thus to a reduction of κ . Temporary

pressure build-up above the throat accelerates flow in addition to the throat effect but Eq.(12.15) cannot separate perching with $[AP < 2 F]$ from pure throat flow with $[AP = 2 F]$.

Case 12.3: *Slopes of increasing $\theta(Z,t)$ -limbs.* The data used to exemplify *Topic 12.6* are deduced from 315 $\theta(Z,t)$ -time series that were monitored at depths from 0.15 to 1.7(m) in 25 different soil profiles representing seven soil suborders (Germann and Hensel, 2006). For investigating *Topic 12.6*, 147 time series were selected from the collection that cover the range from the surface to the 0.8-m depth. In 95 of the 147 cases, or 65(%), was $[1 < \kappa \leq 4]$. Besides acceleration due to the throat effect, Fig. 12.5, there are various combinations of local paths and processes that are feasible and which may lead to $[1 < \kappa \leq 4]$. Thus, the result suggest the need for further research into the validity of Eqs.(12.8) to (12.15) rather than proof of the relationship between flow and the vertical distribution of throats.

Soil morphology suggests that the throat effect gradually wanes with depth similar to other effects of soil forming processes. However, the suggestion awaits experimental testing.

12.5 Viscous flow and capillary heads

Equation (2.17) defines the surface tension σ as force per unit of the triple-contact length, L_{cap} , between the solid and the wetting and non-wetting fluids. Thus, h_{cap} is not a direct property of θ as $h_{cap}(\theta)$, Eq.(2.27), instills. Instead, the intermediate steps of $h_{cap}(L_{cap})$ and of $L_{cap}(\theta)$ seem more appropriate to describe a hydrostatic retention curve with the consequence that the reversible expression $\theta(h_{cap})$ does not mandatorily apply. The ink-bottle effect illustrating hysteresis (Hillel, 1998) actually builds on the intermediate steps of $h_{cap}(L_{cap})$ and of $L_{cap}(\theta)$. Moreover, Figure 12.4 (Lazouskaya et al., 2006; Zheng et al., 2012) demonstrates that an *AWI* from $[F \leq 500(\mu\text{m})]$ acts like a *SWI*. Nevertheless, there is still unhampered viscous flow between the two interfaces. More theoretically, taking into account Section 6.7, viscous flow applies within the range of $[5 \leq F \leq 120(\mu\text{m})]$ while the minimum film thickness of $[F = 3.2(\mu\text{m})]$ was calculated in *Topic 11.1*. Moreover, Lamb's (1932) *Article 330a* demonstrates independence of viscous flow from pressure in the liquid and concludes as

The above results, as thus generalized, have an important application in the theory of Lubrication, which was initiated by Osborne Reynolds [1886] in a classical paper.

This spans elegantly the bridge to the introduction, Section 1.3.

The discussion about the significance of h_{cap} in viscous flow pivots around the WCW 's presumed independence from $h_{cap}(\theta_{init})$. In principle, during the existence of a WCW , the propagating wetting front is affected by four capillary head ranges:

- (i) [$h_{cap} = h_{cap}(\theta_{init})$] ahead of the WCW ;
- (ii) [$h_{cap} = h_{cap}(F)$] at the front of the WCW , Eq.(2.21);
- (iii) [$h_{cap} = h_{cap}(w)$] between the wetting front and the surface of the permeable medium, where [$h_{cap}(w) \approx 0$] during [$T_B \leq t \leq T_E$], (*Topic 11.10*) produced [$0 \geq h_{cap}(w) \geq -0.25(\text{m})$], Fig. 11.6;
- (iv) [$0 \geq h_{cap}(w) \geq h_{cap}(\theta_{end})$] during [$t > T_E$], Fig. 11.6.

Topic 12.7: *Independence of the WCW from hydrostatic $h_{cap}(\theta_{init})$:* F is an exclusive function of v_{Fz} Eq.(2.15) and, as a consequence, so is $h_{cap}(F)$. The independence of $h_{cap}(F)$ from $h_{cap}(\theta_{init})$ is now investigated.

A typical tensiometer cup measures h_{cap} in the permeable medium of its immediate surroundings, while the local h_{cap} -values are smoothed across the cup's control volume because of the short-circuit effect of its porous wall. Thus, no h_{cap} -speciation is possible within volumes smaller than a cup's control volume. In particular, preferential flow along paths that are closer to one another than the extent of tensiometer cups cannot be separated from sequential flow. Thus, the h_{cap} -methodology's spatial insensitivity demands an alternate experimental approach, which is able to discriminate $h_{cap}(w)$ against $h_{cap}(\theta)$.

The mechanical stability of a permeable medium in relation to its water content offers an experimental alternative to circumvent the tensiometer insensitivity. Water-content dependent rigidity of a granular medium is related to the capillarity-induced cohesion. The "sand castle effect", well observable on a beach, may illustrate the concept: An optimal water-content range of the sand is required for castle building. If the sand is too wet, for instance when the tide moves in, the shapes creep away, while too dry a sand resulting from sunshine for instance, will allow a light breeze to erode the shapes. Too high a water content causes high $h_{cap}(\theta)$ resulting in a weak force pulling the sand grains together but in a long L_{cap} , Eqs.(2.18) and (2.21). In contrast, too low a water content exerts a much stronger pull on the sand grains but along a much shorter L_{cap} . Intermediate water content, however, provides optimal combinations of L_{cap} and $h_{cap}(\theta)$, keeping the shapes in place and the sand in a plastic condition.

The velocity of an acoustic wave v_{ac} (m s^{-1}) traveling across a porous medium strongly depends on the medium's rigidity which is expressed with the pressure-wave modulus M_p (Pa). This is the pressure component of the acoustic wave representing the force per unit area required for compressing

the medium in relation to its original extent. Moreover, M_p is linearly related with v_{ac} of the corresponding sound wave. Thus, the determination of $v_{ac}(\theta)$ during infiltration produces $M_p(\theta)$, which is independent of the tensiometry but strongly related to the mechanically acting $h_{cap}(\theta)$, as indicated by the sand castle effect. $M_p(\theta)$ turns into a measure for $h_c(\theta)$ and discriminates it against all the other capillary potentials, in particular against $h_{cap}(w)$.

Case 12.4: *Acoustic velocities during infiltration in a column of an undisturbed soil:* Brutsaert (1964) found the proportionality [$v_{ac} \approx \rho_m^{-1/2}$] between v_{ac} and the medium's total density [$\rho_m = \rho_b + \theta \rho_{HOH}$], where [$\rho_{HOH} = 1.0(\text{Mg m}^{-3})$] is the density of water. Based on the Richards (1931) equation and various other assumptions the linear relationship of $M_p(v_{ac})$ emerges. Brutsaert's (1964) approach shows a monotonous decrease of M_p and v_{ac} with increasing θ up to saturation at [$\theta = \varepsilon$] when the water-incompressibility dominates the hydraulically confined medium's rigidity, Fig. 12.7.

Flammer et al. (2001) presented $v_{ac}(\theta)$ -variations from three successive infiltration experiments. The soil was a Typic Hapludalf with a silt-loam texture derived from loess with [$\rho_b = 1.4(\text{Mg m}^{-3})$] and [$\varepsilon = 0.47(\text{m}^3 \text{m}^{-3})$]. Figure 12.6 depicts the experimental device. An undisturbed column with diameter and length of 0.29 and approx. 1.0(m) was dug out and encased with a fiberglass-polyester mantle. Through holes in the coating one electro-acoustic emitter and one receiver were diametrically attached onto the soil at the 0.37-m depth, and a pair of TDR-wave guides were mounted at the 0.31-m depth. Sprinkling was through 40 capillaries mounted on a rotating disc. Three runs were performed each with [$T_E - T_B = 10'800(\text{s})$] and [$q_s = 4 \times 10^{-6}(\text{m s}^{-1})$]. Table 12.1 summarizes the parameters.

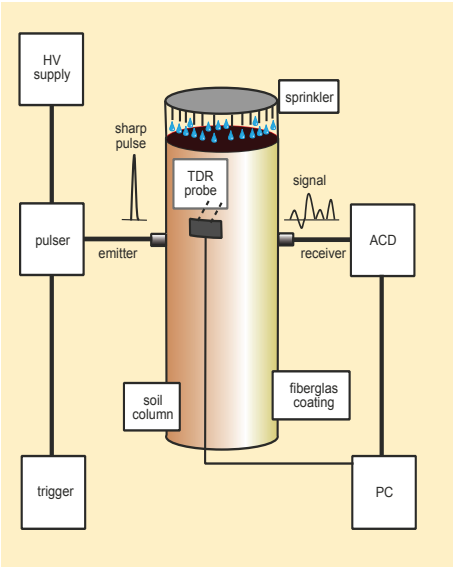


Figure 12.6, Case 12.4:
Experimental set-up to record
acoustic velocities and
volumetric water contents
(Flammer et al., 2001).

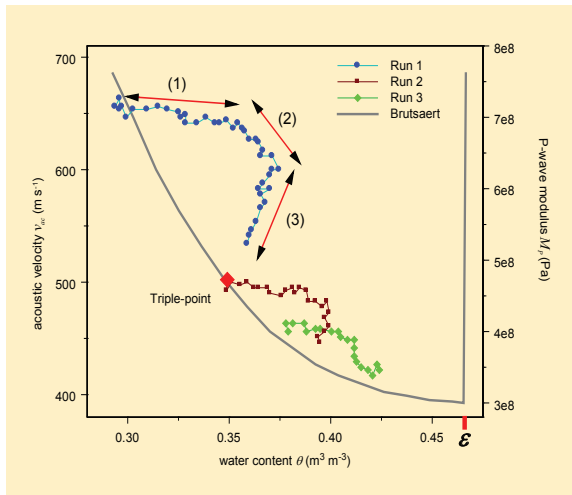


Figure 12.7, Topic 12.7: Pressure-wave modulus, M_p , and acoustic velocity, v_{ac} , vs. volumetric water content θ during three consecutive infiltration runs. Model according to Brutsaert (1964) and Flammer et al. (2001). The red arrows indicate Stages (1), (2), and (3) of Run 1 (see text); note the the triple-point as depicted in Fig. 12.8.

Figure 12.7 shows considerable deviations from Brutsaert’s (1964) approach of $v_{ac}(\theta)$ and $M_p(\theta)$ during dynamic infiltration of Flammer et al. (2001). Three stages of deviation are discernible:

Stage 1 with but little effect of θ on M_p and v_{ac} , $[d(M_p, v_{ac})/d\theta \approx 0]$;

Stage 2 decrease of $v_{ac}(\theta)$ and $M_p(\theta)$ while θ increases;

Stage 3 decrease of $v_{ac}(\theta)$ and $M_p(\theta)$ while θ decreases.

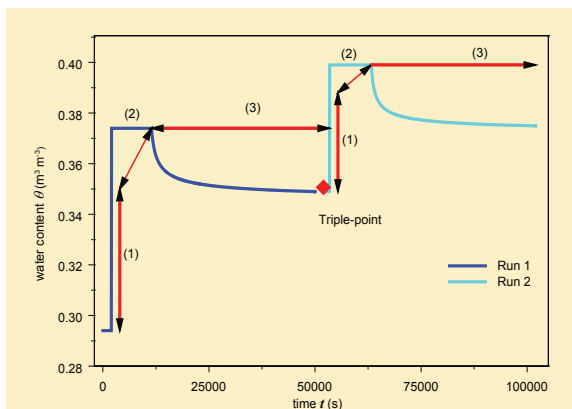


Figure 12.8, Topic 12.7: Viscous-flow reconstruction of the $\theta(Z, t)$ -time series of Run 1 and Run 2 applying the data of Tab. 12.1. The red arrows indicate Stage 1, Stage 2, and Stage 3 which are introduced in the text together with the triple-point.

All three stages were well visible during Run 1, they were less pronounced during Run 2, and *Stage 2* and *Stage 3* were missing during Run 3, where M_p and v_{ac} continuously drop and $\theta(t)$ monotonously increases as it approaches saturation at ε .

In respect to viscous flow, *Stage 1* coincides with the unaffected propagation of the *WCW* when $[\theta_{div}(t) = 0]$, and $[h_{cap}(w) \approx 0]$ is assumed. *Topic 11.10* supports this with $[h_{cap}(w) \approx -0.25(\text{m})]$, Fig. 11.6. The relatively minor deviations of measured $[h_{cap}(w) < 0]$ from expected $[h_{cap}(w) = 0]$ is attributed to the short-circuiting of the tensiometers. *Stage 2* indicates water abstraction due to capillarity before the arrival of the draining front, $[\theta_{div}(t) > 0]$, thus increasing h_{cap} and forcing M_p and v_{ac} to decrease. *Stage 3* indicates abstraction, $[\theta_{div}(t) > 0]$, that continues into the trailing wave with $[d\theta/dt < 0]$. Towards the end of Run 1 the $M_p(\theta)$ - and $v_{ac}(\theta)$ -data series point to the beginning of Run 2, and both seem to agree with Brutsaert's approach at the presumed Triple-point as the red diamond in Fig. 12.6 suggests. On the one hand, Brutsaert's approach to $M_p(\theta)$ - and $v_{ac}(\theta)$ is based on Richards' (1931) sequential flow, hence the smooth function up to $[\theta = \varepsilon]$. On the other hand, the data of Flammer et al. (2001) demonstrate the *WCW*'s basic independence from $h_{cap}(\theta_{init})$ during *Stage 1* and the capillarity's limited impact on $\theta(t)$ during *Stage 2* and *Stage 3*. The presumed Stage-3 approach to the Triple-point indicates non-equilibrium in capillary flow and, given long enough time, the collapse of viscous flow onto hydrostatic $h_{cap}(\theta)$ -conditions. Figure 12.8 summarizes the viscous-flow point of view by projecting the three stages on the modeled $\theta(t)$ -series of Run 1 and Run 2 and positioning the triple-point accordingly. Modeling results presented in the figure are based on Tab. 12.1. During Run 3 $\theta(t)$ increases continuously and it omits Stage 3 probably being close to saturation.

Table 12.1, Topic 12.7: Viscous flow parameters during the three infiltration runs while measuring acoustic velocities (Flammer et al., 2001).

parameters	dimension	Run 1	Run 2	Run 3
θ_{init}	($\text{m}^3 \text{ m}^{-3}$)	0.29	0.34	0.37
θ_{max}	($\text{m}^3 \text{ m}^{-3}$)	0.36	0.39	0.41
$t_W(Z) - T_B$	(s)	2'000	1'400	1400
v_F	(m s^{-1}) $\times 10^{-4}$	1.6	2.2	2.2
F	(μm)	7.0	8.0	8.0
L	(m^{-1})	10'000	6'100	5'000
w_F	($\text{m}^3 \text{ m}^{-3}$)	0.07	0.048	0.04
q_F	(m s^{-1}) $\times 10^{-5}$	1.12	1.06	0.88

Topic 12.8: $h_{cap}(F)$ at the wetting front: The previous topic suggested the independence of $h_{cap}(F)$ from $h_{cap}(\theta_{init})$ and $[h_{cap}(w) \approx 0]$. The *AWI* at the presumed macroscopic wetting front most likely consists of a great number of menisci. Enormous, though undisclosed pressure gradients $[dh_{cap}/dz]$ are active across the interfaces because of the prevailing air pressure short distances both ahead and at a behind them. Microscopic wetting fronts of flow along their individual paths presumably proceed in a jumpy and stumbling manner along uneven *SWIs* such as Haines (1930) introduced. The microscopic *AWIs* will rupture during the progression of the macroscopic wetting front, resulting in bursts and snapping sounds similar to those produced by the clickers ('sheet-metal frogs' in German) allied paratroopers used on D-day of 1944 to camouflage contacting each other after landing behind German enemy lines.

Case 12.5: *Acoustic measurements of pore-scale displacements:* DiCarlo et al. (2003) measured with microphones and hydrophones the acoustic signals during imbibition and drainage in sand columns having diameters and heights of 145 and 40(mm). The columns were packed with two well sorted sands with particle diameters of $1.1 \pm 0.2(\text{mm})$ and $0.7 \pm 0.1(\text{mm})$; the microphone and the hydrophone were placed 20(mm) above and 25(mm) below the sand surfaces. The authors applied three flow rates, 1, 4, and 7(ml/min) and discovered *crackling noise* due to pore-level bursts which they attributed to Haines (1930)-jumps. Further:

The overall structure of the acoustic signal is matched by the hydroacoustic signal, with the addition of some large spikes between 1'200 and 1'800 seconds when the wetting front is close to the active surface of the hydrophone.

Figure 12.9a summarizes the number of acoustic bursts during imbibition in the range of 2 to 100(min⁻¹) vs. their sizes in pressure units as recorded with the hydrophone. Drop-off follows a power-law with a fit factor of -2.6 ± 0.4 . Here, the drop-off is interpreted as the passing of the wetting front. The closer the wetting front is to the hydrophone the stronger are the signals of the bursts. Due to the spherical dissipation of acoustic energy one expects drop-off to be proportional to the inverse squared distance between the burst and the hydrophone resulting in a theoretical power-law factor of -2. The observed drop-off being steeper than the expected one indicates the proceeding of a rather cohesive macroscopic wetting front. Cautiously interpreted, the difference between the theoretical and the observed factor is probably due to the earlier-than-average passing of the wetting fronts of thicker films that may burst with lower energy.

DiCarlo et al. (2003) also investigated acoustic bursts during drainage, with viscous flow coinciding with the passing of the trailing wave. The results are presented in Fig. 12.9b. The authors commented that

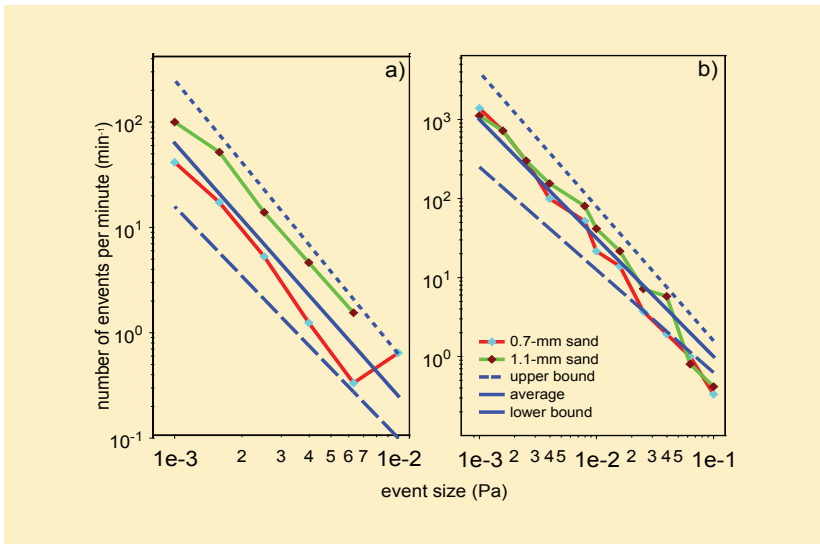


Figure 12.9, Topic 12.8 : Frequencies of acoustic events vs. event sizes during **a)** imbibition and **b)** drainage. Data from DiCarlo et al. (2003).

The magnitude of the acoustic events show a power-law behavior over the complete range of event sizes between the detectable size of $6 \times 10^{-4}(\text{Pa})$ to the largest event of size $2 \times 10^{-2}(\text{Pa})$. The observed power law is independent of the flow rate, but is found to have a slightly smaller value in the larger 1.1-mm sand.

They also reported a power-law factor of -1.7 ± 0.15 indicating a considerably flatter distribution that covers a much broader range than during imbibition but with smaller variation. Again, cautious interpretation in view of viscous flow allows us to conclude that a larger variation of film thicknesses passes the hydrophone. The ensemble of films seems considerably better structured than during imbibition as expressed by the nearly constant water content during $[T_w(Z) \leq t \leq T_d(Z)]$. Also the smooth trailing wave during $[t > T_d(Z)]$ with monotonously decreasing w indicates flow structure, while Z refers to the depth of the hydrophone below the sample surface. Moreover, experimentally carrying further the work of DiCarlo et al. (2003) may provide for a link to the kinetic-energy discussion, Eqs.(3.39) to (3.41), eventually settling the problem of the microscopic nature of a WCW 's wetting front.

12.6 Viscous flow and structural voids

On one side, soil dynamics produce and alter structures and voids that are not foreseeable from texture alone. Void-forming processes may include desiccation and swelling of the matrix, penetration and decay of roots, internal erosion and deposits both mechanical and chemical, external stress and strain, as well as animal burrowing. The resulting structural features are frequently summarized as macropores at large. However, *Case 8.1* demonstrates that viscous flow may not necessarily follow the widest paths, at least not exclusively or predominately. On the other side, it seems reasonable that structural voids are increasingly important in carrying viscous flow with decreasing matrix permeability. Fissures in otherwise poorly water-conducting rock formations, *Cases 9.5 to 9.7*, may serve as examples at the extreme end of the spectrum. The cultivation of poorly drainable, thus poorly aerated soils with plants whose roots are able to penetrate frequently water-logged soils (hydromorphic soils) is a well-established agricultural procedure for site improvements. For example, farmers cultivated species of the cabbage-family (*Brassicaceae spec.*) on newly drained marsh soils in the valley bottom of the river Gürbe near Bern which was drained during the second half of the 19th century. The custom still exists and a small-scale Sauerkraut industry has established since then. Moreover, Jäggi (2001) demonstrated with the viscous-flow methodology that the cultivation of *Miscanthus sinensis* (“China reed”) improved the drainability of a compact B₁-horizon.

Topic 12.9: *Tree roots improve hydromorphic forest soils:* In intensively cultivated areas remaining forests grow frequently on soils unfit for agriculture, and hydromorphic soils are among them. Growing trees with roots capable of penetrating hydromorphic horizons are considered effective a remedy.

Case 12.6: *Relationship between root density and viscous-flow parameters:* With sprinkler-TDR experiments Lange et al. (2009) determined L and F of 21 forest soil horizons with various degrees of hydromorphic features. Rate and duration of input were [$q_s = 1.9 \times 10^{-5}(\text{m s}^{-1})$] and [$T_E - T_B = 1'800(\text{s})$] in all cases. In the same horizons they also determined the density of fine roots, $RD (\text{m}^{-2})$, as root length per volume of soil. The linear regressions

$$L(RD) = uL_1 \cdot RD + uL_2 \quad (12.16)$$

$$F(RD) = uF_1 \cdot RD + uF_2 \quad (12.17)$$

yielded the parameters

$$\begin{array}{ll} [uL_1 = 0.98(\text{m})] & \text{and } [uF_1 = -4.04 \times 10^{-10}(\text{m}^3)] \\ [uL_2 = 1'600(\text{m}^{-1})] & \text{and } [uF_2 = 1.26 \times 10^{-5}(\text{m})] \end{array}$$

with 19 degrees of freedom, and correlation coefficients of [$\mathcal{R}(L, RD) = 0.89$] and [$\mathcal{R}(F, RD) = -0.74$]. Both linear regressions are significant utmost at the 1(%) -error level. Increasing RD also increases L while F decreases with [$uF_1 < 0$], well illustrating that, under the regime of constant q_s , water flows in similarly sized paths. Augmenting their specific lengths thus reduces film thickness.

Neglecting hydrodynamic interactions between L and F , volume flux density as function of root density becomes

$$q(RD) = \frac{g}{3 \cdot \eta} \cdot F(RD)^3 \cdot L(RD) \quad (12.18)$$

Figure (12.10) shows a distinct maximum [$q(RD)_{max} = 2.5 \times 10^{-5} (\text{m s}^{-1})$] at [$RD(q_{max}) = 6'600 (\text{m}^{-2})$] with [$L(q_{max}) = 8'000 (\text{m}^{-1})$] and [$F(q_{max}) = 10^{-5} (\text{m})$]. Equation (12.18) suggests a 4th-power type impact of RD on q_s similar to the radius on flow in a cylinder, Eqs.(5.12) and (5.13). Moreover, the sensitivity of RD on q_s also shows when decreasing [$uL_2 = 1'600, 800, 16 (\text{m}^{-1})$] as Fig. 12.10 demonstrates. However, the analysis is primarily viewed as an example of exploring viscous flow in relation with soil features. Generalization of such results requires more experimental investigations which should include the variation of infiltration rates.

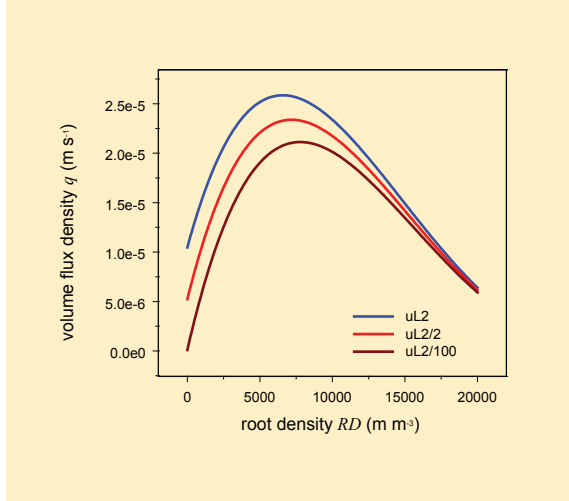


Figure 12.10, Topic 12.9 : Volume flux density of viscous flow, q , as function of root density, RD , according to Eqs.(12.16) to (12.18) with initial RD of [$uL_2 = 1'600, 800, 16 (\text{m m}^{-2})$]. (Lange et al., 2009).

13. On scales and extents of viscous flow

13.1 Introduction

Reflections on scales and dimensions touch on both, principles and applications. They are appropriate topics with which to conclude our discussion of viscous flow in permeable media.

Alterations at the boundary of a system are often referred to as a signal or a disturbance that is passing through and diffusing within a system. Discussions of scales and extents typically pivot around the three questions of how fast a signal may proceed, how long, and how far it may persist. For instance, Blöschl and Sivapalan (1995), in their excellent graph summarizing the scales of the major hydrological processes, placed unsaturated flow on a time scale ranging from about 1(h) to several months, on a space scale ranging from approximately 1 to 100(m), with associated velocities ranging from 5×10^{-7} to $5 \times 10^{-5}(\text{m s}^{-1})$.

Here, scales of viscous flow are looked at from within its theoretical framework. The scale-decisive parameters are the intensity and the duration of an input pulse $P(q_s, T_B, T_E)$ as boundary conditions under the premise of $[q_s \leq K_{sat}]$. The specific contact length L of the P -initiated WCW appears then as the only parameter linking flow with the structure of the permeable medium in all those cases when the film thickness F remains thinner than the widest continuous flow-carrying voids. Viscous flow separates signal velocity from signal magnitude. This results in ordinary differential equations which are easy to solve despite their close relationships between length, time and velocity.

A permeable system is considered homogeneous with respect to viscous flow if a WCW evolves without restriction. The three periods of

- (i) $[T_B \leq t \leq T_E]$,
- (ii) $[T_E \leq t \leq T_I]$, and
- (iii) $[t \geq T_I]$

cover the entire lifespan of a WCW . Thus, T_I and Z_I serve as separators on the t - and z -axis as Fig. 3.1 demonstrates. On the one hand, the periods (i) and (ii) are here drawn together because the wetting and draining fronts during both periods move with constant velocities, while the scaling relationships become linear. On the other hand, there is just one decelerating wetting front occurring in period (iii), while scaling becomes non-linear and has to include the WCW 's total volume $[V_{WCW} = q_s (T_E - T_B)]$, Section 3.3.

13.2 Temporal scaling of viscous flow

The time

$$T_I = \frac{1}{2} \cdot (3 \cdot T_E - T_B) \quad (3.8)$$

separates the life span of a *WCW* into its early and late periods, $[T_B \leq t \leq T_I]$ and $[t \geq T_I]$, respectively. It is also the time of the wetting front intercepting the draining front and it depends exclusively on the duration $[T_E - T_B]$ of P .

Topic 13.1: *Temporal scaling of front velocities:* During $[T_B \leq t \leq T_I]$ the wetting and draining fronts move according to Eq.(2.15) and (3.5) with constant velocities of

$$v_F = \left(\frac{q_S}{L} \right)^{2/3} \left(\frac{g}{3 \cdot \eta} \right)^{1/3} \quad (13.1)$$

and

$$c = 3 \cdot v_F \quad (3.5)$$

The wetting front during $[t \geq T_I]$ decelerates according to Eq.(3.16) as

$$v_F(t) = \left(\frac{q_S}{L} \right)^{2/3} \cdot \left(\frac{g}{3 \cdot \eta} \right)^{1/3} \left(\frac{T_E - T_B}{2 \cdot (t - T_E)} \right)^{2/3} \quad (13.2)$$

The front velocity depends on P -properties, the time $[t - T_E]$ since the cessation of P , and the specific surface area L per unit volume of the permeable medium onto which momentum dissipates. L is the only parameter representing the permeable medium.

The time $t(S_v)$ required for $v_F(t > T_I)$ to reduce to any preset threshold $[S_v \leq 1]$ results from setting the ratio from Eq.(13.2) divided by Eq.(13.1) equal to S_v . Subsequent solving for $t(S_v)$ yields

$$t(S_v) = S_v^{-3/2} \cdot \left(\frac{T_E - T_B}{2} \right) + T_E \quad (13.3)$$

Thus, the time at which $v_F(t)$ reduces to 10^{-1} , 10^{-2} , and 10^{-3} of $v_F(T_I)$ occurs at T_E plus $10^{3/2}$, 10^3 , and $10^{9/2}$ times $[(T_E - T_B) / 2]$, respectively. For example, the wetting front velocity reduces to 1(%) of its original value at 500 times

the duration $[T_E - T_B]$ of $P(q_S, T_B, T_E)$ after the pulse's cessation. After front interception, $[T_E - T_B]$ and q_S scale v_F with $S_v^{-3/2}$ and $S_v^{3/2}$, respectively.

Topic 13.2: *Temporal scaling of mobile water contents:* During $[T_B \leq t \leq T_I]$ the constant mobile water content at the wetting front is

$$w_S = q_S^{1/3} \cdot L^{2/3} \cdot \left(\frac{g}{3 \cdot \eta} \right)^{-1/3} \quad (13.4)$$

The mobile water content at the wetting front during $[t \geq T_I]$ follows from Eq.(3.17) as

$$w_F(t \geq T_I) = q_S^{1/3} \cdot L^{2/3} \cdot \left(\frac{g}{3 \cdot \eta} \right)^{-1/3} \cdot \left(\frac{T_E - T_B}{2 \cdot (t - T_E)} \right)^{1/3} \quad (13.5)$$

Similar to v_F in the previous section w_F depends on P and L .

The time $t(S_w)$ required for $w(t > T_I)$ to reduce to a preset threshold $[S_w \leq 1]$ results from setting the ratio from Eq.(13.5) and Eq.(13.4) equal to S_w . Solving for $t(S_w)$ yields

$$t(S_w) = S_w^{-3} \cdot \left(\frac{T_E - T_B}{2} \right) + T_E \quad (13.6)$$

After front interception, $[T_E - T_B]$ and q_S scale w_F with S_w^{-3} and S_w^3 , respectively.

Topic 13.3: *Temporal scaling of volume flux densities:* During $[T_B \leq t \leq T_I]$ the constant volume flux density is q_S . From Eq.(3.18) follows the volume flux density at the wetting front during $[t \geq T_I]$ as

$$q_F(t \geq T_I) = q_S \cdot \frac{(T_E - T_B)}{2 \cdot (t - T_E)} \quad (13.7)$$

The time $t(S_q)$ required for $q_F(t > T_I)$ to reduce to a preset threshold $[S_q \leq 1]$ results from setting the division of Eq.(13.7) by q_S equal to S_q . Solving for $t(S_q)$ yields

$$t(S_q) = S_q^{-1} \cdot \left(\frac{T_E - T_B}{2} \right) + T_E \quad (13.8)$$

After front interception, $[T_E - T_B]$ and q_s scale q_F with S_q^{-1} and S_q , respectively.

13.3 Spatial scaling of viscous flow

According to Section 13.1 Z_I is the key-depth that scales viscous flow in space. From Eqs. (3.2), (3.5), and (3.7) it follows that the divide of a WCW in an upper and lower section will occur at

$$Z_I = \left(\frac{g}{\eta} \right)^{1/3} \cdot \left(\frac{3 \cdot q_s}{L} \right)^{2/3} \cdot \frac{(T_E - T_B)}{2} \quad (13.9)$$

which is the location where the wetting front intercepts the draining front as expressed by L and the properties of P .

Topic 13.4: *WCW-scaling in the upper depth range of $[0 \leq z \leq Z_I]$:* The four properties of the WCW , wetting front velocity Eq.(2.15), celerity of the draining front Eq.(3.5), mobile water content Eq.(13.4), and volume flux density q_s , remain constant with depth.

Topic 13.5: *WCW-scaling in the lower depth range of $[z \geq Z_I]$:* Scaling follows from solving

$$z_W(t) = \left(\frac{3 \cdot q_s}{2 \cdot L} \right)^{2/3} \cdot \left(\frac{g}{\eta} \right)^{1/3} \cdot (T_E - T_B)^{2/3} \cdot (t - T_E)^{1/3} \quad (13.10)$$

for $[t - T_E]$ and inserting the result into Eqs.(13.2), (13.5), and (13.7), leading to the following spatial variations of the wetting front conditions at the depth range of $[z \geq Z_I]$:

$$v_F(z \geq Z_I) = \frac{3}{4} \cdot q_s^2 \cdot L^{-2} \cdot \left(\frac{g}{\eta} \right) \cdot (T_E - T_B)^2 \cdot z^{-2} \quad (13.11)$$

$$w_F(z \geq Z_I) = \frac{3}{2} \cdot q_s \cdot (T_E - T_B) \cdot z^{-1} \quad (13.12)$$

$$q_F(z \geq Z_I) = \frac{9}{8} \cdot q_s^3 \cdot L^{-2} \cdot \left(\frac{g}{\eta} \right) \cdot (T_E - T_B)^3 \cdot z^{-3} \quad (13.13)$$

Thus, beyond $[z > Z_I]$ the three wetting front properties scale with depth according to the powers of z .

Equation(3.10) is essentially the same as the interception function, Eq.(4.20). Both expressions are suitable for assessing the sensitivity of the temporal wetting front position with respect to the properties of $P(q_s, T_E, T_B)$ and the permeable medium's L . Replacing t in Eq.(3.10) with T_I from Eq.(3.8) yields Z_I according to Eq.(3.19).

13.4 Macropore flow

Section 4.2 introduced the macropore flow constraint of $[dL/dq = 0]$ as a condition for the general applicability of kinematic wave theory in viscous flow. The constraint was included in the macropore flow hypothesis in Section 9.7. Its validity seems feasible in structured permeable media with flow paths wide enough to continuously accommodate $[q_s \leq K_{sat}]$ in the flow direction. However, the applicability of the macropore flow hypothesis to finger flow in apparently unstructured granular media as presented in Section 10.5 would *a priori* require momentum dissipation always onto the same extent of internal surfaces independent from q_s as would be achieved when flows repeatedly occurred along the same fingers.

Topic 13.6: Benefits of macropore flow: Notwithstanding theoretical and experimental difficulties in demonstrating the unrestricted applicability of the macropore flow hypothesis, the potential gains are by far too attractive not to dwell on the consequences. From the macropore flow hypothesis, Eqs.(6.13) and (6.14), it follows that

$$v(q_s) = q_s^{2/3} \cdot (L^*)^{-2/3} \cdot \left(\frac{g}{3 \cdot \eta} \right)^{1/3} \quad (13.14)$$

$$w(q_s) = q_s^{1/3} \cdot (L^*)^{2/3} \cdot \left(\frac{g}{3 \cdot \eta} \right)^{-1/3} \quad (13.15)$$

where L^* is the specific contact length at $[q_s = K_{sat}]$. It is here considered constant but needs more general ascertainment through additional

experimentation. Therefore, in a specific permeable medium the same L^* applies to Eqs.(13.2), (13.5), (13.7), and (13.10) to (13.13). Thus, for instance, the time and the amount of a tracer front arriving at a groundwater table becomes predictable directly for any $[q_{s,max} = K_{sat} \geq q_s > 0]$. Moreover, a validated macropore flow hypothesis would be very beneficial to infiltration-runoff modeling in catchment hydrology.

13.5 Wetting front velocities

Wetting front velocities are readily available from numerous sources. Figure 1.1, for instance, depicts the rise of a groundwater table upon infiltration. From v_F directly follows F which indicates also the minimal widths of the continuous flow paths. Moreover, v_F is the only parameter under the condition of $[\mathcal{R}e \leq 3]$, Eq.(2.16), thus immediately indicating the applicability of viscous flow. Wetting fronts may move across typical scale barriers frequently encountered in hydrology, while the front velocities provide a signal crossing those barriers. The following collection of observed wetting front velocities may serve as an orientation.

Topic 13.7: Documented wetting front velocities: Fig.13.1 provides the frequency distribution of v_F . The data origin from in-situ measurements of sprinkler-initiated soil-water variations. They span a range of about two orders of magnitude. The upper end of the v_F -distribution barely touches the permissible limit of viscous flow at $[\mathcal{R}e \leq 3]$ resulting in $[v_F(\mathcal{R}e_{max}) = 3.1 \times 10^{-2}(\text{m s}^{-1})]$, Eq.(2.16). Table 13.1 compiles wetting front velocities from various sources and systems.

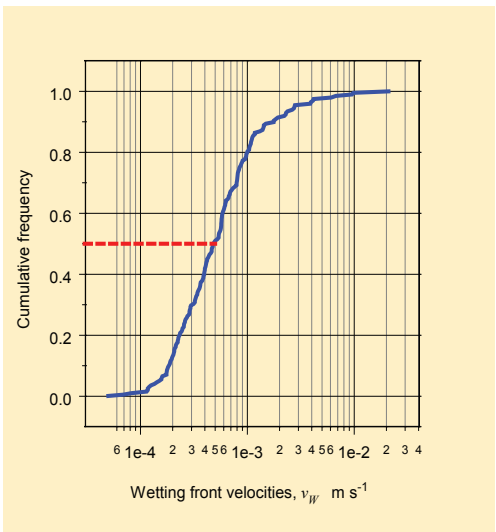


Figure 13.1: Frequency distributions of 215 wetting front velocities v_F (Hincapié and Germann, 2009a). The data are deduced from $\theta(z,t)$ -series that were determined in 25 soil profiles belonging to 7 suborders. The depths ranged from 0.4 to 1.7(m), the sprinkling rates from 5.6×10^{-6} to $2.8 \times 10^{-5}(\text{m s}^{-1})$, and the applications lasted from 1'800 to 7'200(s).

Table 13.1: Collection of wetting front velocities

wetting front velocity v_F (m s ⁻¹)	source	depth (m)	method	system
approx. 10 ⁻³	Fig. 1.1	1.75	groundwater table	in-situ measurements
2.4 x 10 ⁻³	8.1	0.2	drainage flow	artificial column
8.3 x 10 ⁻⁵	8.2	0.1	TDR	natural column
1.7 x 10 ⁻⁴	9.1	0.3	TDR	in-situ experiment
2.0 x 10 ⁻⁴ to 2.0 x 10 ⁻⁵	9.3		2-d images	glass beads
7.3 x 10 ⁻⁴ to 2.5 x 10 ⁻³	9.4	0.28	TDR	natural column
approx. 10 ⁻⁵ to 10 ⁻³	9.5	30 to 60	groundwater table	chalk formations
1.9 x 10 ⁻⁴	9.6	1800	tracer	crystalline rock
1.3 to 5.5 x 10 ⁻³	9.7	0.5	drainage	in-situ, fissured lime stone
4.2 x 10 ⁻⁵ to 1.7 x 10 ⁻⁴	10.1	0.15 to 0.47	TDR	in-situ experiment
1.7 x 10 ⁻⁵ to 4.8 x 10 ⁻⁴	10.2	0.1 to 0.9	TDR	in-situ experiment
2.4 x 10 ⁻⁵	10.3	0.21	TDR	in-situ experiment
2.6 to 5.0 x 10 ⁻⁴	10.4	0.15 to 0.75	TDR	in-situ experiment
4.4 x 10 ⁻⁴	10.5	0.01 to 0.24	neutron radiography	sand box
3.3 x 10 ⁻⁵	11.1	0.2 to 1.8	TDR, tensiometers	sand tank
2.3 x 10 ⁻⁶ to 5.4 x 10 ⁻⁶	Rimon et al., (2007)	21	FTDR	sand dune with clay layer
approx. 9 x 10 ⁻⁵	Germann and Levy (1986)	7.0	groundwater table	in-situ measurements
approx. 10 ⁻⁴	Tröhler (1976)	7.5	groundwater table	in-situ measurements
approx. 3 x 10 ⁻³	Levy and Germann (1988)	0.6	drainage	natural soil block
approx. 5 x 10 ⁻⁷ to 5 x 10 ⁻⁵	Blöschl and Sivapalan (1995)	1 to 100	collection from numerous sources	various

It is interesting to note that the maximum velocity from Blöschl and Sivapalan (1995) overlaps with the minimum velocity of viscous flow only in the range from 2.5×10^{-5} to $5.0 \times 10^{-5}(\text{m s}^{-1})$. With the exception of *Case 13.1*, the transition illustrates well the approximate threshold between the two domains of sequential and preferential flow as discussed in Sections 6.5 and 6.6. Blöschl and Sivapalan's minimum is about four orders of magnitude smaller than the maximum velocity of viscous flow.

13.6 Temporal and spatial extents of viscous flow

From complete momentum dissipation follow two properties of viscous flow that are observable across time and space:

- (i) constant wetting front velocity up to T_i and down to Z_i and
- (ii) absence of hydrostatic pressure.

The observed combination of the two properties is strong evidence of viscous flow, whereas ascertaining just one of them qualifies only as a plausible indication. Information is scarce on long-lasting infiltration experiments in large systems for assessing the evidence of viscous flow, largely because experimenters are hardly aware of this kind of flow.

Topic 13.8: *Spatio-temporal extents of viscous flow*

Case 13.1: *Presumed constant wetting front velocity:* Rimon et al. (2007) investigated groundwater recharge down to the 21-m depth in a sand dune on the central Coastal Plain of Israel. Storms were recorded at 39 days with intensities up to $45(\text{mm d}^{-1})$ during the period from 13 December 2004 to 15 March 2005. A clay-rich layer between the depths of 6.5 and 8.0(m) interrupted the otherwise unconsolidated sand of the now stable dune. The authors equipped three slanted boreholes with a total number of 34 flexible TDR-probes (FTDR) at various depths from close to the soil surface to the 21-m depth.

The data of first wetting front arrivals were taken from their Fig. 5 and are depicted in Fig. 13.2. Three depth sections are there delineated: ΔZ_1 refers to the range from the surface to about 3.5(m) with constant wetting front velocity [$v_F = 5.4 \times 10^{-6}(\text{m s}^{-1})$], with [$\mathcal{R}^2 = 0.83$] of the linear regression between the wetting front arrival times and depths, and 8 d.f.; ΔZ_2 : poorly defined wetting front movement above the clay layer; ΔZ_3 with constant [$v_F = 2.3 \times 10^{-6}(\text{m s}^{-1})$] in the range from about 6.8(m) to the lowest FTDR-probe at 21.0(m) with [$\mathcal{R}^2 = 0.94$], and 13 d.f.. The delineations are based on rather subjective ocular inspection, however, the linear regressions of wetting front depths vs. arrival times in sections ΔZ_1 and ΔZ_3 are significant. They indicate constant v_F and thus justify further viscous-flow interpretations. The

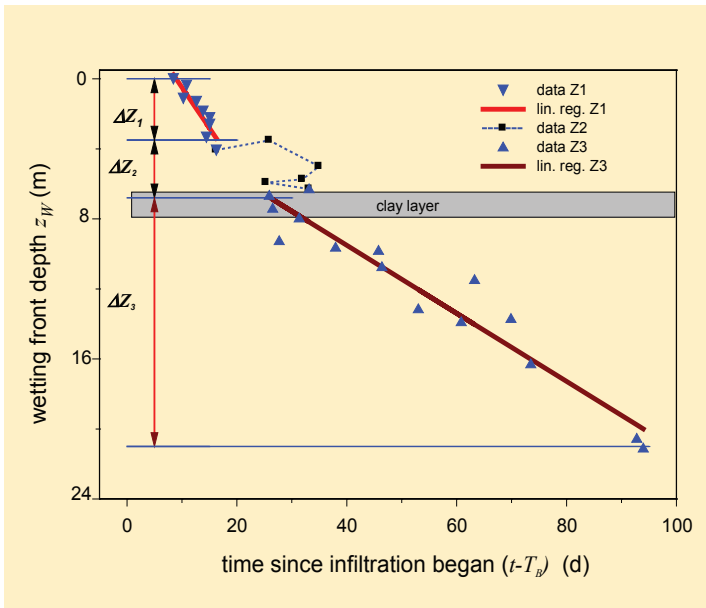


Figure 13.2, Case 13.1: First arrival times of the wetting front at the depths of 34 FTDR-probes in three boreholes. (Data from Rimón et al., 2007, their Fig. 5).

erratic front arrivals in section ΔZ_2 indicate congestion above the clay layer, suggesting *Case 10.4*.

Case 9.6, tracer-front velocity in crystalline rocks, refers to Dubois' (1991) tracer experiment across 1'800(m), yielding an average tracer front velocity of [$v_F = 1.9 \times 10^{-4}(\text{m s}^{-1})$]. The velocity scores well among those reported in Tab. 13.1. In addition, Dubois reported that the water was seeping into the Mt. Blanc car tunnel. This indicates that momentum dissipation continuously consumed the presumed enormous overall hydrostatic pressure. Thus, viscous-flow most likely applies to the case.

The analyses suggest the applicability of viscous flow in both Cases 9.6 and 13.1. The two approximate 100-d periods of infiltration connect well with the upper limit of several months that Blöschl and Sivapalan (1995) presented. However, the vertical distance of 1'800(m) in the crystalline rock by far outweighs their upper spatial limit of about 100(m). In conclusion, viscous flow may apply from typical soil infiltration in the meter-range to the generation of runoff in hillslopes and catchments in the kilometer-range.

13.7 Viscous flow scaling in hillslope hydrology

There are at least three more aspects of flow in hillslopes to consider when compared with infiltration in soil profiles:

- (i) the direction of flow bends from the vertical to a lateral movement. The resulting flow is usually dubbed *subsurface storm flow, SSF*;
- (ii) the slope angle reduces the gravitational force relative to the vertical;
- (iii) the lateral volume flux density increases in the downslope direction.

Topic 13.9: Flow-bending: A layer of reduced conductivity impedes vertical flow and diverts it in the lateral direction, which is referred as flow-bending. *Case 10.4* provides an example of water perching on a horizontal clay-rich B_r -horizon at the 0.8-m depth which would have initiated lateral flow if the horizon were inclined. With but limited results Germann and Zimmermann (2005) tried to determine the vectors of preferential flow in a sloping soil from triplets of TDR-probes that were installed as sides of a tetrahedron with one corner pointing into soil and the other three corners located on the soil surface.

Flow-impeding horizons are often readily discernible in profiles, they are documented in soil surveys, and they are frequently included in run-off models. One condition for a particular pulse P to initiate considerable *SSF* is the relation of its $Z_l(P)$, Eq.(13.9), to the depth Z_{imp} of the impeding layer. If $[Z_l(P) \geq Z_{imp}]$ the wetting front conditions of the upper section of the *WCW* prevail which is only reduced by the local abstraction. *SSF* reacts fast and strongly on P . If $[Z_l(P) \leq Z_{imp}]$ than the *SSF*-reaction is more sluggish and delayed. The degree of the difference between the two reaction types follows from Eqs.(13.10) and (13.12). However, also less obvious permeable-media properties may lead to flow-bending. Nyberg (1995), for instance, reported exponential decline of K_{sat} with depth in soils in the Gårdsjön-catchment in Sweden. The depth of flow-bending would most likely vary with P .

Topic 13.10: Slope angle: Any deviation from the vertical flow direction with an angle $[\beta > 0]$ reduces the impact of gravity on flow to $[\rho g \cos(\beta)]$. It is more convenient to discuss lateral flow in terms of the slope angle α against a horizontal reference plane, where $[\alpha = 90(^{\circ}) - \beta]$ and $[\sin(\alpha) = \cos(\beta)]$. The introduction of gravity reduction to the development of viscous flow, Eqs.(2.9) to (2.15), extends Eq.(3.2) to

$$q(F, L) = \frac{g \cdot \sin(\alpha)}{3 \cdot \eta} \cdot L \cdot F^3 \quad (13.16)$$

Let us assume a layer of coarse grains overlaying a fine-textured layer with the interface sloping at an angle $[\alpha > 0(^{\circ})]$. The well connected voids in the coarse grains permit free-surface flow with the volume flux density of q_{vert} and

q_{lat} , where the indices *vert* and *lat* refer to the vertical and lateral directions. Water perching is excluded at the sloping interface, thus both vertical and lateral flow occur under pressures less than atmospheric i.e., $[q_{lat} = q_{vert}]$.

For the sake of simplicity we assume that $[L_{lat} = L_{vert}]$, while the slope angle impacts only F in Eq. (13.13). From

$$q_{vert} = \frac{g}{3 \cdot \eta} \cdot L \cdot F_{vert}^3 = q_{lat} = \frac{g \cdot \sin(\alpha)}{3 \cdot \eta} \cdot L \cdot F_{lat}^3 \quad (13.17)$$

it follows that the film thickness of vertical to lateral flow scales according to

$$F_{lat} = F_{vert} \cdot (\sin(\alpha))^{-1/3} \quad (13.18)$$

The lateral mobile water content turns to

$$w_{lat} = L \cdot F_{lat} = L \cdot F_{vert} \cdot (\sin(\alpha))^{-1/3} \quad (13.19)$$

while the lateral velocity of the wetting front is

$$v_{lat} = \frac{q_{vert}}{w_{lat}} = \frac{g}{3 \cdot \eta} \cdot (\sin(\alpha))^{1/3} \cdot F_{vert}^2 \quad (13.20)$$

and the lateral celerity becomes

$$c_{lat} = \frac{g}{\eta} \cdot (\sin(\alpha))^{1/3} \cdot F_{vert}^2 \quad (13.21)$$

Beven and Germann (2013) have further explored *SSF*-scaling under the premise of the valid macropore flow hypothesis.

Conversely, the simplifying assumption of $[F_{lat} = F_{vert}]$ while letting the slope angle exclusively impact L produces the following scaling:

$$L_{lat} = L_{vert} \cdot (\sin(\alpha))^{-1} \quad (13.22)$$

The lateral mobile water content turns to

$$w_{lat} = F \cdot L_{lat} = F \cdot L_{vert} \cdot (\sin(\alpha))^{-1} \quad (13.23)$$

the lateral velocity of the wetting front is

$$v_{lat} = \frac{q_{vert}}{w_{lat}} = \frac{g}{3 \cdot \eta} \cdot \sin(\alpha) \cdot F^2 \quad (13.24)$$

and the lateral celerity becomes

$$c_{lat} = \frac{g}{\eta} \cdot \sin(\alpha) \cdot F_{vert}^2 \quad (13.25)$$

Figure 13.3 depicts the functions $[\sin(\alpha)^n]$ with $[n = \pm 1, \pm 1/3]$. If L is assumed not to be affected by α then slope inclinations steeper than 100(%), the equivalent to $[\alpha = 45(^{\circ})]$, cause the parameters of viscous flow to deviate by less than ± 0.12 times from those of vertical viscous flow, while slope inclinations have to be flatter than 13(%) i.e., $[\alpha = 7.5(^{\circ})]$ for at least a doubling of F and w , and a halving of v and c , Eqs.(13.18) to (13.21). Conversely, if F is assumed not to be affected by α then slope inclinations exceeding 100(%) cause the parameters of viscous flow to deviate by less than ± 0.4 times those of vertical viscous flow, while inclinations need to be less than 58(%) i.e., $[\alpha = 30(^{\circ})]$ for at least a doubling of L and w , and a halving of v and c , Eqs.(13.22) to (13.25).

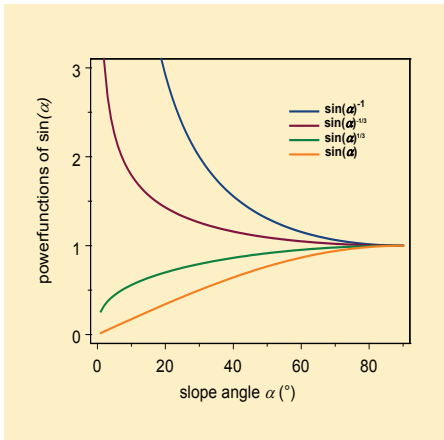


Figure 13.3: Functions of $[\sin(\alpha)]$ with the exponents 1, 1/3, -1/3 and -1, indicating the sensitivities of lateral v and c , and F and L as functions of the slope angle α . Only slopes flatter than $[\alpha < 7.5(^{\circ})]$ or steepness of less than $[\text{tg}(\alpha) < 0.13]$ let F and w more than double, and reduce v and c to less than half of vertical viscous flow due to the reduced gradient of gravity.

Topic 13.11: *Flow integration along a hillslope:* Consider input $P(q_s, T_E, T_B)$ to a soil surface on a slope. It releases a WCW which will bend at some depth Z_{imp} and time T_{imp} , say, due to a layer of lesser permeability (see, for instance, Fig. 10.4). Depth Z_{imp} and time T_{imp} indicate the initiation of SSF . Further, consider a vertical plane at some distance from the divide

(top of the slope) which is oriented in the contour-direction. *SSF* across this plane is the spatio-temporal integration of flow from the divide to the plane's down-slope position. The increasing rate of *SSF* in the down-slope direction will eventually lead to erosive turbulent flow and may create megapores as, for instance, Retter (2007) has found. Further, repeated erosive *SSF* may lead to slope failures. Lateral, down-slope spatio-temporal integration of *WCWs* arriving at an impeding layer is, however, beyond the scope of this book.

List of References

Bold numbers at the citation ends refer to the corresponding chapter.

- al Hagrey, S.A., T. Schubert-Klempnauer, D. Wachsmuth, J. Michaelsen, and R. Meissner. 1999. Preferential flow: First results of a full-scale flow model. *Geophys. J. Int.* 138:643-654. **1, 11**
- Alaoui, A. 1998. Transferts d'eau dans la roche du Jura (Marchairuz). Department of Geography - Internal report (unpublished). **9**
- Alaoui, A., P. Germann, N. Jarvis, and M. Acutis. 2003. Dual-porosity and kinematic wave approaches to assess the degree of preferential flow in an unsaturated soil. *Hydrological Sciences-Journal-des Sciences Hydroligiques* 48(3): 455-472. **1**
- Anderson, S.H., and J. W. Hopmans (Eds.). 2013. *Soil-Water-Root Processes: Advances in Tomography and Imaging*. Soil Sci. Soc. Am. Special Publication 61. **8**
- Beven, K.J., Germann, P.F. 1982. Macropores and water flow in soils, *Water Resour. Res.*, 18(5), 1311-1325, 1982. **1, 8**
- Beven, K.J., Germann, P.F. 2013. Macropores and water flow in soils revisited, *Water Resour. Res.*, doi: 10.1002/wrcr20156. **1, 8**
- Blöschl, G., and M. Sivapalan. 1995. Scale issues in hydrologically modelling – a review. *Hydrol. Process.* 9:251-290. **13**
- Brutsaert, W. 1964. The propagation of elastic waves in unconsolidated unsaturated granular mediums. *J. Geophys. Res.* 69,243-257. **12**
- Brutsaert, W. 2005. *Hydrology – An Introduction*. Cambridge University Press, Cambridge (UK). **2**
- Buckingham, E. 1907. The mechanic of soil moisture. US Department of Agriculture, Division of Soils, Bulletin 10. **1**
- Colbeck, S. 1974. Water flow through snow overlaying an impermeable boundary. *Water Resour. Res.* 10(1):119-123. **5**
- Couette, M. M. A. 1890. Etude sur le frottement des liquides. *Ann. de chimie et phys.* xxi, 433. **2**
- Cueto-Felgueroso, L., and R. Juanes. 2009. A phase field model of unsaturated flow. *Water Resour. Res.* 45. W10409, doi:10.1029/2009WR007945. **3**
- Dane, J.J., and Lenhard, R.J. 2005. Hysteresis. In: D. Hillel (ed.-in-chief). *Encyclopedia of Soils in the Environment*, Vol. 2. Elsevier, Amsterdam. **6**
- Darcy, H. 1856. *Les fontaines publiques de la ville de Dijon*. Dalmont, Paris. **1, 6**
- DiCarlo, D.A. 2004. Experimental measurements of saturation overshoot on infiltration. *Water Resour. Res.* 40, W04,215. **11**
- DiCarlo, D.A., J. I. G. Cidoncha, and C. Hickey. 2003. Acoustic measurements of pore-scale displacements. *Geophys. Res. Lett.* 30(17):190, doi:10.1029/2003GL017811. **13**

- Di Pietro, L., A. Melayah, and S. Zaleski. 1994. Modeling water infiltration in porous media by interacting lattice-gas cellular automata. *Water Resour. Res.* 30:2785-2792. **1**
- Di Pietro, L. 1996. Application of lattice gas numerical algorithm to modelling water transport in fractured porous media. *Transp. Por. Media* 22:307-325. **1**
- Dubois, J.-D. 1991. Typologie des aquifers du cristallin: Exemples des massifs des Aiguilles Rouges et du Mont-Blanc. (Typology of Aquifers in the Cristaline: Examples from the Massifs Aiguilles Rouges and Mt. Blanc). Ph.D.-dissertation 950. Department of Civil Engineering, EPFL, Lausanne (Switzerland). **9, 13**
- Flammer, I., A. Blum, A. Leiser, and P. Germann. 2001 Acoustic assessment of flow patterns in unsaturated soil. *J. of Applied Geophys.* 46:115-128. **12**
- Friedman, S.P. 1999. Dynamic contact angle explanation of flow rate-dependent saturation-pressure relationships during transient liquid flow in unsaturated porous media. *J. Adhesion Sci. Technol.*, 13(12):1495-1518. **6**
- Gerke, H.H., and M. Th. van Genuchten. 1993. A dual-porosity model for simulating the preferential movement of water and solutes in structured porous media. *Water Resour. Res.* 29:305-319. **1**
- Gerke, H.H., P. F. Germann, and J. Nieber. 2010. Preferential and unstable flow: From the pore to the catchment scale. *Vadose Zone J.* 9:207-212. doi: 10.2136/vzj2010.0059. **1**
- Germann, P. 1976. Wasserhaushalt und Elektrolytverlagerung in einem mit Wald und einem mit Wiese bestockten Boden in ebener Lage. *Mitt. Eidg. Anst. forstl. Vers'wes.* 52: 163-309. **11**
- Germann, P. 1980. Untersuchungen über den Bodenwasserhaushalt im hydrologischen Einzugsgebiet Rietholzbach. In: Vischer, D. (ed.): *Mitteilungen der Versuchsanstalt für Wasserbau, Hydrologie und Glaziologie*, Bd. 51: 3-134. **1, 8**
- Germann, P. F. 1985. Kinematic wave approach to infiltration and drainage into and from soil macropores. *Trans. ASAE*, 28(3):745-749. **4**
- Germann, P. 2001. A hydromechanical approach to preferential flow. Chapter 10, p.233-260 in; Anderson, M.G., and P. D. Bates (eds.). *Model Validation: Perspectives in Hydrological Sciences*. John Wiley & sons, Ltd., Chichester etc. **8**
- Germann, P.F., and K. Beven. 1985. Kinematic wave approximation to infiltration into soils with sorbing macropores. *Water Resour. Res.* 21(7):990-996. **4**
- Germann, P.F., and D. Hensel. 2006. Poiseuille flow geometry inferred from velocities of wetting fronts in soils. *Vadose Zone J.* 5:867-876. doi:10.2136/vzj2005.0080. **1, 9**
- Germann, P.F., and S. A. al Hagrey. 2008. Gravity-driven and viscosity-dominated infiltration in a full-scale sand model. *Vadose Zone J.* 7: 1160-1169. doi: 10.2136/vzj2007.0172. **11**
- Germann, P., and B. Levy. 1986. Rapid response of shallow ground water tables upon infiltration – A call for information. *EOS* 2/25/86: 92. **13**

- Germann, P.F., and M. Zimmermann. 2005. Directions of preferential flow in a hillslope soil. Quasy-steady flow. Hydrol. Process. 19:887-899. **13**
- Germann, P.F., W.M. Edwards, and L.B. Owens. 1984. Profiles of bromide and increased soil moisture after infiltration into soils with macropores. Soil Sci.Soc.Am.J. 48(2): 237-244. **1**
- Germann, P.F., R.S. Pierce, and K. Beven. 1986. Kinematic wave approximation of subsurface storm flow in a sloping forest soil. Adv. Water Resources 9:70-76. **8**
- Germann, P.F., M.S. Smith, and G.W. Thomas 1987. Kinematic wave approximation to the transport of *Escherichia Coli* in the vadose zone. Water Resour. Res. 23(7):12281-1287.
- Germann, P.F., L. Di Pietro, and V.P. Singh. 1997. Momentum of flow in soils assessed with TDR-moisture readings. Geoderma 80:153-168. **6**
- Germann, P.F., E. Jäggi, and T. Niggli. 2002a. Rate, kinetic energy and momentum of preferential flow estimated from in-situ water content measurements. Europ. J. Soil Sci.53:607-617. **10**
- Germann, P.F., A. Allaoui, and D. Riesen. 2002b. Drag force approach to the transport of colloids in unsaturated soils. Water Resour. Res. 38(10); doi:10.1029/2001WR000744. **10**
- Germann, P., A. Helbling, and T. Vadilonga. 2007. Rivulet approach to rates of preferential infiltration. Vadose Zone J. 6:207-220. Doi: 10.2136/vzj2006.0115. **9**
- Ghezzehei, T. A., and D. Or. 2005. Liquid fragmentation and intermittent flow regimes in unsaturated fractured media. Water Resour. Res. 41(12): W12406. doi:10.1029/2004WR003834. **6**
- Haines, W.B. 1930. Studies in the physical properties of soil. V. The hysteresis effect in capillary properties, and the modes of moisture distribution associated therewith. J. Agric. Sci., 20:97-116. **12**
- Halliday, D., and R. Resnick. 1978. Physics, Parts 1 & 2. John Wiley & Sons, New York etc., 1131 p. **2**
- Hassanizadeh, S.M., M.A. Celia, and H.K. Dahle. 2002. Dynamic effect in the capillary pressure-saturation relationships and its impacts on unsaturated flow. Vadose Zone Journal 1:38-57. **11**
- Heijs, A. W. J., J. de Lange, J. F. T. Shoute, and J. Bouma. 1995. Computed tomography as a tool for non-destructive analysis of flow patterns in macroporous clay soils. Geoderma 64:183-196. **1**
- Helmholtz, H. 1860. Ueber Reibung tropfbarer Flüssigkeiten. Wien. Sitzungsbericht, xi. 607. **2**
- Hillel, D. 1998. Environmental Soil Physics. Academic Press, San Diego etc. 771 p. **6, 8, 12**
- Hillel, D. 2005. Preface. In: D. Hillel (ed.-in-chief). Encyclopedia of Soils in the Environment, Vol.1. Elsevier, Amsterdam. **1**
- Hincapié, I. 2008. Gravity-driven viscous flow in unsaturated soils, sand and sand stone. Dissertation, Faculty of Sciences, University of Bern (unpublished), 113 p. **10**
- Hincapié, I., and P. Germann. 2009a. Abstraction from infiltrating water content waves during weak viscous flows. Vadose Zone J. 8:996-1003; doi:10.2136/vzj2009.0012. **1**

- Hincapié, I., and P. Germann. 2009b. Impact of initial and boundary conditions on preferential flow. *J. Contaminant Hydrol* 104:67-73. **1, 9**
- Hincapié, I., and P. Germann. 2009c. Gravity-driven viscous flow in sand boxes assessed with neutron radiography. *Vadose Zone J.* 8:891-901; doi:10.2136/vzj2009.003. **9**
- Hincapié, I., and P. Germann. 2010. Water content wave approach applied to neutron radiographs of finger flow. *Vadose Zone J.* 9:278-284; doi:10.2136/vzj2009.0102. **9**
- Jäggi, E. 2001. Strukturverbesserung eines verdichteten Bodens mit Chinaschilf *Miscanthus sinensis*. MSc-thesis, Faculty of Science, University of Bern (Switzerland), unpublished. **12**
- Jarvis, N. J. 2007. A review of non-equilibrium water flow and solute transport in soil macropores: Principles, controlling factors and consequences for water quality. *Eur. J. Soil Sci.*, 58:523-546. doi:10.1111/j.1365-2389.2007.00915.x, 2007. **1**
- José, J.V., and E. J. Saletan. 2000. Classical dynamics - A contemporary approach. Cambridge University Press, Cambridge (UK), 670 p. **2**
- Jury, W.A. 1999. Present directions and future research in vadose zone hydrology. Chapt. 17 in M.B. Parlange and J. Hopmans (Eds.) *Vadose Zone Hydrology-Cutting Across Disciplines*. Oxford University Press, New York, Oxford. **1**
- Jury, W.A., W.R. Gardner, and W.H. Gardner. 1991. *Soil Physics* (5th Edition). John Wiley & Sons, New York. **6**
- Kutilek, M., and P.F. Germann. 2009. Converging hydrostatic and hydromechanic concepts of preferential flow definitions. *J. Contaminant Hydrol* 104:61-66. doi: 10.1016/j.conhyd.2008.06.004. **9**
- Lamb, H. 1932. *Hydrodynamics*. Sixth Edition. Cambridge University Press (UK). **2**
- Lange, B., Germann, P.F., and Lüscher, P. (2011): Runoff-generating processes in hydromorphic soils on a plot scale: free gravity-driven versus pressure-controlled flow. *Hydrological Processes*, 25, 873-885. **12**
- Lange, B., Lüscher, P., and Germann, P.F. (2009): Significance of tree roots for preferential infiltration in stagnic soils. *Hydrology and Earth System Sciences*, 13, 1809-1821. **12**
- Lawes, J.B., J.H. Gilbert, and R. Warington. 1882. On the Amount and Composition of the Rain and Drainage Water Collected at Rothamsted. Williams, Clowes and Sons Ltd., London. 167 p. **1**
- Lazouskaya, V., Y. Jin, and D. Or. 2006. Interfacial interactions and colloid retention under steady flows in a capillary channel. *J. Colloid. Interf. Sci.* 303:171-184. **12**
- Lehmann, E.H., P. Vontobel, and L. Wiesel. 2001. Properties of the radiography facility NEUTRA at SINQ and its potential for use as European Reference Facility. *Nondestructive Testing and Evaluation*, 16 (2-6):191-202. **10**
- Levy, B.S., and P. F. Germann 1988. Kinematic wave approximation to solute transport along preferred flow paths in soils. *J. Contaminant Hydrol.* 9:263-276. **13**

- Lighthill M.J., and G.B. Witham. 1955 a. On kinematic waves, I. Flood movement in long rivers. Proc. R. Soc. London, Ser. A, 229: 281-316. **4**
- Lighthill M.J., and G.B. Witham. 1955 b. On kinematic waves, II. A theory of traffic flow on long, crowded roads. Proc. R. Soc. London Ser. A 229, 317-345. **4**
- Lin, S.P., and C.Y. Wang. 1986. Modeling wavy film flows. p. 931-951. *In: Encyclopedia of Fluid Mechanics*, Vol. 1. Gulf Publishing Co., Houston, TX. **2, 3**
- Maxwell, 1866. On the Dynamical Theory of Gases. Phil. Trans. clxxvii. 49. **2**
- Mdaghri Alaoui, A., P. Germann, L. Lichner, and V. Novak. 1997. Preferential transport of water and ¹³¹Iodide in a clay loam assessed with TDR-techniques and boundary-layer flow theory. Hydrology and Earth System Sciences 4:813-822. **8**
- Newton, I. 1729a. The Mathematical Principles of Natural Philosophy-Translation into English. Vol.III, p.202, Benjamin Motte, London (UK). **2**
- Newton, I. 1729b. The Mathematical Principles of Natural Philosophy-Translation into English. Vol. III, Benjamin Motte, London (UK). **2**
- Newton, I. 1729c. The Mathematical Principles of Natural Philosophy-Translation into English. Vol. I, p.19, Benjamin Motte, London (UK). **2**
- Newton, I. 1729 d. The Mathematical Principles of Natural Philosophy-Translation into English. Vol. II, p.184, Benjamin Motte, London (UK). **2**
- Nyberg, L. 1995. Soil and groundwater distribution flowpaths, and transit times in a small till catchment. PhD Thesis. Department of Hydrology, Uppsala University, Sweden. **13**
- Ohashi, H. 1988. Kinematic Wave Approach to Assess Soil Macropore Deformation Due to Rainfall Impact. M.Sc.-Thesis, Graduate School-New Brunswick, Rutgers, The State University of New Jersey (unpublished) 86 p. **8**
- Poiseuille, J.L.M. 1846. Recherches expérimentales sur le mouvement des liquides dans les tubes de très petits diamètres. Comptes Rendus, xi-xii. Mém. des Sav. Etrangers, ix. **2**
- Ransohoff, T.C., and C. J. Radke. 1988. Laminar flow of a wetting liquid along the corners of a predominately gas-occupied noncircular pore. J. Colloid Interface Sci. 121: 392-401. **3**
- Reeves, M.J. 1979. Recharge and pollution of the English Chalk: some possible mechanisms. Engineering Geol.14:231-240. **9, 13**
- Retter, M. 2007. Subsurface flow formation. Dissertation, Faculty of Sciences, University of Bern (unpublished), 97 p. **13**
- Reynolds, O. 1886. On the theory of lubrication, &c. Phil. Trans. clxxvii. 157. **1**
- Richard, F., P. Lüscher, and T. Strobel. 1978. Physikalische Eigenschaften von Böden der Schweiz. (Physical Properties of Swiss Soils) In: Bosshard, W.(Hrsg.) Bd. 1. Sonderserie der EAFV, Birmensdorf (Schweiz). **5**

- Richards, L.A. 1931. Capillary conduction of liquids through porous mediums. *Physics* 1:318-333. **1, 6**
- Rimon, Y., O. Dahan, R. Nativ, and S.Geyer. 2007 Water percolation through the deep vadose zone and groundwater recharge: Preliminary results based on a new vadose zone monitoring system. *Water Resour. Res.*, 43; W05402; doi:10.1029/2006WR004855. **9**
- Roth, K., R. Schulin, H. Flühler, and W. Attinger. 1990. Calibration of Time Domain Reflectometry. *Water Resour. Res.* 26 (10): 2267-2273. **8**
- Schmalz, B., B. Lennartz, and M.T. van Genuchten. 2003. Analysis of unsaturated water flow in a large sand tank. *Soil Sci.* 168(1): 3-14. **11**
- Schütz, P. 2002. Erfassung der Grobporenstruktur in Ackerböden mittels horizontal und diagonal eingebauter TDR-Sonden. (Macropores in Arable Soils Assessed with Horizontally and Diagonally Installed TDR-probes) M.Sc.-Thesis, Faculty of Science, University of Bern (unpublished, 97 p.). **8**
- Selker, J., J.-Y. Parlange, and T. Steenhuis. 1992. Fingering flow in two dimensions. 2. Predicting finger moisture profile. *Water Resour. Res.* 28:2523–2528. **10**
- Seneviratne, S.I., I. Lehner, J. Gurtz, A.J. Teuling, H. Lang, U. Moser, D. Grebner, L. Menzel, K. Schrott, T. Vitvar, and M. Zappa, 2012: Swiss pre-alpine Rietholzbach research catchment and lysimeter: Analysis of 32-year hydroclimatological time series and 2003 drought. *Water Resour. Res.*, 48, W06526. doi: 10.1029/2011WR011749. **8**
- Shizowa, S., and H. Fujimaki. 2004. Unexpected water content profiles and flux limited one-dimensional downward infiltration in initially dry granular media. *Water Resour. Res.* 40:W07404, doi:10.1029/2003WR002197. **9**
- Sněhota, M., M. Císlarová, G. H. Gao Amin, and L. D. Hall. 2010. Tracing the entrapped air in heterogeneous soil by means of magnetic resonance imaging. *Vadose Zone J.*, 9:373-384, doi:10.2136/vzj2009.0103 **1**
- Sposito, G. 1986. The “Physics” of soil water physics. *Water Resour. Res.* 22(9):83S-88S. **6**
- Stokes, G.G. 1845. On the theories of internal friction of fluids in motion. *Transactions of the Cambridge Philosophical Society* 8, pp. 287-319. **2**
- Stokes, G.G. 1851. On the effect on the lateral friction of fluids on the motion of pendulums. *Trans. Cambridge Phil. Soc.* 9:8-106. **2**
- Swartzendruber, D. 2005. Darcy’s law. In: D. Hillel (ed.-in-chief): *Encyclopedia of Soils in the Environment*, Vol.1. Elsevier, Amsterdam. **6**
- Tröhler, B. 1976. Zur Grösse der Grundwasserneubildung durch Niederschläge in Talebenen des schweizerischen Mittellandes. *Gaz-Eaux-Eaux usées*, 56(7):359-362. **13**
- Tuller, M., and D. Or. 2001. Hydraulic conductivity of variably saturated porous media: Film and corner flow in angular pore space. *Water Resour. Res.* 37(5):1257-1275. **3, 5**
- Vadilonga, T., X. Ubéda, P.F. Germann, and M. Lorca. 2008. Effects of prescribed burning on soil hydrological parameters. *Hydrol. Proc.* 22:4249-4256. **10**

- Veihmeyer, F. J., and A. H. Hendrikson. 1949. Methods of measuring field capacity and permanent wilting capacity of soils. *Soil Sci.* 68:75-94. **6**
- Watson, K. W., and R. J. Luxmoore. 1986. Estimating macroporosity in a forest watershed by use of a tension infiltrometer. *Soil Sci. Soc. Am. J.* 50:578-582. **1**
- Wellings, S.R., and J. P. Bell. 1980. Movement of water and nitrates in the unsaturated zone of upper chalk near Winchester, Hants., England. *J. Hydrol.* 48:119-136. **1**
- Wooding, R. A. 1965. A hydraulic model for the catchment-stream problem. *J. Hydrol.* 3:254-267. **4**
- Zheng, W., Wang, L.-P., V. Lazouskaya, D. Or, and Y. Jin. 2012. Role of mixed boundaries on flow in open capillary channels with curved air–water interfaces. *Langmuir* 28 (35):12753-12761. doi10.1021/la302833p. **12**

List of Topics

Topic 8.1:	Determination of F and L from transient drainage flow	84
Topic 8.2:	Flow path dimensions and viscous flow	87
Topic 8.3:	Determination of L and F from the measured θ_{init} and θ_{max} at depth Z_{meas} , while optimizing $t_W(Z_{meas})$	87
Topic 9.1:	Estimating $t_W(Z_{meas})$ from the increasing limb of $\theta(Z_{meas}, t)$	91
Topic 9.2:	Determination and superposition of a WCW 's rivulets	93
Topic 9.3:	Viscous flow matching under conditions of $[\theta_{div} > 0]$ compared with $[\theta_{div} = 0]$	95
Topic 9.4:	Linear-reservoir approach to drainage flow	97
Topic 9.5:	Darcy-flow vs. viscous flow	99
Topic 9.6:	Interval length required to cover the significant part of $q(Z, t)$	100
Topic 9.7:	Investigation of v_F vs. q_S	101
Topic 9.8:	Viscous flow in fissured rocks	103
Topic 10.1:	Evolution of a WCW from in-situ infiltration experiments	108
Topic 10.2:	Empirical assessment of viscous-flow initiation based on in-situ infiltration	110
Topic 10.3:	Viscous-flow restriction due to a compacted layer	115
Topic 10.4:	Viscous-flow restriction due to a capillary fringe	117
Topic 10.5:	Viscous flow alterations due to abrupt changes in the viscous-flow paths	119
Topic 10.6:	Wetting front velocity during finger flow	120
Topic 10.7:	Analyses of $\theta(t, Z_j)$ -time series at various depths Z_j	122
Topic 10.8:	Water-content profiles, $\theta(z, T_k)$ at specific times T_k	124
Topic 10.9:	Water balance of finger flow	126
Topic 11.1:	Wetting front velocity v_F and film thickness F	136
Topic 11.2:	Matching profile-level $\theta(Z_j, t)$ with viscous flow	136
Topic 11.3:	Matching cumulative drainage flow $V(Z_{N+1}, t)$ with viscous flow	137
Topic 11.4:	Initial $\theta_{init}(Z_j)$ and $h_{cap,init}(Z_j)$ vs. depth	137
Topic 11.5:	Spatial structure of $L_{im}(Z_j)$ and $L_{dr}(Z_j)$	139
Topic 11.6:	Spatial structure of θ_{div}	140
Topic 11.7:	Spatial structure of the slopes $(d\theta/dt)(Z_j)$ of imbibition limbs	140
Topic 11.8:	Impacts of $h_{cap,init}(Z_j)$ and $\theta_{init}(Z_j)$ on the viscous-flow parameters	141

Topic 11. 9:	Delay of GPR-readings	142
Topic 11.10:	Capillary heads h_{cap} during viscous flow	142
Topic 12. 1:	Applicability of viscous flow to superimposed kinematic waves	147
Topic 12. 2:	Theoretical assessment of viscous flow dimensions with a glass-bead model	150
Topic 12. 3:	Tortuosity	152
Topic 12. 4:	Surface tension in the AWI	153
Topic 12. 5:	Throat effect of plane-Poiseuille flow	155
Topic 12. 6:	Throat effect at the profile level	156
Topic 12. 7:	Independence of the WCW from hydrostatic $h_{cap}(\theta_{init})$	158
Topic 12. 8:	$h_{cap}(F)$ at the wetting front	162
Topic 12. 9:	Tree roots improve hydromorphic forest soils	164
Topic 13. 1:	Temporal scaling of front velocities	168
Topic 13. 2:	Temporal scaling of mobile water contents	169
Topic 13. 3:	Temporal scaling of volume flux densities	169
Topic 13. 4:	WCW-scaling in the upper depth range of $[0 \leq z \leq Z_i]$	170
Topic 13. 5:	WCW-scaling in the lower depth range of $[z \geq Z_i]$	170
Topic 13. 6:	Benefits of macropore flow	171
Topic 13. 7:	Documented wetting front velocities	172
Topic 13. 8:	Spatio-temporal extents of viscous flow	174
Topic 13. 9:	Flow-bending	176
Topic 13.10:	Slope angle	176
Topic 13.11:	Flow integration along a hillslope	178

List of Symbols

Symbol	Unit	Section	Definition
A	m^2	2.3	cross-sectional area
Bo	-	6.6	Bond number
C	m^{-1}	2.5	specific water capacity
Ca	-	6.6	capillary number
D	$\text{m}^2 \text{s}^{-1}$	6.5	diffusivity
\mathcal{F}	kg m s^{-2}	2.2	force
F	m	2.3	film thickness
FC	$\text{m}^3 \text{m}^{-3}$	6.5	field capacity
G	$\text{m}^3 \text{kg}^{-1} \text{s}^{-2}$	2.2	constant of gravity
H	m	6.2	total hydraulic head
I	on application	9.3	intercept of linear regression
K	m s^{-1}	6.2	hydraulic conductivity
L	m m^{-2}	3.2	contact length of a WCW per unit A
L	$\text{m}^2 \text{m}^{-3}$	3.2	area of momentum dissipation per unit volume of the medium
L^*	m^{-1}	13.4	L at $q_s = K_{sat}$
M_p	-	12.5	pressure wave modulus
N_p	-	4.1	number
P	m s^{-1}	3.1	input pulse
Q	$\text{m}^3 \text{s}^{-1}$	2.4	volume flux
R	m	5.3	radius
\mathcal{R}	-		linear regression coefficient
\mathcal{R}^2	-	5.4	coefficient of determination
RC	m	12.2	candle radius
RD	m m^{-3}	12.6	root density
$\mathcal{R}e$	-	5.5	scaling factor
\mathcal{T}	$^{\circ}\text{C}$	2.3	temperature
T	s	3.1	point in time
V	m^3	2.2	volume
V	m	3.1	volume per area
W	m^2	2.4	water volume per unit depth
WX	-	12.2	candle-radius coefficient
Z	m	3.3	point at specific depth
Z^*	m	4.7	cessation depth of a WCW with sink
a	m s^{-2}	2.3	acceleration
b	m s^{-1}	4.2	conductance
c	m s^{-1}	2.3	thickness variable

List of Symbols (cont.)

Symbol	Unit	Section	Definition
g	m s^{-2}	2.2	acceleration due to gravity, $9.81 \text{ (m s}^{-2}\text{)}$
h	m	2.2	potential per unit weight
m	kg	2.2	mass
l	m	6.2	length
p	$\text{kg m}^{-1} \text{ s}^{-2}$	2.5	pressure
q	m s^{-1}	3.1	volume flux density
r	m	2.2	radius variable
ret	s	10.5	retardation
rh	m	5.1	hydraulic radius
s	s^{-1}	4.7	sink strength
s_j	s^{-1}	9.3	slopes of rivulets
t	s		variable of time
uF	m^3, m	12.6	parameter of film-thickness function
uL	m, m^{-1}	12.6	parameter of contact-length function
v	m s^{-1}	2.3	velocity
w	$\text{m}^3 \text{ m}^{-3}$	3.2	mobile volumetric water content
x, y	m		variables of the horizontal directions
z	m	2.2	variable of depth
Δ	-	2.2	difference
$\Pi(hcap)$	-	2.5	frequency distribution of menisci
Φ	-	5.4	corner-flow function
α	$^\circ$	2.5	contact angle of wetting fluid
		13.7	slope angle
β	$^\circ$	2.5	contact angle of non-wetting fluid
		13.7	angle of deviation from the vertical
γ	$\text{kg m}^{-2} \text{ s}^{-2}$	2.2	specific weight
γ	$^\circ$	5.4	corner angle
ζ	m	3..	depth interval
ε	$\text{m}^3 \text{ m}^{-3}$	3.5	porosity
η	$\text{m}^2 \text{ s}^{-1}$	2.3	kinematic viscosity
θ	$\text{m}^3 \text{ m}^{-3}$	2.5	total volumetric water content
λ	s^{-1}	9.5	coefficient of linear reservoir
κ	-	12.4	coefficient of funnel flow
μ	$\text{kg m}^{-1} \text{ s}^{-1}$	2.3	dynamic viscosity
ξ	-	12.4	tortuosity factor
π	-		constant ($\approx 22/7$)
ρ	kg m^{-3}	2.2	mass density
σ	kg s^{-2}	2.5	surface tension
τ	s	3.4	time period

List of symbols (cont.)

Symbol	Unit	Section	Definition
φ	$\text{kg m}^{-1} \text{s}^{-2}$	2.3	shear force
ψ	$\text{kg m}^{-1} \text{s}^{-2}$	2.2	potential per unit volume
\varnothing	m	8.3	diameter

List of Subscripts

Symbol	Section	Definition
<i>B</i>	3.1	beginning
<i>Co</i>	5.4	corner flow
<i>D</i>	3.3	draining front
<i>E</i>	3.1	ending
<i>F</i>	8.1	front
<i>G</i>	2.2	gravity
<i>Hg</i>	6.2	mercury
<i>H₂O</i>	6.2	water
<i>HOH</i>	12.5	water
<i>I</i>	3.3	interception
<i>J</i>	4.2	jump of consecutive pulses
<i>M</i>	6.2	manometer
<i>P</i>	2.5	parallel plates
<i>RE</i>	3.3	rear end
<i>S</i>	3.1	surface
<i>W</i>	2.4	wetting front
<i>ac</i>	12.5	acoustic
<i>af</i>	2.5	affinity
<i>b</i>		bulk
<i>cap</i>	2.5	capillarity
<i>char</i>	3.6	characteristic
<i>contr</i>	10.5	control
<i>cyl</i>	2.5	cylinder
<i>dr</i>	8.1	drainage
<i>div</i>	9.4	divergence
<i>fs</i>	5.1	free surface
<i>end</i>	9.4	at the end
<i>im</i>	9.4	imbibition
<i>imp</i>	13.8	impermeable
<i>init</i>	9.4	initial

List of Subscripts (cont.)

Symbol	Section	Definition
<i>j</i>		integer
<i>k</i>		integer
<i>kin</i>	3.6	kinetic
<i>lat</i>	13.8	lateral
<i>lin</i>	9.5	linear reservoir
<i>lo</i>	2.5	lower
<i>max</i>		maximum
<i>meas</i>	8.1	measurement
<i>min</i>		minimum
<i>mob</i>	3.5	mobile
<i>p</i>	6.2	pressure
<i>pm</i>	5.1	porous medium
<i>q</i>	13.2	volume flux density
<i>s</i>	10.5	stored
<i>sat</i>	6.2	saturated permeable medium
<i>thresh</i>	6.5	threshold
<i>tot</i>		total
<i>up</i>	2.5	upper
<i>v</i>	6.3	viscous flow
<i>v</i>	13.2	velocity
<i>vert</i>	13.8	vertical
<i>visc</i>	9.5	viscous flow
<i>w</i>	13.2	mobile water content

List of Acronyms and Abbreviations

Acronym / Abbreviation	Section	Definition
<i>AP</i>	12.4	aperture
<i>AWI</i>	2.5	air-water interface
BAFU		Bundesamt für Umwelt (Swiss Federal Administration for the Environment)
<i>BC</i>	3.6	boundary condition
<i>Co</i>	5.4	corner flow

List of Acronyms and Abbreviations (cont.)

Acronym/ Abbreviation	Section	Definition
EAFV		Eidgenössische Anstalt für das forstliche Versuchswesen (Swiss Forest Research Station)
ETH		Swiss Federal Institution of Technology
FWT	2.5	free water table
FTDR	13.8	flexible time domain reflectometry (Rimon et al. 2007)
GPR	11.3	ground-penetrating radar
<i>HP</i>	5.3	Hagen-Poiseuille
<i>IC</i>	3.6	initial condition
INRA		Institut National de la Recherche Agricole (French National Agricultural Research Institute)
NEUTRA	10.5	Neutron Radiography Facility at the Paul-Scherrer Institute, Villigen (Switzerland)
NSF		National Science Foundation (US)
<i>REV</i>		representative elementary volume
SNF		Schweizerischer Nationalfonds zur Förderung der wissenschaftlichen Forschung (Swiss National Science Foundation)
<i>SWI</i>	2.5	solid-water interface
TDR		time domain reflectometry
<i>WCW</i>	3.1	water-content wave
WSL		Eidgenössische Forschungsanstalt für Wald, Schnee und Landschaft (Swiss Federal Institute of Forest, Snow, and Landscape Research, formerly EAFV)
USDA		US Department of Agriculture
USEPA		US Environmental Protection Agency
<i>d.f.</i>		degrees of freedom
<i>pP</i>	5.2	plane Poiseuille
<i>stdv</i>		standard deviation

Index

A			
abstraction	94, 141	characteristics	38
acceleration		Chernozem	110
due to gravity	14	clay-loam	114
of wetting front	156	clickers	162
acoustic bursts	162	compacted B _T -horizon	116
acoustic velocities	159	conductance <i>b</i>	39
Adelphia	3	confocal microscope	153
affinity	20	connected voids	2
Aguilles Rouges	103	constant wetting	
air-dry	23	front velocity	18, 108, 121, 136
ambiguity	80	contact angle	20
amplitude of a <i>WCW</i>	81	contact length	
annual water balance	1	definition	26
arable soil	108	from drainage	96
area of momentum		from imbibition	96
dissipation of		convex decreasing limb	116
corner flow	57, 59	corner flow	53
cylinder flow	56	Couette-flow	16
free-surface flow	26	creeping flow	12
plane-Poiseuille flow	54	crystalline rocks	103, 175
artificial macropores	85, 87	cross-sectional area	26
<i>AWI</i>	18	cumulative drainage	100, 135
B		D	
Bantiger	87	D-day 1944	162
blocky structure	108	Darcy's law	63
boundary conditions	33, 81	data acquisition	80
Bratislava	111	reliability	148
B _T -horizon	115	deceleration of front	42
C		deductive procedures	13
c-g-s system	16	delay of GPR-readings	136
capillary flow	4, 5, 69	depth of interception	27, 40
capillary fringe	117, 133	depth integration of <i>WCW</i>	28
capillary head		diffuse pores	110, 114
hydrostatic	21	diffusivity	70
in viscous flow	142	dimensions	167
capillary potential	22	Dirichlet boundary	75
capillary rise	20, 71	dispersive wave	38
Catalunia	114	disturbance	167
celerity	27	divergence	95, 139
		draining front	27

drainage, transient	84
dual-porosity concept	6
dual-process	7
dye staining	130

E

editorial note	9, 81
English chalk	103
Eutric Cambisol	115
evapo-transpiration	1
experimental testing	12

F

feeble tensile strength	73
field capacity FC	72
film	
definition	16
determination	82
thickness	18
finger flow	6, 117
fissured rocks	103
flow-bending	175
flow integration	178
flow-path	
dimension	87
level	81, 147
width	115
flow restrictions	115
fluid affinity to solid	20
flux-controlled input	81
forest soils	164
free-surface flow	18, 53
free water table	19
front interception	27

G

gas phase	65
geometry scaling	60
glass beads	101
gradients of potential	14
gradients of h_{cap}	138, 144
gravitational constant	14
gravity head	65
goodness-of-fit	80, 88

GPR	133
gradual increase of WCW	94
gravity	8, 13
ground-penetrating radar	133

H

Hagen-Poiseuille flow	53
Helmholtz Equation	16
hillslope hydrology	175
hydraulic head	14, 65
hydraulic radius	53
hydromorphic soils	164
hydrostatic conditions	138
HYDRUS-2D	146
hysteresis in $[K - \psi - \theta]$	73

I, J

imbibition	140
inductive method	13
infiltration	1
infiltration fronts	2
initial conditions	33
ink-bottle effect	157
input cascading	37
input pulse	25
in-situ experiments	108
interception	1, 27, 40
interception function	42, 44
irrotational flow	12
isotropy	70

K

$K(h_{cap})$	69
$K(q, x, y)$ vs. $K(q, z)$	70
Kiel sand tank	133
kinematic continuity	38
kinematic viscosity	12, 16
kinematic wave	37
kinetic energy of WCW	35
K_{sat}	66

L	
laminae	15
rear ends	27
lateral flow	127
lattice-gas automaton	6
linear reservoir	97
loam	110
local level	81, 91
Lorin's candle	147
lubricity	7
lumen	55
lysimeter	98

M	
MACRO	6
macropore	
artificial	85
flow hypothesis	101, 171
flow restriction	67
Marchairuz	103
maximum pore radius	21
mercury manometer	65
micro channel	153
<i>Miscanthus sinensis</i>	95
mistletoe	15
mobile water	8
model validity	148
Mollisol	110
momentum dissipation	16
Mt. Blanc	103

N	
nabla operator	12
Navier-Stokes equation	6, 12
NEUTRA-facility	118
Neuman boundary	81
Neutron probe	3
neutron radiographs	117
Newtonian fluids	15
non-equilibrium flow	6
non-linearity	
in Darcy's law	67
no-slip condition	18
non-wetting fluid	2

O	
open channel flow	53
ordinary flow	5

P	
parabolic velocity profile	18
particle tracking	153
Paul-Scherrer Institute	118
perching water table	2
plane-Poiseuille flow	53
plow layer	108
ponding	2
pore domains	8
porosity	23
porous matrix	2
pore-scale displacements	162
preferential flow	5
preferential infiltration	2
pressure	8
pressure transducer	2
pressure-wave modulus	158
principle radii	22
procedure level	81
profile level	81, 107
profiles of $w(z,t)$	29, 125
pulse of input	25
pulse routing	25

Q, R	
radiographs	118
rear end of lamina	28
rectangular pulse	37
representative	
elementary volume	24
retention curve	23
REV	24
Reynolds number	19
Richards equation	70
Rietholzbach	98
rivulets	92
roots	95, 164
routing	25

S	
sand castle effect	158
sandy loam	108
sandy substrate	142
saturation	23
scale tolerance	131
scales	167
scaling of	
flow geometries	60
macropore flow	68
viscous flow	176
in hillslopes	176
sequential flow	6
sessile water	8
shear force	17
shapes of $\theta(Z,t)$	111
shock	38
silty clay-loam	114
simple-cubic packing	150
sink term	50
slope angle	176
soil column	89
soils	4
spatial extent	174
spatial scaling	168
spatial structure	139, 140
specific contact length	26
specific water capacity	24
sprinkler device	115
strong tensile strength	73
surface tension	19
superposition	
in candle	147
of rivulets	93
<i>SWI</i>	18
Swiss Jura	103
system level	81, 133

T	
TDR	87, 95, 108, 133
temporal extents	174
temporal scaling	170
tensile strength	7, 79, 159

tensiometer	133
texture effect	142
theory	12
throat effect	
of pP -flow	155
at the profile level	156
time-domain	
reflectometry	133
time of	
beginning of input	105
draining front arrival	105
end of input	105
interception	27, 41, 42, 44
wetting front arrival	105
time series of $w(z,t)$	31
tortuosity	152
trailing wave	28, 41
tractor rut	95
transient drainage	84
transition from linear re- servoir to viscous flow	99
transpiration	2
typic Hapludalf	159

U	
unconfined	14
unconsolidated sand	118, 134

V	
velocity of wetting front	
definition	18
determination	83
examples	172, 173
viscous flow	4, 25
viscosity	8
and temperature	16
<i>Viscum album</i>	15
visible macropores	85, 149

W	
water abstraction	94
water balance	
elements	128

of finger flow	126
water-content	
divergence	95, 105
during imbibition	105
during drainage	105
maximum of WCW	105
prior to infiltration	105
at cessation of WCW	100, 105
profiles	29, 124
time series	33
water-content wave	
amplitude of	81
definition	25
volume flux density	39, 84
water potential	14
water pulse	25
wave velocity	27
of jump	39
weak tensile strength	73, 109
weighing lysimeter	98
wide paths	109
widest aperture	22
wetting fluid	2
wetting shock front	18, 26
wetting front velocities	172, 173

X, Y, Z

Zollikofen	115
------------	-----